Biomechanical and genetic analysis of neural tube closure in the mouse embryo

Abigail Rose Marshall

Developmental Biology and Cancer Department

UCL Institute of Child Health

Thesis submitted for the degree of Doctor of Philosophy

January 2021

Declaration of contribution

I, Abigail Rose Marshall, confirm that the work presented in this thesis is my own.

Most experiments were performed by me. I was assisted by Dr Gabriel Galea for some laser ablation experiments. Dr Zoe Crane-Smith performed differential expression and gene ontology analysis after RNA sequencing.

Where information has been derived from other sources, I confirm that this has been indicated in the thesis.

……

Abigail Rose Marshall

Abstract

Development of the neural tube (NT), the embryonic precursor to the brain and spinal cord, consists of bending and folding of the neural plate into a complete tube during neural tube closure (NTC). Cells and tissues undergo gross changes in position and shape throughout NTC, for which the underlying mechanism ultimately depends on integration of their biomechanics. This thesis focuses on the biomechanical role of the surface ectoderm (SE), the layer of cells that overlies the closing neural folds, in spinal NTC.

Techniques which allow investigation of the biomechanical properties of cells and tissues include cell shape analysis, laser ablation and expression analysis of genes involved in force generation and detection. Throughout this thesis, these techniques are used to probe SE biomechanics in wild type mouse embryos, and in *Grhl-2* and *-3* mutant embryos. *Grhl-2* and *-3* are SE-expressed transcription factors, and mutations in these genes lead to severe neural tube defects (NTDs), making them a valuable model for studying the role of the SE in NTC.

Characterisation of the wild type SE revealed an elongation of SE cells along the rostrocaudal midline. Surprisingly, functional analysis reveals this is not due to high rostrocaudal tension, challenging the classical view that cell shape can be used to predict the forces that cells are under, and raising the hypothesis that elongation may be a result of intrinsic cell behaviour.

The characteristic elongated SE cell shape is lost in *Grhl2* mutants, which also show significantly abnormal cell and tissue level recoil after laser ablation, and disrupted YAP and actomyosin expression. One of the most significant differentially expressed genes in *Grhl2* mutants is E-cadherin. Experimental disruption of E-cadherin function supports the importance of this molecule in causing biomechanical abnormalities – together, these results suggest that cell-cell adhesion is an important player in driving normal closure of the NT. Further studies in this thesis show that NTDs in *Grhl3* gain- and loss-of function mutants are not due to the same molecular mechanisms as for *Grhl2*. RNA sequencing suggests a novel role of desmosomes, which are also important in cell-cell adhesion.

Finally, a novel mechanism which may contribute to severe NTDs in $Vangl2^{Lp};Grhl3^{ct}$ double mutants is explored. Although this thesis does not support reduced tailbud proliferation as a causative mechanism, a novel genetic interaction between $Vangl2^{Lp}$ and overexpression of *Grhl3* is identified.

Impact statement

Development of the early embryonic brain and spinal cord occurs during a process called neural tube closure (NTC). Failure of this process leads to a group of severe congenital disorders called neural tube defects (NTDs). Anencephaly and craniorachischisis, the most severe NTDs, are lethal. Meanwhile, failure of the spinal cord to develop leads to the NTD spina bifida, which is compatible with life but leads to severe disability. Spina bifida has an incredibly complex environmental and genetic aetiology. Identifying the genetic and environmental risk factors behind spina bifida, and the mechanisms which cause increased risk, is a major challenge for developmental biologists.

Genetic mutant mouse embryos provide a valuable model for the study of NTC. Biomechanics is an evolving field of research, and it is becoming increasingly clear that abnormal mechanics can cause NTC to fail in mouse embryos, either as a result of genetic or environmental disruption. The surface ectoderm (SE), which goes on to form the skin, is a poorly understood tissue in the context of NTC, however previous work suggests it may play an important biomechanical role. This thesis characterises the biomechanical properties of the SE in embryos which either succeed or fail to close their neural tube, and provides evidence that specific perturbation of SE biomechanics may predispose to NTDs. This shows that therapies which correct biomechanical defects should be a research focus in the future.

Mouse embryos which have mutations in multiple genes are also valuable for this field of research, as many human NTDs are not caused by a single mutation. Genetic interactions between *Grhl3* and *Vangl2* lead to severe NTDs; this thesis explores a novel cellular mechanism previously suggested to cause these defects, and a new genetic interaction is identified. Discovery and characterisation of novel genetic mutations is vital for the success of screening programmes designed to identify women who are at risk of having affected pregnancies.

Acknowledgements

I would first like to thank my supervisors, Nick Greene, Andy Copp and Gabe Galea, for their constant support throughout my PhD. I can't overstate how valuable it is to have supervisors who are always available to answer questions or help with experiments, and for this I am very grateful.

Thank you to the rest of the neural tube research group, who provided a welcoming environment from the start. Thank you to Sandra and Zoe, who both showed endless patience when helping me with new techniques.

My family and friends have been a steadfast support throughout. I am eternally grateful to my sister Charlie and brother-in-law Stephen, for giving me the study through Lockdown 1.0. I wrote a huge amount of this thesis during that period, taking off a lot of pressure. Thank you to Saba, for always understanding the highs and lows of research over a bottle (or two) of wine. Thank you to Charlotte and Helena, for seeming appropriately impressed and confused by what I do to give me that extra motivation. Thank you to Mum and Dad, for never being pushy parents. Finally, thank you to Charlie – the ultimate calming influence.

Table of Contents

List of Figures

List of Tables

List of Abbreviations

AP	anterior-posterior
BAC	bacterial artificial chromosome
CE	convergent extension
EdU	5-ethynyl-2’-deoxyuridine
EX	exencephaly
IP	intraperitoneal
ML	mediolateral
NE	neuroepithelium
NP	neural plate
NT	neural tube
NTC	neural tube closure
NTD	neural tube defect
PCP	planar cell polarity
PSM	pre-somitic mesoderm
PNP	posterior neuropore
RC	rostrocaudal
SB	spina bifida
SE	surface ectoderm
SR	somite region
TFD	tail flexion defect
ZP	zippering point

Chapter 1 - General introduction

1 .1 - Early mouse development and neurulation

Development of the mouse embryo, from fertilisation at embryonic day (E)0 to birth at E19-20, is a valuable model for the study of mammalian embryogenesis, and has contributed to much of our current understanding. The first signs of structure develop at the 8 cell stage during a process called compaction, where cell-cell adhesions increase to create apico-basal polarity and a more spherical shape; it is a vital process for the viability of the embryo and implantation success (White et al., 2016). At the 16 cell stage, cells spatially segregate to enclose a small number of cells. These inner, apolar cells are biased towards becoming inner cell mass (ICM) and forming the embryo proper and yolk sac. Outer cells, which can be both polar and apolar, become trophectoderm (TE), which forms extraembryonic membranes.

By the 32 cell stage, the fluid-filled blastocoel begins to form, creating a blastocyst. An osmotic gradient generated by Na^+/K^+ ATPases results in inward movement of water, and the maintenance of the blastocoel depends on the epithelial TE and its water-sealing tight junctions (Cockburn and Rossant, 2010). Meanwhile, the ICM begins to further differentiate into the epiblast, which goes on to form the future embryo, and the primitive endoderm (PrE), which forms the yolk sac. At ~E4.5, the still developing blastocyst implants into the uterine wall.

After implantation, the formation of the body axes begins with the anterior-posterior (AP) axis, when a structure called the anterior visceral endoderm (AVE) secretes signals to the adjacent epiblast cells, specifying them as the future anterior embryo. The region of the epiblast which escapes these signals (at the future posterior end of the embryo) forms the primitive streak. A process called gastrulation then occurs, where the three germ layers- ectoderm, mesoderm and endoderm- are specified (Takaoka and Hamada, 2012). Mesoderm and endoderm progenitors migrate through the primitive streak to their future destination, while the remaining epiblast cells go on to form the ectoderm (Mikawa et al., 2004).

It is from the ectoderm that neurulation, the development of the brain and spinal cord, begins. A structure called the node at the anterior end of the primitive streak signals to the nearby ectoderm progenitors to become neural (neuroepithelium), while the remaining cells will form epidermis (surface ectoderm) (see Chapter 1.1.1) (Itasaki, 2015). The neural ectoderm/neuroepithelium (NE) begins as a flat sheet of cells known as the neural plate (NP), which then thickens to form a pseudostratified columnar NE adjacent to the squamous non-neural ectoderm/surface ectoderm (SE). The flat NP subsequently forms the closed neural tube

(NT) in a process called 'neural tube closure' (NTC). This occurs via a series of elevation and folding events, the shape and progression of which varies between species, until the neural folds fuse at the midline and NTC completes (Copp and Greene, 2016). The resulting structure consists of a neuroepithelial tube and an overlying layer of SE. Failure of this process leads to a group of severe congenital disorders known as neural tube defects (NTDs). The remainder of Chapter 1.1 will describe the process and mechanisms of each neurulation event in greater detail.

1.1.1 – Specification of the neural tube and surrounding tissues

In the early 20th century, Spemann and Mangold published a classical transplant experiment on salamander embryos that first revealed an important role of non-autonomous induction during early specification events. In 1924, they transplanted the dorsal lip of a salamander embryo to the ventral side of a host embryo, and showed that a symmetrical body axis developed from the transplant site (Spemann and Mangold, 1924, de Robertis, 2006). This suggested that, within the dorsal lip, an induction centre, or 'organiser', resides. The organiser is now known to reside in the dorsal marginal zone (DMZ) of the dorsal mesoderm (Kiecker et al., 2016). 40 years later, Nieuwkoop cultured the three germ layers of salamander embryos separately or together, and showed that induction of mesoderm required co-culture of presumptive endoderm and ectoderm, and that more specifically, signals from the endoderm induced mesoderm formation, and thus the organiser, from the ectoderm (Nieuwkoop, 1967, Kiecker et al., 2016).

In birds and mammals, the node at the anterior primitive streak is often described as a homologue of Spemann's organiser, based on similar transplantation experiments resulting in duplications of the AP axis (Martinez Arias and Steventon, 2018). The fact that these experiments all lead to formation of a secondary nervous system indicates the importance of 'organisers' in neural induction. It is now known that bone morphogenetic protein (BMP) antagonists, such as Chordin, Noggin and Follistatin, are the major signalling molecules controlling this process (de Robertis, 2006). Secretion of these molecules from the organiser inhibits activation of BMP receptors, promoting neural fate; blocking these antagonists in *Xenopus* disinhibits BMP signalling and neural induction fails (Kuroda et al., 2004, Rogers et al., 2009). Similarly, in the absence of these antagonists, BMP activity promotes epidermal fate (Kudoh et al., 2004). In the mouse, a homologous mechanism appears to be required for anterior neural induction, however the loss of BMP antagonists does not prevent expression of posterior neural genes.

Fibroblast growth factor (FGF) and Wnt signalling have also been implicated in neural induction. FGF inhibitors lead to loss of pan-neural markers in *Xenopus* explants (Rogers et al., 2009), however studies which show that FGF is sufficient are in lower organisms such as ascidians, or in highly artificial conditions, such as in *Xenopus* explants (Stern, 2005). In chick, exposure of the early embryo to an FGF-soaked bead leads to expression of posterior neural markers, but studies such as this cannot dissect out the role of other signalling pathways prior to FGF activity (Storey et al., 1998). Similarly, Wnt signalling has been shown to be necessary but not sufficient for chick neural induction (Patthey et al., 2009). Importantly, both FGF and Wnt have been implicated in BMP inhibition (Pera et al., 2003, Marchal et al., 2009), leading to a model where both Wnt and FGF may act to reinforce BMP antagonism, and potentially explaining why the loss of BMP antagonists is not sufficient to prevent posterior neural induction (Rogers et al., 2009, Andoniadou and Martinez-Barbera, 2013). Clearly, induction of neural fate is a complex process involving many signalling pathways, making it very difficult to isolate the roles of individual molecules, and our understanding of these signalling pathways remains incomplete.

The NT and its surrounding tissues are patterned along the dorsoventral (DV) axis, with the notochord directly underlying the floor plate at the ventral side and the roof plate positioned dorsally (Dessaud et al., 2008). The NT itself is also dorsoventrally specified, forming motor and sensory neurons at the dorsal and ventral NT respectively (Itasaki, 2015). The notochord is a particularly important structure in specifying cell fates along the DV axis. It is present at some point during the life span of all chordates, giving this group their name; in higher vertebrates, the notochord is transient, and is ossified to become part of the vertebrae (Stemple, 2005). Notochord is derived from the mesoderm germ layer - the process of mesoderm induction, as demonstrated by Nieuwkoop, is controlled by Nodal signalling gradients. In zebrafish, high levels of Nodal specify prechordal plate, while low levels specify notochord (Gritsman et al., 2000). In the mouse, notochord, prechordal plate (which goes on to form various ventral tissues of the head) and anterior head processes are derived from a population of cells at the anterior primitive streak, known as the axial mesoderm (Balmer et al., 2016). A possible dose-dependent mechanism which determines axial mesoderm differentiation, homologous to zebrafish Nodal signalling gradients, has been identified under the control of *Smad2/3* expression, which are transcription factors downstream of Nodal signalling. In *Smad2/3* double mutants, progressively more severe axial mesoderm phenotypes are observed, from defective expression of classical axial mesoderm markers (*Foxa2, Shh*) to complete loss of mesoderm (Dunn et al., 2004, Shen, 2007).

A number of signalling pathways play important roles in vertebrate DV patterning. Sonic hedgehog (Shh) and BMP/Wnt signalling domains are present at high concentrations at the ventral and dorsal NT respectively, gradually decreasing in concentration to form opposing morphogen gradients (Sagner and Briscoe, 2019). The resulting expression of homeodomain and basic helix-loop-helix transcription factors forms 11 distinct, spatially segregated domains of neural progenitors, which then differentiate further into specific neuronal subtypes (Sagner and Briscoe, 2019). The notochord is initially responsible for the production of Shh, and induces formation of the floor plate, which itself becomes a Shh producing centre (Dessaud et al., 2008). Mechanical removal of the notochord in chick embryos prevents floor plate formation and a shift of dorsal NT to expression of ventral markers, while transplantation of the notochord to the lateral wall of the chick neural groove leads to formation of an ectopic floor plate and expression of dorsal neuronal markers (Van Straaten et al., 1988, van Straaten and Hekking, 1991, Cleaver and Krieg, 2001). Meanwhile, BMP and Wnt ligands expressed from the roof plate are both sufficient to induce dorsal identities, and ablation of many different BMP and Wnts originating from the roof plate leads to loss of dorsal neuron populations (Sagner and Briscoe, 2019). However, the large number of ligands and receptors involved in these signalling pathways can complicate experiments aiming to further understand DV patterning.

1.1.1.1 - Neuromesodermal progenitors

The traditional dogma that neural cells are derived exclusively from the ectoderm has been challenged since the discovery of cells known as neuromesodermal progenitors (NMPs) (Henrique et al., 2015). NMPs make up a bipotent cell population which were first identified from lineage tracing in mouse embryos, and were shown to contribute to both neural and paraxial mesodermal fates (Tzouanacou et al., 2009). In this study, very low frequency labelling of single cells was achieved using rare spontaneous reversion of an inactive lacZ reporter (termed laacZ) to an active lacZ, leading to expression of β-gal under a ubiquitous Rosa26 promoter. This allowed cells from an individual progenitor, thus representing a single clone, to be tracked, and for their fates to be identified. Surprisingly, this study showed that 37% of neuroectoderm clones analysed at E8.5 also had labelled mesoderm cells, suggesting that ectoderm and mesoderm descendants do not have as distinct a segregation at gastrulation as previously thought. In addition, the frequency of clones contributing to neural and mesodermal lineages increased when analysed at E10.5, supporting the hypothesis that a distinct progenitor population is capable of producing both lineages after gastrulation (Tzouanacou et al., 2009,

Henrique et al., 2015). Most studies have reported coexpression of neural and mesodermal markers in this bipotent population (Olivera-Martinez et al., 2012). More recently this has been challenged, and only cells expressing the mesodermal marker *T* are capable of contributing to both NT and somites, with cells expressing the neural marker *Sox2* contributing only to the NT, suggesting that neural fate is downstream of mesodermal fate (Mugele et al., under review).

What is the function of the NMP population? Further fate-mapping studies using labelling of single epiblast cells at later stages (~E7.5) showed that only cells close to the node, which contribute to regions posterior to the hindbrain, produced neural and mesodermal lineages. Cells further away from the node, contributing to the cranial regions, were already specified as either neural or mesodermal (Henrique et al., 2015). This suggests that NMPs may be important in elongation of the spinal cord and posterior paraxial mesoderm. This is further supported by the fact that teratomas in the extreme spinal region often consist of multiple cell types (Copp and Greene, 2016). In one study, the number of T-expressing cells in chick and human chordoneural hinge (the site of NMPs in the midline of the tailbud) was shown to suddenly decrease towards the end of axial elongation, supporting the hypothesis that NMPs are important in late extension of the spinal NT (Olivera-Martinez et al., 2012). However, the degree to which this is the case, and the relative importance of NMPs compared to pre-specified cell populations, remains a subject of debate.

1.1.2 - Extension and shaping of the neural plate

At the same time as neurulation, the mouse embryo continues to grow. It is essential that during growth the NP is shaped in such a way to allow successful closure. Specifically, the process of convergent extension (CE), which extends the NP in the AP axis while simultaneously narrowing the mediolateral (ML) axis, is required, forming an embryo which is broader at the cranial region and narrower at the future spinal cord (Copp et al., 2003). CE is a highly conserved process which is essential for many developmental processes across species; it is believed to be cell autonomous as some tissues continue to undergo CE when isolated (Keller et al., 2000). CE was first identified as a mechanism during *Xenopus* notochord development, and has since been observed in multiple developmental contexts, such as *Drosophila* germ band extension and mouse cochlea development, among others (Keller et al., 2000, Wang et al., 2005, Shindo, 2018).

1.1.2.1 - The Planar Cell Polarity pathway

The major signalling pathway controlling CE is the planar cell polarity (PCP) pathway. So named due to its role in controlling orientation of epithelial cells by asymmetric distribution of PCP proteins, it is one of the three types of Wnt signalling pathways, the 'non-canonical' Wnt PCP pathway (Davey and Moens, 2017). It was originally discovered in mutant screening of *Drosophila*; the core family of PCP genes are the transmembrane receptors *Frizzled (Fz), Van gogh (Vang)* and *Flamingo (Fmi),* and the cytosolic proteins *Dishevelled (Dvl), Diego (Dgo)* and *Prickle (Pk)* (Peng and Axelrod, 2012). Regulation of cell polarity via this signalling pathway relies on the initial interactions between the transmembrane *Fz* receptor and cytosolic *Dvl* and *Dgo*, which are localised at the distal pole of the cell. At the same time, the proximal side of the cell is determined by a complex containing *Vang, Pk* and *Fmi* (Peng and Axelrod, 2012). This core pathway is highly evolutionarily conserved- vertebrates have a group of homologous genes, complicated by the fact that each group of genes contains several members. A second group of genes has also been identified as running in parallel or upstream of the core PCP pathway – known as the Fat/Dachsous/Four-jointed (Ft/Ds/Fj) pathway, it is similarly conserved in vertebrates, however its function is less well characterised in higher organisms (Matis and Axelrod, 2013, Blair and McNeill, 2018).

In NTC, PCP signalling is vital for successful completion. Mutations in core PCP genes in multiple species lead to severe NTDs, and somatic mutations have been associated with NTDs in humans (Tian et al., 2020). For example, injection of mutant *Dvl* into *Xenopus* blastomeres leads to failure of NTC, ranging from only a small lesion to the entire NT remaining open (Wallingford, 2002). In such models, abnormal CE causes the NP to remain too wide for the neural folds to fuse at the midline (Nikolopoulou et al., 2017). In the mouse, a number of severe NTD models result from mutations in the PCP pathway: homozygous mutants of the *loop-tail* mouse strain, for example, exhibit 100% of the most severe NTD craniorachischisis, and carry mutant alleles of *Vangl2*; this model will be reviewed in Chapter 1.3.2 (Kibar et al., 2001, Murdoch et al., 2001). As the less well characterised PCP pathway, Ft/Ds/Fj signalling is not as widely studied in the context of NTDs. Although multiple mutants have NTDs (e.g. $Fat1^{-/-}$ and $Fat4^{-/-}$ mouse embryos develop cranial and spinal defects respectively), these are not as severe as core PCP pathway mutants, and whether failed neurulation in these mutants arises from defective CE remains unknown (Nikolopoulou et al., 2017). In addition, mutation of PCP members at later stages of neurulation can lead to NTDs via mechanisms independent of CE, which will be discussed in Chapter 1.5.3.3.

1.1.3 - Neural plate bending

The folding of the NE and subsequent fusion at the midline is a discontinuous process in more complex species such as the chick and the mouse. This allows the embryo to continue to grow after closure has already begun. The point at which the neural folds first reach the midline, thus beginning closure, is known as an initiation site. In the mouse, four initiation sites have been identified (Figure 1.1). The first site, closure 1, forms at the cervical-hindbrain boundary at E8.5, before axial rotation. Closure 2 subsequently forms at the forebrain-midbrain boundary and closure 3 at the anterior extreme of the embryo (Greene and Copp, 2014). Finally, closure 5, which was hypothesised in humans based on the position of spina bifida lesions but only conclusively identified recently in the mouse, does not form until closure is almost complete (E10.5) at the most posterior end of the embryo (Van Allen et al., 1993, Galea et al., 2017). The naming of this initiation site as closure 5 is because the existence of a closure 4 was hypothesised in the literature at a more rostral position in the hindbrain, however this has never been conclusively identified (Golden and Chernoff, 1993, Van Allen et al., 1993). From these initiation sites, closure progresses bidirectionally from closures 1 and 2, caudally from closure 3 and, at the very end of closure, rostrally from closure 5. Primary neurulation completes with the closure of anterior, hindbrain and posterior neuropores, which are the terms given to the open NT before fusion (Copp and Greene, 2016, Galea et al., 2017). This progressive closure is known as zippering, as opposed to the simultaneous fusion of the entire AP axis seen in species such as *Xenopus (*Nikolopoulou et al*.,* 2017*)*.

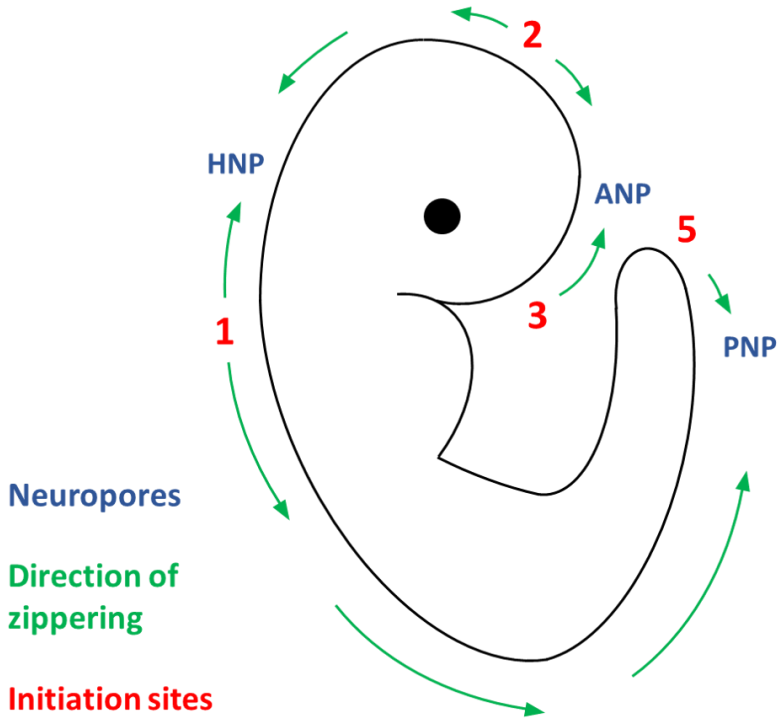

Figure 1.1 - The initiation sites of primary neurulation.

There are four initiation sites during primary neurulation, from which closure progresses bidirectionally to shorten and eventually close three neuropores. Closure 1 is at the cervical-hindbrain boundary. Closure 2 is at the forebrain-midbrain boundary. Closure 3 is at the anterior end of the embryo. Closure 5 is at the posterior end of the embryo. ANP = anterior neuropore. HNP = hindbrain neuropore. PNP = posterior neuropore.

During spinal closure, the type of folding which occurs and the resulting morphology of the NT differs depending on the position along the AP axis. This was described in 1993 as the three modes of closure: mode 1, which occurs in the anterior NT until somite 18 in wild types, is characterised by formation of a single fold at the midline (the medial hinge point, MHP), with the neural folds remaining otherwise straight to form a slit-shaped lumen; mode 2 occurs between somites 17 and 27, and demonstrates formation of an MHP and two paired folds dorsolaterally (dorsolateral hinge points (DLHPs)), with the neural folds remaining straight and resulting in a diamond shaped lumen; mode 3, which occurs mostly between somites 24 and 31 in wild types but has been identified further rostrally, shows curved neural folds with no identifiable hinge points, resulting in a circular lumen (Figure 1.2) (Shum and Copp, 1996).

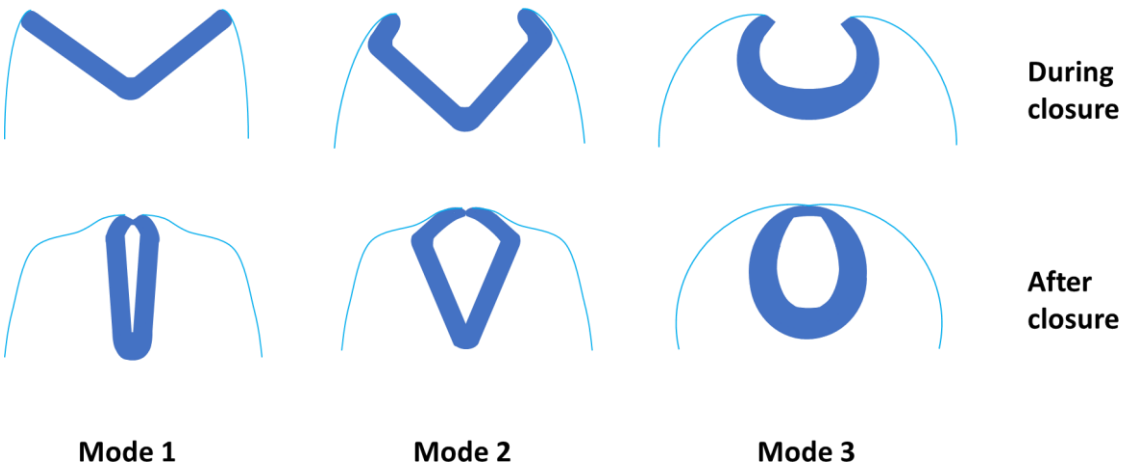

Figure 1.2 - The three modes of spinal closure.

The SE is shown in light blue, while the NE is represented in dark blue. Mode 1 – only a medial hinge point forms, resulting in a NT with a slit-like morphology. Mode 2 – both a medial hinge point and paired dorsolateral hinge points form, resulting in a NT with a diamond-like morphology. Mode 3 – neither hinge points form, resulting in a NT with a rounded morphology.

There are several cellular mechanisms implicated in neural fold bending. The most well characterised mechanism is contraction of actin microfilaments in the apical NE, leading to formation of wedge-shaped cells and subsequent inward bending (Nikolopoulou et al., 2017). Enrichment of actin and non-muscle myosin are observed in the apical region of NP cells, along with regulatory proteins such as RhoA and Shroom3. This accumulation is required for closure in some contexts- for example, in *Xenopus*, loss of Shroom-dependent enrichment of actin at

the apical NP prevents apical constriction and subsequently causes NTC to fail (Haigo et al., 2003, Escuin et al., 2015, Nikolopoulou et al., 2017). However, in higher vertebrates, several lines of evidence suggest alternative actin-independent mechanisms might be involved. In higher vertebrate neurulation, actin and Shroom3 are not localised specifically to hinge points; in addition, disruption of microfilaments using cytochalasin D treatment in culture causes cranial NTC to fail, while spinal neurulation continues normally (Ybot-Gonzalez and Copp, 1999).

In the pseudostratified NE of chick and mouse, an additional mechanism has been identified which drives apical constriction – interkinetic nuclear migration (IKNM). Nuclear position partly determines the shape of pseudostratified epithelia, and indeed the proportion of cells in S-phase of the cell cycle (with a basal nucleus) and the length of the cell cycle is higher at the site of MHP formation, at 7 hours compared to 4 elsewhere (Schoenwolf and Franks, 1984, McShane et al., 2015). Interestingly, alterations in the cell cycle are not observed at presumptive DLHPs in regions undergoing mode 2, suggesting a different mechanism of DLHP formation. Differences in cell proliferation and ventro-dorsal translocation of neuroepithelial cells have led to the hypothesis that high cell density at the DLHP induces apical constriction at the point where NE meets SE, due to physical constraints imposed by the SE (McShane et al., 2015).

The molecular pathways which induce and regulate NP bending are well characterised, with signals from the notochord and SE influencing the NE from the ventral and dorsal directions respectively (Nikolopoulou et al., 2017). Shh signalling from the notochord and floor plate promotes ventral differentiation and inhibits dorsal neuron differentiation (see Chapter 1.1.1), and is important in MHP formation (Ybot-Gonzalez et al., 2002). Meanwhile, at the dorsal side, BMP2 is secreted from the SE. It has since been shown that BMP2 signalling inhibits the formation of DLHPs, and that antagonism of BMP2 by noggin expression in the spinal region disinhibits DLHP formation (Ybot-Gonzalez et al., 2007a). In the cranial regions, Shh activity represses noggin expression, which disinhibits secretion of BMP2 from the SE and in turn prevents DLHP formation (Ybot-Gonzalez et al., 2007a, Nikolopoulou et al., 2017). The fact that Shh expression is graded from high to low along the AP gradient means that DLHP formation is gradually derepressed, and helps explain the transition between modes 1-3. Further evidence for this pathway comes from the study of mutants lacking notochord signalling. Mutant mouse embryos with defective notochord and floor plate development, such as *Shh*$^{-/-}$ embryos, and mouse embryos with the notochord removed by microdissection, undergo successful spinal NTC, despite the loss of MHP formation (Chiang et al., 1996, Davidson et al., 1999). This is because, in the absence of Shh signalling, DLHPs form in their place and allow successful closure (Nikolopoulou et al., 2017).

1.1.4 - Midline adhesion and completion of closure

Once the neural folds reach the midline, stable connections between opposite NE and SE layers must be made to complete closure. This process involves a switch in adhesion from NE-SE layers on either side of the midline, to NE-NE and SE-SE, in order to create the two distinct layers which go on to form the nervous system and skin. The mechanisms which control junctional remodelling are not yet understood, however the role of apoptosis at the boundary between the neural folds and the formation of protrusions are both implicated in the process.

Apoptosis has been identified in a number of regions during NTC, most notably in the open forebrain neural folds and the dorsal midline of the closed NT (Massa et al., 2009b). It has been suggested that cells without the appropriate NE-SE adhesions, or cells which lose their connections to the extracellular matrix (ECM) during remodelling, may be selectively triggered to undergo cell death, a process known as 'anoikis' (Massa et al., 2009a). This hypothesis is supported by the phenotype of *Merlin*$^{-/-}$ mutant mouse embryos. The *Nf2* tumour suppressor Merlin is important for cell-cell adhesion, and in a model of mosaic Merlin deletion, NTC failed - importantly, a reduction in stable adherens junctions and tight junctions led to a significant increase in apoptosis (McLaughlin et al., 2007). On the other hand, preventing apoptosis using a pan-caspase or p53 inhibitor on mouse embryos in culture does not prevent closure, and in *Casp3*$^{-/-}$ embryos, the majority of the NT (excluding the midbrain and hindbrain) closes successfully (Massa et al., 2009b). Nevertheless, it cannot be excluded that other types of non-apoptotic cell death are involved, and therefore more work must be done before the role of cell death at the neural folds during fusion can be elucidated (Yamaguchi and Miura, 2013).

In the 1970s, scanning and transmission electron microscopy were used to analyse the morphology of the neural folds just before completion of closure; such studies identified the presence of protrusions in a range of species, from *Xenopus* to mouse, and it is these which undergo the first point of contact (Waterman, 1976, Mak, 1978). These protrusions are described as either sheet-like 'ruffles' (lamellipodia) or spike-like filopodia (Nikolopoulou et al., 2017). Morphological analyses using EM images have shown that the cell of origin of these protrusions varies between species. In mouse, the first point of contact is between NE cells in the forebrain, and between SE cells in the midbrain, hindbrain and spinal region (Geelen and Langman, 1979, Rolo et al., 2016b). Further characterisation has shown that, in the mouse spinal region, the predominance of protrusion type varies over time. Filopodia are present in abundance at early stages of neurulation (from 7 somites), and this transitions to a mixture of

filopodia and lamellipodia at mid stages (from 12 somites), to a majority of lamellipodia at late stages (from 24 somites) (Rolo et al., 2016b).

Two small GTPases of the Rho family, Rac1 and Cdc42, are important for protrusion formation by regulating actin-cytoskeleton turnover; specifically, Rac1 and Cdc42 are crucial for lamellipodia and filopodia formation respectively, with Rac1 photoactivation sufficient to induce lamellipodia, and dominant-negative Cdc42 preventing formation of filopodia (Govind et al., 2001, Wu et al., 2009, Ridley, 2011). In order to identify the cell origin, mutant mouse embryos with NE or SE specific knock-out of Cdc42 or Rac1 were analysed. This showed that knockout of neither GTPase in the NE influenced protrusion formation or closure. On the other hand, lamellipodia produced by SE cells are essential for late stage spinal closure, as knock-out of Rac1 specifically in the SE led to spina bifida in 89% of embryos (Rolo et al., 2016b). Because SE specific knockout of Cdc42 at early stages of neurulation is embryonic lethal before neurulation completes, its necessity could not be determined. However, these mutants showed a loss of filopodia and increase in lamellipodia, showing that filopodia in the spinal region also originate from SE cells (Rolo et al., 2016a, Rolo et al., 2016b).

The fusion of the neural folds is the final event of primary neurulation. As described in Chapter 1.1.3, NTC is a discontinuous process - the gradual zippering of the NT therefore forms three open structures known as the neuropores, which decrease in length and width as closure progresses. The anterior neuropore, between closures 2 and 3, and the hindbrain neuropore, between closures 1 and 2, close by ~E9.0 in wild type mouse embryos, while the posterior neuropore (PNP), between closures 1 and 5 at the extreme caudal end of the embryo, closes at ~E10.0, thus completing primary neurulation (Greene and Copp, 2014).

1.1.5 - Secondary neurulation

It has long been known that in higher vertebrates, including mice and humans, a further extension of the caudal NT is formed by a different mechanism, termed secondary neurulation. Rather than the bending and folding of the NP characteristic of primary neurulation, secondary neurulation involves formation of a lumen continuous with the primary NT from an initially solid mass of neural precursor cells (Shum and Copp, 1996, Copp and Greene, 2016). These precursors originate from the pluripotent NMP population in the tailbud, condense to form longitudinal cell masses, and finally undergo mesenchymal-epithelium transition (MET) and canalisation to form a lumen (Schoenwolf, 1984, Shum et al., 2010, Copp and Greene, 2016). Early studies of

canalisation in chick revealed that multiple lumina form during canalisation, which coalesce into the final complete NT; some human tail buds appear to contain multiple lumina, however these have not been identified in mouse, and their relevance in mammalian secondary neurulation remains unknown (Lemire, 1968, Schoenwolf and Delongo, 1980, Schoenwolf, 1984, Lew and Kothbauer, 2007). Failures in secondary neurulation are often associated with closed NTDs, which are found at low spinal regions. Importantly, condensation and canalisation of the secondary NT occurs beneath an intact SE, potentially explaining why skin-covered closed NTDs are common in this region.

1.1.6 - The mouse as a model of human neurulation

The mouse embryo is the most popular model for the study of early human development, due to its obvious morphological similarities, its rapid gestational length, and ease of genetic manipulation. As in the mouse, human neurulation shows multiple closure sites, although only closures 1 and 3 have been conclusively identified (Nikolopoulou et al., 2017). Interestingly, some mouse strains also lack closure 2, and undergo successful cranial closure ~80% of the time, potentially explaining why humans have evolved to develop without it (Copp and Greene, 2010). The recent discovery of closure 5 begs the question of whether human embryos also have a closure 5 – this is of particular interest due to the high proportion of NTDs which are found at the extreme caudal end of the spinal cord. Another major benefit of mouse studies is genetics. The long history of mouse inbreeding and creation of transgenic lines has provided a wealth of genetic mutants with which to study failure of NTC (discussed in Chapter 1.3).

However, there are a number of limitations holding back our understanding of human neurulation. A major challenge is the lack of human embryos displaying normal closure, as the majority of samples at this very early gestational stage display NTDs. This prevents many new findings in mouse from being compared in humans, thus making it difficult to predict the true relevance of mouse studies. Furthermore, the majority of NTD mouse models result from failure of primary neurulation, leading to a lack of secondary neurulation research; this is particularly concerning given that closed NTDs are predicted to arise from abnormal secondary neurulation.

Finally, as will be discussed in the remainder of this chapter, NTDs are highly complex conditions, with risk increased by a large variety of both environmental and genetic factors. While mouse models are important for studying single gene mutations and a range of environmental factors, these cannot reflect the reality of most human cases.

1.2 - Neural tube defects

Neural tube defects (NTDs) are one of the most common groups of congenital disorders, occurring when NTC fails. NTDs are categorised as either open or closed. Closed NTDs are skin-covered lesions which are always found at the lower sacral and coccygeal level of the spinal cord. Closed spina bifida (spina bifida occulta) develops when some of the spinal vertebrae are not completely fused but the affected area remains covered with skin and an intact menginges. Meningocele occurs when openings in the vertebrae lead to skin-covered protrusions of the meninges filled with CSF; this can be repaired by a simple surgery after birth. Importantly, closed NTDs do not display an exposed spinal cord, and are therefore mostly asymptomatic (Copp et al., 2015). However, symptoms associated with tethered cord syndrome (TCS) are common in these cases (Hertzler et al., 2010). Closed NTDs are predicted to result from failed secondary neurulation, based on the fact that they are found at the most posterior spinal region and neural tissue is not exposed to the environment (Copp et al., 2015).

Open NTDs result from termination of zippering at any point along the AP axis, leaving the brain and/or spinal cord open to the amniotic fluid and leading to degeneration of exposed neural tissue (Copp and Greene, 2013). Open NTDs affect ~1 in 1000 births, and vary in severity depending on the point at which primary neurulation fails (Copp and Greene, 2016). Failure of closure to initiate at closure site 1 leads to the most severe NTD, craniorachischisis. While closures 2 and 3 fuse normally, resulting in an intact forebrain and optic vesicles, the entire hindbrain and spinal cord fail to close. An open cranial NT is known as exencephaly (EX) in the developing embryo, and manifests as the clinical condition anencephaly at birth. This is a more varied condition, as either closures 2 or 3 can fail, leading to open midbrain and hindbrain or split face respectively (Copp and Greene, 2016). Finally, open spina bifida (SB), or myelomeningocele, occurs when zippering fails at any point along the spinal cord. This is the most common open NTD, and includes an open spinal cord and a meningeal sac. Traditionally, failure of initiation at a closure site was not implicated in SB, however the discovery of closure 5 at the most posterior spinal cord suggests that this could be responsible in some cases (Galea et al., 2017).

While craniorachischisis and anencephaly are both lethal before or shortly after birth, open SB is compatible with life. The initial developmental defect and the subsequent trauma is sometimes referred to as the 'two-hit' hypothesis, with failure of NTC the first 'hit' and in-utero nerve degeneration the second (Adzick et al., 2011, Saadai and Farmer, 2012). Depending on the

size of the lesion, open SB can cause severe, life-limiting symptoms which require ongoing medical care and represent a significant burden on the patient and their families. Below the lesion site, degeneration of nervous tissue leads to loss of motor function, and urinary and faecal incontinence is frequent (Copp et al., 2015).

At the level of the brain, structural abnormalities and resulting intellectual disabilities vary dramatically between patients. Decreased cortical thickness has been identified in affected human foetuses as early as 11 weeks gestation, and has been attributed to reduced proliferation of neuronal precursors (Fietz et al., 2020). In addition, enlarged ventricles are present in ~90% of cases, with hydrocephalus requiring surgery in 50-80% of cases (Del Bigio, 2010). Hydrocephalus is associated with Chiari type-II malformation, where a small posterior fossa causes the hindbrain (specifically the cerebellar vermis) to herniate through the base of the skull (Copp et al., 2015). However, whether the malformation is a cause or consequence of hydrocephalus is unclear, especially as either defect can be present without the other (Bell et al., 1980, Shoja et al., 2018). Enlarged ventricles lead to structural changes in the brain, caused by stretching of the white matter, and leading to cognitive disabilities. In one study, a group of 16 SB patients showed on average a 15% decrease in total cerebral white matter and a decrease in cortical thickness in all regions except the frontal lobe compared to controls (Juranek et al., 2008). In another study, diffusion tensor imaging revealed abnormal development of long-range connections in several pathways, such as between the occipital and temporal lobes, occipital and frontal lobes, and Broca's and Wernicke's areas (Hasan et al., 2008).

The fact that neurulation occurs so early in embryogenesis means that interventions to prevent NTDs completely are not possible, not least because many women do not know they are pregnant until after neurulation is complete. The major limiting factor for interventions designed to improve clinical outcome is timing. Screening and diagnosis for NTDs varies worldwide, with many developing countries failing to diagnose early- this is believed to contribute to the higher number of affected live births, as there are fewer elective terminations in such countries (Ntimbani et al., 2020). On the other hand, many countries offer first trimester ultrasounds from as early as 8 weeks, although in reality SB cannot be detected until ~12 weeks (Borg, 2017). In the UK, NTDs are not routinely screened for until the 20 week scan. National screening programmes to detect elevated maternal-serum alpha-fetoprotein (AFP) are also widespread, replacing early diagnostic tests for increased amniotic fluid levels of AFP, which were invasive and increased chance of miscarriage (Boyd et al., 2008, Copp et al., 2015, Palomaki et al., 2020).

The importance of early diagnosis is increasing as intra-uterine surgery to repair open SB becomes a reality. The aim of such surgery is to close the lesion and protect the open spinal cord from further degeneration. Indeed, affected foetuses display leg movements at earlier stages in gestation, showing the importance of early intervention (Korenromp et al., 1986). The first clinical trial of open fetal surgery, the Management of Myelomeningocele (MOMS) trial, showed that clinical outcomes are improved after surgery, such as need for a hydrocephalus shunt and motor function (Adzick et al., 2011). More recently, fetoscopic surgery has become more widespread, as this reduces the risks associated with open fetal surgery, such as preterm birth, maternal pulmonary edema and placental abruption (Adzick et al., 2011, Pedreira et al., 2016). Unfortunately, the success of these surgeries will always be limited by the degree of nerve degeneration that occurs before lesion repair. Therefore, preventative measures are a vital area of research.

1.2.1 - Environmental factors and prevention of neural tube defects

There are a number of environmental factors known to affect risk of NTDs, including maternal diabetes, obesity, valproic acid usage and impaired vitamin B-12 status (Eichholzer et al., 2006, Hughes et al., 2018). The most well-known preventative measure is the use of maternal folic acid supplements. This was proven to reduce the incidence of affected pregnancies, first in double-blind clinical trials and later in studies of countries which adopted mandatory food fortification (MRC Vitamin Study Research Group, 1991, Eichholzer et al., 2006). The mechanism behind this preventative effect is not thought to be a result of rescuing deficient folate levels, as the majority of affected pregnancies are not folate deficient (Kirke et al., 1993). Rather, it is thought that folate supplementation may act to support key cellular mechanisms required for closure. For example, one-carbon metabolism (of which folate is a vital player) is important in producing pyrimidines and purines for DNA synthesis, and in methylation (Copp and Greene, 2013). However, many NTDs are not preventable by folic acid. Other nutritional factors are therefore of interest in the hope of preventing folate-resistant cases. For example, inositol is a six carbon sugar alcohol which, when deficient in mouse and rat embryo culture, can cause NTDs. Furthermore, deficiency and supplementation of inositol can both worsen and rescue NTDs in folate-resistant genetic mouse models (Cockroft et al., 1992, Greene and Copp, 1997, Greene et al., 2017). As a promising alternative preventative supplement, a randomised clinical trial is ongoing (Greene et al., 2016).

Understanding why many NTDs are folate-resistant is an important question in furthering our understanding of their aetiology. It is known that some families show a genetic predisposition to having affected pregnancies; this has proven useful in identifying target genes through familial association studies (Greene et al., 2009), although this approach is limited as the more severe NTDs are not passed on through generations due to lethality. However, the majority of what we now know about the genetic pathways involved in neurulation comes from the study of mouse mutants which develop severe NTDs.

1.3 - Mouse models of neural tube defects

There are many mouse models which show NTDs, all with varying severity and penetrance, which can be used to study development of the NT (Copp and Greene, 2010). Some of these have clear single gene causes, such as the *loop-tail* mouse (Chapter 1.3.2), whereas others have complex modifying interactions between a number of genes, such as *curly-tail* (Chapter 1.3.3). Before the details of some of these mutant lines are discussed, it is necessary to give a brief introduction on how genetic mouse models are created.

1.3.1 - Generation of transgenic mouse lines

The suitability of mouse embryos as a model for studying human development (Chapter 1.1.6) is partly due to the large number of genetic mutants available. Many of the available models of NTDs are from non-targeted or spontaneously mutated inbred mouse strains. In the early days of mouse research, spontaneous mutants which arose by repeated inbreeding were popular. However, the rate of spontaneous mutations in the germ line was very low, so an alternative approach was found - chemical or X-ray induced mutagenesis, such as *N*-ethyl-*N*-nitrosourea (ENU), which could produce mutations at a rate ~250 times higher (1.5×10^{-3} per locus) than the spontaneous rate (5×10^{-6} per locus) (Nomura, 1988, Stanford et al., 2001, Kile and Hilton, 2005). A disadvantage to these models is that the mutation can be difficult to isolate, and in some cases multiple mutations converge on one or multiple phenotypes (Roths et al., 1999).

Advancements in genetic technologies have switched the focus from forward genetics to reverse genetics, the targeted creation of transgenic animals, to study the function of single or multiple genes. Further control over phenotypes can be introduced by tissue specific promoters and/or inducible mutations. The classical approach to generating transgenic animals was by

manipulating the DNA of mouse embryonic stem (ES) cells using targeted homologous recombination, followed by injection of ES cells into a mouse blastocyst, transfer into a pseudo-pregnant female by pronuclear injection to generate chimeras, and finally backcrossing and intercrossing the chimeras to generate homozygous mutants (Justice et al., 2011, Gurumurthy and Lloyd, 2019). The constructs used for targeted homologous recombination are usually designed to knockout genes by deleting or replacing parts of the gene. However, generating specific constructs for every experiment is difficult and time consuming, especially given that many designed constructs lead to phenotypes preventing the study of the target gene, such as embryonic lethality or genetic redundancy (Stanford et al., 2001).

Gene trap technology has proven a popular solution, where one of a number of universal constructs containing a reporter gene downstream of a splice acceptor sequence is randomly inserted into cells. If the vector is inserted into a gene, the splice acceptor sequence fuses the gene with the reporter, creating a fusion transcript (Forrai and Robb, 2005). This simultaneously allows the gene to be functionally disrupted, and its spatial and temporal expression patterns to be elucidated (Evans et al., 1997, Stanford et al., 2001). The reporter gene most frequently used is *β-geo,* which is a fusion protein encoded by *lacZ* (expressing β-galactosidase) and *neo* (conferring resistance to the neomycin antibiotic) (Borghi et al., 2012). Importantly, the *neo* gene is expressed under a constitutive promoter while the *lacZ* has no promoter, and is therefore under the control of the gene it has inserted into (Lee et al., 2007). This allows selection of cells which contain the vector by antibiotic resistance, and gene expression analysis using *β-galactocidase* expression. The fact that a universal vector is used allows identification of the integration site of a vector using 5'-RACE PCR (Forrai and Robb, 2005).

Another popular tool for generating transgenic mice is the Cre-*loxP* system. This enables an additional level of control, both temporally and spatially. The expression of Cre recombinase under a tissue specific promoter recombines two *loxP* sites flanking a region of interest, therefore disrupting the target sequence (Justice et al., 2011). If a promoter does not confer the temporal control required for a given experiment, a Cre-estrogen receptor ($CreER^T$) fusion protein can be used, which is only activated in the presence of 4-hydroxytamoxifen (Feil et al., 1996).

Although gene-traps and conditional mutagenesis are useful tools to study gene function, more precise genetic manipulation techniques are advancing rapidly, utilising programmable endonucleases for this purpose. Such techniques are particularly useful when attempting to recapitulate human mutations that can be as small as single nucleotide polymorphisms (SNPs).

The principle of this technique is that endonucleases will create a double-stranded cut in the DNA, and that this will be repaired by non-homologous recombination (which is prone to errors) or by homologous recombination using a DNA template (Guha et al., 2017). Homing endonucleases, zinc-finger endonucleases, transcription activator-like effector nucleases, and clustered regularly interspaced short palindromic repeats (CRISPRs) have all be used for this purpose (Gurumurthy and Lloyd, 2019). The CRISPR/Cas9 system is the most advanced and widely used of these techniques, as it uses guide RNAs to dramatically increase precision and efficiency (Hsu et al., 2014).

Finally, transgenic animals do not necessarily need to contain the gene of interest in the first place - insertion of a transgene (i.e. DNA from an external source) can be useful to determine the function of human specific genes of which there is no homologue (Justice et al., 2011). Bacterial or yeast artificial chromosomes (BACs or YACs respectively) are frequently used for such experiments, due to the ability to clone and insert very large constructs (Giraldo and Montoliu, 2001). The importance of such large cloning capacity is the ability to include a larger region up- and down-stream of the gene in order to avoid position effects; if only the coding region of the gene is inserted, its regulatory sequences will not be included and therefore its expression relies on its position of insertion (Giraldo and Montoliu, 2001).

1.3.2 – *Loop-tail*

The *loop-tail* mouse, so named due to its kinked tail phenotype, arose spontaneously in the 84th generation of an inbred colony over 70 years ago (Strong and Hollander, 1949, Stein and Rudin, 1953). Initial outcrosses identified the *Lp* mutation as dominant, and crosses between affected mice caused lethal craniorachischisis in ~25% of embryos, suggesting that this was the homozygous phenotype (Strong and Hollander, 1949). It was quickly confirmed in later studies that heterozygotes show 100% tail flexion defects (TFDs) with varying severity, and homozygotes show 100% craniorachischisis, demonstrating that *Lp* is semi-dominant (Copp et al., 1994).

An important question when studying mutants displaying NTDs is when the primary defect in closure arises. In 1994, a microsatellite sequence *Crp* was discovered, which was of a different length in *Lp* and wild type alleles (Copp et al., 1994). This allowed genotyping of embryos before defects were visible, which had not previously been possible in this strain. By analysing the phenotype of embryos from a *Lp/+* x *Lp/+* cross, the authors showed that homozygous mutants failed to form closure 1 at the hindbrain/cervical boundary (Copp et al., 1994). The morphology

of NP bending was later shown to be abnormal, appearing broader at the MHP and resulting in neural folds significantly further apart (Greene et al., 1998). Closure 2 formed normally in all genotypes, showing that the primary defect is in initiation of closure 1. With regards to the looped tail phenotype in heterozygotes, a delay in PNP closure by 4-6 hours was identified (Copp et al., 1994); this mechanism had previously been identified as the causative mechanism behind NTDs in the *curly-tail* strain (Copp, 1985) (see Chapter 1.3.3). Another observation was that in *Lp/Lp* embryos, axial elongation of the NP and associated tissues was significantly less, and the overall body was markedly shorter (Smith and Stein, 1962). The hypothesis arising from this study, that axial extension abnormalities are mechanistically causative, was eventually proven correct by the identification of the mutant gene as a member of the PCP pathway.

Positional cloning studies at the beginning of this century localised the mutation to chromosome 1 and identified the mutant gene as the *Drosophila Van Gogh (Vang)* homologue *Ltap/Lpp1* (Kibar et al., 2001, Murdoch et al., 2001). A missense mutation causing a change in the amino acid sequence (serine to asparagine) in a conserved C-terminus domain was determined as the causative mutation (Kibar et al., 2001, Murdoch et al., 2001). This gene is now known as *Vangl2*, and the missense mutation prevents binding of the protein to *Dvl* proteins, thus disturbing the core PCP signalling pathway (Torban et al., 2004). *Vangl2*$^{Lp/Lp}$ mutants express decreased levels of VANGL2 protein by ~80%, and some global *Vangl2* knockout lines show complete craniorachischisis, suggesting that loss-of-function may cause the phenotype (Torban et al., 2007, Murdoch et al., 2014, Ramsbottom et al., 2014). However, the fact that some protein remains shows that the *Lp* allele does not cause complete loss-of-function, but may instead affect its cellular activity- indeed, mutant VANGL2 protein is not present at the cell membrane, which is observed in wild types, but is exclusively localised in intracellular compartments (Torban et al., 2007). In addition, one *Vangl2*$^{-/-}$ line shows only 74% craniorachischisis, whereas 100% of *Vangl2*$^{Lp/-}$ embryos generated from the same knockout are affected (Yin et al., 2012). Together, these results suggest that the *Lp* allele is a dominant negative mutation.

As one of the core members of the PCP signalling pathway, *Vangl2*^{Lp} prevents normal CE during extension and shaping of the NP, explaining the short and wide body seen in homozygotes (Smith and Stein, 1962). In one study, CE in *Lp* embryos was analysed by injection of DiI into the node at E7.5. Wild type embryos showed rostral extension of the labelled region in 94% of embryos, whereas this extension was only identified in 47% of mutants (Ybot-Gonzalez et al., 2007b). In addition, chimeras containing GFP-expressing *Vangl2*^{Lp} mutant cells showed a significantly greater proportion of GFP-negative wild type cells in the midline of E8 embryos

compared to mutant GFP-positive cells, suggesting that the CE defect is cell autonomous (Ybot-Gonzalez et al., 2007b).

The cellular mechanisms which cause CE to fail and subsequently prevent closure are not fully understood. PCP signalling controls polarity of cells, suggesting that a failure of cells to undergo polarised intercalation could be the mechanism – however, in one study live imaging of E8-8.5 *Lp/Lp* embryos demonstrated that mutant cells show normal elongation and alignment along the ML axis, comparable to wild types (Williams et al., 2014). The authors reported that mutant embryos showed a significant decrease in neighbour exchange, suggesting an alternative mechanism where abnormal turnover of adherens junction proteins, such as cadherins, may prevent junctional remodelling. This hypothesis is further supported by the fact that RNAi knockdown of *Vangl2* impairs cell-cell adhesion (Lindqvist et al., 2010).

1.3.3 – *Curly-tail*

The *curly-tail* mouse strain, like *loop-tail*, arose spontaneously in an inbred colony, and was so named due to the TFDs seen in ~50% of mice (Gruneberg, 1954). *Curly-tail* has been maintained in a random-bred closed colony since its initial discovery, and all mice subsequently referred to as *ct* are assumed to be homozygous mutant unless otherwise specified. Some *ct* mice have SB or EX, however the penetrance of these phenotypes has fluctuated over time (van Straaten and Copp, 2001). Litters collected before birth from the original colony (produced from a GFF x CBA/Gr cross) showed ~40% SB with curled tail, ~10% TFDs only, and ~50% phenotypically normal (Gruneberg, 1954). The occurrence of SB has since dropped dramatically, fluctuating around 10-15%. EX has also been identified in a consistently small proportion of embryos, between 0-5%, showing that the *curly-tail* defect primarily affects spinal closure (van Straaten and Copp, 2001).

The mechanism behind NTDs in *ct* is well understood. Injection of dye into the closed NT can act as a readout of spinal NTC, as an open PNP will allow the dye to leak out. Using this technique, it was shown that ~50% of *ct* embryos show delayed PNP closure by E10.0, corresponding to those with TFDs (Copp et al., 1982). Culture of embryos later allowed the correlation between delayed closure and NTD phenotype to be further proven: individual embryos were followed, revealing that embryos with TFDs have delayed NTC which does eventually complete, whereas SB is always preceded by failed NTC (Copp, 1985).

The proof that delayed spinal NTC leads to NTDs in *ct* mice was followed by analysis of the mechanism. Using mitotic index, [^{3}H]thymidine labelling and length of S phase as indicators of proliferation rate, it was found that the hindgut endoderm and notochord have a reduced proliferation rate in *ct* embryos with a large PNP compared to a small PNP, while the rate in the NE is unchanged (Copp et al., 1988). As a result of this proliferation imbalance, the caudal region of *ct* embryos has faster dorsal growth than ventral, which leads to excessive curvature (Brook et al., 1991, Peeters et al., 1997). Manipulating this mechanical deficit proves its causative effect- by inserting an eyelash tip into the hindgut lumen, the excess ventral curvature was prevented, in turn ameliorating the delay in NTC (Brook et al., 1991).

Despite *ct* remaining the most popular NTD model, identifying the causative gene has been an ongoing challenge. There are a number of modifying loci which affect NTD penetrance in *ct*, for example *lmnb1, mthfd1L* and *mct1*, showing that the genetics is more complex than a single gene causation (Letts et al., 1995, De Castro et al., 2012, Sudiwala et al., 2016). In the 1990s, linkage studies localised the *ct* mutation to distal chromosome 4, although it was unclear which gene specifically was the culprit (Neumann et al., 1994). Subsequent studies of genes in the vicinity of the localised region (e.g. *Pax7, Glut-1*) failed to find any sequence changes which would result in amino-acid changes (Beier et al., 1995, Peeters et al., 1998). Nevertheless, a compelling candidate has since been identified: the transcription factor *Grainyhead-like-3 (Grhl3)*, supported by several pieces of evidence.

Grhl3 is found in distal chromosome 4, consistent with *ct* linkage studies, and *Grhl3* expression, which is primarily in the SE of the closing NT and the hindgut during neurulation stages, is decreased in *ct* embryos (Ting et al., 2003a). Mice homozygous for the null *Grhl3* allele die at birth, showing NTD penetrance of 100% SB and 2-14% EX (Ting et al., 2003a, Yu et al., 2006). Finally, the most definitive evidence for *Grhl3* being the *ct* gene comes from a study from our group in 2007. Overexpression of *Grhl3* in *ct* mice, by insertion of a BAC transgene that includes the entire *Grhl3* coding and regulatory regions, rescues the proliferation defect and leads to complete rescue of both TFDs and SB (Gustavsson et al., 2007). Despite such convincing evidence, no causative mutations in the coding region have been identified, and only a single-nucleotide substitution (C-21350T) in a putative enhancer region has been found, suggesting that *Grhl3* is a hypomorphic allele (Gustavsson et al., 2007).

1.4 – The *Grainyhead* family of transcription factors

1.4.1 - *Grainyhead*

The endodermal and ectodermally expressed transcription factor Grainyhead was first isolated from *Drosophila* neuronal extracts (Bray et al., 1988). Originally called element-l-binding activity (Elf-1) or neuronal-transcription-factor 1 (NTF-1), it was found to be one and the same as the *Grainyhead (Grh)* gene. *Grh* had earlier been identified as an embryonic lethal locus in a *Drosophila* forward genetic screen and so named due to the distinctive phenotype of the head skeleton, which appeared grainy and discontinuous (Nusslein-Volhard et al., 1984, Bray and Kafatos, 1991, Kudryavtseva et al., 2003) .

The *Grh* family has since expanded with the discovery of six mammalian proteins showing homology to the DNA binding site of the original *Drosophila* transcription factor. These proteins are divided into two groups of three, depending on N-domain homology: the first group, class I, is made up of *Grainyhead-like-1* (*Grhl1,* or mammalian grainyhead (*MGR*)), *Grhl2* (or brother-of-MGR (*BOM*)), and *Grhl3* (or Grainyhead-like epithelial transactivator (*Get1*) or sister-of-MGR (*SOM*)); class II contains *LBP-9/CRTR-1*, *LBP-1c/CP-2*, and *LBP1s/NF2d9* (Wilanowski et al., 2002, Kudryavtseva et al., 2003, Ting et al., 2003b).

Interestingly, there are many structural differences between *Grh* and its mammalian homologues. Both *Grh* and all three *Grhl* transcripts are spliced to form several functional isoforms – however, the longest isoform of GRH protein is significantly longer than any GRHL proteins, at 1063 amino acids, compared to the longest GRHL member, GRHL3, at 626 amino acids (Reese et al., 2019).

Early studies investigating the structure of *Grh* identified two important domains – first, an isoleucine-rich transactivation motif, and second a ~400 amino acid long DNA binding and dimerisation domain at the carboxyl terminus, containing a region with similarities to helix-loop-helix protein DNA-binding domains (Attardi and Tjian, 1993). Deletion of various regions showed that the transactivation domain is required for function, and that loss of this region is dominant negative, despite the fact that DNA binding is still normal (Attardi et al., 1993). However, *Grhl* members do not show significant homology with the *Grh* transactivation domain- mapping studies showed that the transactivation domain of all three *Grhl* genes is found in the N-terminus region, from amino acids 30-95 (Wilanowski et al., 2002, Ting et al., 2003b). Glutamic acid and aspartic acid, at amino acids 32 and 33, appear to be particularly important in transactivation activity, and are conserved across all *Grhl* members (Reese et al., 2019).

Meanwhile, the DNA binding domain shows some conservation. *Grh* contains a 52 amino acid sequence which is essential for strong DNA binding, in addition to a second separate DNA binding core which binds with lower affinity (Uv et al., 1994). Surprisingly, it is the low-affinity region which is perfectly conserved in all three *Grhl* genes, while the high affinity sequence is not present (Reese et al., 2019).

The mechanism by which GRH and GRHL proteins act as transcription factors may be more similar than their structures suggest. Both GRH and GRHL proteins have been further classified as 'pioneer' transcription factors, meaning that they promote open chromatin structures to enhance expression of genes (Reese et al., 2019). Binding of GRH functions by displacing nucleosomes, thus 'priming' genes for expression- a similar role has been identified in all three GRHL proteins (Jacobs et al., 2018).

1.4.2 – *Grainyhead-like 2*

Grhl2 is expressed from early neurulation in the SE and hindgut endoderm (Figure 1.3A), but not in the NE, and later is expressed in other organs such as the kidney and the lungs (Werth et al., 2010, Brouns et al., 2011, Kersbergen et al., 2018). It has been shown to play an important role in regulating epithelial properties in multiple contexts, most widely in cancer and epithelial-mesenchymal-transition (EMT) (Reese et al., 2019).

Grhl2 has displayed clear tumour-suppressant roles in various cancer cell lines, including breast, ovarian, oral, prostrate and lung cancer (Werner et al., 2013, Chung et al., 2016, Chen et al., 2016, Paltoglou et al., 2017, Pan et al., 2017). In some studies, loss of *Grhl2* stimulates EMT, and conversely, overexpression of *Grhl2* reverses cancer cells to a more epithelial phenotype (Cieply et al., 2012, Cieply et al., 2013). Surprisingly, although some cancers show decreased *Grhl2* levels, these findings are rarely supported in the clinic, with high *Grhl2* correlating with poor prognosis in several studies (Yang et al., 2013, Torres-Reyes et al., 2014, Quan et al., 2015, Pan et al., 2017, Yuan et al., 2020). As a transcription factor, *Grhl2* has many downstream target genes and multiple functional isoforms, and it is possible that its downstream function varies depending on context, explaining why it can act as both a tumour suppressor and oncogene.

Abnormal EMT as a result of *Grhl2* mutations has also been reported in other contexts, including palate development and NTC (Ray and Niswander, 2016, Carpinelli et al., 2020). One study reported that the cranial SE in *Grhl2*$^{-/-}$ mouse embryos expresses ectopic vimentin during NTC, and that this, along with a disrupted SE morphology, indicates a transformation of the SE

towards a mesenchymal phenotype (Ray and Niswander, 2016). However, work from our lab has not supported these findings. While the SE does indeed lose epithelial properties in *Grhl2*$^{-/-}$ mutants, we did not detect EMT – rather, mutant cells display properties characteristic of a neural phenotype (Nikolopoulou et al., 2019). This work will be discussed further in Chapter 5.

1.4.3 – *Grainyhead-like 3*

Like *Grhl2, Grhl3* is expressed in the SE during neurulation stages, however its expression is more restricted to the edges of the neural folds (Figure 1.3B). It also shows scattered expression in the NP, and by E10.5 is expressed in the hindgut (De Castro et al., 2018a, Mole et al., 2020). The functions of *Grhl3* are less widely studied than *Grhl2*, despite its comparably large number of expression domains (Auden et al., 2006). The majority of phenotypes in *Grhl3* mutants result from failed epidermal development and wound repair, homologous to its role in cuticle development in *Drosophila*. *Grhl3*$^{-/-}$ mouse embryos die at birth from dehydration, as a result of failed barrier formation (Ting et al., 2005). These embryos show abnormal lipid metabolism due to decreased expression of one of the only confirmed target genes of *Grhl3, Transglutiminase-1*, which crosslinks proteins and lipids into the cornified envelope (Ting et al., 2005).

Epidermis-specific knockout of *Grhl3* using a keratin-14 promoter prevents a normal immune response to epidermal damage, with mutant skin lesions failing to heal as a result of hyperplastic epidermis and a failure of immune suppression (Gordon et al., 2014). Further, *Grhl3* is upregulated in human psoriasis lesions, which are characterised by excessive growth of the skin (Gordon et al., 2014). Epidermis-specific knockouts also display soft tissue syndactyly in ~25% of mice (Kashgari et al., 2020). In normal digit separation, *Grhl3* controls localisation of adhesive proteins and instructs the periderm to form a barrier between epithelia of individual digits; when *Grhl3* is lost, the periderm is able to adhere to opposite periderm cells, causing digits to fuse (Kashgari et al., 2020). Similarly, the periderm in early ear canal invagination prevents premature fusion of the primary canal, which occurs in *Grhl3*$^{-/-}$ embryos due to defective periderm development (Fons et al., 2020).

Finally, *Grhl3* has been linked to cancer, although to a lesser degree than *Grhl2*, as both a tumour suppressor and promoter (Sundararajan et al., 2020). Higher mRNA and protein levels of all three *Grhl* members are expressed in human colon cancer cells (Yuan et al., 2020). Conversely, and in agreement with its role in wound healing, *Grhl3* acts to suppress hyperproliferation in squamous cell carcinoma (Darido et al., 2011).

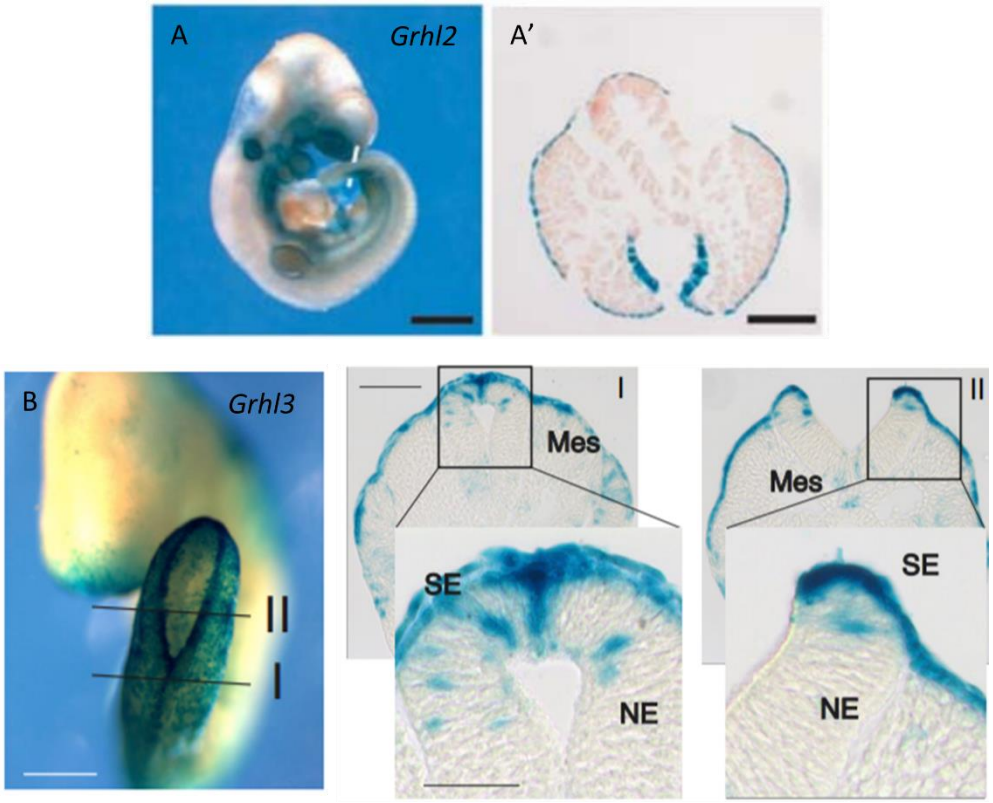

Figure 1.3 – Expression patterns of Grhl-2 and -3 in neurulation stage embryos.

A) Grhl2 expression revealed by X-gal staining in Grhl2$^{GT/+}$ embryos at E10.5 in wholemount (A) and caudal section (A', section indicated by white line in A). Scale bars 1 mm (A) and 100 µm (A'). Taken from Brouns et al., 2011. B) Grhl3 expression revealed by X-gal staining in Grhl3-Cre;Itgβ1^{LacZ} embryos at E9.5 in whole mount embryos (B) and sections I and II (indicated by black lines in B). Scale bars 500 µm (B) , 100 µm in I and II, and 50µm in I and II (zoom). Mes = paraxial mesoderm. Taken from Mole et al., 2020.

1.4.4 – Neural tube defects and *Grainyhead-like* genes

The importance of *Grhl2* in NTC is clear from the phenotypes in both overexpression and null mutant mice. The *Axial defects (Axd)* mutant appeared spontaneously in an inbred *muscular dysgenesis (mdg)* colony; two males displaying a kinked tail phenotype and lacking the *mdg* gene were subsequently bred with wild-type females and a new closed colony was generated (Essien et al., 1990). Some progeny in this colony developed severe SB, and this varied with background. The *Axd* mutation was eventually transferred to the BALB-c background to generate the colony widely used today. Homozygotes from this colony display fully penetrant SB, and it is now known that an overexpression of *Grhl2* is the causative mutation- the mutation has been linked to a region 1.1Mb in size, however no coding mutation has yet been identified (Brouns et al., 2011, Nikolopoulou et al., 2019). Meanwhile, loss-of-function also leads to severe NTDs. *Grhl2*$^{-/-}$ mice

have severe cranial NTDs with split face (100% penetrance) and high frequency SB (88-100%) (Rifat et al., 2010, Brouns et al., 2011).

Grhl3 is also an important player in NTC. *Grhl3*$^{-/-}$ mouse embryos develop fully penetrant NTDs, with 100% of embryos displaying SB and a low frequency also developing EX (2-14%) (Ting et al., 2003a, Yu et al., 2006). Similarly to *Grhl2*, overexpression of *Grhl3* leads to NTDs, albeit with lower severity and frequency (67% SB and 8% EX) (De Castro et al., 2018a). Finally, as previously discussed, it is the strongest candidate for the *ct* gene.

The fact that these genes contain homologous DNA binding domains, and that mutations result in NTDs, leads to the question of their functional redundancy. Compound heterozygotes (*Grhl2*$^{+/-}$*;Grhl3*$^{+/-}$) develop low frequency NTDs (14%), including 5% mid- and hindbrain EX and 6% low sacral SB (Rifat et al., 2010). *Grhl2*$^{+/-}$*;Grhl3*$^{-/-}$ embryos develop 100% SB as expected, but also display fully penetrant EX (again mid- and hindbrain only) (Rifat et al., 2010). Finally, double homozygotes succeed only in closing the most rostral region of the spinal cord, demonstrating that closure 1 alone does not depend on *Grhl* gene function (Rifat et al., 2010).

There are two possible explanations for both loss- and gain-of-function mutations leading to NTDs. First, it could be that there is a threshold of expression for both genes within which successful neurulation can occur. Alternatively, because GRHL2 and GRHL3 proteins can form heterodimers, overexpression of one gene could increase the proportion of heterodimers, thereby reducing the proportion of homodimers with the other protein (Ting et al., 2003b). The latter is unlikely for two reasons: first, increasing *Grhl2* expression by addition of an *Axd* allele in *Grhl3* overexpression mutants does not rescue NTDs, and in fact exacerbates the phenotype, with 100% of embryos displaying SB (De Castro et al., 2018a); second, overexpression of *Grhl3* does not cause highly penetrant EX, unlike in *Grhl2*$^{-/-}$. The threshold hypothesis is therefore most likely, and is summarised in Figure 1.4.

Importantly, the varying penetrance and phenotypes in mutant embryos suggests there are crucial differences in their downstream target genes and function, despite their structural homology. The mechanisms by which these genes contribute to NTC remain only partially understood, although their expression patterns and the timing of NTDs suggest the crucial tissue is the SE. This question will be discussed in detail in Chapter 5.

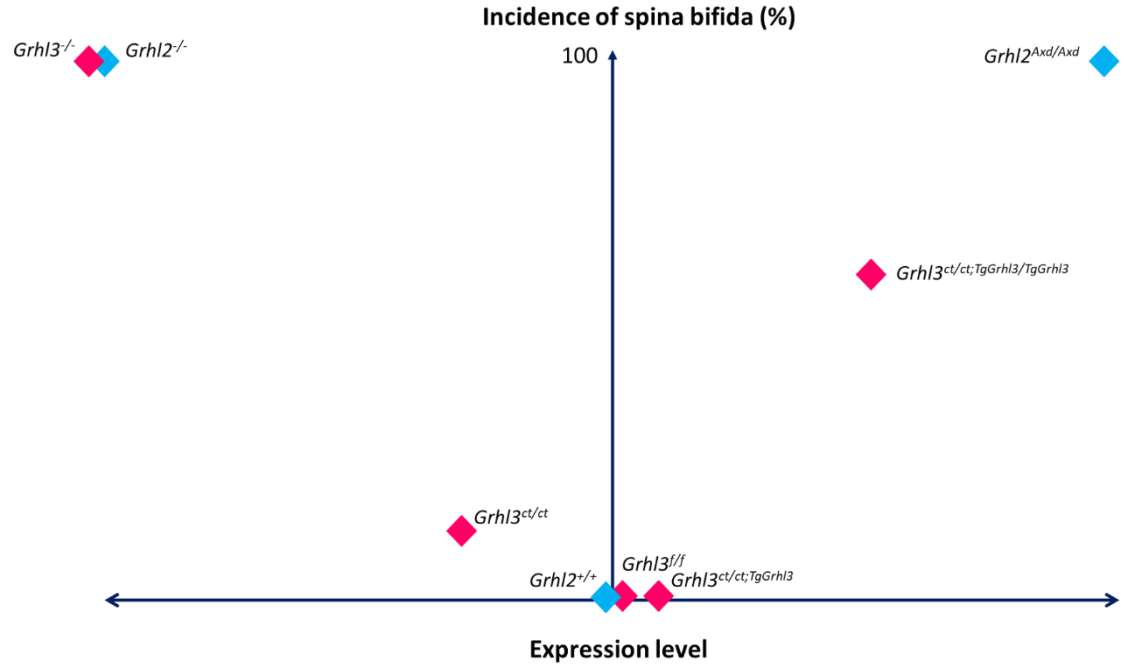

Figure 1.4 - The relationship between Grhl2/3 expression and incidence of spinal NTDs.

Each diamond represents a Grhl2 (cyan) or Grhl3 (magenta) mutant strain. Homozygous null mutants ($Grhl2^{-/-}$, $Grhl3^{-/-}$) and $Grhl2^{Axd/Axd}$ all show 100% spina bifida. Overexpression of Grhl3 in $Grhl3^{ct/ct;TgGrhl3/TgGrhl3}$ causes 68% incidence of spina bifida. Hypomorphic $Grhl3^{ct/ct}$ embryos show a varying penetrance of ~10% spina bifida.

1.5 - Biomechanics in developmental biology

As the number of genes and signalling pathways involved in development increase by the day, so does the need to integrate such molecular data into global mechanisms. Biomechanical research is at the heart of such attempts, aiming to understand the mechanisms by which cells generate, detect and transmit force. The field of developmental biomechanics has increased in popularity over the last 100 years, since D'Arcy Thompson's seminal work 'On Growth and Form', arguably the first literature discussing the field, was published. This increased popularity is in part due to advancements in techniques which allow us to manipulate and measure complex mechanical forces, such as atomic force microscopy (AFM) and laser ablation, and computational techniques which allow developmental processes to be modelled and manipulated at will (Binnig et al., 1986, Montell et al., 1991, Morelli et al., 2012). In this section, actomyosin activity and Hippo signalling, which are perhaps the most widely studied signalling networks involved in biomechanics, are discussed in the context of development, finishing with

a general overview of our current understanding of the biomechanical mechanisms involved in NTC.

1.5.1 – Actomyosin in development

The actomyosin network is an evolutionarily conserved system vital in the production and transmission of forces within tissues. Morphogenesis is a process which involves large-scale changes in cell shape, size and position, and is therefore closely dependent on actomyosin activity. Actin filaments are the major component of the cell cytoskeleton but can also be found as long continuous structures linking cells ('cables', discussed in Chapter 1.5.3.2) and as extracellular protrusions powering interactions with the environment, i.e. lamellipodia and filopodia. Actin itself can create cytoskeletal rigidity, but it is only through interactions with myosin motors (activated by ATP hydrolysis) that contractile forces are generated (Munjal and Lecuit, 2014).

The interactions between actin filaments and non-muscle myosin II are tightly controlled. Actin filaments are continuously assembled and disassembled by regulatory molecules, such as formin, the ARP2/3 complex, and cofilin (Lecuit et al., 2011, Murrell et al., 2015). The generation of active myosin II bipolar minifilaments from inactive homodimers is also regulated. For example, several kinases (Rho kinase (ROCK) and myosin light chain kinase (MLCK)) control the phosphorylation of two myosin II residues which promote homodimer activation (Amano et al., 2010, Lecuit et al., 2011). Further complexity arises with regards to physical limits – the interactions between actin and myosin must be regulated to enforce this, for example the concentration of cross linkers (α-actinin) between them must be high enough to allow coordinated movement, but low enough to prevent the tissue from being too stiff (Bendix et al., 2008, Murrell et al., 2015).

In order for cells to change shape and position, the contractile forces must be communicated both to other cells and to the underlying ECM. Structures called adhesive clusters, or adhesive complexes, facilitate these interactions – primarily cadherin (discussed in Chapter 4.1) and integrin clusters transmit forces to neighbouring cells and the ECM respectively (Lecuit et al., 2011). The complexity of the system is highlighted by the number of adaptor proteins which bind the actomyosin network to cadherins and integrins: β- and α-catenin and vinculin are recruited to adhesion complexes, and similarly talin and vinculin are known to regulate integrin-ECM interactions. The recruitment of such regulators can therefore be used as 'readouts' for

force transduction at adhesive complexes (Parsons et al., 2010, Yonemura et al., 2010, Thomas et al., 2013, Klapholz and Brown, 2017, Kale et al., 2018).

Crucially, forces and adhesion complexes can regulate each other. Adhesion complexes can activate or repress actomyosin assembly, for example cadherins can promote actin assembly by associating with the ARP2/3 complex (Kovacs et al., 2002, Lecuit et al., 2011). Conversely, the shape and size of adhesion complexes can be regulated by actively generated forces, such as tension, or properties of the cell's surroundings, such as tissue stiffness. For example, during early *Drosophila* morphogenesis, tensile and shear stress upregulate and downregulate E-cadherin respectively, via actomyosin acting either in the medial cortex or at the junction of cells (Kale et al., 2018).

1.5.2 - Hippo signalling and YAP/TAZ in mechanotransduction

One of the major fields of study in biomechanics is how cells and tissues can detect and respond to forces, either internally or externally generated. Developmental biologists are particularly interested in this, as it is directly related to the fundamental question of how organs and organisms develop into given sizes and shapes with such consistency. The Hippo pathway is one of the fundamental signalling cascades which has been found to detect and respond to a cells mechanical environment, termed 'mechanotransduction'.

Hippo signalling was first identified in a series of forward genetic screens in *Drosophila*; two core growth regulators, Hippo (Hpo) and Warts (Wts), were identified, mutations in which led to hyperproliferation and resistance to apoptosis of the imaginal discs and adult cuticle (Halder and Johnson, 2011, Piccolo et al., 2014). Both Hippo and Warts are kinases; Hippo, with its cofactor Salvador (Sav) phosphorylates and activates Warts, which itself acts with its cofactor Mob as tumour suppressor (Mats) to phosphorylate the transcription factor Yorkie (Yki) (Halder and Johnson, 2011). Yorkie can be phosphorylated at three sites, but phosphorylation at Ser168 is particularly critical, and acts to prevent the nuclear translocation and subsequent transcriptional activity of Yorkie (Oh and Irvine, 2009). In the absence of Hippo activation, Yorkie can enter the nucleus and activate expression of target genes via the downstream mediator Scalloped (Sd); Yorkie itself does not bind to DNA but partners with Scalloped and instructs it to do so (Wu et al., 2008). Target genes are involved in a large range of cellular process, such as promoting proliferation and survival and blocking apoptosis (Halder and Johnson, 2011). A mammalian equivalent of the Hippo signalling cascade has since been identified; Mst1/2 (homologues of Hippo) act with Sav1 to phosphorylate Lats1/2 (Wts homologues), which with its cofactor

Mob1A/B (Mats homologues) phosphorylates the Yorkie homologues Yes-associated protein (YAP) and transcriptional coactivator with PDZ-binding motif (TAZ) (Halder and Johnson, 2011). In the absence of LATS1/2 dependent phosphorylation, YAP and TAZ activate gene expression using TEAD1-4 as binding platforms (Panciera et al., 2017).

The role of YAP and TAZ in mammals is more complex than Yorkie, not least because these are two Hippo effectors rather than one (Halder and Johnson, 2011). As a vital regulator of tissue growth and differentiation, YAP/TAZ signalling has been implicated in many developmental and adult systems such as angiogenesis (Boopathy and Hong, 2019), gastrointestinal tract development (Cotton et al., 2017) and embryonic and adult proliferation and differentiation in lung cells (Lange et al., 2015). Unsurprisingly, its role in growth means it has become an important target in studies of cancer, with mutations in several Hippo pathway components identified in human tumour cell lines, and indeed it has been shown to be a positive regulator of EMT (Tapon et al., 2002, Lai et al., 2005, Zhang et al., 2009).

YAP/TAZ signalling is regulated by multiple cellular properties, such as cell polarity and mechanical cues. For example, the planar polarised Ft/Ds/Fj complex has been shown to repress Yki/YAP/TAZ signalling, in turn preventing tissue overgrowth (Blair and McNeill, 2018, Davis and Tapon, 2019). The response of YAP/TAZ to mechanical cues is perhaps the area of most current interest in the field. This was triggered by the finding that growing mammary epithelial cells on polyacrylamide gels of high stiffness leads to increased YAP/TAZ nuclear localisation and expression of YAP/TAZ regulated genes compared to soft substrates (Dupont et al., 2011). Cell shape and ECM stiffness have now been associated with various stereotypical YAP/TAZ dependent behaviours: a small cell (resulting from a restricted ECM and small adhesive area) and a soft ECM shows cytoplasmic YAP/TAZ and lack of cell proliferation; conversely, a large cell and stiff ECM triggers YAP/TAZ nuclear translocation and increases proliferation (Piccolo et al., 2014). Interestingly, these two phenotypes are further associated with different differentiation pathways from the same type of progenitor (Piccolo et al., 2014).

An important question is whether this mechanosensitive response is via classical Hippo signalling or an entirely independent mechanism (Elbediwy et al., 2018). Characteristics of epithelial cells such as cell-cell adhesion and apical-basal polarity have been shown to regulate Hippo signalling. For example, in *Drosophila,* the proteins Merlin (Mer) and Expanded (Ex) localise to apical epithelial cells and induce Hippo signalling by binding to Kibra and Crumbs (Crb) respectively-importantly, these complexes are linked to the cytoskeleton, suggesting a potential mechanism of mechanical sensing (Elbediwy and Thompson, 2018). Homologous mammalian signalling via

Crb3 and Nf2 (homologues of Crb and Mer) has been identified. At the basal side of epithelial cells, a homologous mechanism via an integrin-mediated cascade has been identified that may be unique to mammals (Elbediwy and Thompson, 2018).

Both apical and basal mechanotransduction mechanisms have been shown to activate Yki/YAP mediated transcription via classical Wts/LATS1/2 binding. However, non-epithelial isolated cells are also mechanosensitive, suggesting alternative upstream signalling pathways independent of regulatory epithelial complexes might be at play. Indeed, cells exposed to low mechanical stress do not show a rescue of YAP/TAZ inhibition by inactivation of LATS1/2, suggesting a Hippo-independent mechanism prevents YAP/TAZ nuclear translocation in these contexts (Piccolo et al., 2014). In one study, a potential mechanism was identified where YAP was directly phosphorylated by Src family kinases via integrin-linked Enigma signalling. Human YAP5SA cells, which express mutant YAP incapable of LATS1/2-mediated phosphorylation, show normal variation in nuclear translocation when grown on different substrates, but this pattern is lost in the presence of Src family kinase inhibitor, suggesting mechanosensitive YAP/TAZ signalling is not dependent on Hippo activity (Elbediwy et al., 2018).

Ultimately, while a clear role in mechanotransduction has been demonstrated, it is a highly complex signalling network that functions in a wide range of contexts. The complexity of the YAP/TAZ mechanotransduction pathway could be evolutionarily beneficial- functional redundancy may maintain the ability of developing embryos to regulate their growth and shape - one of the most important functions in embryogenesis.

1.5.3 - The biomechanics of neural tube closure

1.5.3.1 – Actomyosin turnover

As discussed in Chapter 1.1.3, actin-mediated apical constriction is an important mechanism for MHP bending in the NP. Despite its prevention of cranial closure, actin filament disassembly allows spinal closure to progress in some contexts, such as after culture in blebbistatin, cytochalasin D or Latrunculin B, suggesting that this mechanism is more complex than originally believed (Escuin et al., 2015). It is now appreciated that in some cases actin accumulation can prevent closure from progressing. For example, inhibition of F-actin turnover can exacerbate PCP closure phenotypes in *Vangl2*$^{Lp/Lp}$ mutant embryos, suggesting it may play a role in initiation (Mahaffey et al., 2013). It has also been clearly implicated in progression of spinal closure, although the mechanisms are not well understood.

The RhoA-ROCK-LIMK-Cofilin signalling pathway is known to play an important role in regulating actin turnover. 100% of non-muscle (n)-cofilin-null (*Cfl1*$^{-/-}$)$^{-}$ embryos show severe cranial NTDs and an enlarged PNP, concomitant with misaligned somites, abnormal neural crest migration to cranial mesenchyme and reduced NE proliferation (Gurniak et al., 2005). As an F-actin depolymerising protein, the role of n-cofilin in F-actin turnover was later further analysed independently. In this study, two additional models of disrupted F-actin disassembly and turnover were analysed, by culturing E8.5 mouse embryos after Jasplakinolide treatment and ROCK inhibition. In both groups spinal NTC failed, associated with accumulation of actin turnover. Crucially, the defects in these mutants and in *Cfl1*$^{-/-}$ embryos could be partially or wholly rescued by treatment with blebbistatin, which prevents actomyosin cross-linking by blocking myosin-II (Escuin et al., 2015).

Blockade of actin turnover does not prevent formation of DLHPs in most cases, suggesting that actomyosin activity plays an additional important role in closure other than in apical constriction. A possible interpretation of these findings, partly based on the consistently straight morphology of the elevating neural folds, is that excessive neuroepithelial tension causes the NP to become too stiff for closure to succeed (Escuin et al., 2015). As with many biomechanical mechanisms, this suggests that the correct balance of pro- and anti-closure forces must be obtained for closure to succeed.

1.5.3.2 – The actomyosin cable

An additional mechanism which may be important in NTC is formation of an actomyosin cable, which has been identified in the closing PNP (Galea et al., 2017) and HNP (Maniou et al., 2021). Supra-cellular actomyosin cables are conserved biomechanical structures involved in a wide range of developmental processes (Munjal and Lecuit, 2014). They are known to be tension-bearing in other models of tissue closure, such as mouse eyelid (Hislop et al., 2008, Heller et al., 2014) and *Drosophila* dorsal closure (Hutson et al., 2003, Ducuing and Vincent, 2016, Pasakarnis et al., 2016), and promote gap closure during development and wound repair via the 'purse-string' mechanism (Begnaud et al., 2016).

The importance of the actomyosin cable in development is not yet fully understood. In two independent studies, loss of the cable in *Drosophila* embryos does not prevent dorsal closure: in the first, the geometry of epithelial cells was abnormal at the leading edge, resulting in morphogenetic scarring and suggesting that the cable acts to control cellular organisation and

increase closure efficiency (Ducuing and Vincent, 2016); in the second study, loss of the cable in alternating stripes showed that cells lacking a cable in fact advanced dorsally ahead of cable-associated cells, suggesting that the cable can restrict the movement of cells (Laplante and Nilson, 2011). Together, these studies imply that, while not required for dorsal closure, the cable may act as a coordinating structure to regulate efficient collective movement of cells.

Whether the actomyosin cable in the developing NT is required for closure remains unclear. At earlier stages of spinal closure, the cable runs along part of the neural folds but does not enclose the PNP, suggesting that the traditional 'purse-string' mechanism is not at play in this context. However, at late stages the cable forms a ring and encircles the entire PNP after closure 5 formation. Ablation of the region where closure 5 forms leads to significant recoil, but only after the actomyosin cable has encircled the PNP. On the other hand, the presence or absence of the cable does not successfully predict completion of closure. Several NTD mutants do not have a clearly visible cable, for example *Kumba* (*Zic2*$^{Ku/Ku}$) and *Grhl2*$^{-/-}$ embryos (Galea et al., 2017, Nikolopoulou et al., 2019). However, embryos with selective deletion of *Vangl2* (see Chapter 1.5.3.3) or *Itgβ1* in the SE fail to close due to biomechanical defects, despite the presence of a normal cable (Galea et al., 2018, Mole et al., 2020). Together, these findings suggest that the actomyosin cable is not sufficient for closure, but is likely an important biomechanical structure alongside other pro-closure mechanisms.

1.5.3.3 – PCP signalling in late spinal neurulation

Interestingly, the role of PCP signalling is not limited to CE during early neurulation, and conditional knock-out models have provided evidence for more subtle PCP mechanisms at later stages of neurulation. For example, when *Vangl2* is selectively deleted in the SE and in a proportion of NE cells, late stage SB occurs in 67% of embryos, with a further 12% of embryos showing delayed closure as evidenced by TFDs (Galea et al., 2018). In the late stage PNP, NE cells show an upregulation of F-actin along ML-oriented borders. These ML-oriented 'apical profiles' are lost in mutants, and the orientation of SE cell borders are also significantly disrupted, resulting in a 'bulging' NE within the PNP and significantly everted neural folds (Galea et al., 2018). This leads to failure of closure 5 to form, providing evidence for its active role in spinal closure. Importantly, the incomplete penetrance of NTDs in these mutants is probably due to variability in the proportion of recombined cells, suggesting that normal PCP signalling must occur in a high enough proportion of cells for closure to succeed (Galea et al., 2018). However,

the mechanisms by which PCP signalling in the NE contributes to formation of closure 5 remain poorly understood.

1.5.3.4 - The role of the extracellular matrix

The extracellular matrix (ECM) is a network of proteins which make up the supporting scaffolding for cells. It is chiefly described as a mechanical support for cells, but cell-matrix interactions can trigger a wide range of important cellular processes, such as migration, differentiation and proliferation, and are important in transmitting biomechanical signals between and within tissues (Frantz et al., 2010, Rozario and DeSimone, 2010). The main components of the ECM are fibrous proteins (including collagens, fibronectins, laminins and elastins) and proteoglycans (e.g. perlecan and aggrecan, among many others); crucially, the makeup of the ECM varies both between and within tissues, making it a highly heterogenous structure (Yanagishita, 1993, Frantz et al., 2010). In the NT, a specialised type of ECM known as basement membrane is deposited first between the NP and the mesoderm, and second between the SE and NE (Nikolopoulou et al., 2017). However, the relative contribution of the ECM in normal NTC remains elusive, possibly due to the large number of ECM components in mammals and considerable heterogeneity, or because of early embryonic lethality in some mutants (Nikolopoulou et al., 2017).

One of the largest protein families involved in ECM function are the integrin receptors. Transmembrane integrin complexes bind extracellular ligands such as fibronectins and laminins, conveying a large range of downstream functions via both 'outside-in' and 'inside-out' signalling cascades (Barczyk et al., 2010, Campbell and Humphries, 2011). Perhaps the integrin of most interest is integrin β_1. *Itgb1*$^{-/-}$ embryos arrest at E5.5, possibly due to abnormal BM deposition in the early blastocyst, or loss of β_1-mediated survival signals (Fassler and Meyer, 1995, Bouvard et al., 2001). It is the β subunit with the largest number of binding α subunits, potentially explaining why it has the most severe phenotype of all integrin mutant mice (Bouvard et al., 2001). The early lethality of these mutants makes it difficult to dissect its role in NTC. However, fibronectin mutants arrest around neurulation initiation, with embryos showing shortened AP axes and loss of notochord and somites due to defective mesoderm function (George et al., 1993). This points towards an important role of integrin-fibronectin interactions during NTC.

During the initiation stages of neurulation, PCP signalling and the ECM are closely linked. In *Xenopus* explants, the DEP domain of Dsh protein (downstream of non-canonical Wnt signalling) is required for the deposition of fibronection during CE (Dzamba et al., 2009). In another

example, VANGL2 protein regulates expression of the matrix-metalloproteinase MMP14, thus preventing ECM degradation (Williams et al., 2012). Conversely, disruption of the ECM leads to failure of CE by preventing normal polarised cell intercalation, clearly demonstrated by the short AP axis of fibronectin-null mouse embryos (Watt and Hodivala, 1994).

A recently published study from our lab investigated the role of integrin-fibronectin interactions at later stages of neurulation. At E9.5, the integrin α5β1 complex is upregulated at the spinal ZP. Meanwhile, fibronectin forms a dense network between the SE and NE, organising into dorsolaterally oriented fibrils further rostrally from the ZP (Mole et al., 2020). Using a conditional *Grhl3-Cre-Itgb1*$^{f/f}$ mouse line, it was shown that *Itgb1* expression originates from SE cells, with these mutants developing SB in 56% and a kinked tail in 22% of cases. Focal ZP integrin-β1 persisted in NE specific KO embryos, and these mice did not develop NTDs (Mole et al., 2020). Cell shape studies revealed a semi-rosette organisation of SE cells directly around the ZP in wild types, suggesting that the integrin-rich ZP provides a focal adhesion point to which SE cells anchor. Live-imaging of zippering revealed that indeed, SE along the open neural folds shorten in the RC direction, bringing them into the semi-rosette configuration and into contact with contralateral SE. Once contact is initiated, cells can undergo neighbour exchange, before being released from the adhesion site and becoming incorporated into the closed SE. *Grhl3-Cre-Itgb1*$^{f/f}$ mutants showed a loss of rosette formation, supporting the importance of this mechanism in facilitating closure (Mole et al., 2020). Interestingly, a similar sequential shortening and lengthening of cells along the neural folds had previously been identified in *Ciona* (Hashimoto et al., 2015). Although this study did not consider the role of the ECM, it suggests local cellular-ECM interactions could be an important and conserved mechanism in propagating NTC.

1.6 – Summary of thesis

This thesis aims to answer two main questions. First, does SE biomechanics play an active role in spinal NTC? This question is explored using wild type mouse embryos, and genetic and experimental models of spinal NTDs. In Chapter 3, the biomechanical properties of the wild type SE are characterised in detail. Cell shape and YAP nuclear translocation are analysed, followed by a functional mapping of SE recoil in different regions of the closed NT. Surprising contradictions are presented between cell shape and SE recoil, challenging the dogma that cell shape can be used to predict tension. Chapter 4 investigates the active role of the SE in spinal neurulation, by asking if experimentally disrupting SE biomechanics can perturb closure. Blockade of E-cadherin provides causative evidence that normal SE biomechanics (specifically

related to cell-cell adhesion) is a requirement for NTC. In Chapter 5, *Grhl-2* and *-3* loss- and gain-of-function mutants are studied, as they are valuable models for NTDs caused by abnormalities in the SE. Although a biomechanical mechanism is presented in *Grhl2* mutants, an analogous role of *Grhl3* is not identified, suggesting these transcription factors have different target genes.

Finally, in Chapter 6, a second question is explored. The mechanism behind severe NTDs in *Vangl2*$^{Lp/+}$*;Grhl3*$^{ct/ct}$ double mutants remains poorly understood, however previous work has suggested that reduced proliferation in the tailbud may be a causative mechanism resulting from the *Grhl3*^{ct} genotype. This hypothesis is not supported in this chapter, however a novel genetic interaction between the *Lp* mutation and *Grhl3* overexpression is identified.

Chapter 2 - Methods

2.1 - Animals

All mice were kept in the Biological Services Unit animal facility at University College London, in rooms kept at 22 °C and with a 12 hour light/dark cycle. Males and females were weaned separately, and were used for mating on reaching sexual maturity (6-8 weeks of age depending on strain). Sibling pairings were avoided where possible. Males were kept alone, while up to five females were housed in each cage. For experimental crosses, animals were paired either in the morning or the evening and females were checked for a copulation plug the same evening or the next morning respectively. Plugged females were designated as pregnant with E0.5 embryos. Animal care and procedures were performed according to the UK Animals (Scientific Procedures) Act 1986 and following the guidelines of the Medical Research Council's Responsibility in the Use of Animals for Medical Research (1993).

2.1.1 - Mouse colonies

Experimental mouse colonies were as follows:

- *ct/ct - curly-tail*, spontaneous mutant line, *Grhl3* hypomorph (Gruneberg, 1954). Derived from crossing an affected *ct/ct* female (from the original GFF inbred strain) with a CBA/Gr male (van Straaten and Copp, 2001). Maintained as a closed colony, with all offspring considered as homozygous for *ct*.
- *Lp/+ - loop-tail,* spontaneous mutant line, *Vangl2* dominant mutant (Strong and Hollander, 1949). Obtained from Harlan Laboratories (UK). Maintained by crossing of heterozygous mice, heterozygous offspring identified by looped tail phenotype.
- *ct/ct$^{TgGrhl3/0}$ - curly-tail* rescue by insertion of *Grhl3* BAC (Gustavsson et al., 2007). Created in house, by pronuclear microinjection of purified BAC RP24-327D13 (containing the intact *Grhl3* gene) into fertilised *ct* oocytes, which were transferred to CD1 surrogate mothers. Maintained by crossing *ct/ct* females with *ct/ct^{TgGrhl3}* males.
- *Grhl3$^{f/-}$* - floxed *Grhl3* to generate knockout embryos (Yu et al., 2006). Generated by injection of mutant ES cells into blastocysts and crossing of the resultant chimeras. Obtained from the Anderson lab (University of California, CA). Maintained by crossing of heterozygous males with *Grhl3$^{f/f}$* females.
- *Grhl2$^{Axd/+}$- Grhl2* overexpression, spontaneous mutant line (Essien et al., 1990). Rederived from cryopreserved embryos (Rutgers University, NJ, USA) and backcrossed

onto a *BALB/c* background (Brouns et al., 2011). Maintained by crossing heterozygous *Grhl2*$^{Axd/+}$ with wild type *BALB/c* females.

- *Grhl2*$^{+/-}$ - *Grhl2* gene-trap to generate knockout embryos (Brouns et al., 2011). Generated by injection of mutant ES cells into blastocysts and subsequent crossing of chimeras. Maintained by crossing heterozygous *Grhl2*$^{+/-}$ with wild type *BALB/c* females.
- *C57BL/6* – wild types derived from heterozygous *Gldc* strain (Pai et al., 2015).

2.1.2 - Animal treatments and procedures

Treatments designed to stimulate proliferation in Chapter 6 were as follows. Pregnant females were given drinking water supplemented with formate or inositol from the day of plugging to embryo collection. Formate (Sigma Aldrich) or myo-inositol (Sigma Aldrich) were dissolved in tap water at a concentration of 5 mg/ml and kept at 4 °C. Water bottles were replenished every 2-3 days. Alternatively, adenine (Sigma Aldrich) and thymidine (Sigma Aldrich) were supplemented by intraperitoneal (IP) injection. A stock solution of thymidine at 8 mg/ml in Milli-Q water was stored at -20 °C. Adenine was dissolved in MilliQ water, NaOH and HCl to create a stock solution at concentration 4 mg/ml, corrected to pH 7 and stored at -20 °C. For injection, the adenine and thymidine solutions were further diluted together in MilliQ water to a final concentration of 2 mg/ml. The solution was injected intraperitoneally at day E7.0, 8.0 and 9.0 at a concentration of 20 mg/kg.

For *in vivo* 5-ethynyl-2'-deoxyuridine (EdU) administration, powder EdU (Sigma Aldrich) was dissolved in MilliQ water at a concentration of 5 mg/ml and stored at -20 °C. Pregnant females were injected intraperitoneally with EdU solution at a concentration of 50 mg/kg, and litters were collected after 15 minutes and rapidly transferred to ice-cold DMEM to prevent continued EdU uptake.

2.2 - Embryo collection and processing

Pregnant females were culled by cervical dislocation at the appropriate day of gestation. The uterus was removed using dissection forceps and scissors, and any excess fat and blood vessels were removed. Embryos from E8.5-E13.5 were transferred to a 5 ml bijoux or 15 ml falcon containing warm Dulbecco's Modified Eagles Media (DMEM; Life Technologies) with 10% heat-inactivated fetal bovine serum (FBS; Invitrogen), except for the EdU pulse experiment, where the uterus was immediately transferred to ice cold DMEM.

Individual decidua were dissected out of the uterus into dishes containing warm DMEM + 10% FBS (with the exception of EdU experiments, where ice cold DMEM was used). A small hole was made over each implantation and gradually widened until the underlying decidua began to protrude from the opening. Care was taken when removing the layers of the uterine wall to keep the embryonic membranes intact, as a build-up of pressure could lead to the embryo popping out of the yolk sac. For all experiments excluding culture, embryos were dissected out of the yolk sac and the amnion was removed.

2.2.1 - Dissection for culture

Once individual decidua at E8.5-9.5 were obtained, a central incision was made around the circumference of the decidua, and the decidua was removed to expose the ectoplacental cone and adjacent trophoblast. A second incision was made in the trophoblast and Reichert's membrane, pulling them away from the underlying yolk sac, and these were carefully removed leaving the ectoplacental cone intact.

2.2.2 - Preparation of rat serum

Rat serum was used as medium for all culture experiments. The serum was prepared from fresh rat blood collected from anaesthetized Sprague-Dawley rats at the UCL Biological Services Unit. Blood was collected in 15 ml glass falcon tubes and centrifuged for 5 minutes at 1200 xg. The tubes were then left at room temperature for >20 minutes, which separated red blood cells from the plasma. A fibrin clot formed in the red blood cell-free plasma, which was subsequently squeezed using sterile forceps. Care was taken to prevent disturbance of the red blood cell layer. The tubes were centrifuged for 5 minutes at 4000 rpm at 4 °C, causing the squeezed clot to collapse and leaving clear serum on the upper surface of the clot. This serum was decanted using a sterile pipette into 50 ml falcon tubes, which were centrifuged for 5 minutes at 4000 rpm at 4 °C to separate any remaining red blood cells. Clear serum was decanted into fresh sterile 50 ml falcon tubes and heat-inactivated in a 55 °C water bath for at least 30 minutes. Finally, 2-3 ml of serum at a time was aliquoted into 5 ml tubes and stored at -20 °C. Aliquots were thawed immediately before use.

2.2.3 - Preparation for culture

Embryos were size matched according to the size of their yolk sacs and distributed alternately into the appropriate number of experimental groups. This was to ensure there was a spread of somite stages between groups.

For micro-injection of functional-grade E-cadherin antibody (CD324, anti-rat, Thermo Fisher Scientific), a mouth-controlled pipette was used with an attached micro-needle. The needle was manually passed through the yolk sac and amnion, avoiding blood vessels. The solution was visualised using CellMask (Thermo Fisher Scientific) or FastGreen (Sigma Aldrich), and injected until the amnion had been filled but the solution was not spilling into the yolk sac.

Rat serum was filtered using a 0.45 µm pore size filter into sterile culture tubes (size 50 ml for >3 hours, 5 ml for <3 hours culture). Appropriate concentrations of EdU or blebbistatin (Calbiochem) were made up in rat serum for these experiments, and for blebbistatin experiments the culture tube was covered in foil to prevent photo-degradation. Embryos were then added to the serum, taking care to prevent the addition of DMEM. Vacuum grease was applied around the rim of the culture tubes, and the tube was gassed for 30 seconds using a glass Pasteur pipette (5% CO_2, 5% O_2 for E8.5; 5% CO_2, 20% O_2 for E9.5), before being sealed and added to a rolling apparatus. For a 24 hour culture, embryos were gassed 2-3 times over the experimental time period.

2.2.4 - Embryo processing for immunofluorescence

After dissection, embryos were either fixed in 4% PFA for 2-24 hours, or fixed in ice-cold acetone/methanol (50/50) for 20 minutes before transfer to ice cold 100% methanol. Phenotypes were scored (Chapter 2.2.6) before acetone-methanol fixing, as this protocol makes embryos lose their transparency. These measurements could be taken before or after PFA fixation. PFA fixed embryos for whole mount immunofluorescence were kept in PBS + 0.1% Sodium Azide at 4 °C. PFA fixed embryos for immunofluorescence on sections were sequentially dehydrated in 25%, 50% and 70% ethanol in PBS for at least 15 minutes per solution on a shaker at room temperature, and were stored in 70% ethanol in PBS at 4 °C. Embryos in methanol were stored at -20 °C.

2.2.5 - Tissue collection for RNA and protein extraction

Tissue for RNA and protein experiments was dissected from whole embryos removed from the yolk sac and amnion, washed in DEPC PBS and snap frozen on dry ice. Whole embryos were used for testing antibodies for western blotting. For all other experiments, the caudal region of the embryo was used, cut at the 5th somite from the caudal end using sharp dissection forceps. For RNA sequencing, the caudal region was microdissected along the ventrodorsal axis, to separate out the hindgut from the SE. Microdissection was performed using plates half filled with 4% agarose in PBS, and the caudal region fixed into place using microsurgical needles (11-0 Mersilene and 10-0 Prolene, Ethicon). A disposable ophthalmic scalpel (Feather) was used to create individual cuts sequentially from rostral to caudal, and the ventral and dorsal halves were gently separated using dissections forceps. All tissue was stored at -80 °C.

2.2.6 - Phenotype scoring

From E8.5-9.5, somites were counted and the length of the PNP was measured using a graticule at 4x zoom, or by analysis of confocal images using FIJI. For some experiments, the curvature of the PNP was also measured by analysis of confocal images. At E9.5, the cranial phenotype was scored if the cranial NT was still open, and the regions which were open were recorded (forebrain, midbrain, hindbrain and frontonasal prominence).

The cranial phenotypes of later stage embryos were scored as above. The spinal phenotype was scored as straight tail (no defect), tail flexion defect (curled or kinked tail), mild spina bifida or severe spina bifida.

2.3 - Genotyping

2.3.1 - Extraction of genomic DNA

After embryo dissection, either the yolk sac (if the whole embryo was needed) or a small amount of tissue from the embryo was washed in PBS and collected in a 0.2 ml tube. DNA was collected from postnatal litters by ear clipping. 45 - 49 µl standard PCR lysis buffer and 1 - 5 µl 10 mg/ml proteinase K (PK) enzyme were added to each DNA sample and left overnight in a 55 °C water bath. PK was then deactivated by a 15 minute incubation at 85 °C. These samples could then be used directly in a PCR.

For genomic qPCR, DNA was extracted using an ethanol precipitation method. DNA samples were collected in a 1.5 ml Eppendorf, 476 µl DNA extraction buffer (Table 2.1) and 24 µl 10 mg/ml PK enzyme was added, and the samples were digested overnight in a 55 °C water bath. The next day, 80 µl 3 M sodium acetate was added and mixed, and the samples were centrifuged at 13,200 rpm for 20 minutes at 4 °C. In fresh tubes, the supernatant was added to 1 ml ice cold 100% ethanol, left on ice for >15 minutes, and centrifuged at 13,200 rpm for 20-30 minutes at 4 °C. The supernatant was discarded and 250 µl 70% ethanol in MilliQ water was added, and the samples were centrifuged at 13,200 rpm for 5-10 minutes at 4 °C. The supernatant was poured away and the sample was centrifuged for 1 minute at 13,200 rpm at 4 °C, and the remaining ethanol was removed using a pipette. Finally, the pellet was left to air dry, before being resuspended in 20-30 µl MilliQ water.

Reagent	Volume (ml)	Final concentration
1 M Tris-HCL (pH 8.5)	12	100 mM
0.5 M EDTA (pH 8.0)	1.2	5 mM
5 M NaCl	4.8	200 mM
10% SDS	2.4	0.2%

Table 2.1 - DNA extraction buffer recipe used in ethanol DNA precipitation.

2.3.2 - Polymerase Chain Reaction (PCR)

The components of each reaction and the temperatures/timings during the reaction varied between genotypes, and are summarised in Tables 2.2 and 2.3. All primers and a brief summary of each reaction are shown in Table 2.4. PCR products were visualised using gel electrophoresis on agarose gels (agarose powder (Thermo Fisher Scientific) dissolved in 100 ml TAE buffer), using 5 µl Ethidium Bromide (Thermo Fisher Scientific) to stain DNA. High percentage gels (4-5%) were made using 50/50 standard agarose and low-melting-point agarose (Thermo Fisher Scientific).

Step	Description	Temperature (°C)	Duration
1	Initial heating block	94 – 96	2 – 5 minutes
2	Denaturation	94 – 96	30 seconds – 1 minute
	Annealing	54 – 60	30 seconds – 1 minute
	DNA extension	72	45 seconds – 1 minute
3	Final extension	72	5 – 10 minutes

Table 2.2 – PCR reaction steps.

Step 2 was cycled 32-35 times. Temperatures and duration varied with reaction.

	General PCR reaction - for *Grhl3*$^{x/x}$ and *Grhl2*$^{x/x}$	Grhl3_UF10/ UR10 – for *Grhl3*$^{ct/x}$	Grhl3-BAC - for *TgGrhl3*	Crp microsatellite - for *Vangl2*^{lp}	D4Bwg1551e – for *Grhl3*$^{ct/x;TgGrhl3}$
10x Taq polymerase buffer	3	3	5	5	5
dNTP	1.5; 25 mM	1.5; 25 mM	5; 25 mM	5; 25 mM	5; 25 mM
$MgCl_2$	0.7; 25 mM	0.7; 25 mM	1.5; 25 mM	1.5; 25 mM	1.5; 25 mM
Primers	1.5 forward, 1.5 reverse ; 10 µM	1.5 forward, 1.5 reverse ; 10 µM	0.3 ; 40 µM	0.3 ; 40 µM	2.5 forward, 2.5 reverse ; 10 µM
Taq polymerase	0.15; 5 units/µl	0.3; 5 units/µl	0.25; 5 units/µl	0.5; 5 units/µl	0.5; 5 units/µl
Betaine	-	5	-	-	-
H_2O	20.65	15.5	35.95	35.7	31
DNA template	1	1	2	2	2
Total volume	30	30	50	50	50

Table 2.3 – PCR mixture components.

Different PCR reactions are summarised in each column. All volumes are in µl.

Primer Name	Primer Sequence	Annealing Temperature	Description
GRHL3_UF10 (forward) GRHL3_UR10 (reverse)	5'-TTGTATTTTCTTGCTTGAAACG-3' 5'- TCAGCGTAAGAAAGCTGTGG-3'	54 °C	AciI digestion of 551 bp band to distinguish between *ct/ct* and *ct/+* or to indicate presence of the *Grhl3* BAC
Rocky1 (forward) Rocky2 (reverse)	5'-GTCGACATTTAGGTGACACTA-3' 5'-TCACGTGGTCATCATTAGGG-3'	54 °C	Single 230 bp band indicates presence of the *Grhl3* BAC.
Get1 flox F Get1 flox R	5'-GAGCCCAGGGTGTATTCAAA-3' 5'-ATGACAATGGCTCCCTCAAC-3'	60 °C	Single 199 bp band indicates presence of the floxed *Grhl3* allele
Get1 del F Get1 del R	5'-GAATTACAAGTCTGTGCCACCA-3' 5'-ATTTGCTGACCTTTTTCTGAGC-3'	60 °C	Single 204 bp band indicates deletion of *Grhl3*
Lp F Lp R	5'-GAGGGAGAAGAATTATGTCTG-3' 5'-AGAATCTGACTTACCCATGGT-3'	58 °C	Wild type allele gives 150 bp band, mutant allele gives 140 bp band
D4Bwg1551e–L D4Bwg1551e–R	5'-AAAGGGAGTGTGCACGG-3' 5'-TTTGGGACTGGCCAGGA-3'	60 °C	Wild type allele gives 122 bp band, mutant allele gives 125 bp band
Grhl2_F14 Grhl2_R16	5'-AGACCAGCGAAGACACTCACA-3' 5'-GGATCTGAACTCATGACTGGG-3'	60 °C	Amplifies ~1 kb band within intron 14 in wild type *Grhl2*, absent in mutants due to presence of gene trap.
Grhl2_IntF13 Grhl2_En2	5'-TTGCTCTGCTCTTACCACACG-3' 5'-TCAACTTTGGAGACATGCGGG-3'	60 °C	Single band, with the forward primer in intron 14 and the reverse primer in the gene trap, indicates the presence of the *Grhl2* gene trap vector
D15MIT250_F D15MIT250_R	5'-TATCCTTTGACCTCCATGTGTG-3' 5'-TCAGTACAAATCATGTTAATCTGTGTG-3'	60 °C	Wild type allele gives 107 bp, mutant allele is polymorphic
Grhl3_Int2-3_F Grhl3_Int2-3_R	5'-TGCAGGCTGTTAGTGTCTGG-3' 5'-CACAGCCCTGAAAATGACCT-3'	60 °C	Used in genomic qPCR, with *Grhl2* expression used as a reference. Approximately twice the levels of *Grhl3* expression are expected in $ct/ct^{TgGrhl3/TgGrhl3}$ compared to $ct/ct^{TgGrhl3/+}$
Grhl2_Int1-2_F Grhl2_Int1-2_R	5'-TGGCAACTGGTTTGTTGTGT-3' 5'-CCCTGAATCGGGGTAGAAAT-3'	60 °C	

Table 2.4 – Summary of PCR reactions for genotyping.

Primer name and sequence, annealing temperature used in the reaction and summary of each PCR for genotyping.

2.3.3 - Genotyping *Grhl3*$^{ct/x}$

The Grhl3_UF10/UR10 PCR yields a 551 bp band on a 2% agarose gel. Both wild type and *ct* DNA produce a band, however a digestion reaction was used to detect the presence or absence of the C-21350T mutation (see Chapter 1.3.3).

For the digestion, 10 µl of PCR product was added to an enzyme mix containing 0.3 µl AciI enzyme, 1.5 µl CutSmart Buffer and 3.2 µl H_20, mixed thoroughly and incubated for at least 3 hours in a 37 °C water bath. The C-21350T mutation leads to loss of an AciI digestion site, resulting in 2 bands on a 2% agarose gel for homozygous mutants and 4 for heterozygotes (Figure 2.1). Wild type DNA lacking a copy of mutant *ct* gives 3 bands.

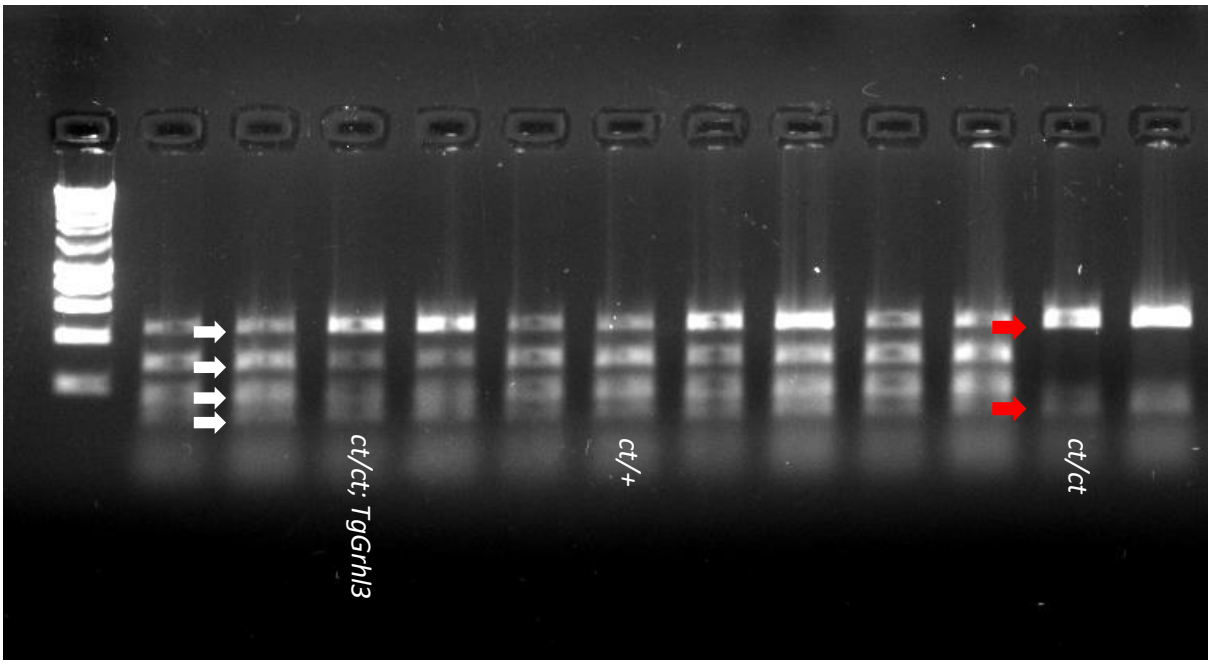

Figure 2.1 - Digestion reaction for genotyping.

Presence of the C-21350T mutation leads to loss of an AciI digestion site. Homozygous ct/ct therefore only have 1 digestion site within the 510 bp UF10/UR10 PCR product, and show 2 digestion bands (red arrows). The presence of two AciI digestion sites, present either in the wild type Grhl3 locus in heterozygous ct/+ DNA or in the wild type BAC in ct/ct^{TgGrhl3} *DNA, gives four bands (white arrows).*

2.3.4 - Genotyping *Grhl3*$^{ct/ct;TgGrhl3}$

As an alternative to the digestion reaction as above (the presence of 4 bands on a homozygous *ct* background indicated the presence of the BAC), the insertion of the BAC could be detected

by amplifying a region within the BAC. The forward primer (Rocky1) was located within the BAC vector, and the reverse primer (Rocky2) was located within the *Grhl3* gene. This PCR generated a single 230 bp band on 2% agarose gel in the presence of the BAC.

2.3.5 - Genotyping *Grhl3*$^{f/-}$

Two separate reactions are required to detect the floxed *Grhl3* allele and the deletion allele (Yu et al., 2006). The wild type PCR amplifies a 199 bp product within exons 4-6, which are deleted in null samples. The deletion PCR amplifies exons 3-8, giving a 204 bp product in null samples. The product is too large to be amplified in floxed samples, therefore there is only a band in samples containing a deleted allele. Both products are visualised on a 2% agarose gel.

2.3.6 - Genotyping *Vangl2*^{Lp}

The Lp PCR amplifies a microsatellite Crp which is linked the mutant *Lp* allele on chromosome 1 (Copp et al., 1994). The PCR amplifies a band which is 150 bp in wild type and 140 bp in mutants, which can be distinguished on a 4% agarose gel.

2.3.7 - Genotyping *Grhl3*$^{ct/x;TgGrhl3}$

In the presence of the *Grhl3* transgene, it is not possible to distinguish between c*t* heterozygotes and homozygotes using the digestion method. The polymorphic microsatellite D4Bwg1551e on chromosome 4 was therefore amplified for genotyping. The PCR amplifies a band which is 122 bp in wild type and 125 bp in mutants, which can be distinguished on a 5% agarose gel.

2.3.8 - Genotyping *Grhl2*$^{-/+}$

Two separate reactions are required to detect the wild type *Grhl2* allele and the gene-trap allele. The wild type PCR amplifies an ~1 kb product within intron 14, which is disrupted by the gene trap in mutant samples. The deletion PCR uses a reverse primer inserted into the gene trap and a forward in intron 14, giving a product in mutants only (Brouns et al., 2011) .

2.3.9 - Genotyping *Grhl2*$^{Axd/+}$

The Axd PCR amplifies a polymorphic marker, D15Mit250, which is closely linked to the *Axd* locus (Brouns et al., 2011). The PCR amplifies a band which is 107 bp in wild type and mutants are polymorphic, which can be distinguished on a 5% agarose gel.

2.3.10 - Genotyping *Grhl3*$^{ct/ct;TgGrhl3/TgGrhl3}$

Distinguishing *Grhl3*$^{ct/ct;TgGrhl3;TgGrhl3}$ from *Grhl3*$^{ct/ct;TgGrhl3/0}$ is not possible with the standard PCR as both are positive for the BAC. Genomic qPCR is therefore required, as *Grhl3*$^{TgGrhl3;TgGrhl3}$ will show higher expression of genomic *Grhl3* than *Grhl3*$^{TgGrhl3/0}$. Intronic primers for *Grhl2* and *Grhl3* were designed for this purpose (De Castro et al., 2018a).

Before qPCR the DNA lysis solution was purified by DNA precipitation (Chapter 2.3.1). For genomic qPCR, the reaction mixture is shown in Table 2.5. Concentration of DNA was measured using a NanoDrop (ND-1000 Spectrophotometer) and all mixtures were diluted to 100 ng/µl.

Triplicates of each DNA sample were added to a 96 well plate followed by the reaction mixture. Blanks were also included, by adding water instead of DNA. The plate was sealed and briefly centrifuged. The protocol was a two-step qPCR, with an initial 2 minute pre-run at 95 °C. There were then 40 cycles of the following: 5 second denaturation at 95 °C and 30 seconds annealing/extension at 60 °C. Finally, a heat curve was obtained by gradually increasing the temperature by 0.5 °C. Bio-Rad CFX Manager software was used for subsequent data analysis. When triplicates showed a Cq with a standard deviation of >0.3, the most divergent sample was discarded.

Reagent	Volume (µl)
iTaq	10
Forward primer (10 µM)	1.6
Reverse primer (10 µM)	1.6
DNA	1 - 2
H_2O	4.8 - 5.8

Table 2.5 – Genomic PCR reaction mixture.

2.4 - RNA based techniques

2.4.1 - RNA extraction

The RNeasy micro/mini kits (Qiagen) were used for RNA extraction, depending on the amount of tissue used. Where different conditions are used for each kit, the first condition given is for the micro kit and second for the mini. All buffers were provided in the kit. Tissue was disrupted and homogenized in 350 µl Buffer RLT + 3.5 µl β-mercaptoethanol per sample. 350 µl 70% ethanol in SIGMA water was added to the sample and mixed thoroughly by pipetting. The total 700 µl was then transferred to an RNeasy spin column and centrifuged for 15 seconds at ≥ 10,000 rpm. 350/700 µl Buffer RW1 was added to the column and centrifuged at ≥ 10,000 rpm for 15 seconds, and the flow-through was discarded. (For the RNeasy micro kit, DNase digestion was then performed by adding 80 µl DNase I incubation mix to each column (70 µl Buffer RDD and 10 µl DNase I stock solution) and incubating for 15 minutes. 350 µl buffer RLT was added to the column and centrifuged at ≥ 10,000 rpm for 15 seconds. Flow-through was discarded and the column was added to a new collection tube.) 500 µl Buffer RPE was added and the column was centrifuged at ≥ 10,000 rpm for 15 seconds. 500 µl 80% ethanol/Buffer RPE was then added and the column centrifuged at ≥ 10,000 rpm for 2 minutes. Flow-through was discarded, the column was transferred to a new tube and centrifuged for 5/1 minute(s) at ≥ 10,000 rpm to remove any excess buffer. The column was then transferred to a 1.5 ml collection tube, 14/30 µl SIGMA water was added and centrifuged for 1 minute at ≥ 10,000 rpm. For the mini kit, the eluate was added to the same column and spun for a final time to maximise yield.

After the mini kit only, DNAse and RNAse were removed by adding 1.05 µl RNAse inhibitor, 3.75 µl DNAse I buffer and 0.75 µl DNAse I, mixing and incubating at 37 °C for 30 minutes. 3.75 µl DNAse inactivation reagent was then added, mixed and left at room temperature for 2 minutes. Finally, the mix was centrifuged at maximum speed for 2 minutes, supernatant collected in new tubes and frozen at -80 °C.

2.4.2 - qRT-PCR

For cDNA synthesis, the RNA concentration was measured and 14 µl of 500 ng/µl per sample was added to 4 µl 5X Superscript Vilo Reaction Mix (Thermo Fisher) and 2 µl 10X Enzyme mix. Samples were then incubated at 25 °C for 10 minutes, 42 °C for 60 minutes, and finally the reaction was terminated at 85 °C for 5 minutes. qRT-PCR was carried out as described in Chapter 2.3.8, using GAPDH as the housekeeping gene.

2.4.3 - RNA sequencing

RNA sequencing was performed at the University College London Genomics Facility. RNA samples were delivered to the facility on dry ice and RNA quality was assessed using the High Sensitivity RNA ScreenTape assay (Agilent). If the quality was high, single end RNA sequencing was then performed and differential expression and gene ontology analysis was performed by an in-house written pipeline using R.

2.5 - Protein based techniques

2.5.1 - Protein extraction

Samples were transferred from -80 °C to dry ice until immediately before protein homogenisation. To prevent proteolysis, a 1:1000 dilution of protease inhibitor was first added to the Radio-Immunoprecipitation buffer (RIPA buffer, Thermo Fisher Scientific). 30-50 µl of the solution was added to each sample one at a time, to ensure processing before the sample could defrost. The sample and lysis buffer mixture was sonicated until clear, using only 3-5 pulses at a time to prevent overheating, and immediately cooled on ice. Samples were then centrifuged at 10000 x g for 15 minutes at 4 °C, and the supernatant was transferred to fresh 1.5 ml Eppendorf tubes.

A Bradford assay was used to analyse the protein content before blotting. 1 µl of sample was diluted to 5 µl in MilliQ water and added to 995 µl protein assay dye (Bio-Rad). Varying concentrations of BSA (from 0 – 25 µg/ml, made up to 25 µl in MilliQ water) were added to 975 µl protein assay dye as reference concentrations. The dye was added immediately before measuring. Optic density was measured on the NanoDrop to calculate protein concentration. If not used in a western blot immediately, protein samples were stored at -80 °C.

2.5.2 - Western blotting

First, the protein samples were separated by molecular weight using one-dimensional protein gel electrophoresis. Samples were kept on ice for all steps before loading. Each sample was diluted to the desired concentration in loading buffer (1:1 Laemmli Sample Buffer, BIORAD) to 20 µl total, and 2.5% (0.5 µl) β-mercaptoethanol was added. Samples were briefly centrifuged before loading.

Ready-made 1 mm thick Bis-Tris gels (NuPage System, Invitrogen) were used for this experiment. To prepare the gel, the plastic packaging was removed and the gel was thoroughly washed with MilliQ water. The plastic comb was then removed and the gel was washed in 1X NuPage MOPS running buffer (Thermo Fisher Scientific); extra care was taken to remove excess gel from the wells. The gel was added to the tank inside the cassette and running buffer was added. The cassette was checked for any leaks, and finally the remainder of the tank was filled with running buffer, ensuring it remained below the level of the cassette. Samples were loaded into separate wells and 10 µl of protein marker (Precision Plus Protein Standards, Dual Colour, BIORAD) was also loaded into one gel for reference, before running for 2-2.5 hours at 100 V.

Protein transfer was via a wet transfer method using the XCell II Blot Module (Invitrogen). While the gel was running, the membranes were prepared. Two pieces of membrane (Immobilon-P, PVDF, 0.45 µm pore size Millipore) and filter paper (3MM, Chromatography paper, Whatman) were cut to size for each gel. Care was taken to avoid touching the membrane, which is stored between two sheets of paper. Using forceps for handling, membranes were briefly washed in methanol and then transferred to Milli-Q water for 2 minutes, before a final wash in transfer buffer for > 15 minutes.

Once electrophoresis was complete, the filter paper was briefly soaked in transfer buffer and laid on top of the gel. The gel was flipped, wetted with transfer buffer using a plastic pipette, and the membrane was transferred from the buffer to lie on top of the gel. Filter paper was added to the top of the membrane and a roller was used to remove air bubbles. The layers of filter paper, gel and membrane were placed on top of two blotting pads soaked in transfer buffer within the transfer cell. A final two soaked blotting pads were placed on top of the filter paper, completing the layers.

The transfer cell was closed and placed in the gel tank. The transfer buffer was topped up if it did not cover the blotting pads, and the outer buffer chamber was filled with MilliQ water to the same level. The unit lid was closed and the transfer was run for 1 hour at 25 V.

From this stage, unless otherwise specified, all washes and incubations were in small rectangular trays, just larger than the size of the membrane to allow movement. After transfer, the membrane was removed from the layers and washed immediately in 1X Tris buffer saline (TBS). Membranes were incubated for 1 hour in blocking solution (TBS + 0.1% Tween-10 (TBST) + 5% non-fat dried milk) on a shaker at room temperature. The membrane was then transferred to a 50ml falcon tube containing 1:1000 or 1:10000 of primary antibody (YAP (rabbit, D8H1X, Cell Signalling, 1:1000); pYAP (rabbit, pSer127, Sigma Aldrich, 1:1000); GAPDH (mouse, #MAB374,

Millipore, 1:10000)) diluted in 5 ml blocking solution, and left overnight at 4 °C (YAP, pYAP) or for 1 hour at room temperature (GAPDH) on a rolling apparatus.

The membrane was removed from the primary antibody solution and washed 3 x 5 minutes in TBST on a shaker at room temperature. It was then incubated in the appropriate concentration of secondary antibody conjugated to horseradish peroxidase (Anti-rabbit HRP, P0448, DAKO, 1:5000; anti-mouse HRP, P0260, DAKO, 1:50000) diluted in blocking solution for 1 hour at room temperature, followed by 3 x 5 minute washes in TBST. Meanwhile, 2 ml/membrane of the chemiluminescent solution (Amersham ECL Prime Western Blotting Detection Reagents, Sigma Aldrich) was prepared according to manufacturer's instructions. The membrane was transferred to a cling-film covered surface and the chemiluminescent solution was added using a pipette. The membrane was incubated in the solution for 5 minutes before transferring to dry cling film. The membrane was blotted using clean tissue to remove excess liquid, was wrapped in cling film and immediately inserted into a cassette with a Hi Speed X intensifying screen. Care was taken to avoid wrinkles in the cling film and to protect the cassette from light. Finally, the membrane was exposed to an X-ray screen inside the cassette for between 1 second and 1 minute and the film was developed in an Autorad Developer. The film was scanned using a GS-800 Densitometer (Bio-Rad) using Quantity One software (Bio-Rad).

2.6 - Immunofluorescence

2.6.1 - Whole mount immunofluorescence

Before immunostaining, acetone-methanol fixed embryos were sequentially rehydrated in 75%, 50% and 25% ice cold methanol in PBS for 20 minutes per solution.

Embryos were initially permeabilised for 1 hour in PBS + 0.1% Triton (0.1% PBST) at room temperature. Embryos were then blocked overnight in blocking buffer (BB, 0.1% PBST + 4% bovine serum albumin (BSA)) at 4 °C.

The next day, BB was removed and 100 µl primary antibody in BB was added, before overnight incubation at 4 °C. Primary antibodies, host and concentration are shown in Table 2.6.

Target	Species raised in	Concentration	Manufacturer
YAP (D8H1X)	Rabbit	1:50	Cell Signalling (#14074)
E-cadherin	Mouse	1:200	BD Bioscience (610181)
E-cadherin (24E10)	Rabbit	1:200	Cell Signalling (#3195)
ZO1	Rabbit	1:100	Thermo Fisher Scientific Invitrogen (402200)
MHC-IIb	Rabbit	1:200	BioLegend (PRB-445) or Abcam (3H2)

Table 2.6 – Primary antibodies for whole mount immunofluorescence.

Details for each primary antibody used, including species raised in, concentration for whole mount immunofluorescence and manufacturer.

Embryos were then washed 3 x 1 hour in BB. 100 µl of secondary antibody solution (antibody diluted in BB) was then added (all Alexa Fluor, Thermo Fisher Scientific, 1:500). This solution also contained Phalloidin in appropriate experiments (Alexa Fluor 647, Thermo Fisher Scientific, 1:50). Embryos were incubated for either 2 hours at room temperature or overnight at 4 °C. If a 2 hour incubation was performed, DAPI was also included in the secondary antibody solution at 1:5000 concentration. If incubated overnight, embryos were washed and incubated for 10 minutes in 1:5000 DAPI in BB. Embryos were finally washed for 1 hour in BB, followed by 1 hour in 0.1% PBST and a final hour in PBS. Embryos were kept in PBS + 0.1% Sodium Azide at 4 °C before imaging.

2.6.2 - Paraffin embedding and sectioning

Embryos were fully dehydrated with sequential washes of at least 15 minutes in 85% and 95% ethanol in PBS, followed by 2 x 15 minutes in 100% ethanol. Embryos were then transferred to glass moulds and cleared for 2 x 15 minutes in Histoclear (National Diagnostics). These steps were all at room temperature on a shaker. Embryos were then further cleared for 2 x 15 minutes in Histoclear in a 60 °C oven. A mix of 1:1 liquid paraffin wax and 60 °C Histoclear was then added and the embryos were cleared for 30 minutes in the 60 °C oven. Finally, embryos were incubated in at least 4 x 30 minutes washes of 100% wax. Embryos were embedded in the final wax wash using a stereoscope for visualising the position of the embryo. Forceps were kept hot using an oil burner so that wax could be melted on the upper layers. This was to allow wax to set around

the bottom layers first (and therefore around the embryo), ensuring accurate positioning. The wax was then allowed to set completely overnight at room temperature.

Once the wax had set, the glass moulds were cooled at -20 °C until the wax could be easily removed from the moulds. The wax was cut down to size, adhered to a wooden block using liquid wax and allowed to set. A microtome was used to obtain 5 µm thick sections, which were added to a water bath at ~35 °C to remove wrinkles. The sections were placed on glass slides, left to partially dry flat at room temperature for ~1 hour, and finally left overnight at 37 °C.

2.6.3 - Immunofluorescence and EdU detection on paraffin sections

All of the following steps were performed at room temperature unless otherwise stated. Two opaque slide holders were alternately used for washes, to prevent sections drying out between washes.

Sections were first deparaffinised in Histoclear for 2 x 10 minutes. Sections were then sequentially rehydrated in 100%, 75%, 50% and 25% ethanol in PBS for 5 minutes, before leaving under running water. Care was taken to keep the flow of water away from the surface of slides, in order to prevent damage of sections. The sections were heated to 110 °C for 2 minutes in 500 µl 1X antigen retrieval solution (1.47 g Tris Sodium Citrate + 0.25 ml Tween20 made up to 500 ml in MilliQ H_2O and pH corrected to 6) using a pressure cooker. Once the slides had cooled, they were washed under running water for 5 minutes, followed by 2 x 5 minutes in 0.1% PBST. Slides were then incubated in 300 µl blocking solution (150 mg glycine + 200 mg BSA + 100 µl Triton X-100, made up to 100 ml in PBS) + 10% heat-inactivated sheep serum (HISS) for 1 hour in a humidified chamber. Slides were then incubated in 250 µl primary antibody diluted in blocking solution + 1% HISS in the humidified chamber overnight at 4 °C. The primary antibody used in this experiment was pHH3 (Ser10, anti-rabbit, Millipore).

The next day, slides were washed in 0.1% PBST for 3 x 5 minutes. Sections were incubated in the humidified chamber for 30 minutes in 300 µl EdU detection solution (Click-iT kit, Table 2.7). Sections were washed in 0.1% PBST for 3 x 5 minutes, and incubated in a humidified chamber for 1hr in secondary antibody diluted in blocking solution + 1% HISS. The secondary antibody used in this experiment was Alexa Fluor 568 (anti-mouse, 1:500).

Slides were washed in 0.1% PBST for 3 x 5 minutes and were incubated for 5 minutes in 500 µl Sudan Black (diluted in 70% ethanol in PBS) to reduce autofluorescence. Slides were washed in 0.1% PBST for 3 x 5 minutes and were incubated in 1:10000 Hoescht in PBS for 30 minutes, or

for 5 minutes in 1:10000 DAPI. Slides were washed in PBS for 3 x 5 minutes. Finally, slides were gently tapped to remove excess PBS, and mounting medium (VectaShield, Vector Laboratories or ProLong Gold, Thermo Fisher Scientific Invitrogen) was added. Coverslips were added to the slides, taking care to minimise air bubbles. Slides were left to dry overnight and sealed using clear nail polish the next day.

Reagent	Volume per sample (µl)
1X Reaction Buffer	258
$CuSO_4$	12
Alexa Fluor (488)	0.72
1X Additive	30

Table 2.7 – EdU detection solution for Click-iT kit.

2.7 - Confocal imaging and ablations

Imaging of whole embryos (live and fixed) and all laser ablations were carried out on an inverted LSM880 confocal microscope (Zeiss). Imaging of sections were carried out on upright fluorescence microscopes (3 colour, Leica and 4 colour, Zeiss Observer).

2.7.1 - Embryo positioning

For whole embryo imaging, embryos were positioned in 60 mm dishes on 4% agarose in PBS. Microsurgical needles (11–0 Mersilene; TG140-6; Ethicon and 10–0 Prolene; BV75-3; Ethicon) were used for positioning. For ablations, whole decidua were placed in 1.5 ml Eppendorf tubes containing DMEM + 10% FBS, briefly gassed with 20% O2 and 5% CO2, and kept on a 37 °C heated plate. Embryos were then dissected from the decidua and all the underlying membranes immediately before staining and positioning.

To position embryos for ZP ablations and whole mount immunofluorescence imaging, a small hole was made in the agarose and the embryo was held in place using a suture needle through the heart into the side of the hole, with the PNP visible above the surface of the agarose (Figure 2.2A). Care was taken to keep the PNP away from the heart, as the heart continued to beat steadily throughout the experiment. For larger embryos, a second needle was sometimes used

for extra stability, by pinning through another part of the embryo (avoiding the PNP) or by resting the embryo on the side of the needle.

For single border laser ablation, the embryo was briefly stained in CellMask (Thermo Fisher Scientific) diluted in DMEM + 10% FBS. The caudal half of the embryo was then separated from the rostral half immediately before positioning, as the beating heart would cause too much movement to accurately ablate single borders. The caudal region was positioned by piercing the needle through the most ventral part of the tissue, avoiding the region where the ablations would take place (Figure 2.2B).

For whole mount immunofluorescence imaging, embryos were mounted in dishes with PBS. For ablation experiments, embryos were mounted in DMEM + 10% FBS kept at 37 °C. The imaging chamber was maintained at 37 °C during laser ablation and image acquisition.

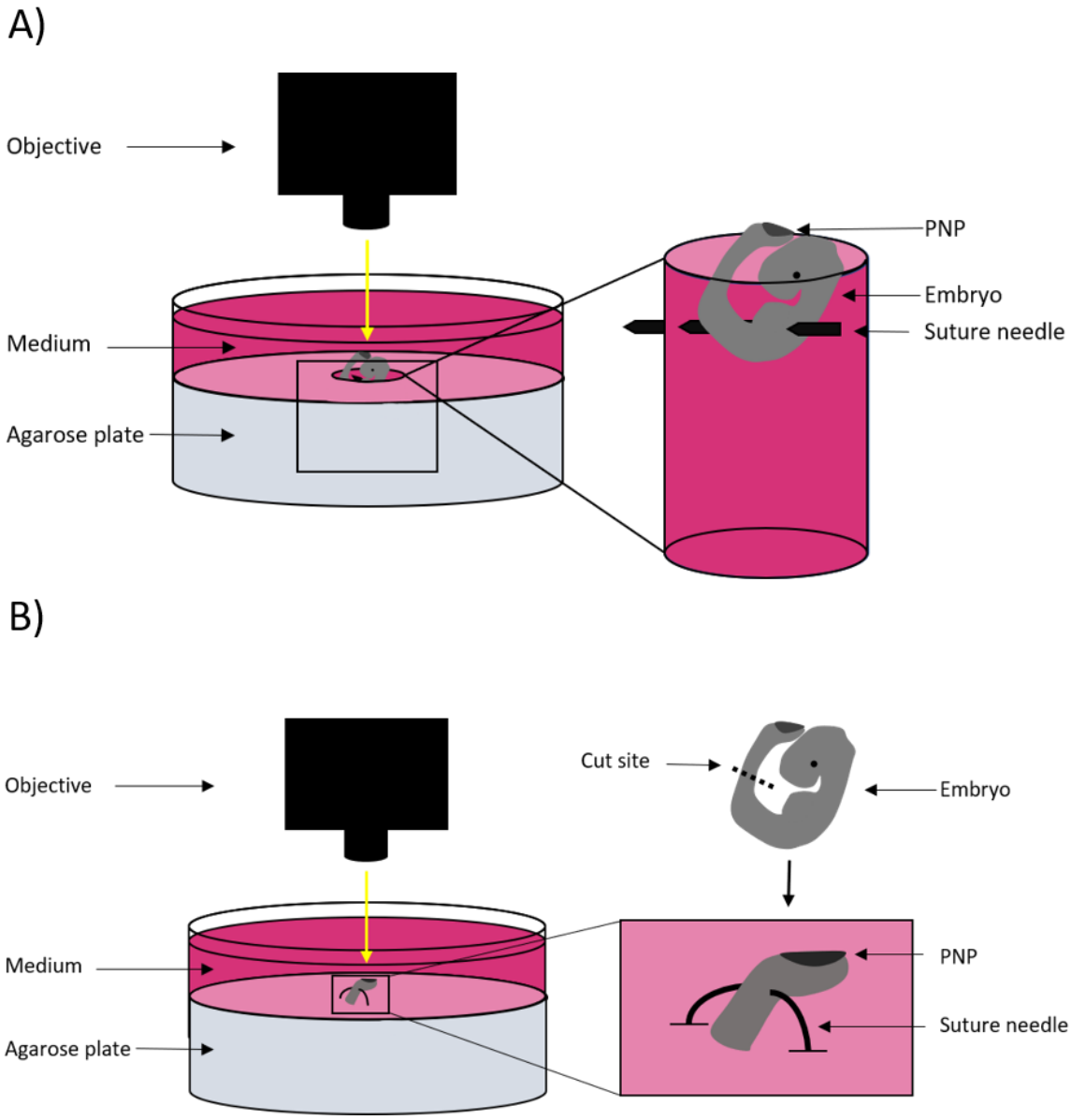

Figure 2.2 – Embryo positioning for whole mount imaging and ablations.

A) For ZP ablations and whole mount immunofluorescence imaging, whole embryos were positioned by creating a hole in the agarose plate and piercing the embryo through the body to the walls of the hole using a suture needle. B) For single cell ablations, the caudal region of the embryo was cut and positioned by piercing the ventral half of the tissue using a curved suture needle. The tissue was then held in place with both ends of the suture needle fixed in the agarose.

2.7.2 - Imaging settings

Imaging settings for different experiments are summarised in Table 2.8. For immunofluorescence, laser power and gain were kept constant within each experiment. For standard confocal multitrack imaging, the track was changed after every z stack to minimise time taken for each image.

For single border ablations, a single z-slice of the target region was imaged for 2 frames, ablated, and then imaged for a further 18 frames. Each frame was ~0.9 seconds and the total imaging time was ~18 seconds. The region of interest for ablation was manually drawn as a rectangle of 1 pixel in width and approximately constant length. Laser power was varied for the imaging depending on CellMask signal, while laser power for the ablation was always at 100%.

ZP ablations were carried out as first described (Galea et al., 2017). To show the overall shape of the PNP, a z-stack was taken of the PNP before and after ablation. The ZP was then ablated using manually drawn regions of interest, moving sequentially through the z-stack (i.e. dorsoventrally) to ensure all of the ZP was successfully ablated. Ablations were carried out from the ZP rostrally for 300 - 500 µm. Laser power for these ablations was always at 100%.

Experiment	Objective(s)	Lasers used	Laser power	Zoom	Pixel dwell (µsec)	Iterations	Area imaged (pixels)
Immuno-fluorescence (whole mount)	20x/NA1.0 Plan Apochromat, 10x/NA0.5 Plan Apochromat	405, 488, 561, 633	Varied, kept constant within experiments where possible	1.5x, 1x, 0.7x for tilescan	N/A	N/A	1024 x 1024
Single border ablations (imaging)	20x/NA1.0 Plan Apochromat	633	Varied depending on CellMask signal	4x	N/A	N/A	1024 x 1024
Single border ablations (ablation)	20x/NA1.0 Plan Apochromat	710 (MaiTai)	100%	4x	0.34	20	1024 x 1024
ZP ablations (imaging)	10x/NA0.5 Plan Apochromat	633	Varied	0.7x	N/A	N/A	1024 x 1024
ZP ablations (ablation)	10x/NA0.5 Plan Apochromat	800 (MaiTai)	100%	0.7x	16.38	1	1024 x 1024

Table 2.8 – Imaging settings for immunofluorescence and ablations.

2.8 - Image analysis

All images were analysed using the image analysis software FIJI (Schindelin et al., 2012).

2.8.1 - Surface subtraction

To improve SE signal, an in-house surface-subtraction macro was used to remove unwanted signal from the NE (Galea et al., 2018). This macro identifies the upper surface of a resliced image of an E9.5 NT by detecting the first pixel to have positive signal, after scanning from the top (i.e. above the dorsal NT) to the bottom (i.e. ventrally, deep in the tissue) of the image. A region of set pixel width is then taken from the surface of the PNP, and any signal outside of this region is

removed. The width of this region differed depending on the objective used and zoom of the image, but varied between 30 - 70 pixels.

2.8.2 - Cell shape analysis

Cell shape was analysed using an inbuilt FIJI plugin, TissueAnalyzer (Aigouy et al., 2016). Cells within a region of constant size rostral to the ZP were segmented. Depending on the clarity of the image, some borders were manually selected. Different groups of cells were selected for analysis using the tracing tool in FIJI. A straight line drawn along the rostrocaudal (RC) axis of the analysis region was used to select cells along the midline (Figure 2.3A) or laterally (Figure 2.3B). For some analyses, all cells within the analysis region were selected. An ellipsis was fitted to each selected cell using the 'select measurements' tools in FIJI, and aspect ratio and angle of the long axis was measured. Cell circularity and area were also calculated from the raw segmentation.

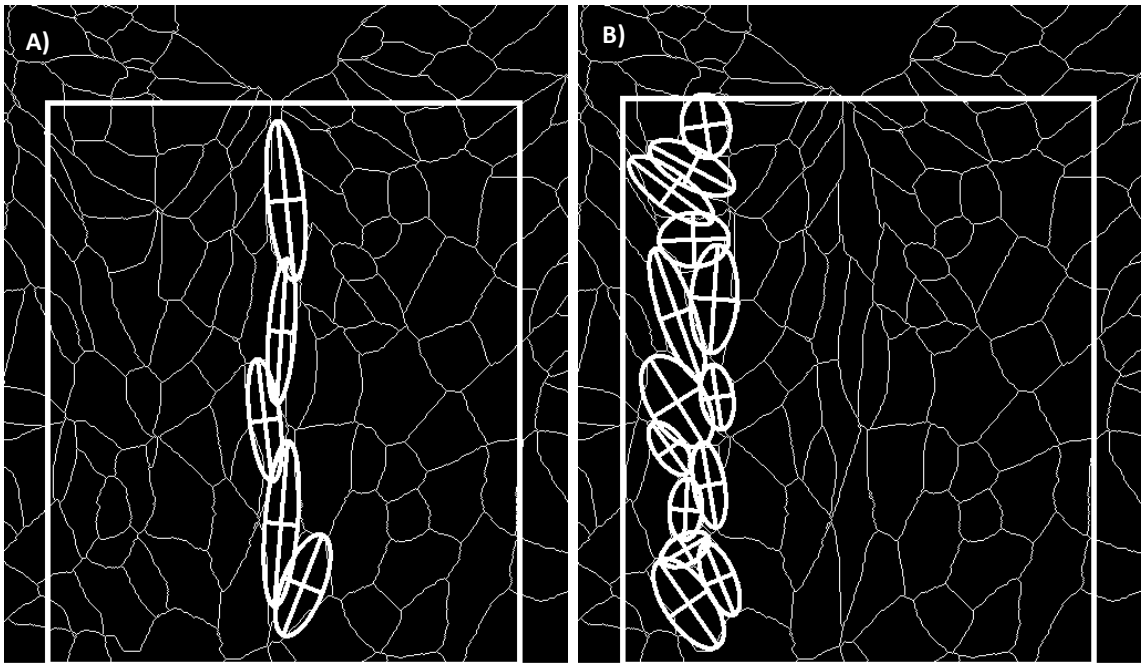

Figure 2.3 – Cell shape analysis method.

Example segmented images of the closed region of an E9.5 NT, with ellipses fitted to cells along the midline (A) or laterally (B).

2.8.3 - Nuclear segmentation

For YAP nuclear segmentation, the DAPI channel was selected and a morphological filter from the FIJI MorphoLibJ plugin was applied to all slices to remove small bright objects (Legland et al., 2016). The result was then binarised, a watershed filter was applied, and particles with an area of 2 - 100 μm^2 and circularity 0.6 - 1 were segmented to create a mask (Figure 2.4B).

To determine the overall intensity of YAP or DAPI in individual nuclei, the 3D objects counter plugin was used, with the intensity measurements redirected to the channel of interest (Bolte and Cordelieres, 2006). In order to compare YAP cytoplasmic and nuclear intensity, a z-projection of the mask and the YAP channel was created. An outline of the mask (Figure 2.4A,B) was used to subtract the background (Figure 2.4C) or the nuclei (Figure 2.4D), and an average of the intensity over a region of set size was taken.

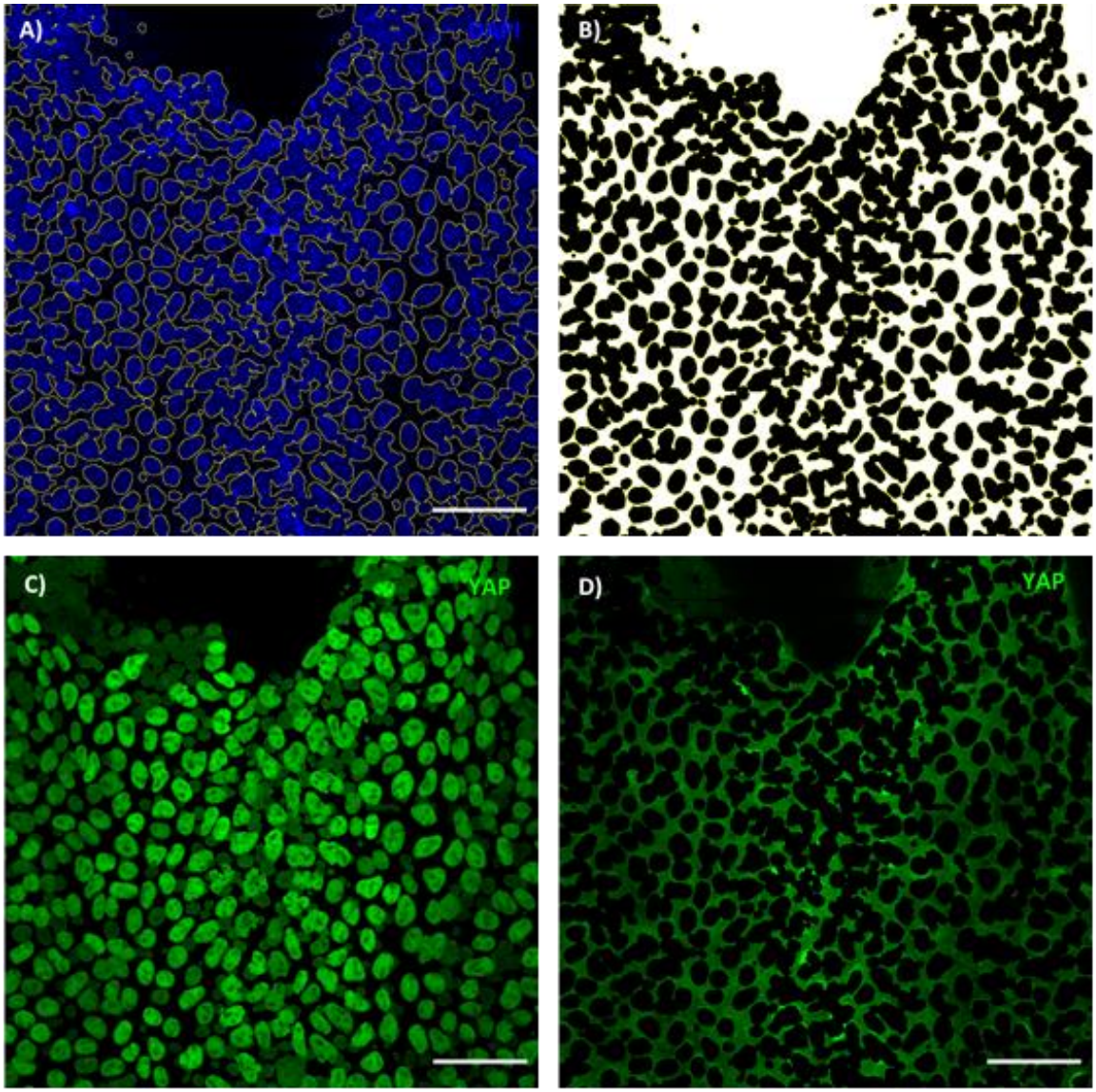

Figure 2.4 – YAP nuclear segmentation method.

A) Representative z-projection of DAPI staining, which is used for nuclear segmentation. Outline in yellow is a projection of an example segmentation back onto the original image. B) Example mask of nuclei after segmentation. C) YAP nuclei after subtraction of cytoplasm. D) YAP cytoplasm after subtraction of nuclei. Scale bars = 50 µm.

2.8.4 - Recoil analysis

Before images were analysed, ablations which met the following conditions were excluded:

1. Ablation hit two or more borders
2. Embryo appeared damaged (i.e. significant blebbing)

In some cases, a border did not recoil after ablation, giving a value of 0 μm and suggesting that the border was bleached. However, as it could not be determined if this was due to a lack of tension or bleaching, these samples were included in the analysis to eliminate bias.

For single cell ablations, frames were registered to correct for any movement using an inbuilt FIJI stack registration plugin. Two reference points on either side of the ablation were chosen, and the distance between these points was measured before and after ablation (Figure 2.5A). The angle of the ablated border was also measured. The average of ablations of the same type (i.e. same direction or region) was taken for each individual embryo.

For ZP ablations, any rotation of the PNP after ablation was corrected manually by reslicing in both Y and Z and subsequent rotation. A 3D registration inbuilt plugin was then used, and a maximum z-projection was created to check that registration was successful. A reslice in Y was then generated and the distance between the neural folds was measured to give initial ZP recoil (Figure 2.5B).

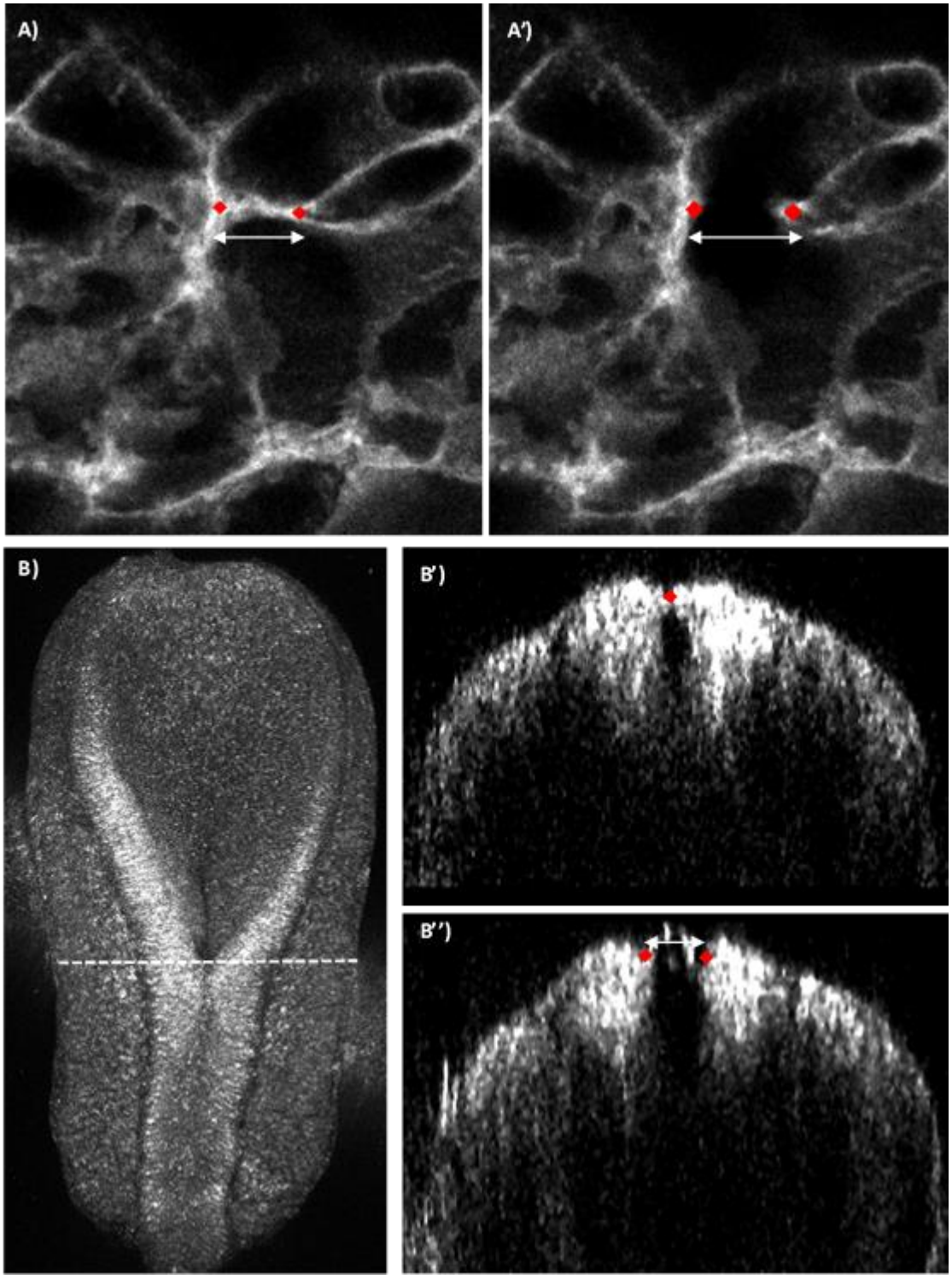

Figure 2.5 – Recoil analysis method after cell or tissue laser ablation.

A) Two reference points were chosen on either side of the ablation site, and the distance between them before (A) and after (A') were measured. B) A reslice in Y was taken of the ablated PNP. The slice at the ZP (white dotted line) was identified, and the distance between the neural folds before (B', taken as recoil 0) and after (B'') were measured.

2.8.5 - PIV analysis

PIV analysis used an inbuilt FIJI plugin (Tseng et al., 2012). PIV works by comparing pixels within an 'interrogation window' of specified size between two frames (in this case, before and after ablation). A vector output is given, which gives direction and magnitude of movement of pixels within each window. A bandpass filter was first applied, followed by the PIV plugin, which ran 3 times with interrogation windows of decreasing size.

2.8.7 – Western blot analysis

Images were first extracted from the Quantity One software as TIF files. These could then be analysed in FIJI. A rectangular ROI of equal size was used to measure the average grey value of each band, in order to compare the intensity.

2.9 - Statistical analysis

All statistical analyses were carried out using Origin versions 2017 - 2020 (OriginLab, Northampton, MA). An ANOVA was used to test if a linear fit correlation was significantly different from 0. Comparison of correlations was by creating a linear fit to each sample group and comparing the linear fits using an f test. Chi Square and Fisher's exact tests were performed using the cross tabulation function.

Heat maps for YAP nuclear intensity and cell shape parameters were generated using measurements extracted from FIJI- cell/nuclear position was given as X and Y coordinates, and the Z axis was defined as either normalised intensity (from 0 - 1, where 1 = maximum intensity) or raw cell shape parameters.

All graphs except compass plots were generated using Origin versions 2017 - 2020 (OriginLab, Northampton, MA). All box plots included the median (line) and mean (square box).

A custom built MATLAB script was used to generate compass plots from PIV data.

Chapter 3 - Investigating the biomechanical properties of the surface ectoderm in wild type embryos

3.1 - Introduction

Much of what we know about the biomechanical processes and underlying cellular mechanisms required for successful NTC comes from the study of genetic mutants. However, because of the highly complex nature of the process, from initiation to the final fusion event, the number of genes and regulatory factors involved make this a limited strategy. It is therefore important to understand the global biomechanical mechanisms underlying NTC in wild type embryos, as well as focusing on the role of individual genes and signalling pathways.

Cell shape is one of the most important and highly studied parameters used to extract data and to infer the forces occurring within a cell population. A large proportion of biomechanics research at the level of cell populations comes from studies of morphogenesis in live *Drosophila* embryos or computer modelling. This is because these types of studies benefit from data collection over a long period, which can more easily be achieved in *Drosophila* than more complex organisms, allowing the relationships between cell shape and global tissue movements to be elucidated.

There are many examples where cell shape changes control and/or reflect individual morphogenetic events. In *Drosophila* germ band extension, cells intrinsically polarise myosin heavy chain (MHC) and myosin regulatory light chain (MRLC) at 'type 1' borders (adjacent to the direction of elongation), which then constrict in order to transition to 'type 3' junctions (parallel to the direction of elongation). This transition acts to intercalate lateral cells towards the midline and extend the germ band (Bertet et al., 2004). In NTC specifically, a homologous T1-exchange mechanism has been observed during CE in the chick and the mouse, with contraction of mediolaterally oriented borders mediating AP elongation (Nishimura et al., 2012; Williams et al., 2014). Live imaging of the E8.0 mouse NP for 8 hours reveals greater complexity in higher organisms, with cells rearranging via division, cell intercalation, rosette resolution and T1-exchange (Williams et al., 2014). In another example, the superficial layer of *Xenopus* NP cells become wedge-shaped via apico-basal elongation and apical constriction, thus facilitating NP bending (Sawyer et al., 2010, Suzuki et al., 2012). A similar mechanism occurs in birds and mammals, although the shape of cells is also linked to nuclear position (Nikolopoulou et al., 2017) (see Chapter 1.1.3).

In other cases, it is not the shape of cells that determine successful development, but their orientation. In a study of *Drosophila* follicle elongation, 3D confocal imaging and subsequent morphometric extraction was used to analyse the effect of abnormal cell shape and orientation in *fat2* mutants (Chen et al., 2019). In the wild type, a subset of cells orient towards the anterior-posterior (AP) axis, while the majority are elongated in the mediolateral (ML) axis. It was shown that, while cell shape was not different at the stages where follicle elongation was beginning to fail, the mutant cells were initially significantly more oriented towards the AP axis. The authors suggested that the shift from ML to AP in a subset of cells was crucial for follicle elongation as it resulted in net cellular intercalation.

Computational models can be used to predict the importance of cell shape and position during morphogenesis. The advantage of such studies is that they allow other biomechanical parameters, such as tissue stiffness and total area, to be set at defined values, whereas biological manipulations are more difficult to control. In a model of germ-band retraction, the role of amnioserosa cell elongation was analysed and found to be essential for retraction initiation (McCleery et al., 2019). In this model, the initial shape of individual cell types was altered without changing the initial overall tissue shape, and it was shown that rounding of individual amnioserosa prevented germband retraction (McCleery et al., 2019).

Most biomechanical research does not simply rely on cell shape to predict the forces a cell is under, but uses active manipulation techniques which physically alter the cell or tissue and measures the response (Basoli et al., 2018). A popular technique is laser ablation, where lasers either in the UV (350-400nm) or near far red (700-800nm) range are targeted at cells or tissues to destroy them (Farhadifar et al., 2007, Liang et al., 2016). A major advantage of this technique is that it can be used at any developmental stage and on any accessible tissue or cell. By utilising laser pulses only femtoseconds in length, thus minimising the build-up of thermal energy, laser ablation technologies have advanced to such a degree to allow ablations at the micrometre scale with minimal damage to surrounding tissues (Tsai et al., 2009).

Using laser ablation at the single cell level has become popular *in vitro* and in invertebrates such as *Drosophila*, however it has yet to be used in higher organisms at stages later than implantation (Bambardekar et al., 2015, Loyer et al., 2015, Samarage et al., 2015, Smutny et al., 2015). While tissue level ablation in the mouse embryo has been useful in elucidating gross features of the mechanical forces driving NTC (Galea et al., 2017), such a technique would allow more fine-tuned characterisation of the process.

3.2 - Results

3.2.1 - Surface ectoderm cells are elongated along the midline

Cell shape is classically used as an indicator of the forces which individual cells or cell populations are under or producing. Therefore, cell shape was analysed in the SE of the recently closed spinal NT in mouse embryos. Whole-mount immunofluorescence of the tight-junction protein ZO-1 was used to visualise apical cell borders in the closing spinal NT of E9.5 C57BL/6 wild type embryos (Figure 3.1A, B). E-cadherin staining, which is specific for the SE and not the NE, was used simultaneously to ensure that SE cells could be identified at the border between SE and NE (Figure 3.1C). A region of set area directly rostral to the zippering point (ZP) was selected, and cell shape was analysed using the Tissue Analyser plugin, using best fit ellipses to extract length, width and orientation parameters (Figure 3.2A, method described in Chapter 2.8.2). This analysis revealed significant elongation of midline cells compared to lateral cells (Figure 3.2B). Furthermore, the long axes of midline cells were significantly more oriented towards the rostrocaudal (RC) axis (defined as 0°) than lateral cells (Figure 3.2C). Cell area did not differ between regions (data not shown).

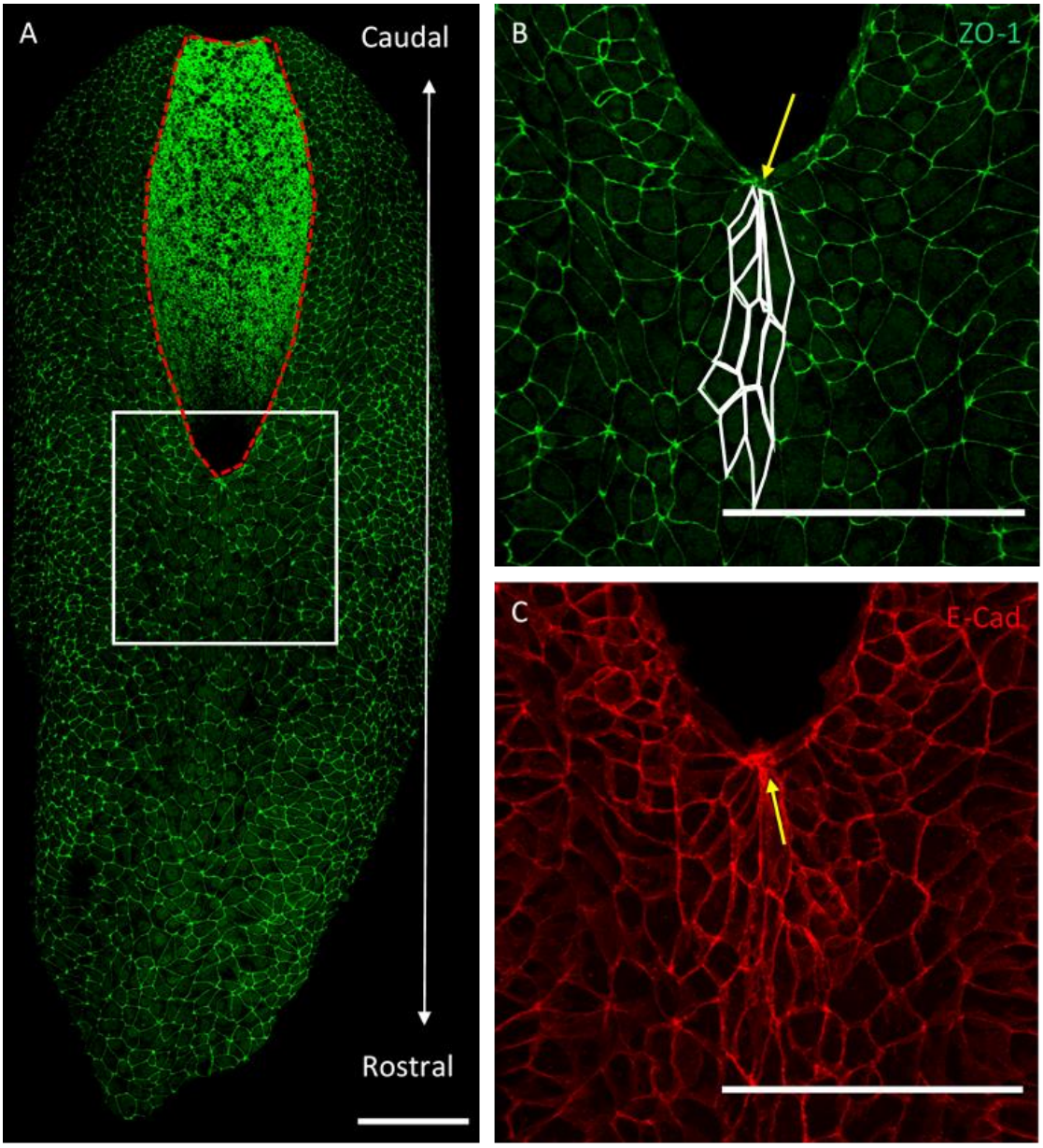

Figure 3.1- Example confocal image of an E9.5 PNP from the dorsal view.

A) A representative E9.5 open PNP (red dashed outline). ZO-1 immunofluorescence was used to visualise clear apical borders of SE and NE cells. B) Inset of white box in (A). White outline demonstrates midline RC elongation of cells. Yellow arrow = ZP. C) E-Cadherin immunofluorescence was used to distinguish SE and NE cells, which was useful at the SE-NE border along the neural folds. Yellow arrow = ZP. Scale bars = 100 µm.

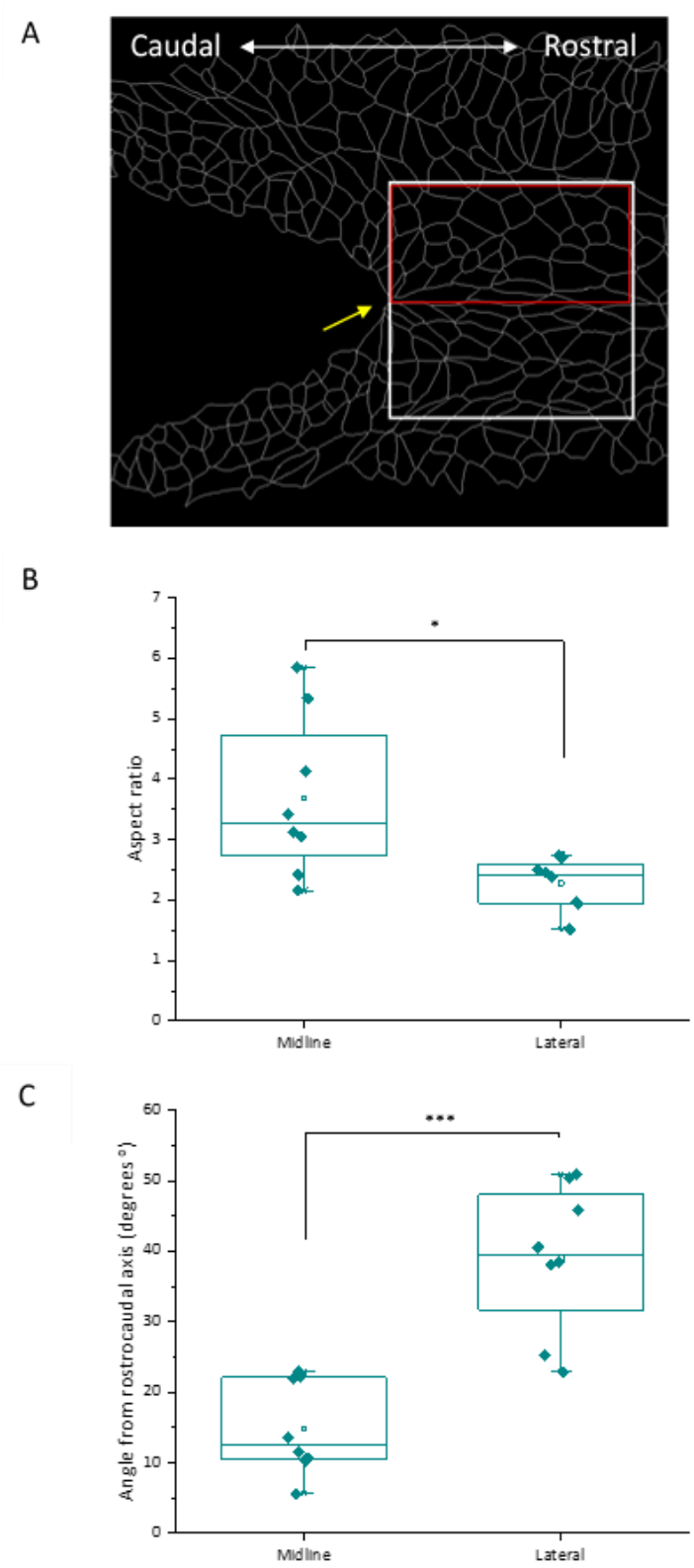

Figure 3.2- SE cell aspect ratio and orientation quantification.

SE cells are significantly oriented towards and elongated along the RC axis. A) A region of set area was used for all cell shape analysis (white box). A smaller region was used for heat map analyses, as no differences are expected between the left and right side of the midline (red box). The ZP is indicated by a yellow arrow. B) The aspect ratio of midline cells is significantly greater than lateral cells (t-test, $p < 0.05$). C) Midline cells are significantly more oriented along the RC axis compared to lateral cells (t-test, $p < 0.0001$).

A more detailed spatial analysis was obtained by generating heatmaps. These included all cells from all samples – each cell was plotted on a 3D map, with the centroid coordinates (X,Y) plotted on the X and Y axes and the analysed parameter on the Z axis (visualised using a colour gradient (Figure 3.3)). Finally, the assumption was made that there would be no left/right differences, so the midline was set as X=0 and any negative X values were made positive, essentially reflecting both left and right onto one side of the midline. This was to ease visualisation and to maximise the number of data points. The heat maps obtained revealed a striking ML gradient of elongation which was significantly different from 0, meaning that midline cells were more elongated than lateral cells (Figure 3.3A, B, ANOVA, $p < 3.0 \times 10^{-13}$). There was no significant RC gradient of elongation (Figure 3.3C, ANOVA, $p > 0.05$). An orientation gradient was also observed, with lateral cells becoming significantly less oriented towards the RC axis compared to midline cells (Figure 3.3D, E, ANOVA, $p < 3.0 \times 10^{-26}$). Interestingly, there was a significant negative orientation gradient moving rostrally from the ZP, suggesting that the orientation of cells towards the midline persists along the RC axis (Figure 3.3F, ANOVA, $p < 8 \times 10^{-10}$).

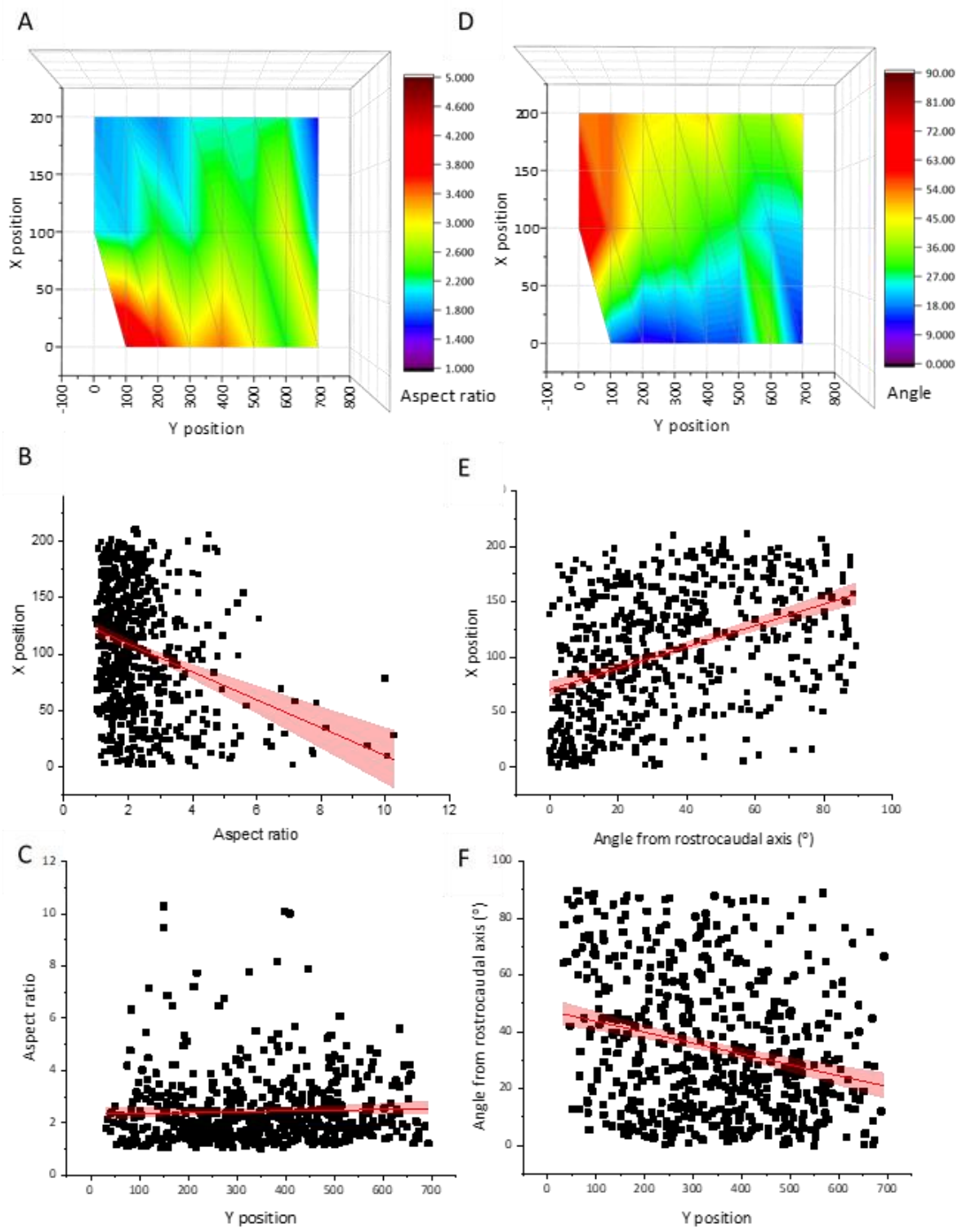

Figure 3.3 – Spatial heat maps of SE cell shape.

A,D) Heat maps showing aspect ratio and orientation of cells according to their position relative to the ZP (0,0). The X and Y axes represent the ML and RC axes respectively. B) Cells become significantly less elongated from the midline to lateral (ANOVA, $p < 3.0 \times 10^{-13}$). C) There is no significant RC aspect ratio gradient (ANOVA, $p > 0.05$). E) Cells become significantly less oriented towards the RC axis from midline to lateral (ANOVA, $p < 3.0 \times 10^{-26}$). F) Cells become significantly more oriented towards the RC axis from caudal to rostral (ANOVA, $p < 8.0 \times 10^{-10}$). Red shading = 95% confidence interval.

Finally, the shape of SE cells along the neural folds, which form new junctions at the midline as closure progresses, was analysed. This analysis was based on the observation that cells along the neural folds frequently displayed an elongated shape, with the long border running along the open PNP, and secondly based on several closure models where cells along a leading edge 'match up' with each other. Cells were analysed by pairing cells opposite each other (i.e. on either side of the PNP) sequentially from rostral to caudal, with cells directly rostral to the ZP denoted 'pair 1' (Figure 3.4A). As expected, the cells directly rostral to the ZP, pair 1, showed significantly shorter PNP borders compared to all pairs along the neural folds (Figure 3.4B, ANOVA, $p < 2 \times 10^{-6}$). The 'cell matching' hypothesis was tested by analysing the difference in length of cells within each pair– surprisingly, pair 2 showed the greatest difference in size as well as the greatest variability in length differences (Figure 3.4C, ANOVA, $p < 0.02$, post-hoc Tukey, $p < 0.03$).

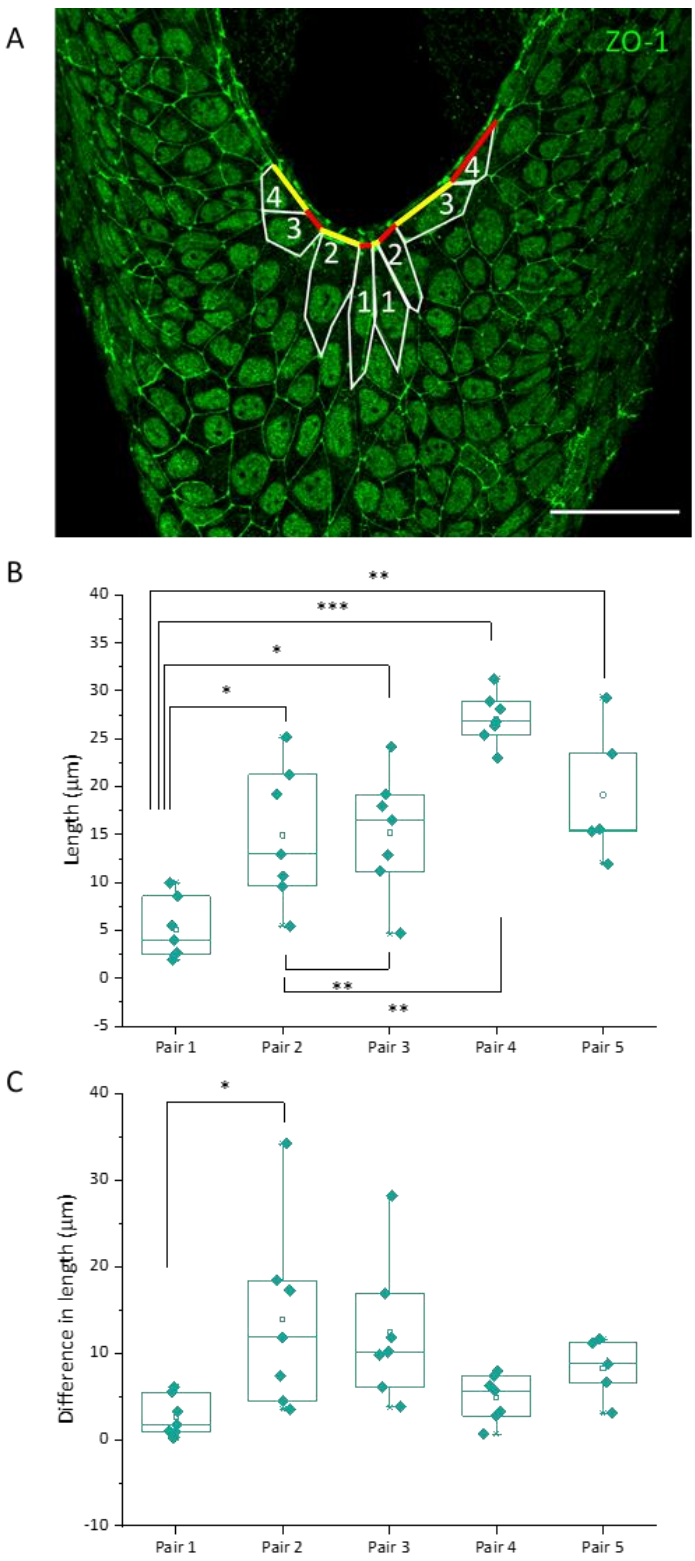

Figure 3.4 – SE cell shape analysis along the neural folds.

SE borders adjacent to the open PNP are longer along the neural folds than directly rostral to the ZP. A) Representative wild type spinal NT immunostained for ZO-1. Example cells chosen for analysis (i.e. with borders along the open PNP) are highlighted, and the numbers indicate pairs of cells. The lengths of borders outlined in red and yellow were measured. B) The cells bordering the PNP directly rostral to the ZP have significantly shorter neural fold borders than any cells lateral to the PNP (ANOVA, $p < 2 \times 10^{-6}$). C) The second pair of cells are significantly more different to each other in length compared to the first pair of cells (ANOVA, $p < 0.02$, post-hoc Tukey, $p < 0.03$). Scale bar = 50 µm.

3.2.2 - YAP nuclear translocation varies along the mediolateral axis

SE shape suggests that cells at the midline are under high RC tension. YAP is known to translocate to the nucleus when cells are stretched (Dupont et al., 2011), and its expression was therefore analysed by immunostaining (Figure 3.5A). YAP nuclear fluorescence intensity was compared to DAPI intensity (YAP/DAPI), to correct for any spatial differences in YAP fluorescence due to tissue curvature, and was normalised to give a maximum YAP/DAPI value of 1, to allow for differences in overall staining intensity between samples. Interestingly, a clear ML gradient was observed, with higher nuclear YAP/DAPI intensity along the midline compared to laterally (Figure 3.5B, slope significantly different from 0, ANOVA, $p < 3 \times 10^{-78}$).

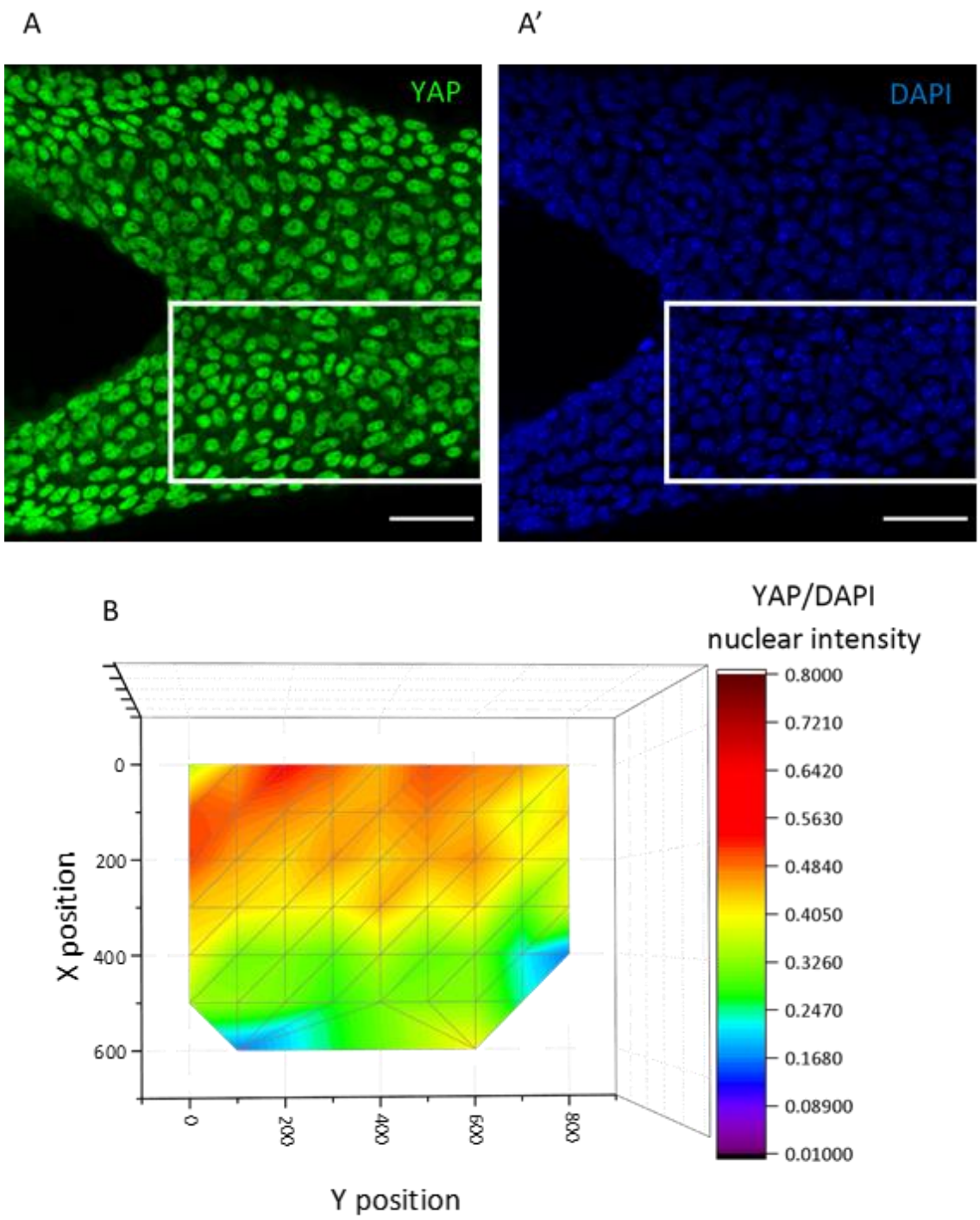

Figure 3.5 – Spatial analysis of YAP nuclear translocation.

YAP nuclear translocation shows a clear ML gradient in the wild type SE rostral to the PNP. A) Representative E9.5 spinal NT immunostained for YAP (A) and DAPI (A'). White boxes correspond to heat map in (B). B) Heat map showing YAP/DAPI fluorescence of individual cell nuclei in the region rostral to the ZP (0,0). X and Y axes represent ML and RC axes respectively. There is a significant ML gradient of nuclear YAP intensity (ANOVA, $p < 3 \times 10^{-78}$), with midline cells showing higher levels of translocated YAP compared to DAPI. Scale bars = 50 µm.

3.2.3 - Single cell laser ablation as a tool to analyse SE biomechanics

Biomechanical properties of the mouse SE have thus far only been predicted from cell shape. Therefore, a technique to ablate single SE cell borders in live mouse embryos was developed, in order to test the hypothesis that high RC tension leads to SE cell elongation.

Using a multi-photon LSM800 confocal laser, live E9.0–10.0 embryos were ablated in the recently closed SE, in the region rostral to the open PNP. Entire embryos were briefly stained in Cell Mask (Life Technologies) to visualise cell borders (Figure 3.6A). Ablations were of approximately equal length and width and were oriented in the RC or ML direction (Figure 3.6A). All subsequent images of ablations are shown in this orientation. Four distinct regions were ablated: along the neural folds where the actomyosin-cable is located (see Chapter 1.5.3.2), in the region of the ZP directly rostral to the open PNP (up to six cells rostral to the ZP), over the pre-somitic mesoderm (PSM), and over developed somites (somite region, SR) (Figure 3.6B, Figure 3.7 for examples from each region). After ablation, staining with propidium iodide, which can only enter cells when the cell membrane is damaged, showed that this technique successfully disrupted cell borders (Figure 3.6C). Ablations were stable over the imaging period (18 seconds) in most cases (Figure 3.6D). However, ablations which recovered and did not recoil were still included in the analysis to eliminate bias, as it could not be determined if the border did not recoil or was bleached. Immediate recoil was measured using two reference points and measuring the distance between the points before and after ablation (see Chapter 2.8.5 for method).

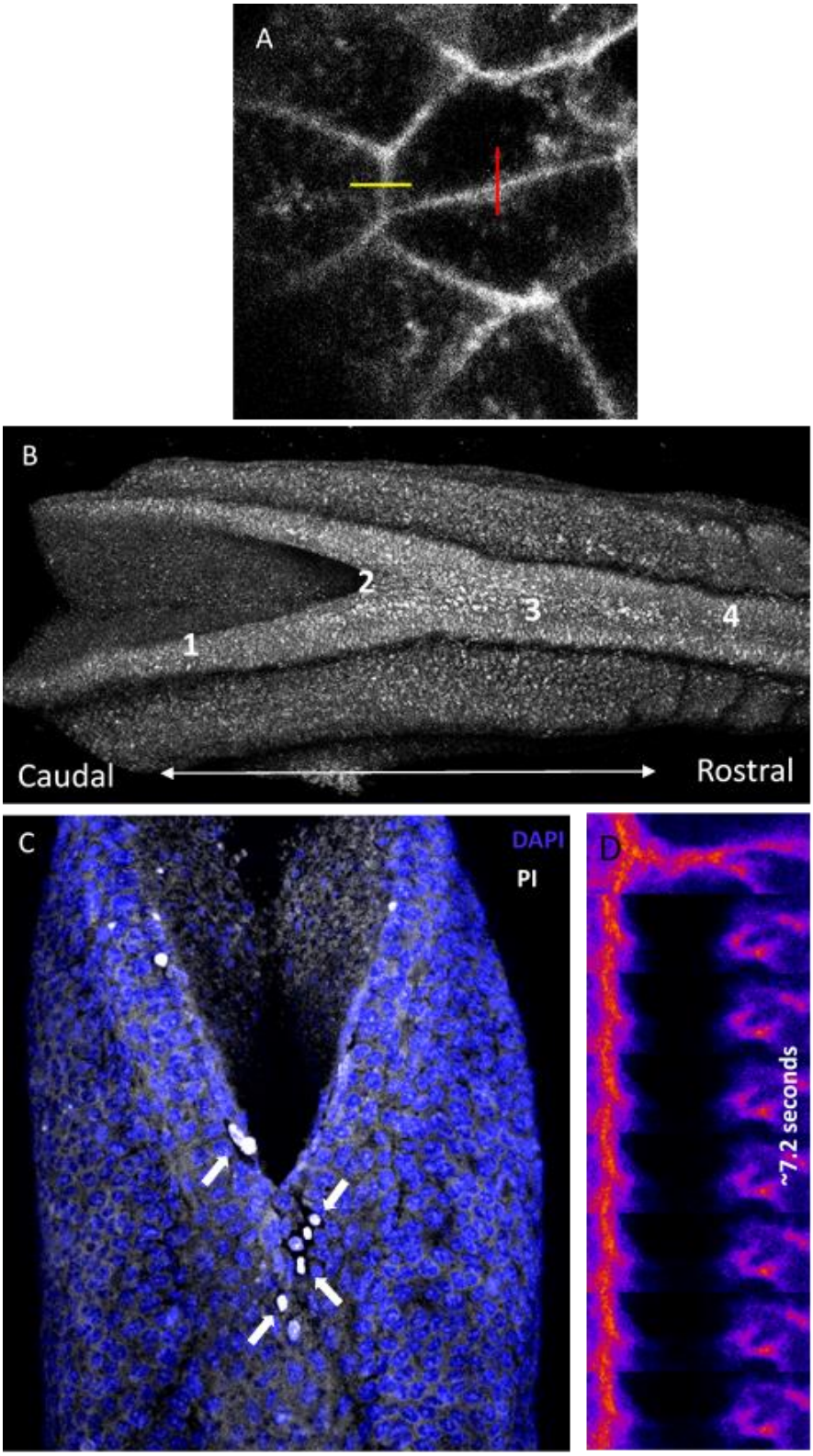

Figure 3.6 – Analysis of SE cell recoil using laser ablation.

A) E9.5 embryos were stained briefly with Cell Mask to visualise cell borders. Ablations were at 90°, in the RC (yellow) or ML (red) direction. B) Ablations were carried out in four regions: 1 – cable; 2 – ZP; 3 – PSM; 4 – SR. C) Propidium iodide staining after 3 SE and 1 cable ablation confirms that single border laser ablation destroys the cell border, allowing propidium iodide to pass through the cell membrane. D) Ablated border before (panel 1) and after ablation over a period of 7.2 s.

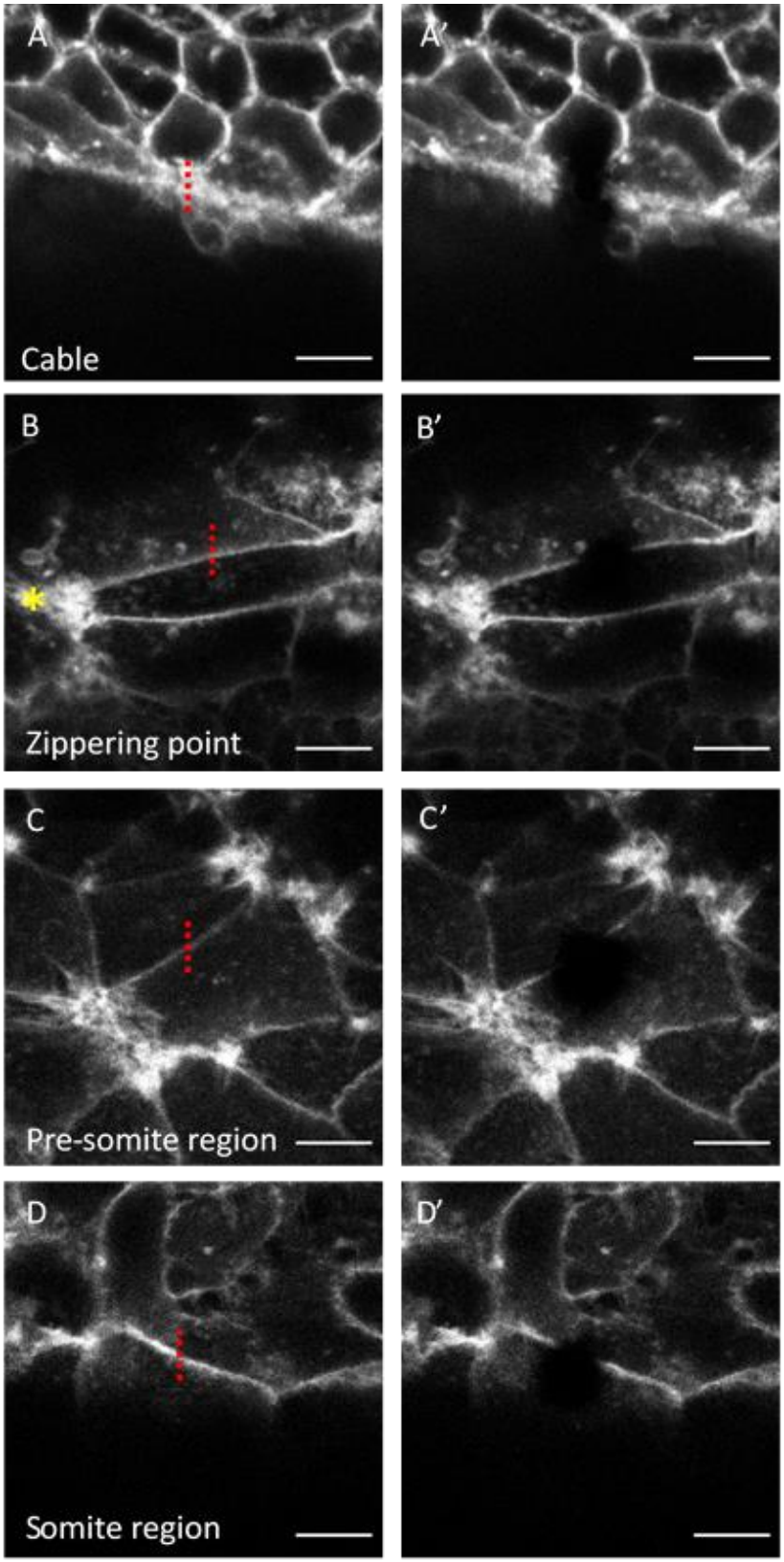

Figure 3.7 – Example laser ablations from each region showing SE recoil.

A) Cable ablation before (A) and after (A') ablation. B) Ablation at the ZP (yellow asterix) before (B) and after (B') ablation. C) Ablation over the PSM before (C) and after (C') ablation. D) Ablation in the region where somites have formed, before (D) and after (D') ablation. Red dashed lines indicate site of the ablation. Scale bars = 10 µm.

Tissue movement of the whole region imaged after a single cell border ablation could be analysed using particle image velocimetry (PIV, see Chapter 2.8.5 for method). This is a useful method of analysing recoil as it is non-subjective, unlike manual recoil measurements. PIV output consisted of individual vectors with magnitude and direction, corresponding to each region of the image analysed (Figure 3.8A, B). These vectors could also be plotted on compass plots, appearing to show that the angle of greatest recoil was at or close to 90° from the direction of ablation (Figure 3.8C).

The main weakness of PIV analysis is that it is hard to compare recoil between samples due to the large amount of data generated. A smaller region including the ablated border could reduce unnecessary data (Figure 3.8D), however noise was still picked up due to the sensitivity of the method. Furthermore, the variability in the degree of noise between images meant that pre-processing had to vary for PIV to successfully detect borders, and therefore quantitative comparisons were not possible. Manual measurement of immediate recoil as described in Chapter 2.8.4 was therefore used to analyse SE recoil in wild type embryos.

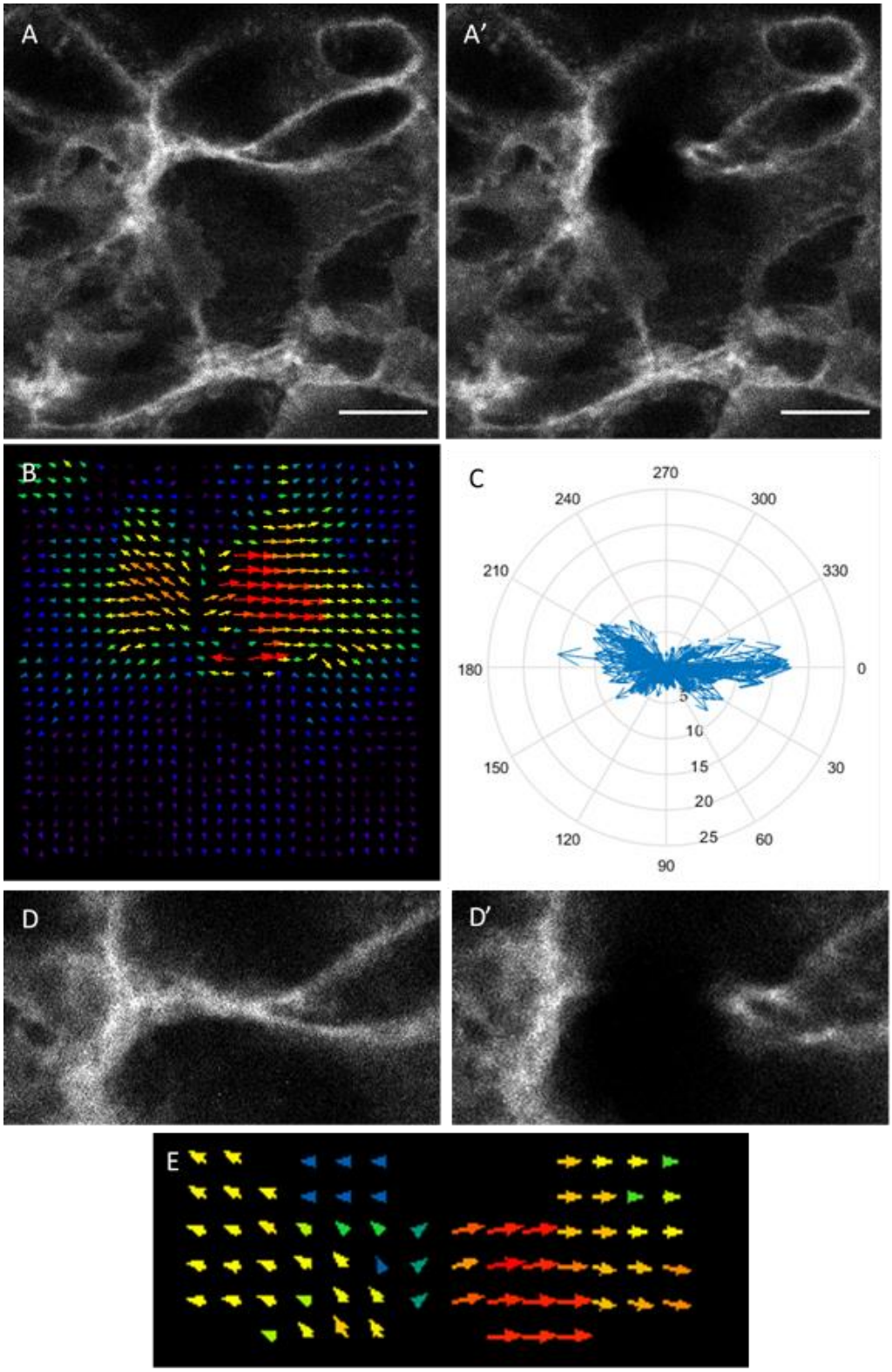

Figure 3.8 – PIV and compass plot recoil analysis.

PIV analysis and compass plots can be used to visualise tissue recoil after ablation. A) Example image before (A) and after (A') ablation used for analysis. B) PIV plot showing tissue movement after ablation in (A). C) Compass plot generated from PIV vector values in (B). Angle in degrees represents direction of movement. Length of arrows represent magnitude of tissue movement. D) Cropped regions of (A) used for focused PIV analysis of the ablation site. E) PIV plot showing tissue movement after ablation in (D). Scale bars = 10 µm.

3.2.4 - Single cell laser ablation reveals regional differences in SE recoil

To perform a comprehensive analysis of SE biomechanics during spinal NTC, ablations were carried out over a large range of somite stages. First, the relationship between recoil and somite number was analysed, as the embryos analysed ranged from early 9.0 to late E9.5. There was no significant correlation between somite number and recoil when all SE regions and ablations in both directions were included (Figure 3.9A, ANOVA, $p > 0.05$). Individual samples were then separated into four somite groups encompassing early E9.0 – late E9.5 (11-15, 16-20, 21-25 and 26+). No significant difference was found between somite groups, either in the RC or ML direction, or when both directions were included (Figure 3.9B-D). All somite stages were therefore included in subsequent analyses.

Initially cable recoil was excluded from analyses, so that regions of SE rostral to the PNP could be compared. RC recoil was found to be significantly higher than ML recoil when all three SE regions were included (Figure 3.10A, t-test, $p < 0.004$). Analysis of each region individually revealed that RC and ML recoil was comparable, however all regions showed a trend towards higher RC recoil compared to ML (Figure 3.10B - D); in the SR, this difference almost reached significance (Figure 3.10C, t-test, $p = 0.051$). RC and ML recoil were therefore analysed separately for the remainder of the analysis.

Between regions of SE (excluding the cable), the ZP showed significantly lower RC recoil than the PSM (ANOVA, $p < 0.004$); the SR also showed greater recoil than the ZP, although this did not reach significance (Figure 3.11A). There was no difference in ML recoil between SE regions (Figure 3.11B). When the cable was included in analyses, it was found to show significantly higher RC recoil than any of the SE regions (Figure 3.11C, ANOVA, $p < 7 \times 10^{-8}$). Because the cable runs along the neural folds (i.e. in the RC direction), only RC recoil could be compared to the SE ablations.

To test the hypothesis that elongated cells along the midline are under RC tension, recoil between the midline and lateral cells within the ZP region were compared. Midline RC recoil was significantly higher than lateral recoil (Figure 3.12A, t-test, $p < 0.04$). This led to the question of whether cell shape can predict recoil. Therefore, the relationship between recoil and orientation or length of ablated cells was analysed. The distribution of border angles across the sample population confirmed that the majority of ablated cells were oriented close to 90° from the angle of the ablation (0° and 90° for RC and ML ablations respectively, Figure 3.12B). Surprisingly, there was no significant correlation between border length or angle and recoil, in either the RC or ML ablation groups (Figure 3.12C-F, ANOVA, $p > 0.05$). This relationship was also analysed for RC

recoil in the individual regions, as this could have been a confounding factor in this analysis, however again there was no correlation between recoil and length or angle (ANOVA, $p > 0.05$, data not shown).

To further validate these findings, a mixed model analysis was carried out on SE ablations (excluding the cable), including litter number as a factor which could introduce variability. ZP ablations were not defined as midline or lateral, as ablations in the PSM and SR were not identified as either. Factors which were non-significant in causing variation were sequentially removed from the analysis until a significant factor was identified. With variability of litter included, RC recoil at the PSM compared to the ZP did not quite reach significance ($p = 0.051$), suggesting that litter number introduced variability into the data.

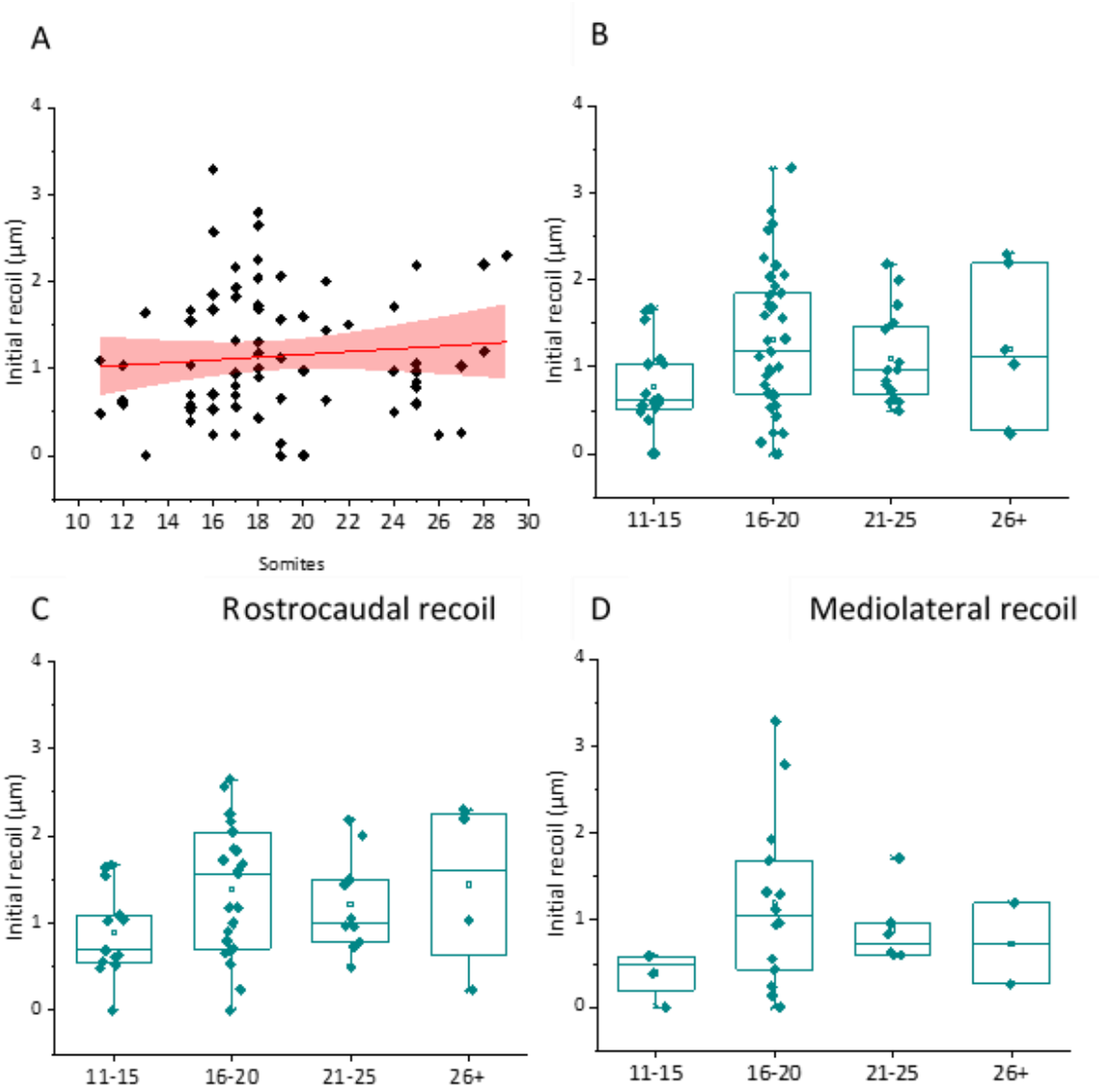

Figure 3.9 – SE recoil analysis by somite stage.

SE recoil after laser ablation does not vary by somite stage. A) There is no significant correlation between somite stage and initial recoil when all SE regions and both directions are included (ANOVA, $p > 0.05$). B) There is no significant difference in recoil between somite groups when ablations in both directions are included (ANOVA, $p > 0.05$). C) There is no significant difference in RC recoil between somite groups (ANOVA, $p > 0.05$). D) There is no significant difference in ML recoil between somite groups (ANOVA, $p > 0.05$).

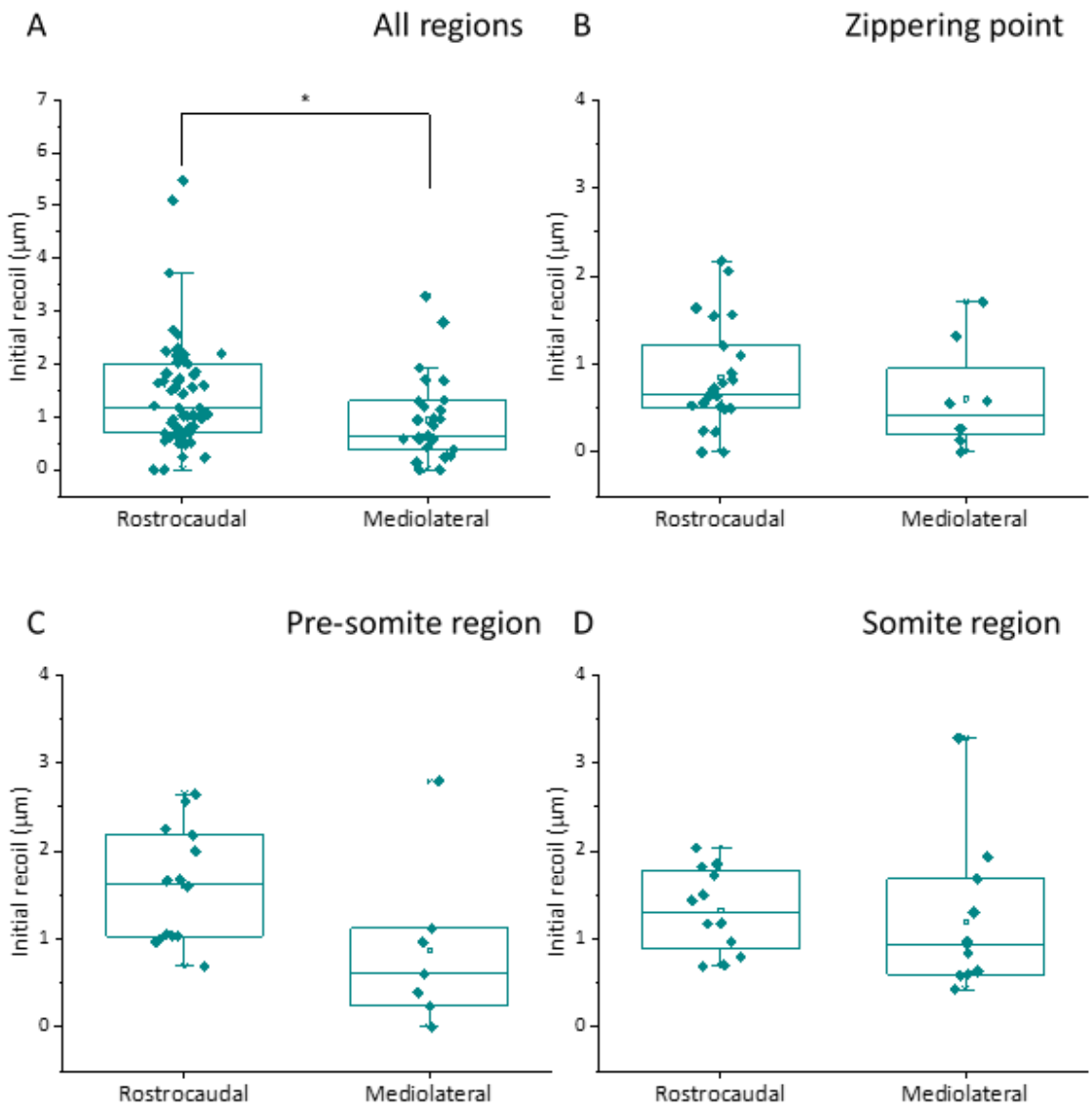

Figure 3.10 – SE recoil analysis by direction.

RC recoil is significantly higher than ML recoil. A) When all regions of the SE are included, RC recoil is significantly higher than ML recoil (t-test, $p < 0.03$). B) There is no significant difference between RC and ML recoil at the zippering point (t-test, $p > 0.05$). C) There is no significant difference between RC and ML recoil over the PSM (t-test, $p > 0.05$). D) There is no significant difference between RC and ML recoil over the SR (t-test, $p > 0.05$).

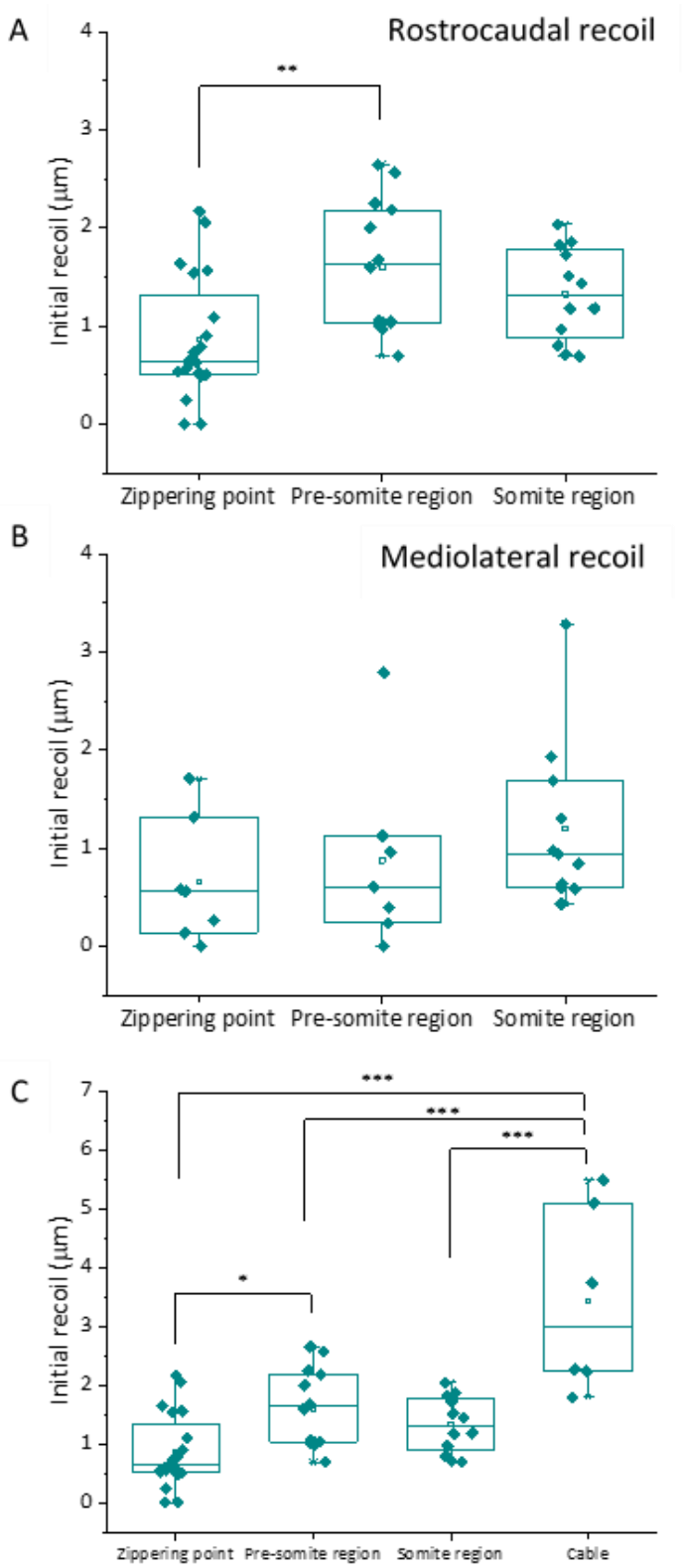

Figure 3.11 – SE recoil analysis by region.

There is a significant variation in RC SE recoil after ablation between regions, but not in ML recoil. A) RC recoil of SE cells is significantly higher over the PSM than at the zippering point (ANOVA, $p < 0.004$, post-hoc Tukey, $p < 0.003$). B) There is no significant difference in ML recoil between regions. C) The cable showed significantly higher recoil than any SE regions (ANOVA, $p < 7 \times 10^{-8}$, post-hoc Tukey, $p < 2 \times 10^{-8}$ (cable v zippering point), $p < 7 \times 10^{-5}$ (cable v PSM), $p < 8 \times 10^{-6}$ (cable v SR)).

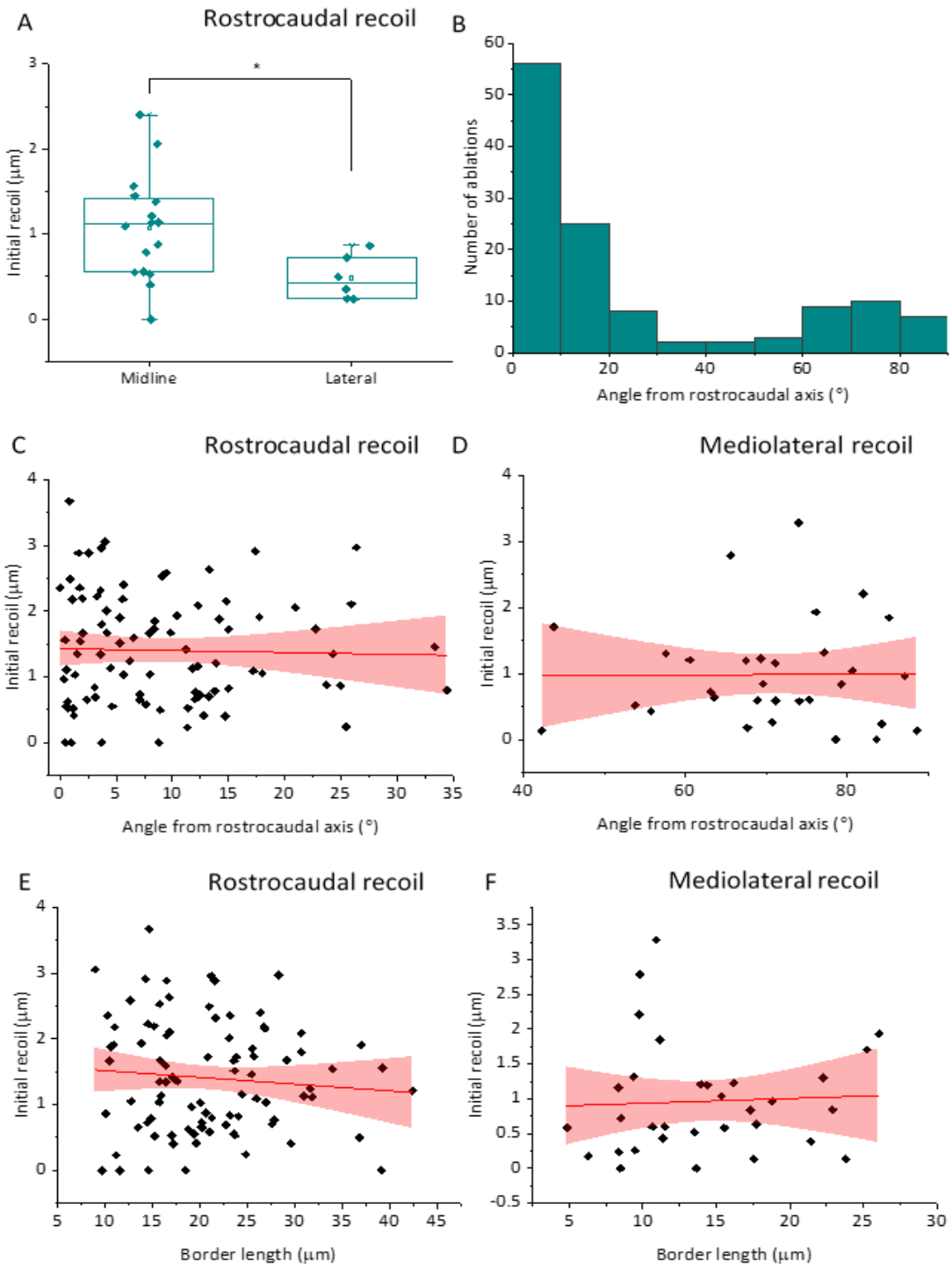

Figure 3.12 – SE recoil analysis by cell shape.

RC recoil is higher along the midline compared to laterally at the zippering point, however there is no correlation between cell shape and recoil, suggesting the SE is not under high RC tension. A) At the zippering point, RC recoil is significantly higher at the midline compared to laterally (t-test, $p < 0.04$). B) A histogram showing the number of ablated borders at given angles, showing that the majority were close to 90° from the direction of the ablation. All ML oriented ablations were on borders between 0-40° from the RC axis, while all RC oriented ablations were on borders over 40° from the RC axis. C, D) There is no significant correlation between cell orientation and RC (C) or ML (D) recoil (ANOVA, $p > 0.05$). E, F) There is no significant correlation between cell border length and RC (E) or ML (F) recoil (ANOVA, $p > 0.05$).

3.3 - Discussion

One of the most common inferences on the relationship between shape and force is that elongated cells are under tension in the direction of the elongation. Artificial mechanical stimulation of endothelial and fibroblast cells in culture can cause elongation in the direction of stretching (Buck, 1980, Dartsch and Betz, 1989). *In vivo*, the shape and orientation of cells can also reflect external forces, such as endothelial cells of blood vessels responding to blood flow (Langille and Adamson, 1980).

However, not all elongated cells are under high tension. In the *Drosophila* notum, epithelial cells are significantly elongated, but show nominal recoil compared to more lateral cells due to cell crowding (Marinari et al., 2012). In this model, the mitotic spindle orients along the long axis of elongated cells, but only in lateral tissues which are under higher tension, and the spindles in the elongated midline cells fail to orient (Lam et al., 2020). Studies such as these indicate that cell shape is not sufficient to predict force-dependent behaviours.

In this chapter, SE cells were shown to have a clear elongated phenotype along the midline of the closing PNP, suggesting that these cells are being stretched (Figures 3.2 - 3.3). This hypothesis was further supported by higher nuclear translocation of YAP along the midline compared to laterally (Figure 3.5), which is a known indicator of cells under stress (Dupont et al., 2011). Finally, at the ZP, midline cells show significantly higher recoil than lateral cells (Figure 3.12), correlating with the region of elongation. Surprisingly however, laser ablation of cells in different regions showed that cells at the ZP recoil significantly less than cells further rostrally (Figure 3.11). There was also no correlation between cell shape or orientation and recoil in any of the regions analysed (Figure 3.12).

There are several possible explanations for why the observed elongated cells do not show high RC recoil. First, compression of the midline by lateral tissues may cause this shape. Such a mechanism has been identified in chick embryos, where the posterior PSM actively compresses the axial tissues to promote tissue elongation (Xiong et al., 2020). However, SE compression at the ZP but not further rostrally does not fit with this model, and compression would be expected to give lower ML recoil at the ZP, which was not observed (Figure 3.11). Secondly, stretched cells at the ZP may be stabilised by attachment to the ECM. Fibronectin in the caudal mouse embryo is known to mature during neurulation and to show regional differences in expression, with an organised network of mediolaterally oriented fibrils in the rostral regions and a dense focal point of fibronectin and integrin expression directly at the ZP (Mole et al., 2020). Again, this is unlikely to explain the differences in regional recoil. Only cells which directly contact the focal point at

the ZP would be expected to be stabilised, and very few ablated cells in the ZP region would have been in direct contact with this point. In addition, the dense and organised network of fibronectin further rostrally would be expected to cause lower rostral recoil compared to the ZP, the opposite to what was observed. Finally, cell crowding at the ZP could prevent substantial recoil after ablation. However, it is difficult to compare the degree of cell crowding between regions, and cells at the ZP in fact have fewer rows of cells around them compared to rostral regions due to the open space of the PNP, making this explanation unlikely.

The most likely explanation is therefore that cell shape is a product of intrinsic cell behaviours. Mesenchymal cells in culture show an elongated shape as they migrate along a substrate by generating actin-polymerisation mediated protrusions at the leading edge and 'pulling' the remainder of the cell forwards (Vicente-Manzanares et al., 2005). Traditionally, this comparison of epithelial cell shape during morphogenesis and mesenchymal cell shape during cell migration would have been disregarded, due to the classical misnomer that epithelial and mesenchymal cells have entirely separate molecular signatures, morphologies and behaviour. It is now more widely accepted that cells can show characteristics of both, and that an epithelial-mesenchymal spectrum is more appropriate (Nieto, 2013, Campbell and Casanova, 2016).

In agreement with this model, SE cells have several properties which are not traditional 'hallmarks' of an epithelial signature. Firstly, they display clear filopodia and lamellipodia, which are classically defined as mesenchymal characteristics- these protrusions are one of the critical properties of the SE leading edge cells and are required for successful NTC (Rolo et al., 2016b) (see Chapter 1.1.4). Secondly, live imaging of the SE around the closing HNP and PNP has shown the SE to be highly dynamic (Maniou et al., 2021). On the other hand, the SE expresses high levels of E-cadherin and other adherens and tight junction components, which are implicated in ensuring epithelial cell integrity and preventing individual cell motility (Campbell and Casanova, 2016). Nonetheless, some studies have suggested that E-cadherin might be required for migration in certain contexts. For example, knockdown of E-cadherin in border cells of the developing *Drosophila* egg chamber leads to a significant decrease in directional persistence of cell migration (Cai et al., 2014). It is unknown how tightly the cells in the SE are adhered to each other. It is likely that, in a structure which requires formation of new junctions at the ZP, the adherence of cells to each other is transient.

Bringing these findings together, a model where cell elongation is a result of active cell migration seems most likely. Cell crawling has been implicated in several developmental and adult gap closure events, such as dorsal closure in *Drosophila* and wound healing (Begnaud et al., 2016).

Computational modelling of HNP closure based on live imaging data suggests that the actomyosin cable acting via a 'purse-string'-like mechanism cannot successfully generate the forces required for closure. However, when medial crawling of the lateral SE is added to the model, closure completes (Maniou et al., 2021). In the PNP, RC elongation suggests that cell crawling is in either the rostral or caudal direction. It is unlikely that caudal movement is occurring for two reasons: by definition, cell crawling requires a substrate on which to create traction, and the PNP is a fluid filled space; it is improbable that cells would need to migrate back towards the PNP, as these cells have already completed closure and no longer need to be associated with the ZP. Rostral crawling therefore seems more plausible. This is supported by the elongated cell shape along the neural folds of the open PNP prior to their entry to the ZP (Figure 3.4). Elongation directly rostral to the ZP may be a remnant of these neural fold cells having made new contacts, before they become fully incorporated in the closed region and recover their shape. Once a cell has completed closure, migration away from the ZP could facilitate formation of new cell-cell junctions along the midline. Live imaging of cell reorganisation at the ZP will be important in answering these questions, along with an understanding of cell shape and biomechanics in models where NTC fails.

Chapter 4 – Direct perturbation of surface ectoderm biomechanics and its effects on neural tube closure

4.1 -Introduction

4.1.1 – The importance and challenges of developmental biomechanics

Much of our understanding of cell and tissue biomechanics comes from genetic and experimental disruption of mechanical properties. It is widely accepted that an abnormal biomechanical environment can have a detrimental effect on development. For example, developmental dysplasia of the hip (DDH) is a musculoskeletal disorder highly associated with biomechanical abnormalities such as breech position and oligohydramnios (Chan et al., 1997). This is believed to be due to restricted kicking and a resulting reduction in strain on the developing skeleton (Verbruggen et al., 2018). Mechanical stimuli are also important at much earlier stages of gestation. In one study, Chan et al. showed that during blastocyst development, there is an increase in luminal pressure over time. By disrupting luminal pressure increases by blocking fluid influx, they showed that the increases in luminal pressure are essential for increases in tissue stiffness, cell cortical tension and tight junction maturation, which is in turn required for accommodation of embryo growth (Chan et al., 2019). While studies such as these clearly demonstrate the importance of the mechanical environment on the developing embryo and foetus, they represent examples at the extreme early and late stages of embryogenesis. Early stage studies in mice benefit from the small number of cells and the ability to study blastocysts *in vitro*, allowing a more thorough analysis of different cell types. Late stage studies in humans largely focus on global phenotypes, thus disregarding cellular and molecular changes. Understanding the stages in between remains a challenge due to the large number of cell types and difficulties in accessing and manipulating embryos.

Culture of mammalian embryos was a major aim for developmental biologists throughout the 20th century, as this technique would allow direct administration of drugs and control of the environment. *Ex utero* culture of rat embryos was first developed in the mid-1960s by Denis New, who was by the late 1970s able to successfully maintain culture for the equivalent of 4-5 days *in vivo* (New, 1966, New, 1978). Mouse embryos initially proved more difficult, however by 1979, ~48 hour cultures were successfully achieved (Sadler, 1979).

This technique is now widely used to further understand mechanisms of neurulation. For example, as discussed in Chapter 1.5.3.1, culture of mouse embryos in multiple cytoskeletal

inhibitors reveals an important role of maintaining actomyosin turnover during NTC (Escuin et al., 2015). However, studies which analyse biomechanical properties after treatment in culture at the tissue and cellular level are lacking. In Chapter 3, a comprehensive descriptive analysis of SE biomechanics was given. Whether the SE plays a direct biomechanical role in spinal NTC is unknown; in this chapter, embryos were cultured in the presence of drugs which are predicted to alter SE biomechanics, and properties including cell shape and recoil were subsequently analysed, to begin to answer this question.

4.1.2 – Molecular requirements for epithelial morphogenesis

Unsurprisingly, a major player in controlling epithelial morphogenesis is the actomyosin network. For cells to change shape, contractile actomyosin networks generate forces, which are detected and transmitted to cells borders, thus triggering junctional remodelling (Lecuit et al., 2011). Asymmetric generation of forces by the actomyosin network have been implicated in multiple developmental contexts. As described in Chapter 3.3, a classic example is the T1-exchange during *Drosophila* germ band extension, where planar-polarised Myosin-II leads to contraction and shrinkage of junctions perpendicular to the axis of extension (Bertet et al., 2004). In the closing NT, apical accumulation of actomyosin is important (but not required in all contexts) for apical constriction during neural fold bending (Chapter 1.1.3). Thus, disrupting the actomyosin network is a common strategy for probing its role in morphogenesis.

Blebbistatin is a popular pharmacological inhibitor of myosin light chain kinase (MLCK), resulting in inhibition of non-muscle myosin-II and reduced actin contractility. Due to the importance of F-actin motor proteins in formation of contractile structures, the effect of blebbistatin on cell contractile behaviours and morphology has been widely studied in cell lines. For example, inhibition of myosin II activity reduces formation of stress fibres and lamellipodia, and decreases contractile activity in mouse hepatic stellate cells (Liu et al., 2010).

Interestingly, *Drosophila* non-muscle myosin-II is insensitive to blebbistatin (Heissler et al., 2015), and as the most commonly used *in vivo* model for laser ablation studies and other biomechanical assays, the effects of blebbistatin treatment on cellular behaviour *in vivo* are poorly characterised. In one study of wound healing in the hydrozoan *Clytia hemisphaerica*, actomyosin cable mediated contraction was abolished by blebbistatin treatment, concomitant with loss of characteristic changes in epithelial cell shape around the wound boundary (Kamran et al., 2017). However, whether the changes in cell morphology were due to the disrupted cable or abnormalities at the cellular level cannot be elucidated in this example. Unfortunately, due

to the difficulties in carrying out laser ablations in mouse embryos as discussed in Chapter 3, the effect of blebbistatin on mammalian epithelia is not yet known.

The ability of cells to adhere to each other, but also to reorganise their junctions, is fundamental to changes in cell shape and position. The molecular players involved in cell-cell adhesion must be strong enough to maintain cell contacts but mobile enough for junctional remodelling (Schneider and Kolligs, 2015). There are three main adhesive complexes, all of which have varied and distinct roles: tight junctions, which primarily act as a permeability barrier, desmosomes, which are found in tissues under particularly high stress and are thought to infer strain resistance, and adherens junctions (AJs), which initiate and control the maturation and maintenance of cell-cell contacts, and are important in communication between the ECM, cell membrane and actin cytoskeleton (Hartsock and Nelson, 2008, Capaldo et al., 2014, Schneider and Kolligs, 2015).

The interactions between AJs, the ECM and the actin cytoskeleton are vital for mechanical transmission and generation (Chapter 1.5.1). Cadherins, which are membrane associated glycoproteins, are the main components of AJs, conferring cell-cell contacts through calcium dependent homo- or hetero-philic interactions (Schneider and Kolligs, 2015). One of the first cadherins to be identified, Cadherin1 (Cdh1) or Epithelial (E)-cadherin, is one of the main AJ components, and is widely studied in the biomechanics field.

The role of E-cadherin mediated adhesion in mouse development begins as early as compaction at the 8 cell stage; homotypical E-cadherin interactions are redistributed from all membrane surfaces to only cell-cell borders, giving the early embryo its first signs of structure (Hyafil et al., 1981, Fleming et al., 2001). Although compaction does occur in *Cdh1*$^{-/-}$ mice due to residual maternal E-cadherin, these homozygous mutants are embryonic lethal, with embryos arresting before implantation as a result of failed trophectoderm formation (Larue et al., 1994).

Because of its early significance, it can be difficult to elucidate how E-cadherin contributes to multiple developmental processes including NTC, however pharmacological blockade of E-cadherin has provided important clues. During gastrulation, epiblast cells undergo EMT to form migratory mesoderm – this correlates with the cessation of E-cadherin expression. In explant culture of primitive streak epiblast, blockade of E-cadherin in the epiblast causes cells which would normally exhibit an epithelial phenotype to instead become migratory (Burdsal et al., 1993). Culture of embryonic brain cells similarly showed that E-cadherin is important in the formation of segregated clusters, and thus predicted to play a role in spatial patterning during brain development – this was supported by culture with an antibody that blocked E-cadherin,

which compromised function and altered the overall morphology of brain explants *in vitro* (Shimamura and Takeichi, 1992). *Ex utero* culture of rat embryos in the presence of oligodeoxynucleotides complementary to E-cadherin cDNA leads to high incidence of cranial NTDs, although interestingly, this study suggested that a reduction in yolk sac and not SE E-cadherin was the causative mechanism (Chen and Hales, 1995). Clearly, the roles of E-cadherin are multiple and widespread.

In relation to a possible role of E-cadherin during NTC, E-cadherin is expressed at high levels specifically in the SE during neurulation and subsequently in all layers of the epidermis (Jensen et al., 1997). Knockout of E-cadherin in the developing epidermis using a keratin-14 promoter to drive Cre expression leads to perinatal lethality one day after birth (Tunggal et al., 2005). This is due to failure of epidermal barrier formation and consequent dehydration, comparable to the phenotype seen in *Grhl3*$^{-/-}$ mice (Chapter 1.4.3). E-cadherin is also one of the major target genes of *Grhl2*, and is significantly dysregulated in both overexpression and knockout mutants (Nikolopoulou et al., 2019) – its function is implicated in the biomechanical deficits of these mutants during NTC, which is further discussed in Chapter 5. In the *Grhl2* mutant models of NTDs, E-cadherin is one of multiple targets of *Grhl2*, and K14-Cre is not expressed until after neurulation. Therefore, an ongoing question is the direct impact of disrupted E-cadherin function in the SE during neurulation.

This chapter uses pharmacological inhibition of E-cadherin and MLCK, by culture of embryos undergoing spinal NTC in E-cadherin blocking antibody and blebbistatin respectively, to analyse the role of these molecules in the SE during spinal neurulation. A second objective is to use these treatments, which are predicted to disrupt SE properties, to validate the methods used in Chapter 3 as biomechanical readouts, i.e. SE cell recoil after laser ablation, YAP nuclear translocation, and cell shape.

4.2 – Results

4.2.1 – Culturing mouse embryos in blebbistatin does not affect SE recoil

The ability to culture mouse embryos from E8.5 for up to 48 hours provides a powerful tool to study the mechanisms of spinal neurulation. Blebbistatin is a widely used inhibitor of myosin light chain kinase (MLCK) and reduces actin contractility in cells and animal models. Blebbistatin was therefore used to analyse the role of actin contractility in SE recoil after laser ablation, an important question to test the validity of our ablation method as a tool to measure cellular tension.

E9.5 embryos were cultured for 2 hours in 50 µM blebbistatin, a dose previously shown to disrupt actomyosin crosslinking without delaying PNP closure (Escuin et al., 2015). Culture of E9.5 mouse embryos with or without blebbistatin and subsequent laser ablation of the SE and the cable revealed no significant difference in recoil between groups (Figure 4.1, t-test, $p > 0.05$). However, there was a trend towards reduced recoil after blebbistatin treatment which almost reached significance ($p < 0.06$). Post-hoc power analysis reveals that a larger experiment with 40 samples showing the same mean would be statistically significant at the standard 0.80 level. In an independent experiment, embryos were cultured for 2 hours in the presence of 50 µM blebbistatin and immunostained for YAP, to ask whether the ML gradient of YAP nuclear translocation was still present. In both the vehicle and treatment groups, there was a negative gradient of nuclear YAP intensity with increasing distance from the midline, i.e. the amount of YAP in the nucleus compared to DAPI in the midline is significantly higher than laterally (Figure 4.2, ANOVA, $p < 2.2 \times 10^{-11}$ in vehicle, $p < 7.7 \times 10^{-44}$ in blebbistatin treated). Interestingly, the treatment group had a much higher level of significance than the vehicle (f-test, $p > 0.05$), suggesting a more pronounced ML gradient is present, however both groups show a lower level of significance than wild type groups in independent experiments (Chapter 3.2.2 and 5.2.2), suggesting culture conditions may have an effect on YAP nuclear translocation.

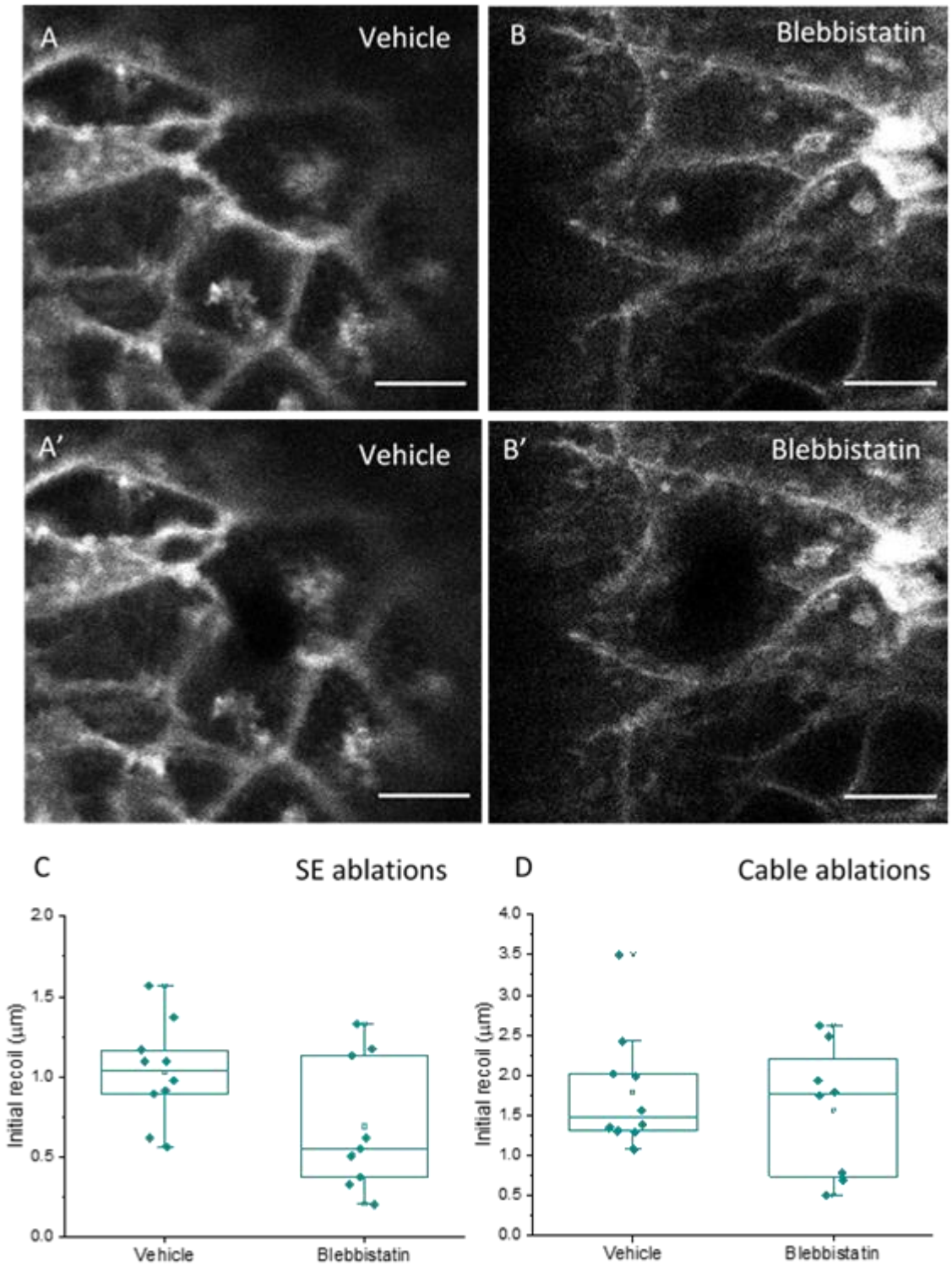

Figure 4.1 – Recoil analysis in embryos treated with blebbistatin.

E9.5 mouse embryos cultured for 2 hours in blebbistatin do not show a significant difference in SE or cable recoil after laser ablation. A, B) Representative images of SE cells in vehicle (A) and blebbistatin treated (B) embryos, before (A, B) and after (A', B') single border laser ablation. C, D) Blebbistatin treatment does not cause a significant change in SE or cable recoil after laser ablation (t-test, $p > 0.05$), however there is a trend towards reduced SE recoil after treatment. Scale bars = 10 µm.

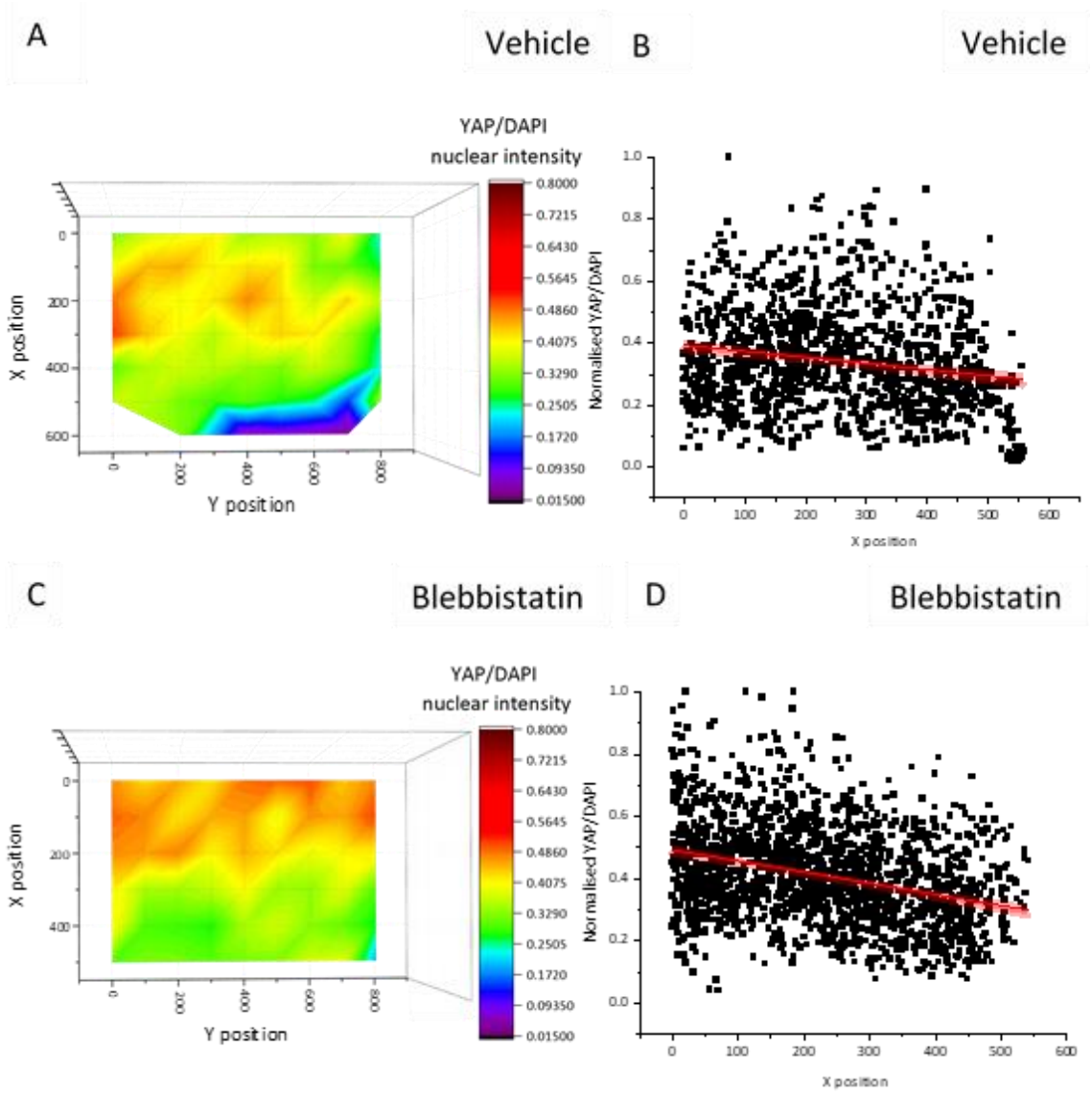

Figure 4.2 – Spatial analysis of YAP nuclear translocation in embryos treated with blebbistatin

Culture of E9.5 embryos in blebbistatin does not disrupt the ML gradient of YAP nuclear translocation. X and Y axes represent the ML and RC axes respectively. A,C) Heat maps showing YAP/DAPI nuclear intensity along the ML axis in vehicle treated (A) and blebbistatin (C) treated embryos, with the midline X position = 0. B, D) Scatter plot showing the YAP/DAPI nuclear intensity for individual nuclei for vehicle (B) and blebbistatin (D) treated embryos, with the midline X position = 0. Both slopes are significantly different from 0 (B = ANOVA, $p < 2.2 \times 10^{-11}$; D = ANOVA, $p < 7.7 \times 10^{-44}$). These slopes are significantly different from each other (f-test, $p < 0.05$).

4.2.2 – Microinjection of FastGreen is toxic to embryos

For a treatment in culture to have a direct effect on the embryo, the treatment must transport through the yolk sac and amnion. However, some molecules cannot penetrate the yolk sac, and must be injected directly into the amnion before culture. A requirement for this technique is to be able to visualise the treatment solution, so that the correct volume can be injected to fill the amnion. Two dyes have been used for this purpose previously in the lab – CellMask and FastGreen – however these have not previously been compared with regards to their toxicity and/or effects on PNP closure. E8.5 CD1 embryos were therefore cultured after injection with each dye for 24 hours, and the PNP length was compared to embryos injected with PBS or non-injected controls.

Neither dye significantly affected PNP closure at any of the analysed somite stages (Figure 4.3A, ANOVA, $p > 0.05$). The most affected groups were PBS injection only at 18-19 somites, and CellMask injection at 20-22 somites. In the former case, injection with PBS alone is practically very difficult due to an inability to see the solution, which meant that some embryos may have been injected with too much solution, potentially causing mechanical damage. Variability in the effect of CellMask at 20-22 somites was a potential downside to this treatment.

However, a clear effect on cranial closure was observed in embryos injected with FastGreen. 5/10 embryos showed severe cranial closure defects, which is significantly different to that expected by chance and was not observed in any other treatment group (Figure 4.3B, Chi Square, $p < 0.01$). It was therefore decided that CellMask would be used in all injections for culture.

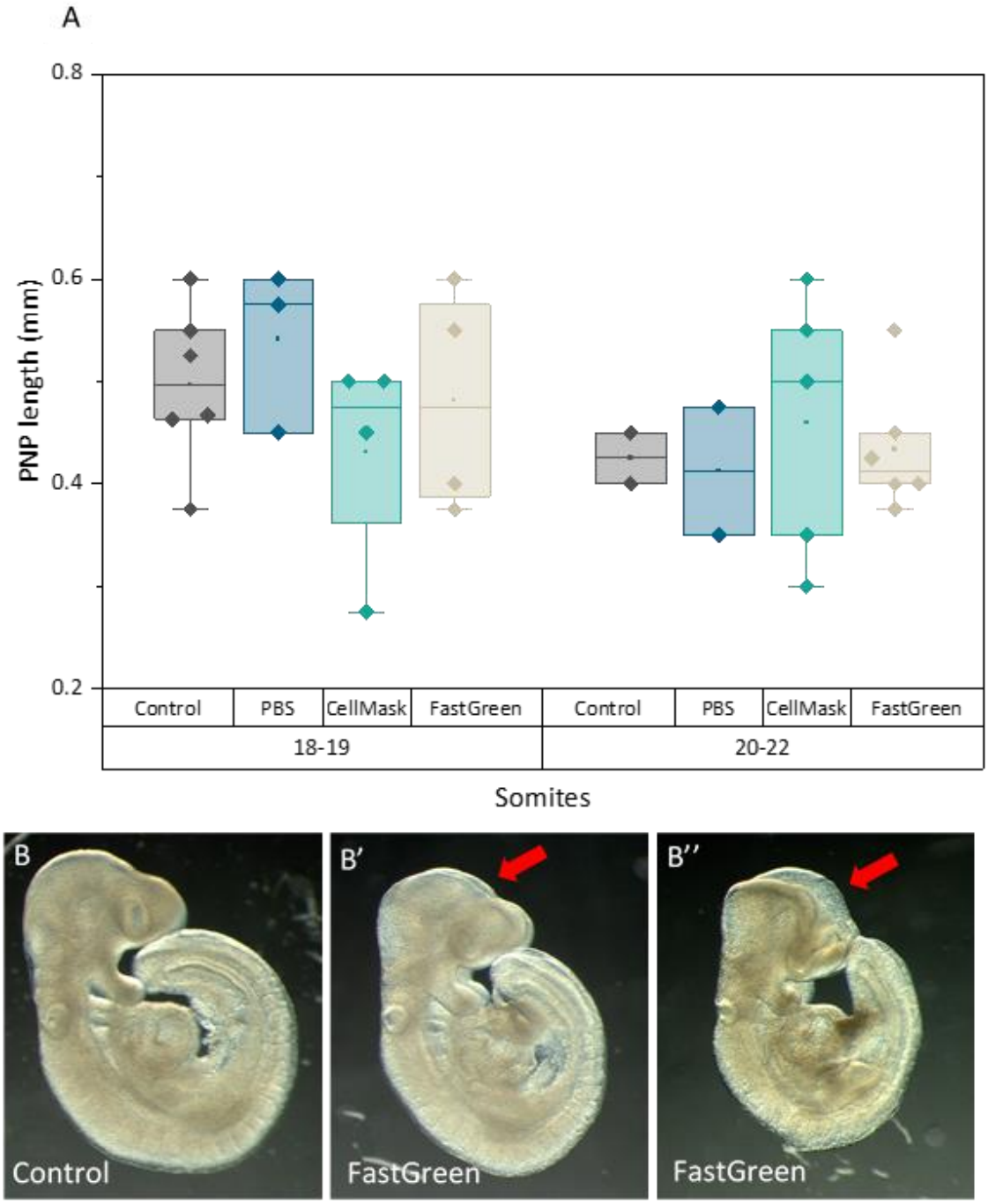

Figure 4.3 – The effects of FastGreen or CellMask on NTC

Culture of E8.5 embryos after injection with either FastGreen or CellMask does not have a significant impact on PNP closure, however FastGreen causes severe cranial defects in a large proportion of embryos. A) Injection with PBS, CellMask or FastGreen does not have a significant impact on PNP closure at any stage analysed. B) Control embryos do not show NTDs after culture (B), while 5 out of 10 embryos injected with FastGreen displayed cranial NTDs (red arrows, B', B'').

4.2.3 – E-cadherin inhibition has variable effects on PNP length and biomechanical properties

In order to analyse the potential biomechanical role of E-cadherin in the closing spinal NT, E8.5 CD1 embryos were cultured after injection of functional-grade E-cadherin blocking antibody. First, the approach was validated by analysing the ability of this antibody to bind to the SE in culture. Embryos were injected with either vehicle or E-cadherin blocking antibody and cultured for 1.5 hours, before immediate fixation. Whole mount immunofluorescence revealed clear binding of the blocking antibody to the SE, with controls showing no positive signal other than autofluorescence (Figure 4.4A, B). The blocking antibody was found mostly in the SE overlying the lateral mesoderm, including inside the cytoplasm, and appeared to be lacking in the midline and along the neural folds (Figure 4.4B). Interestingly, both groups show a clear accumulation of non-blocking E-cadherin antibody along the midline (Figure 4.4A', B'), however a direct comparison of overall protein level is not meaningful in whole mount immunofluorescence experiments.

To analyse if blocking E-cadherin affects PNP closure, embryos were cultured with different concentrations of blocking antibody, and the length of their PNPs were compared to controls (either embryos injected with vehicle or non-injected embryos) (Figure 4.5A, B). There was no significant effect of the treatment on closure, however there was a trend towards increased PNP length with higher antibody concentrations at the 17-19 somites stage (Figure 4.5). Many of the groups showed large variability, suggesting that any effects of the antibody were not consistently affecting all samples – indeed, embryos treated with 1:50 blocking antibody at the 20-22 somites stage showed a significantly larger variance compared to controls (two-sample test for variance, $p < 0.04$).

Analysis of confocal images of some embryos after culture revealed a striking difference in the morphology of the ZP. The angle of the ZP was analysed using curvature, which is equal to the diameter of a circle fitted to the ZP and is a more reproducible measurement for ZP angle than a V-shape (Nikolopoulou et al., 2019). Embryos cultured in 1:200 blocking antibody showed a significantly larger PNP curvature than both the control and 1:50 groups (Figure 4.6A - E). These PNPs were noticeably wide, and showed a similar curved morphology to *Grhl2*$^{-/-}$ embryos (Figure 4.6B, C) (Nikolopoulou et al., 2019). Interestingly, embryos treated with 1:50 blocking antibody did not show this morphology, and had narrower PNPs than embryos injected with vehicle. One embryo had a noticeably narrow PNP, reminiscent of the morphology of *Grhl2*$^{Axd/Axd}$ embryos (Nikolopoulou et al., 2019). Finally, it was noted that 3 embryos (1 in the 1:200 group, 2 in the 1:50 group) developed EX (data not shown). The effects of E-cadherin on cranial closure were

not further pursued but this finding does provide support for the hypothesis that blocking E-cadherin function disrupts NTC.

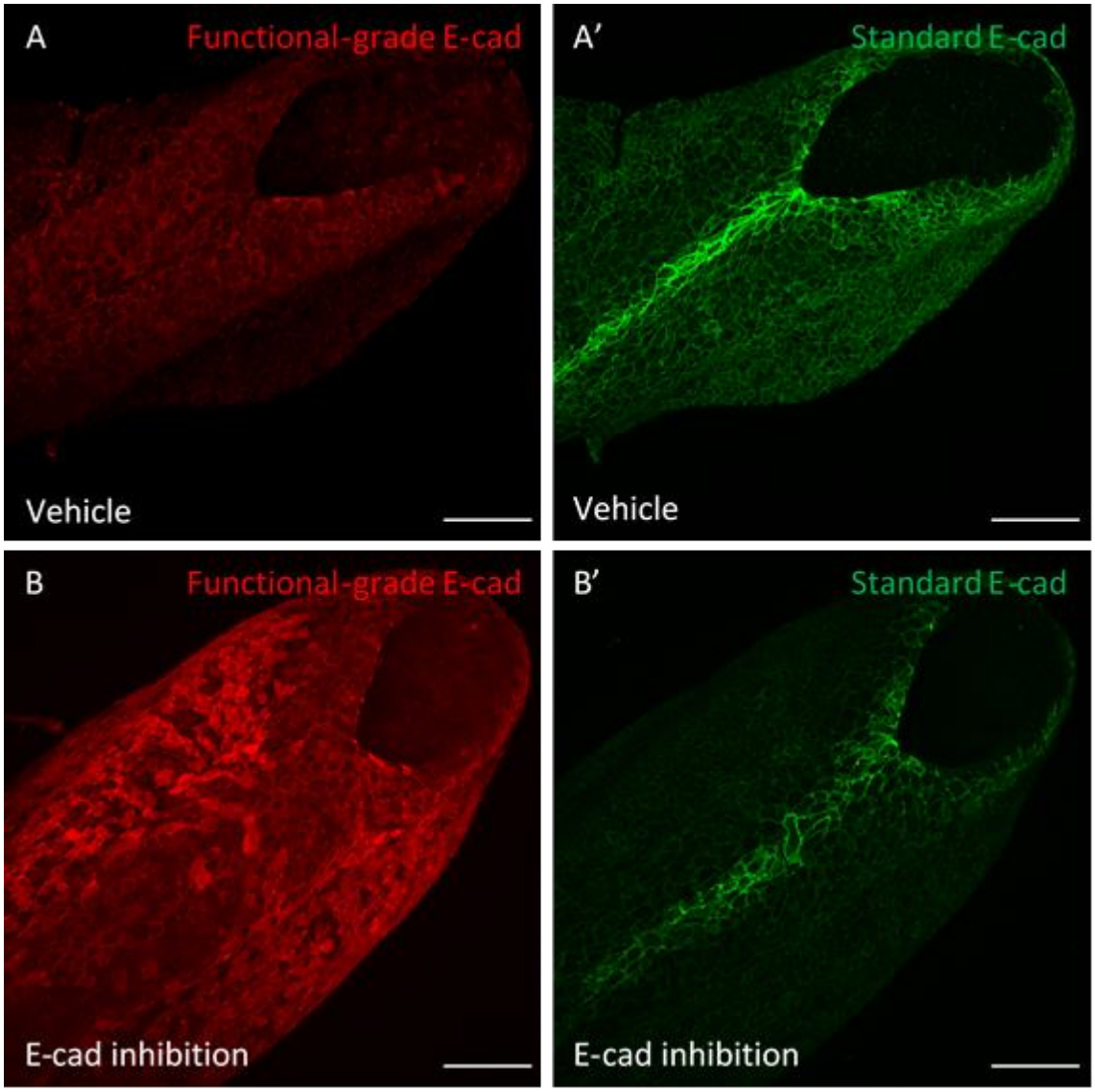

Figure 4.4 – Immunostaining to test for binding of functional-grade E-cadherin blocking antibody.

Functional-grade E-cadherin blocking antibody binds to the SE in culture. A,B) Immunofluorescence to detect blocking antibody after 1.5 hours in culture showed clear binding, especially in the SE overlying the lateral mesoderm. Non-specific binding was detected in the cytoplasm of SE cells (B). Vehicle injected embryos showed no positive signal for the blocking antibody (A). A',B') Both vehicle and blocking antibody treated groups showed accumulation of E-cadherin along the midline. Scale bars = 100 µm.

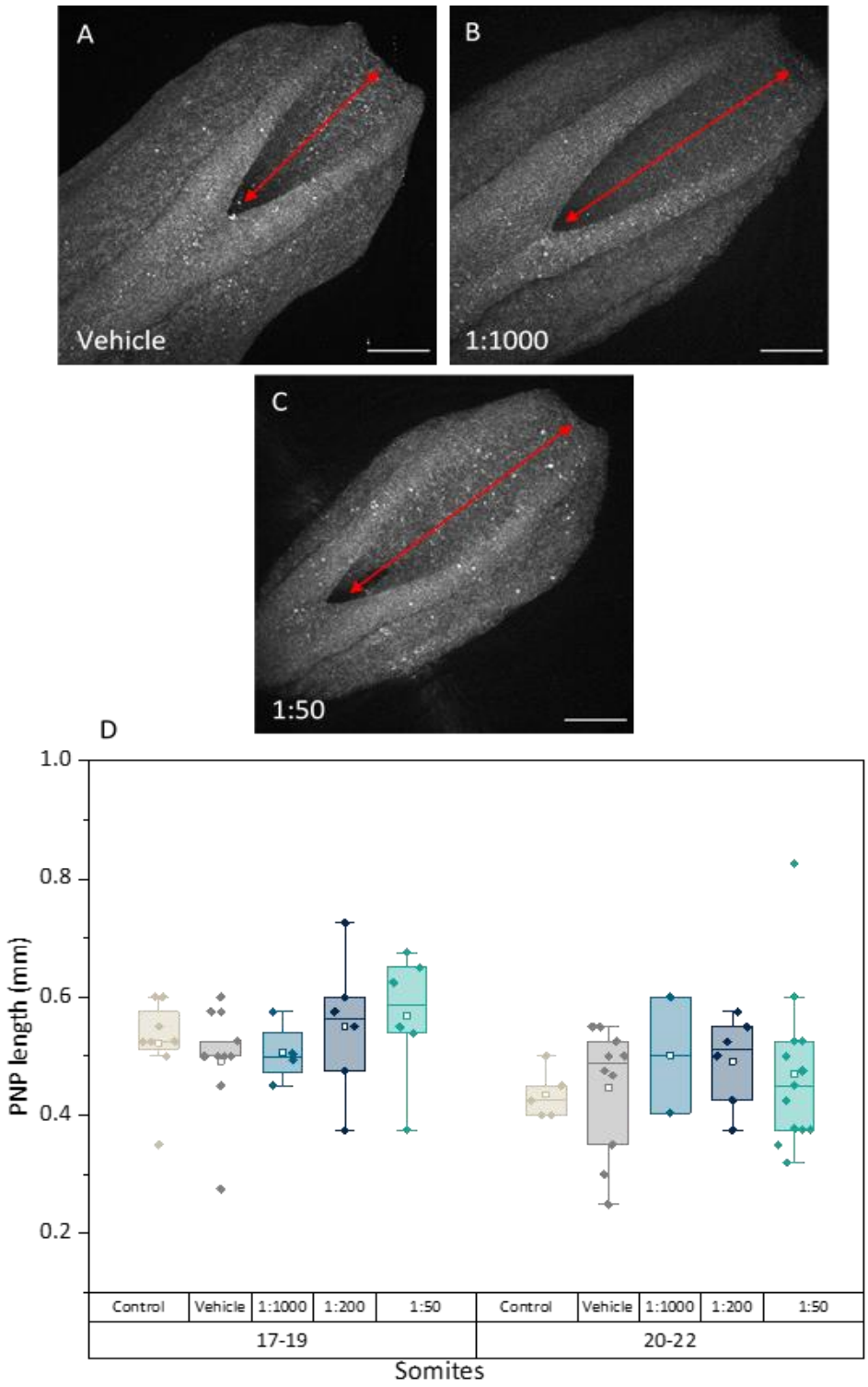

Figure 4.5 – The effects of E-cadherin blocking antibody on PNP length

There is no significant difference in PNP length after 24 hr culture with E-cadherin blocking antibody. A,B,C) Representative PNPs of E9.5 embryos after 24 hr culture in vehicle (A), 1:1000 blocking antibody (B) or 1:50 blocking antibody (C). D) Quantification of PNP lengths of embryos after 24 hr culture, with no microinjection (control), injection of vehicle, injection of different concentrations of blocking antibody. There is no significant difference in PNP length between treatment groups (ANOVA, $p > 0.05$), however there is a trend towards increased length in 1:200 and 1:50 groups in both somite groups compared to controls. Scale bars = 100 µm.

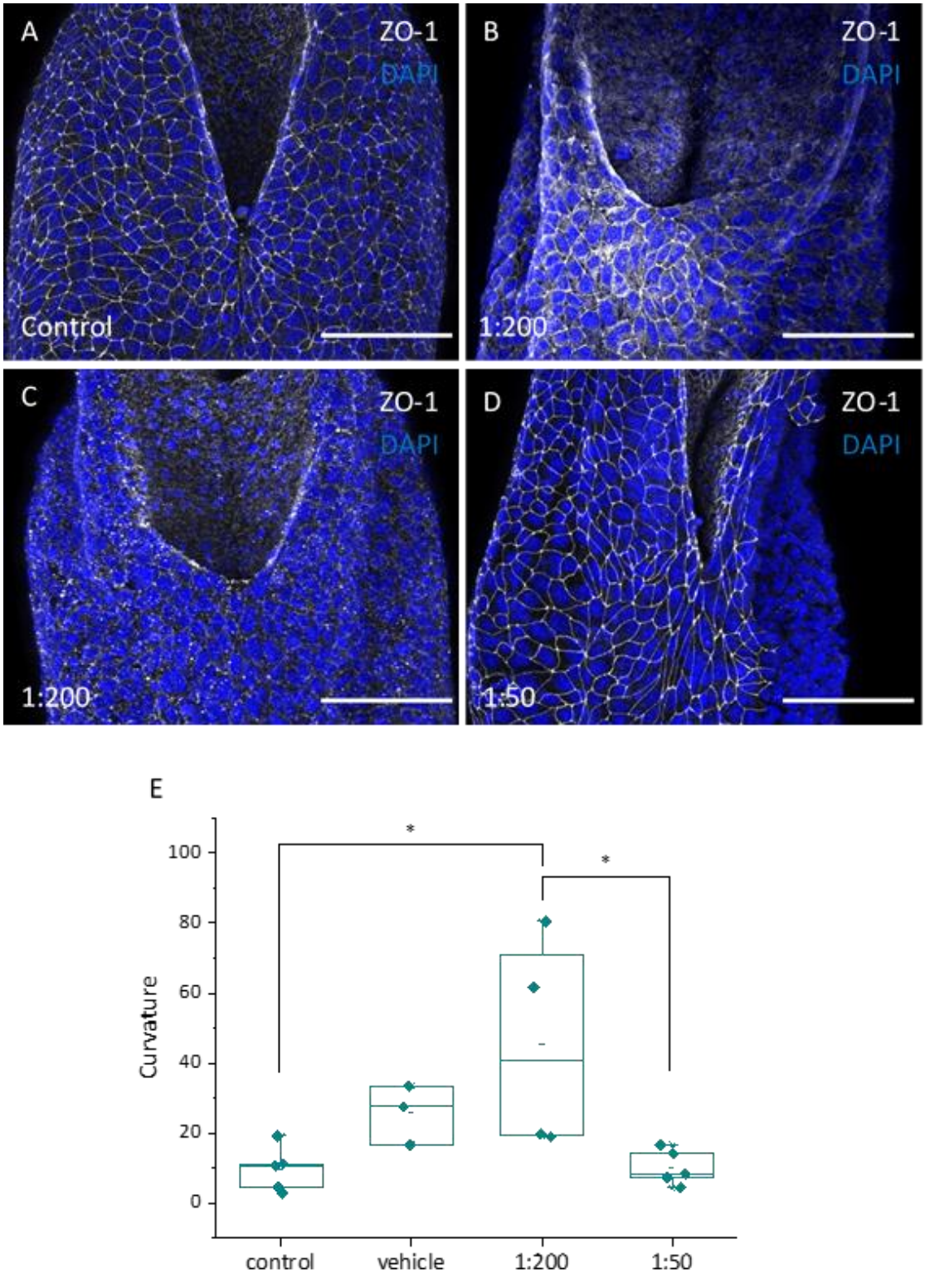

Figure 4.6 – The effects of E-cadherin blocking antibody on PNP curvature

There is a significant increase in zippering point angle after 24hr culture in 1:200 E-cadherin blocking antibody. A, B, C, D) Representative PNPs of E9.5 embryos after 24 hr culture in vehicle (A), 1:200 blocking antibody (B,C) or 1:50 blocking antibody (D). E) Quantification of PNP angle using the diameter of a fitted circle reveals a significantly larger curvature in embryos treated with 1:200 antibody (ANOVA, $p < 0.02$, post-hoc Tukey, $p < 0.03$ for both 1:200 v control and 1:200 v 1:50.) Scale bars = 100 µm.

The biomechanical properties of the SE after 24 hr blocking antibody treatment were then analysed in more detail using immunofluorescence. Although it had already been shown that the blocking antibody effectively bound to cells (Figure 4.4), by 24 hrs the localisation of E-cadherin expression had almost entirely recovered to normal. The absolute levels cannot be meaningfully compared using this method, and there was no noticeable reduction in expression levels (Figure 4.7A - C). Nevertheless, there were a small number of cells in the 1:50 group which showed higher expression compared to the surrounding SE, which could be a result of higher expression levels or residual blocking antibody which had not yet been degraded (Figure 4.7C, inset).

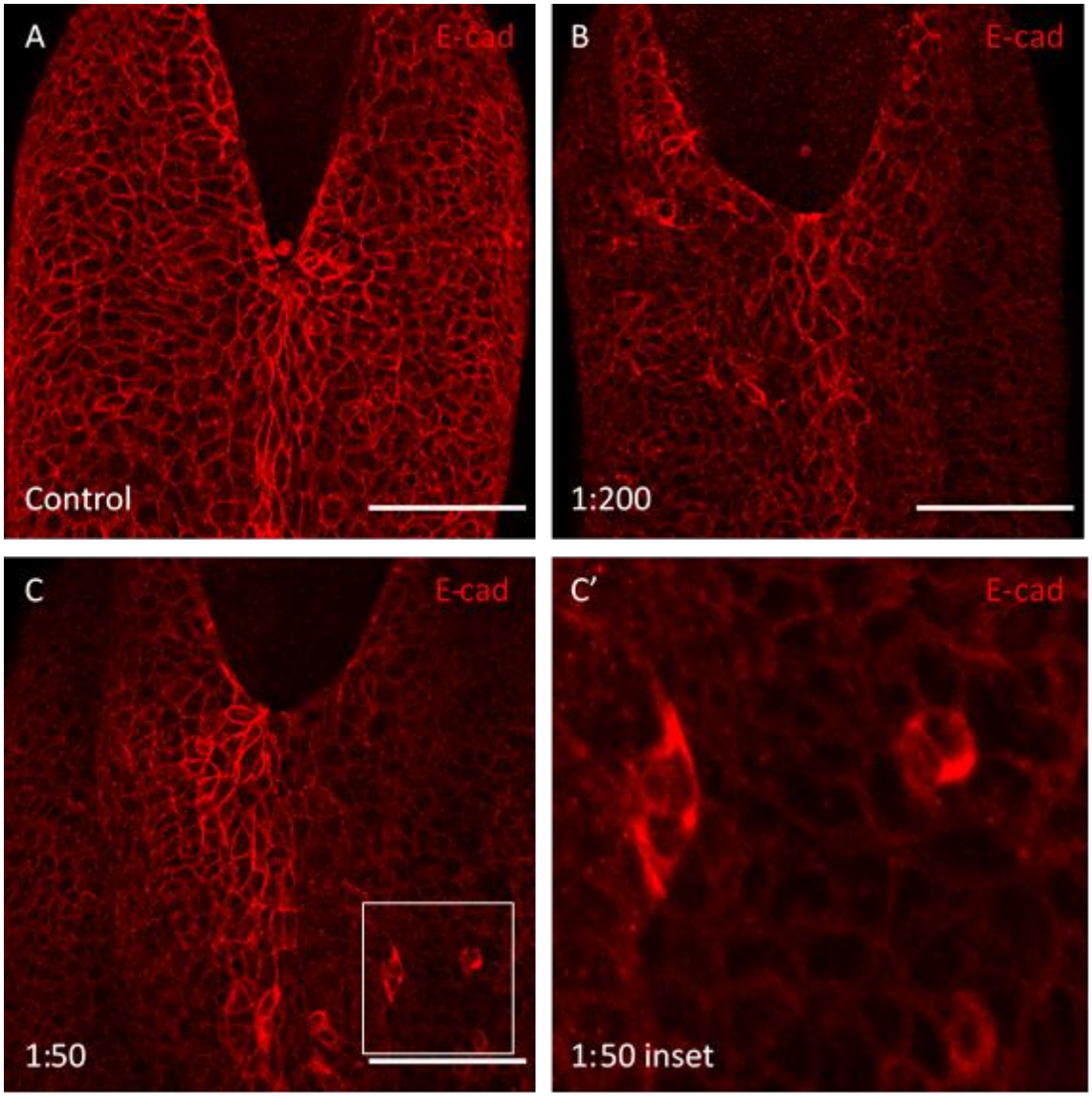

Figure 4.7 – E-cadherin immunofluorescence after 24 hr culture in blocking antibody.

E-cadherin levels mostly recover after 24hr culture in E-cadherin blocking antibody. A, B, C) Representative PNPs of E9.5 embryos after 24 hr culture in vehicle (A), 1:200 blocking antibody (B) or 1:50 blocking antibody (C). After culture in 1:50 blocking antibody, some cells show brighter E-cadherin fluorescence (C', inset of C), possibly due to residual blocking antibody detected after immunofluorescence or higher E-cadherin expression levels. Scale bars = 100 µm.

Phalloidin staining revealed that the F-actin cable was present in all embryos examined from the control and 1:50 E-cadherin blocking antibody groups, however there was a clear lack of a cable in two 1:200-treated embryos analysed (Figure 4.8 A - E). This was quantified using a fluorescence profile of a mediolaterally oriented line just over the ZP region (yellow line, Figure 4.8A - D). The presence of a cable, which stains very brightly due to high expression of F-actin, is indicated by a peak in the centre of the profile, where fluorescence levels reach the maximum of 255. All samples displayed a peak except for both embryos treated with 1:200, which had a relatively flat fluorescence profile (red and black lines, Figure 4.8E). Also of note was the 1:50 sample which had previously been shown to have a very narrow PNP – this sample had an abnormally bright F-actin cable. The cable phenotypes of the 1:200 and 1:50 treated embryos are comparable to *Grhl2*$^{-/-}$ and *Grhl2*$^{Axd/Axd}$ embryos respectively (Nikolopoulou et al., 2019). Unfortunately, Phalloidin staining was not of a high enough quality in the other group of immunostained embryos to further support these findings.

As in Chapter 3, ZO-1 staining was used to analyse cell shape after treatment. For each shape parameter, the value given for each embryo was the average of the total midline cells (range 7-12 cells per embryo). Most samples in all groups showed the expected elongated and rostrocaudally oriented SE cells (Figure 4.9A). However, some embryos treated with either 1:200 (2/4 embryos) or 1:50 (2/5) blocking antibody did not appear normal, and showed atypically small or wide cells, especially in the region directly rostral to the PNP (red arrows, Figure 4.9B, C). There were also some exceptionally long and narrow cells in the 1:50 group (yellow arrow, Figure 4.9C). However, quantification of aspect ratio and orientation of midline cells did not reveal a significant difference in any treatment group (Figure 4.10A - B).

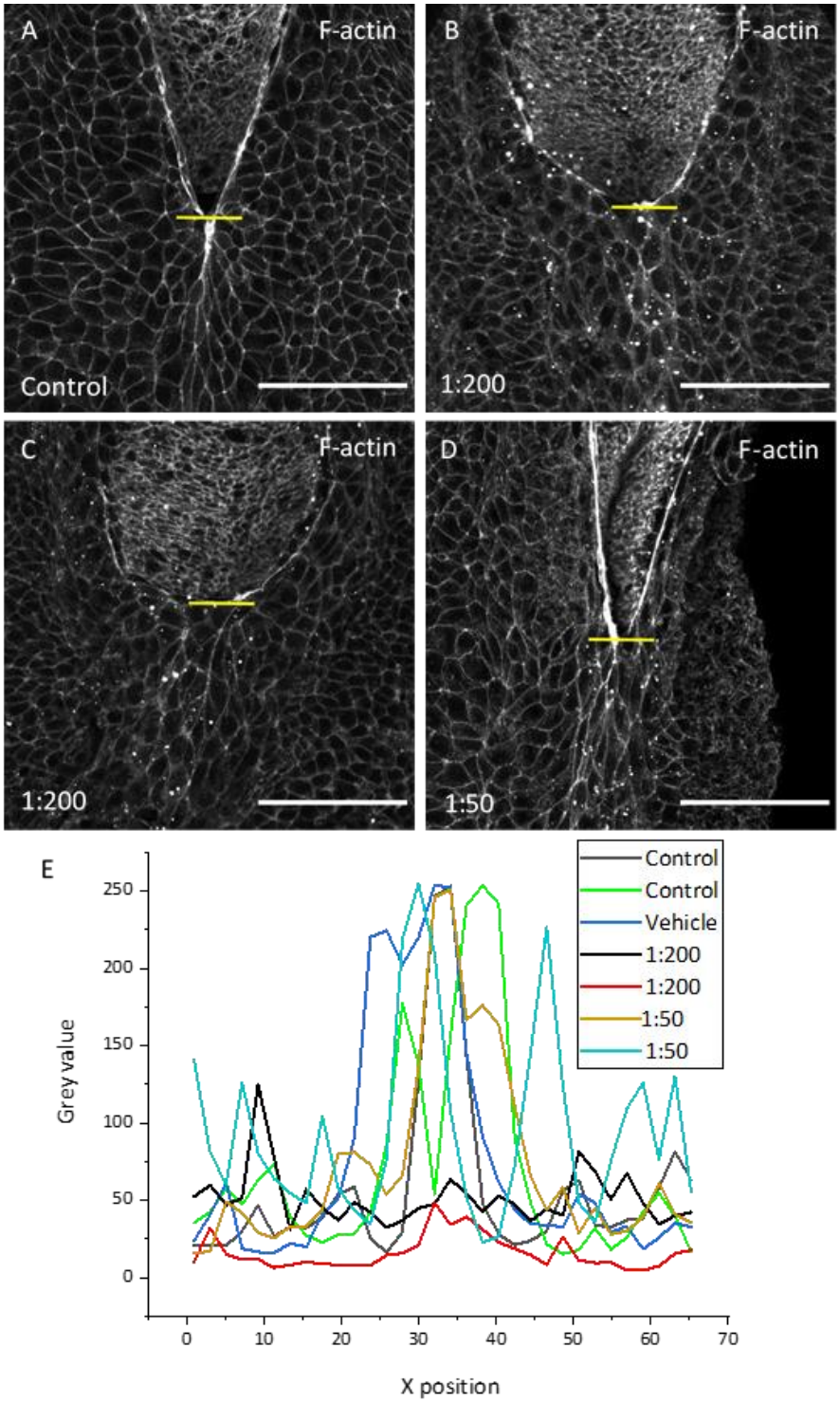

Figure 4.8 – F-actin immunostaining and fluorescence quantification after 24 hr culture in E-cadherin blocking antibody.

The F-actin cable is absent from embryos cultured for 24hrs in 1:200 E-cadherin blocking antibody. A, B, C, D) Representative PNPs of E9.5 embryos after 24 hr culture in vehicle (A), 1:200 blocking antibody (B,C) or 1:50 blocking antibody (D). The presence of the cable was measured by creating a fluorescence profile along the yellow line in each sample. E) Fluorescence profiles of each sample revealed that both embryos treated with 1:200 blocking antibody (black and red lines) did not have a cable, which is otherwise indicated in other samples by a peak reaching the maximum fluorescence value of 255. Scale bars = 100 µm.

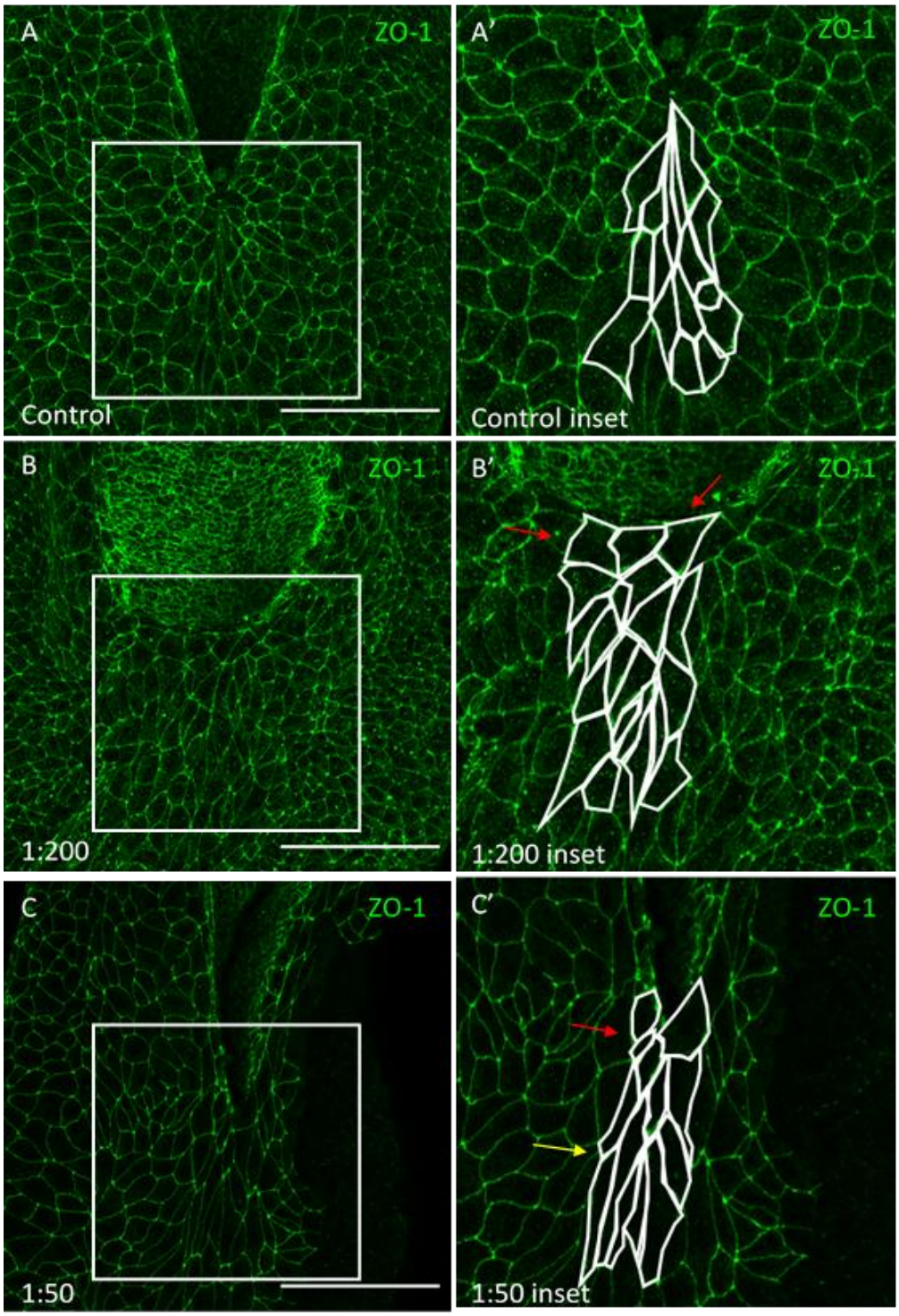

Figure 4.9 – The effects of E-cadherin blocking antibody on cell shape.

Cell shape is abnormal in some embryos after 24hr culture in E-cadherin blocking antibody. A, B, C) Representative PNPs of E9.5 embryos after 24 hr culture in vehicle (A), 1:200 blocking antibody (B) or 1:50 blocking antibody (C). Control embryos mostly show the expected SE elongated shape (A). Some embryos treated with 1:200 blocking antibody appear to lose this elongation, with some abnormally wide cells directly rostral to the ZP (red arrows) (B). The expected elongated shape is present in embryos treated with 1:50 blocking antibody, however some abnormally small cells are present (red arrow), and the elongation seems particularly extreme in other cells (yellow arrow). Scale bars = 100 µm.

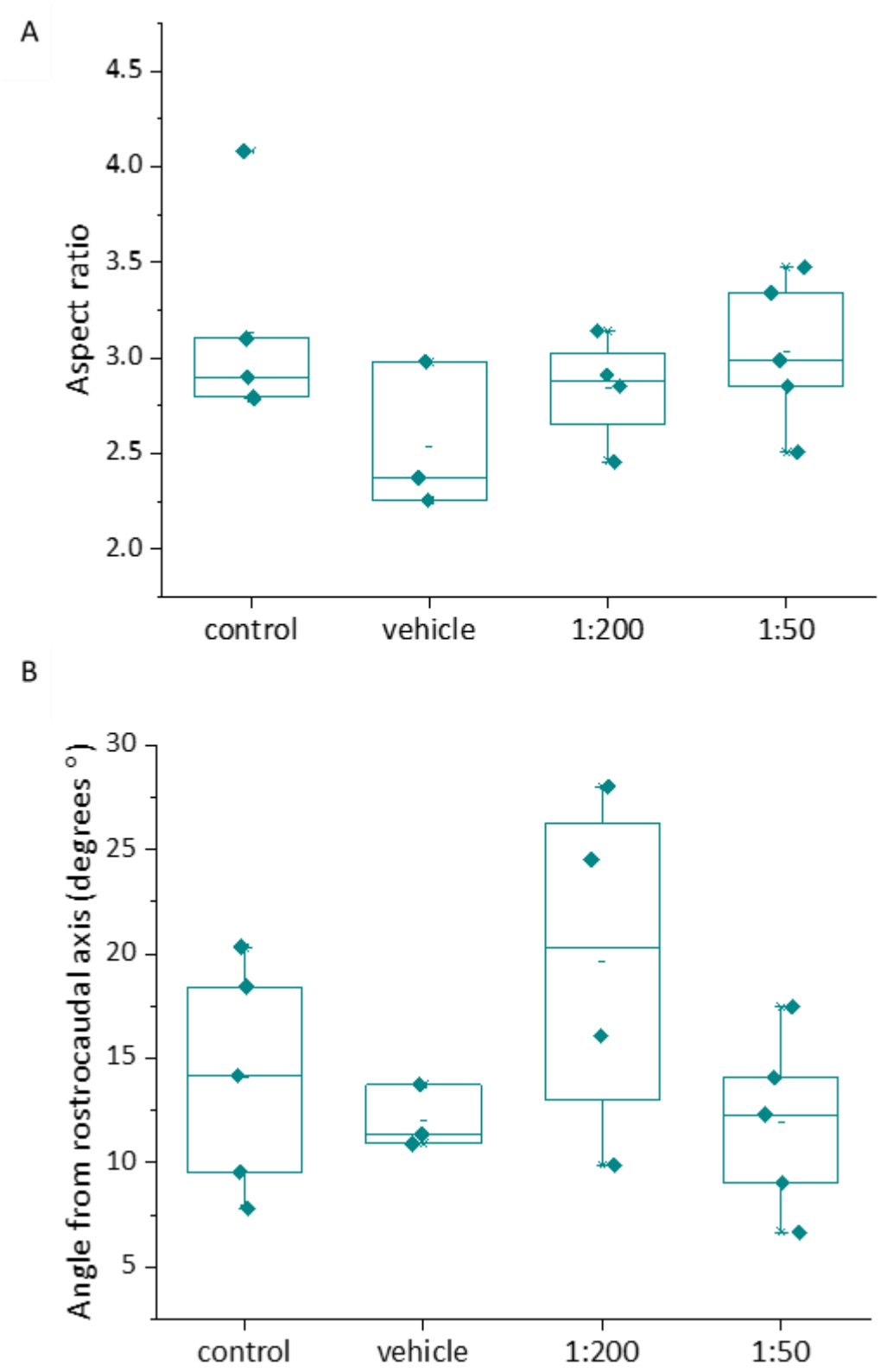

Figure 4.10 – Cell shape quantification in embryos cultured for 24 hrs in E-cadherin blocking antibody.

Quantification of midline SE cell shape parameters reveals no significant difference between embryos after 24 hr culture in E-cadherin blocking antibody. A) There is no significant difference in mean aspect ratio between treatment groups (ANOVA, $p > 0.05$). B) There is no significant difference in cell orientation between treatment groups (ANOVA, $p > 0.05$).

Because there was a large variability in the PNP length and cell shape, the relationship between cell shape and PNP morphology was analysed. Overall, only aspect ratio and PNP length showed a significant relationship, with smaller average midline aspect ratio (i.e. less elongated cells) correlating with a longer PNP (pink line in Figure 4.11A, slope significantly different from 0, ANOVA, $p < 0.04$). When individual treatment groups were separated, 3 of 4 groups showed a negative correlation between aspect ratio and PNP length (Figure 4.11A), supporting this observation – the fourth group which showed a positive correlation had a very small range of PNP lengths, making this correlation less meaningful. Aspect ratio is less clearly correlated with PNP curvature (Figure 4.11B), although the outlier samples with a very large curvature show a low aspect ratio. The samples with a very low curvature (< 10, i.e. very narrow PNPs) also show lower aspect ratios (Figure 4.11B). Orientation of midline SE cells does not clearly correlate with PNP length or curvature, either when groups are separated or combined (Figure 4.12).

Finally, SE recoil after laser ablation was analysed in E9.5 embryos cultured for 2 hrs in vehicle or 1:50 blocking antibody (Figure 4.13A - C). There was a trend towards increased recoil in treated embryos compared to controls, although this did not quite reach significance (Figure 4.13C, t-test, $p < 0.06$).

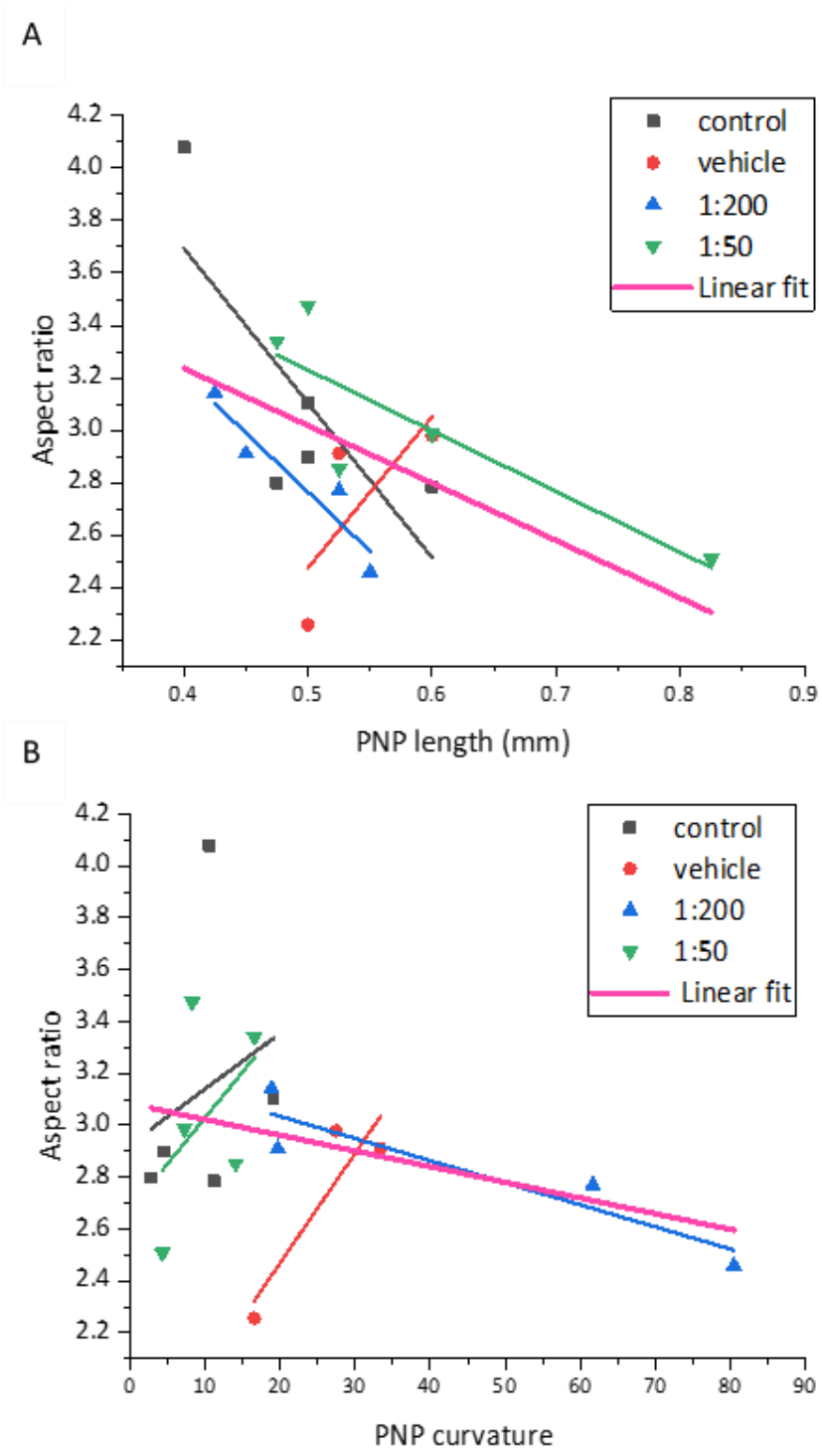

Figure 4.11 – Correlation between PNP morphology and cell aspect ratio after 24 hr culture in E-cadherin blocking antibody.

A low aspect ratio correlates with a longer PNP. A) There is an overall negative correlation between aspect ratio and PNP length (ANOVA, $p < 0.04$). In 3 of 4 treatment groups, there is a negative correlation between aspect ratio and PNP length. The outlier with a very long PNP has a very low AR. B) There is an overall negative correlation between aspect ratio and PNP curvature, although this is not significant. Aspect ratio does not appear to show a strong relationship with PNP curvature, however the outlier samples with very high PNP curvature have a low aspect ratio.

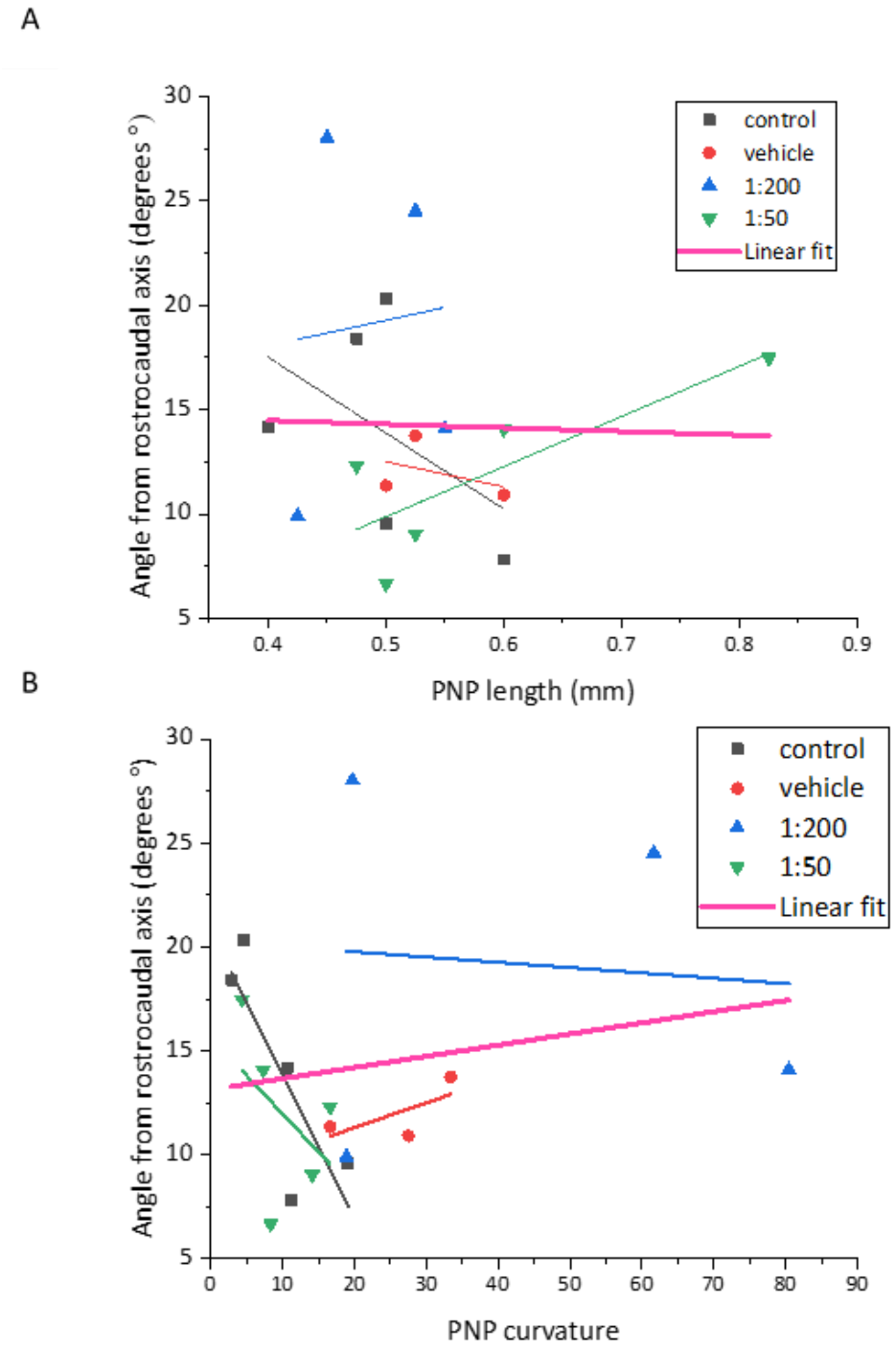

Figure 4.12 – Correlation between PNP morphology and cell orientation after 24 hr culture in E-cadherin blocking antibody.

Orientation of SE cells does not correlate with abnormal PNP morphology. A) There is no clear trend between orientation of cells along the RC axis and PNP length, although the 1:50 blocking antibody treated group does show a positive correlation, with the largest PNP also showing the least rostrocaudally oriented SE cells. B) There is a small positive correlation between cell orientation and PNP curvature, although this is not significant. There are no clear correlations between orientation of cells along the RC axis and PNP curvature in individual groups.

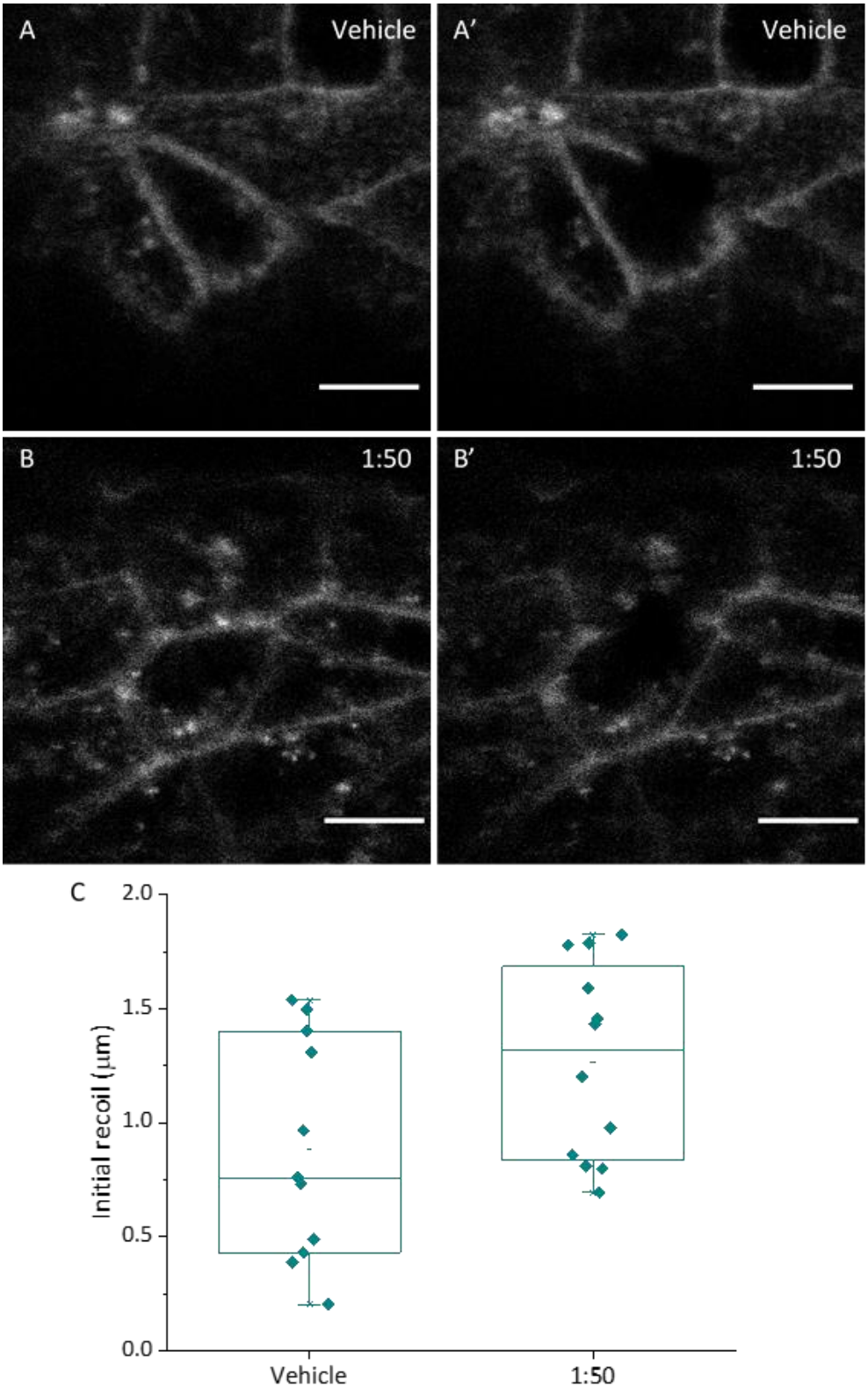

Figure 4.13 – SE recoil analysis after 24 hr cultures in E-cadherin blocking antibody.

There is a trend towards increased SE recoil in embryos cultured for 2 hrs in 1:50 E-cadherin blocking antibody. A, B) Representative images of SE cells in vehicle (A) and 1:50 blocking antibody treated (B) embryos, before (A, B) and after (A', B') single border laser ablation. C) Blocking antibody treatment does not cause a significant change in SE recoil after laser ablation (t-test, $p > 0.05$), however there is a trend towards reduced SE recoil after treatment. Scale bars = 10 µm.

4.3 -Discussion

In this chapter, the effect of disrupting actomyosin activity or E-cadherin function was investigated to ask whether either can alter SE biomechanics, and whether this can have an effect on NTC. The results presented here present evidence that SE biomechanics are important for normal closure. Although many of the phenotypes after treatment are very mild, the difference between short term pharmacological experiments and genetic mutants must be considered; disrupted gene expression in mouse models over a longer period is predicted to cause more global changes than can be expected over 24 hours or less.

It is already appreciated that blebbistatin treatment alone (at a sub-toxic dose) does not prevent spinal NTC progression, although it does cause cranial defects (Escuin et al., 2015). It's ability to rescue the effects of actin accumulation suggests that an inability to affect PNP closure is not due to a lack of blebbistatin activity in the spinal NT (Chapter 1.5.3.1). Therefore, it was predicted that blebbistatin may affect SE properties as revealed by laser ablation. The results in Chapter 3 suggest that elongated cells do not show high recoil, raising the important question of whether the laser ablation method is sensitive to actomyosin-determined tension. If blebbistatin treatment supported this methodology, this would inform the finding that elongated cells do not show increased recoil. Indeed, the majority of samples analysed showed a visibly lower recoil after ablation compared to control. Although the effect of this treatment did not reach statistical significance, a technique involving embryo culture can be expected to show variability, due to differences in size altering the concentration of drug passing through the yolk sac, and differences in embryo viability after culture. These parameters were minimised by using embryos with an intact yolk sac, strong heartbeat and visible circulation, however differences are still expected in such conditions.

Inhibition of E-cadherin in the developing embryo is one of the only pharmacological treatments that could potentially distinguish the roles of the NE and SE during neurulation. It's specificity to the SE, and the fact that it is one of the main dysregulated genes in the *Grhl2* mutant models of NTDs, makes it the ideal target for this purpose.

The first preliminary experiment using this treatment asked if blocking antibody successfully binds to SE cells. This confirmed specific binding of blocking antibody to the SE, and identified a clear difference in the localisation of antibody, with high fluorescence in the lateral regions but little along the midline (Figure 4.4B). The low midline levels of blocking antibody could be due to the position of the embryo within the embryonic membranes – after the embryo has turned,

the caudal dorsal part of the embryo, including the PNP, is facing outwards towards the amnion, and depending on how close these surfaces are, the amnion may limit binding of the antibody to the midline. Alternatively, the apparent lack of midline antibody staining could be due to higher turnover in the midline restoring E-cadherin levels. Cadherin turnover is known to be crucial for many developmental processes involving extensive cellular remodelling. For example, blockade of clathrin-mediated endocytosis of C-cadherin in *Xenopus* animal cap explants using dynamin prevents CE due to a large upregulation of C-cadherin levels (Jarrett et al., 2002). It is expected that SE cells along the neural folds will be undergoing greater turnover of AJ components, both by endocytosis and degradation, as they disassemble and reassemble cell-cell contacts during fusion (Nanes and Kowalczyk, 2012). Turnover of AJs along the midline may be either a residual effect of midline fusion, or due to an active reorganisation of borders in the region rostral to the progressing ZP.

Once binding of E-cadherin blocking antibody had been validated, the effects after 24 hours in culture were analysed. Mean PNP length was not significantly altered after treatment (Figure 4.5), although one 1:50 treated sample in the 20-22 somites stage group was a significant outlier, with an exceptionally large PNP. PNP curvature, which is a measure of the ZP angle, showed a more striking difference, with 1:200 treated embryos showing a significantly higher curvature compared to controls, a phenotype previously observed in *Grhl2*$^{-/-}$ mutants (Nikolopoulou et al., 2019). Phalloidin staining revealed a striking loss of the F-actin cable in the 1:200 treatment group, but not the 1:50 group. The correlation between the loss of cable and wide PNP morphology lends further support to the hypothesis that the F-actin cable acts as a pro-closure force, and suggests that formation and/or regulation of the F-actin cable may be modulated by AJ function (Galea et al., 2017).

Cell shape was less clearly affected by E-cadherin inhibition, although a negative correlation between AR and PNP length was observed when treatment group was not considered, supporting the hypothesis that elongated cell shape reflects intrinsic cell behaviours during normal progression of NTC. The fact that PNP length but not curvature correlated with cell shape supports the hypothesis that elongated cell shape is due to active cell migration. A migratory mechanism would not be expected to have an effect on the laterally pulling anti-closure forces or tissue integrity which are predicted to alter PNP width. The lack of significantly different cell shape parameters (aspect ratio and orientation) in embryos treated with E-cadherin blocking antibody could reflect the fact that PNP length is not significantly altered, while PNP curvature is significantly higher. Alternatively, a lack of cell shape phenotype after 24 hours could be due

to recovery of cell behaviour. Based on the hypothesis presented in Chapter 3, if cell shape is due to an intrinsic reorganisation of junctions, recovery of E-cadherin could allow this process to resume. It could therefore be interesting to analyse cell shape in the regions laterally, where E-cadherin turnover may not be as high, or to analyse cell shape after repeated administration of blocking antibody.

Finally, SE recoil was analysed using laser ablation after a 2 hour culture. Although this difference did not quite reach significance, there was a clear trend towards increased recoil in the E-cadherin treated group, which is also observed in *Grhl2*$^{-/-}$ embryos (data presented in Chapter 5). The increase in SE recoil could be explained by a reduction in the strength of AJs, which may in wild types resist recoil after ablation. This raises the question of any regional differences in adhesion and a possible link with the regional differences in recoil identified in Chapter 3, however there were no clear differences in E-cadherin staining along the RC axis.

A disadvantage to the SE laser ablation experiment was the stage of the embryos – plugs from overnight mating of CD1 mice generates relatively late stage E9.5 embryos when cultured first thing in the morning, which is at a later stage than the embryos ablated in Chapters 3 and 5. It would potentially be more valid to analyse SE recoil around E8.5 after 2 hour culture in this experiment, when the blocking antibody is injected for 24 hour culture, to explore the potential role of altering SE tension on PNP closure. However, E8.5 embryos are more difficult to ablate, due to their smaller size and less robust tissue, which is more prone to damage during positioning. In addition, the SE ablation technique in the spinal region is optimised in E9.5 embryos, and potential differences between regions and somite stages at E8.5 are not yet characterised.

The effects of E-cadherin inhibition after 24 hours were not expected to recapitulate the *Grhl2*$^{-/-}$ phenotype, as these mutants show dysregulation of multiple cell adhesion components in addition to E-cadherin (Nikolopoulou et al., 2019). Furthermore, blocking antibody was administered only once, at the start of the culture. Although cadherins have a relatively long metabolic half-life of 5-10 hours, it is unlikely any blocking antibody would remain after 24 hours (Nanes and Kowalczyk, 2012). The observation that some of the features of *Grhl2* mutant phenotypes were present, in particular the *Grhl2*$^{-/-}$ wide PNP morphology and lack of F-actin cable in the 1:200 treatment group, encourages the view that the E-cadherin blocking antibody does affect function. More surprising was the *Grhl2*$^{Axd/Axd}$-like PNP morphology and abnormally bright F-actin cable in one of the 1:50 samples. A potential explanation is that the very high concentration of blocking antibody at the beginning of the culture triggered a responsive change

in E-cadherin expression, leading to abnormally high levels by the end of the 24 hours. A useful future experiment would be to repeatedly administer blocking antibody over the culture period, to explore if more severe phenotypes are observed in either group.

One potential caveat to these experiments is the method of antibody administration. Although embryos develop normally after microinjection of PBS with CellMask, there may be subtle changes in NTC rate and biomechanical properties. Indeed, vehicle treated embryos showed a small, non-significant increase in PNP curvature (Figure 4.6) and PNP length in the older somite group (Figure 4.5) compared to non-injected controls. Microinjection is a technique which may be subject to variability: the size of the needle tip must be large enough to allow the solution to be taken up and successfully expelled into the amnion, but must also be small enough to cause minimal damage to the embryonic membranes and prevent the solution from escaping back into the culture medium; the original size of embryos are different, so although injected concentration is controlled, the total volume required to fill the amnion differs. Although the small size of the needle prevents the solution from being ejected too quickly, increased pressure is likely to occur during the injection, which is known to affect embryo development. A collapsed amnion, which is presumed to increase the pressure exerted on the embryo, increases ventral curvature and delays PNP closure (Peeters et al., 1996). In addition, loss of Reichart's membrane, which is believed to act as a 'shock absorber' by protecting the embryos from uterine contractions, leads to severe morphological abnormalities in the embryo after implantation (Ueda et al., 2020). Nevertheless, it is assumed that any pressure differences resolve once the needle is removed, and this possible effect is unlikely to cause significantly different phenotypes.

Overall, this chapter suggests that, even with relatively short culture in the presence of a single inhibitor, SE biomechanics can be altered, leading to disrupted PNP morphology. Future work should focus on further characterising these models. Questions of particular interest are: if repeated administration of E-cadherin blocking antibody gives a more severe phenotype after 24 hours; if SE tension is altered at the earlier, critical stages of spinal closure; if the apparently opposing phenotypes of embryos treated with 1:200 or 1:50 E-cadherin blocking antibody are due to a responsive upregulation of E-cadherin expression.

Chapter 5 - Analysing surface ectoderm biomechanics in *Grhl-2* and *-3* mutant embryos

5.1 - Introduction

5.1.1 - *Grhl2* knock-out and overexpression mutants show defective SE biomechanics

As discussed in Chapter 1.4.4, both loss- and gain-of-function mutations in *Grhl2* lead to severe NTDs, however the mechanism by which NTDs are caused is poorly understood. High expression levels of *Grhl2* in the SE during neurulation, and the timing of closure defects prior to expression in other tissues, suggests that its role during neurulation is in this tissue. It is already known that the SE regulates formation of DLHPs in the spinal region by release of signalling molecules such as BMPs (see Chapter 1.1.3), however *Grhl2* mutants already show a larger PNP, indicating delayed closure, before the stage at which DLHPs are required for closure (Ybot-Gonzalez et al., 2007a, Nikolopoulou et al., 2019). This suggests that abnormal DLHP formation is not the causative mechanism in these mutants. Furthermore, the protrusions which initiate contact during fusion appear normal in *Grhl2* mutants (Nikolopoulou et al., 2019). Therefore, it is possible that an unknown role of the SE is responsible.

In a recent study from our lab, RNA-seq was used to examine this potential mechanism in *Grhl2*$^{-/-}$ and *Axd/Axd* mutant mice (Nikolopoulou et al., 2019). The caudal embryo (including the PNP) was dissected, and gene expression was compared between mutants and their corresponding wild type controls. This analysis identified 22 genes that were upregulated in *Axd* and downregulated in *Grhl2*$^{-/-}$, the majority of which corresponded to an epithelial signature, including *Cdh1*, *EpCAM* and *Cldn-4*. Microdissection of the dorsal SE-containing caudal embryo from the ventral hindgut region found that the genes specifically misexpressed in the SE region included *Cdh1* and *Cldn4*, which encode E-cadherin and Claudin-4 respectively. Interestingly, immunostaining of classical SE expressed genes revealed ectopic expression of N-cadherin in the SE of *Grhl2*$^{-/-}$; based on the literature suggesting that *Grhl2* acts to suppress EMT (see Chapter 1.4.2), it was hypothesised that these cells might be undergoing EMT. However, while vimentin expression was not different, these N-cadherin expressing clusters were positive for Sox2, suggesting a transition from an epithelial to a more neural phenotype. Meanwhile, E-cadherin and claudin-4 appeared to be more abundant in *Axd*. These findings together suggest that *Grhl2* is important for conveying epithelial characteristics on the SE, with knockouts showing a more neural phenotype and *Axd* embryos showing a 'super-epithelium' phenotype (Nikolopoulou et al., 2019).

Further analysis of these mutants revealed several biomechanical deficits. Classical indicators of biomechanical abnormalities are cell shape and actomyosin expression (discussed in Chapters 1.5 and 3.1). Immunostaining for F-actin and pMLC-II were both upregulated along the midline and along the cable in *Axd* embryos, whereas in *Grhl2*$^{-/-}$ they appeared as a disorganised mesh in the region rostral to the ZP. Cell shape was abnormal in both mutants: the orientation of SE cells along the midline in *Axd* embryos was significantly disrupted from the RC orientation of wild type embryos and the SE was thicker. The aspect ratio of SE cells in both mutants were significantly lower compared to wild types. This was then validated using needle incision and recoil analysis as a functional read-out of altered biomechanics. Needle incision in the SE rostral to the ZP revealed increased recoil in *Axd* embryos, but no change in *Grhl2*$^{-/-}$ mutants (Nikolopoulou et al., 2019). Overall, it is clear that loss- and gain-of-function mutations in *Grhl2* lead to biomechanical deficits in the SE, however whether these are a cause or consequence of failed NTC remains unknown.

5.1.2 - The role of the SE in *Grhl3* mutants is unknown

Study of *Grhl2* mutants has advanced our knowledge of this gene in SE biomechanics, however *Grhl3* mutants are more poorly understood. *Grhl3* is also predominantly expressed in the SE, however in a more restricted region (see Figure 1.3)- the *Grhl3*-Cre mouse line drives high Cre expression in the SE along the neural folds and just rostral to the ZP, and sporadic expression in the NE (Camerer et al., 2010, Mole et al., 2020). At the later stages of spinal neurulation there is also abundant expression in the hindgut (Gustavsson et al., 2007, Gustavsson et al., 2008). From studies of *curly-tail* mutant embryos, it is known that decreased *Grhl3* expression in the hindgut leads to reduced proliferation and a subsequent biomechanical deficit owing to increased ventral curvature, resulting in delayed NTC (Copp et al., 1988, Brook et al., 1991, Peeters et al., 1997). However, *Grhl3* expression in the hindgut is from late stages of neurulation, and furthermore the delay in NTC in *curly-tail* embryos is not apparent until ~E10.0. Knockout of *Grhl3* in all tissues leads to defective neurulation from E8.5, suggesting that loss of expression in tissues other than the hindgut at earlier stages are the first causative defect in these mutants. Conditional knockout in the NE does not lead to NTDs, while conditional knockout in the hindgut does; importantly however, these NTDs are at a lower severity and penetrance than ubiquitous knockouts (60% SB in *Sox17*$^{Cre/+}$*;Grhl3*$^{f/-}$), which is comparable to heterozygous *Grhl3*$^{ct/-}$ embryos (50% SB) (De Castro et al., 2018a, De Castro et al., 2018b). Conditional knockout in the SE in this study was not possible, as the only known drivers for SE Cre expression are the *Grhl3-Cre* line or

other drivers that are not SE specific. However, these findings, along with the expression pattern of *Grhl3,* suggest that the first defect in *Grhl3*$^{-/-}$ embryos is in the SE.

The fact that *Grhl-2* and *-3* have highly homologous DNA binding domains, and that double heterozygous mutants show exacerbated phenotypes, suggests that these genes may share transcriptional target genes and thus could play similar roles during development (Rifat et al., 2010). A recent study has shown that GRHL3 protein is co-localised with PCP proteins in the closing NT, and is important for the SE to develop biomechanical properties, i.e. actomyosin enrichment and tissue stiffness (Kimura-Yoshida et al., 2018). However, the specifics of how *Grhl3* controls biomechanical properties in the SE is an ongoing challenge.

5.2 - Results

5.2.1 - *Grhl2*$^{-/-}$ mutants have increased tissue and cell level recoil after laser ablation

Previous work has shown that both overexpression and knockout mutants of *Grhl2* have abnormal SE biomechanics (Chapter 5.1.1). This includes greater SE tension in *Axd/Axd* embryos, as revealed by recoil after needle incision (Nikolopoulou et al., 2019). However, how this relates to overall tension at the ZP, including the NE, is unknown. Laser ablation as a functional readout of disrupted biomechanics was utilised to analyse this question, in two different regions of the closing spinal region – first, the ZP tissue was targeted to analyse neural fold recoil, which included ablation of the SE and the NE, and second, single cell borders were ablated as first described in Chapter 3.

Interestingly, recoil at the ZP was comparable between *Axd/Axd* and wild type embryos. This was surprising as the SE in these embryos was previously found to show greater recoil compared to controls after needle incision. However, *Grhl2*$^{-/-}$ embryos showed significantly greater recoil ($p < 3 \times 10^{-4}$, Figure 5.1). SE recoil directly rostral to the ZP was therefore measured using single cell laser ablation. Similarly to tissue level recoil and in contrast to needle incision recoil, these cells showed significantly higher recoil compared to wild types in *Grhl2*$^{-/-}$ embryos ($p < 0.009$) but not in *Axd/Axd* (Figures 5.2, 5.3). Cable recoil was comparable in both groups (Figures 5.4, 5.5), although in *Grhl2*$^{-/-}$ the cable was often hard to identify, consistent with previously published data showing disorganisation or absence of a cable in these mutants (Nikolopoulou et al., 2019).

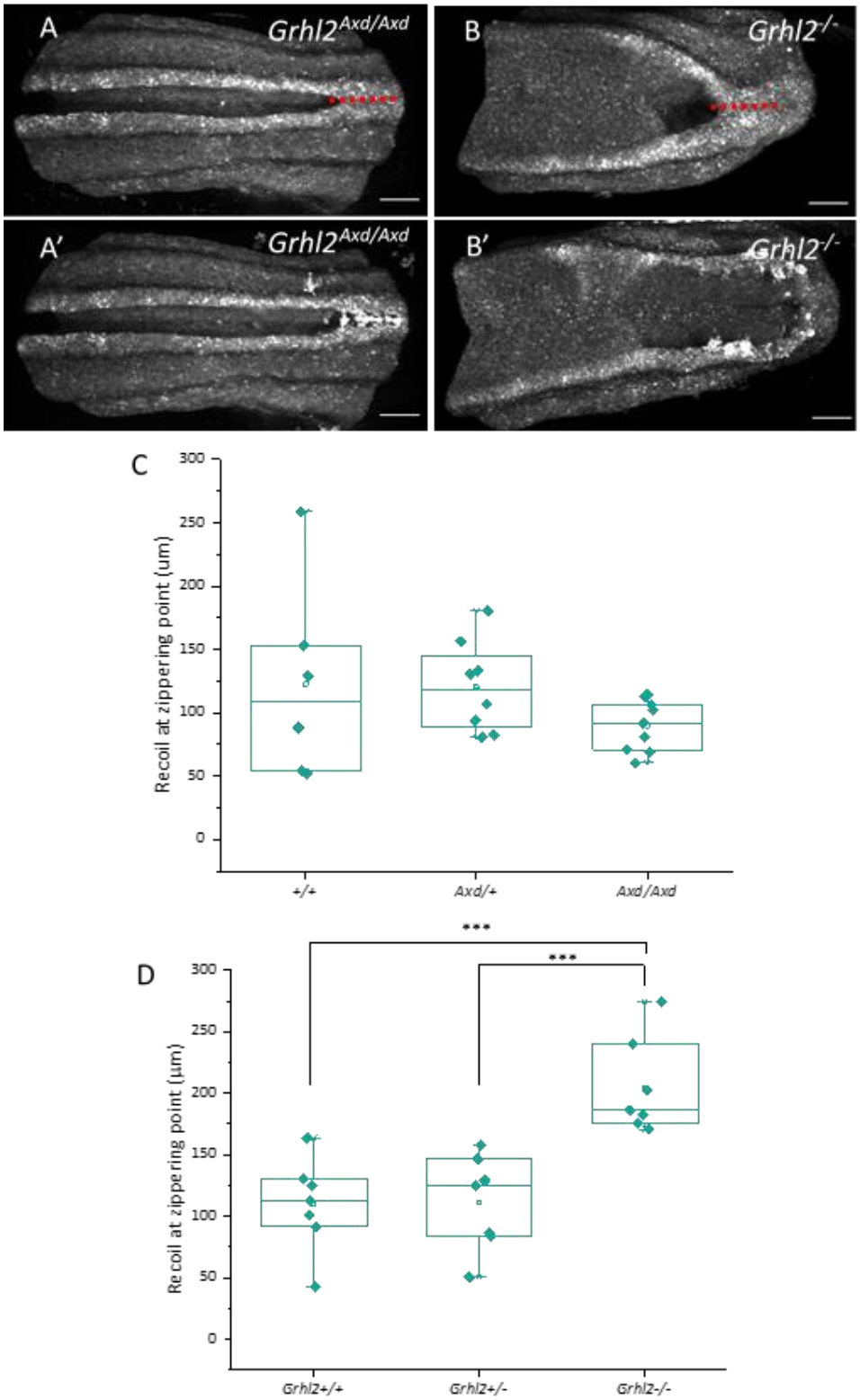

Figure 5.1 – Tissue laser ablation of the ZP in Grhl2 mutant embryos.

Recoil at the ZP is significantly greater in Grhl2$^{-/-}$ embryos than controls and unchanged in Grhl2$^{Axd/Axd}$ embryos. A) Representative image of the PNP of a Grhl2$^{Axd/Axd}$ mutant before (A) and after (A') laser ablation. Red dashed line = site of ablation. B) Representative image of the PNP of a Grhl2$^{-/-}$ mutant before (B) and after (B') laser ablation. Red dashed line = site of ablation. C) Quantification of lateral recoil at the ZP in control, Grhl2$^{Axd/Axd}$ and Grhl2$^{Axd/+}$. D) Quantification of lateral recoil at the ZP in control, Grhl2$^{+/-}$ and Grhl2$^{-/-}$. Grhl2$^{-/-}$ recoil is significantly higher than other genotypes (ANOVA, $p < 3 \times 10^{-4}$). Scale bars = 100 µm.

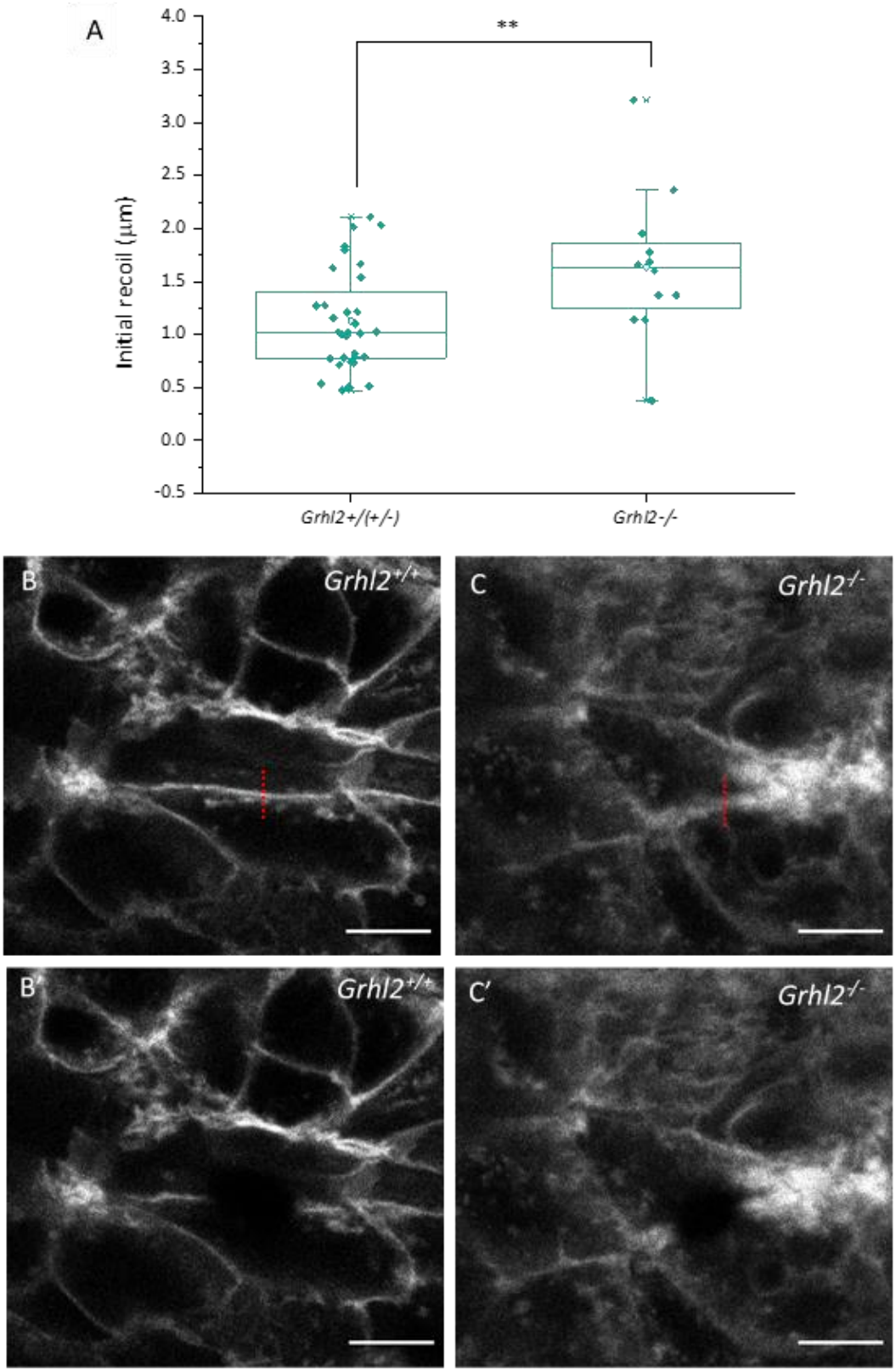

Figure 5.2 – Single cell laser ablation in Grhl2$^{-/-}$ embryos.

Single cell recoil after laser ablation is significantly greater in the SE of Grhl2$^{-/-}$ mutant embryos compared to controls. A) Quantification of initial recoil of individual cell borders after ablation. Mutant embryos showed significantly higher recoil (t-test, $p < 0.009$). B, C) Representative images of single cell laser ablations of a control Grhl2$^{+/+}$ embryo before (B) and after (B') ablation, and a Grhl2$^{-/-}$ mutant before (C) and after (C') ablation. Red dashed line = site of ablation. Scale bars = 10 µm.

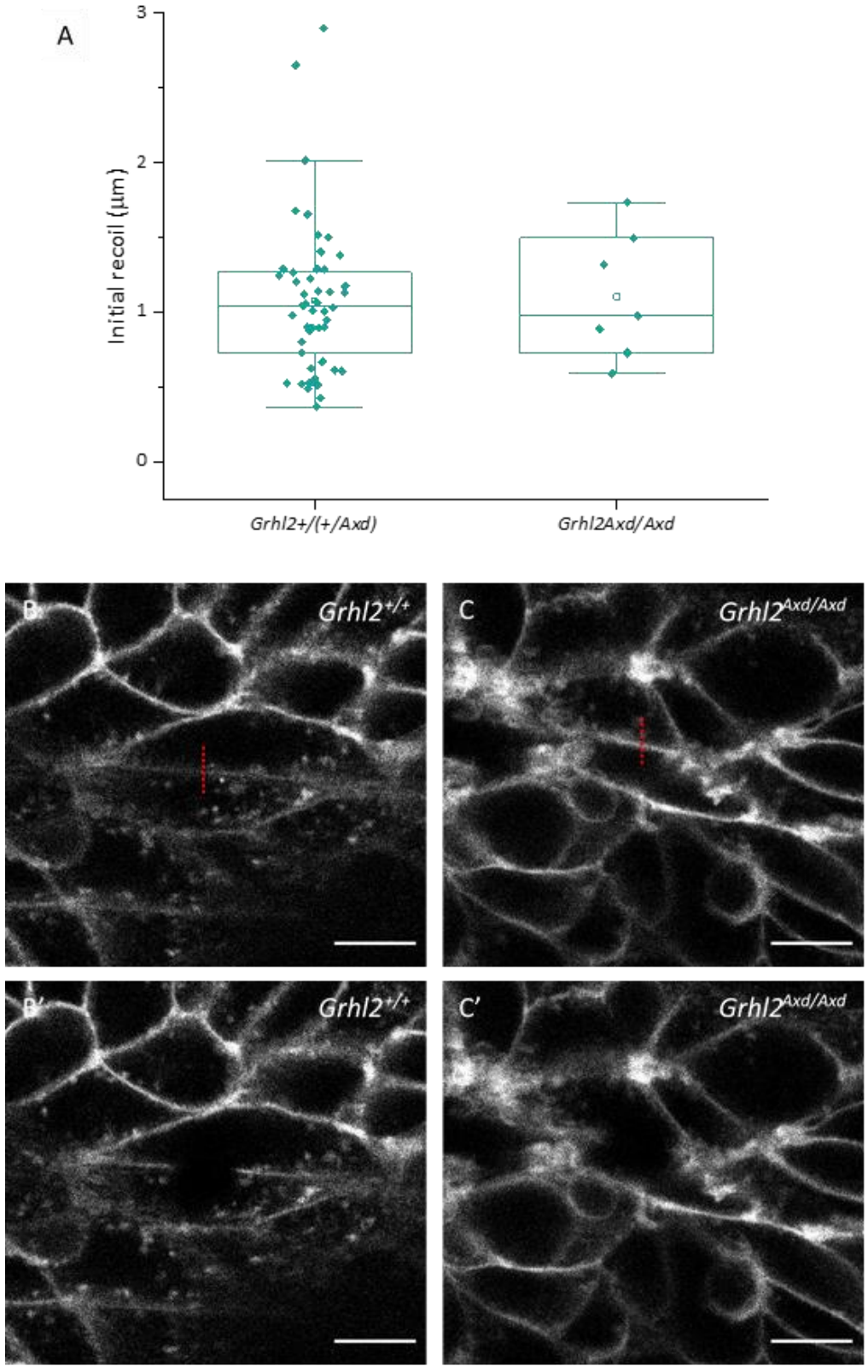

Figure 5.3 – Single cell laser ablation in Grhl2$^{Axd/Axd}$ embryos.

Single cell recoil after laser ablation is comparable in the SE of Grhl2$^{Axd/Axd}$ mutant embryos compared to controls. A) Quantification of initial recoil of the individual cell borders after ablation. There is no significant difference between controls and mutants. B, C) Representative images of single cell laser ablations of a control Grhl2$^{+/+}$ embryo before (B) and after (B') ablation, and a Grhl2$^{Axd/Axd}$ mutant before (C) and after (C') ablation. Red dashed line = site of ablation. Scale bars = 10 µm.

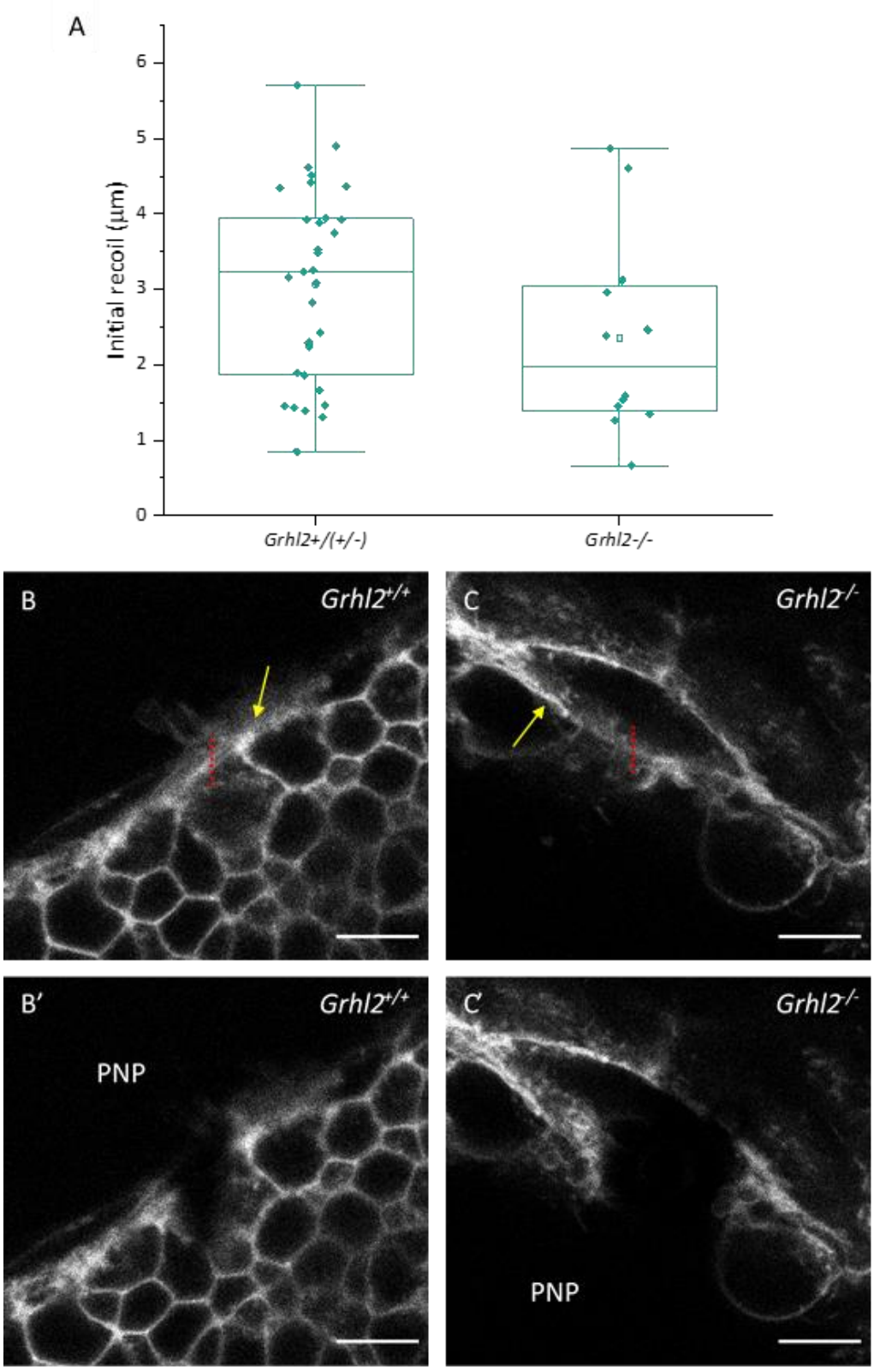

Figure 5.4 – Cable laser ablation in Grhl2$^{-/-}$ embryos.

Cable recoil after laser ablation is comparable in Grhl2$^{-/-}$ mutant embryos compared to controls. *A) Quantification of initial recoil of the cable after ablation. There is no significant difference between controls and mutants. B, C) Representative images of cable laser ablations of a control Grhl2$^{+/+}$ embryo before (B) and after (B') ablation, and a Grhl2$^{-/-}$ mutant before (C) and after (C') ablation. Yellow arrow = cable. Red dashed line = site of ablation. Open PNP is indicated in (B',C'). Scale bars = 10 µm.*

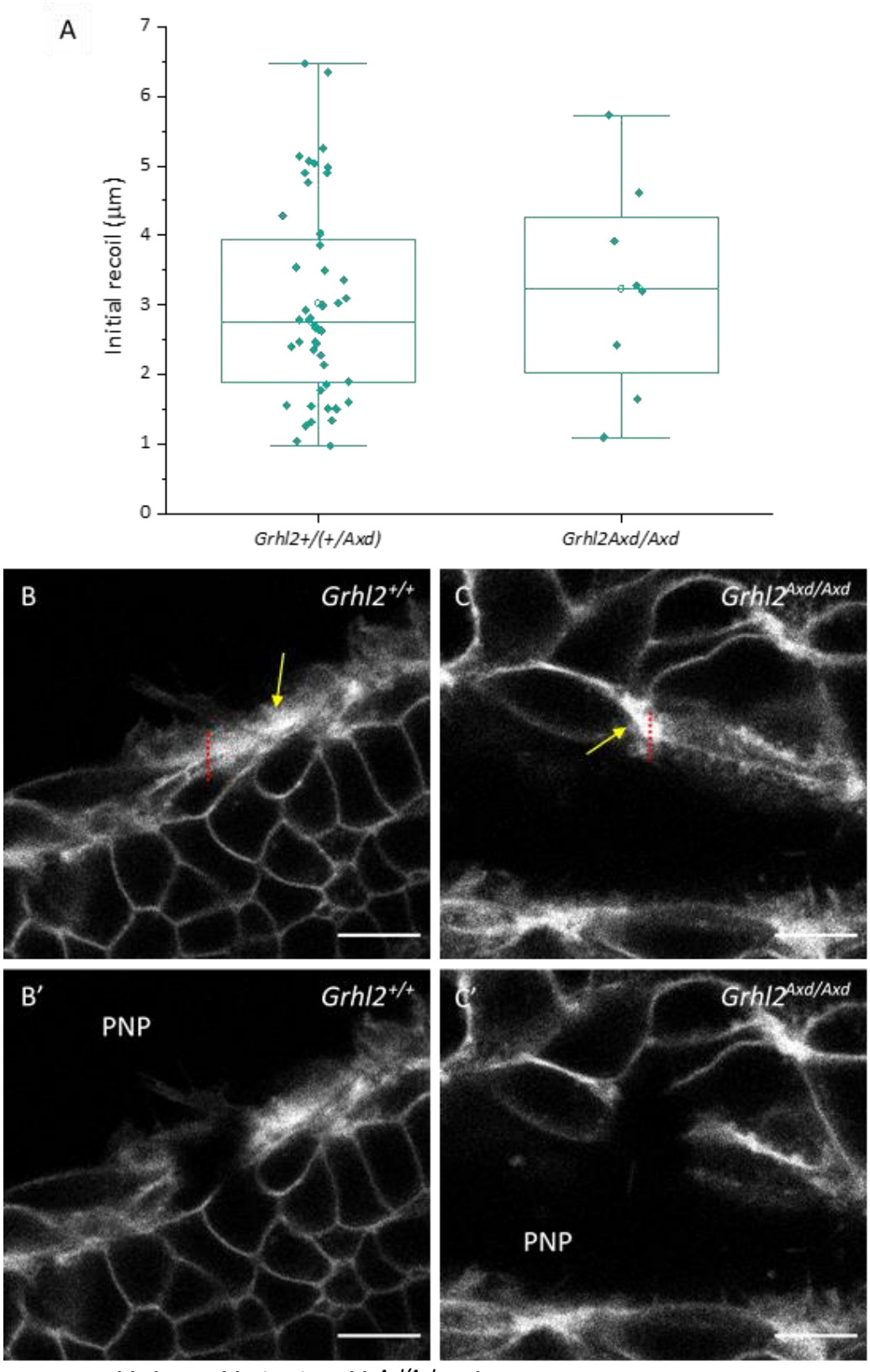

Figure 5.5 – Cable laser ablation in Grhl2$^{Axd/Axd}$ embryos.

Cable recoil after laser ablation is comparable in Grhl2$^{Axd/Axd}$ mutant embryos compared to controls. A) Quantification of initial recoil of the cable after ablation. There is no significant difference between controls and mutants. B, C) Representative images of cable laser ablations of a control Grhl2$^{+/+}$ embryo before (B) and after (B') ablation, and a Grhl2$^{Axd/Axd}$ mutant before (C) and after (C') ablation. Yellow arrow = cable. Red dashed line = site of ablation. Open PNP is indicated in (B',C'). Scale bars = 10 µm.

5.2.2 - *Grhl2*$^{-/-}$ mutants show disrupted YAP nuclear translocation

Given that single cell laser ablation reveals a difference in SE recoil in *Grhl2*$^{-/-}$ mutants, and that cell shape is known to be different in this region (Nikolopoulou et al., 2019), YAP nuclear translocation was analysed. Wild types showed a striking ML gradient of nuclear translocation (ANOVA, $p < 2 \times 10^{-59}$), with YAP fluorescence significantly higher in midline nuclei compared to laterally, consistent with the same experiment in Chapter 3.2.2. Interestingly, this gradient is significantly disrupted in *Grhl2*$^{-/-}$ mutants (f test, $p < 0.05$), although the negative gradient was still present (ANOVA, $p < 7 \times 10^{-11}$) (Figure 5.6). The SR was also analysed, and although wild types showed a negative gradient significantly different from 0 (ANOVA, $p < 8 \times 10^{-10}$), this was less significant than the gradients in both wild types and mutants at the ZP (Figure 5.7). The negative gradient in *Grhl2*$^{-/-}$ mutants at the SR was not significantly different from 0 (ANOVA, $p > 0.05$), and was significantly different to wild types (f test, $p < 0.05$).

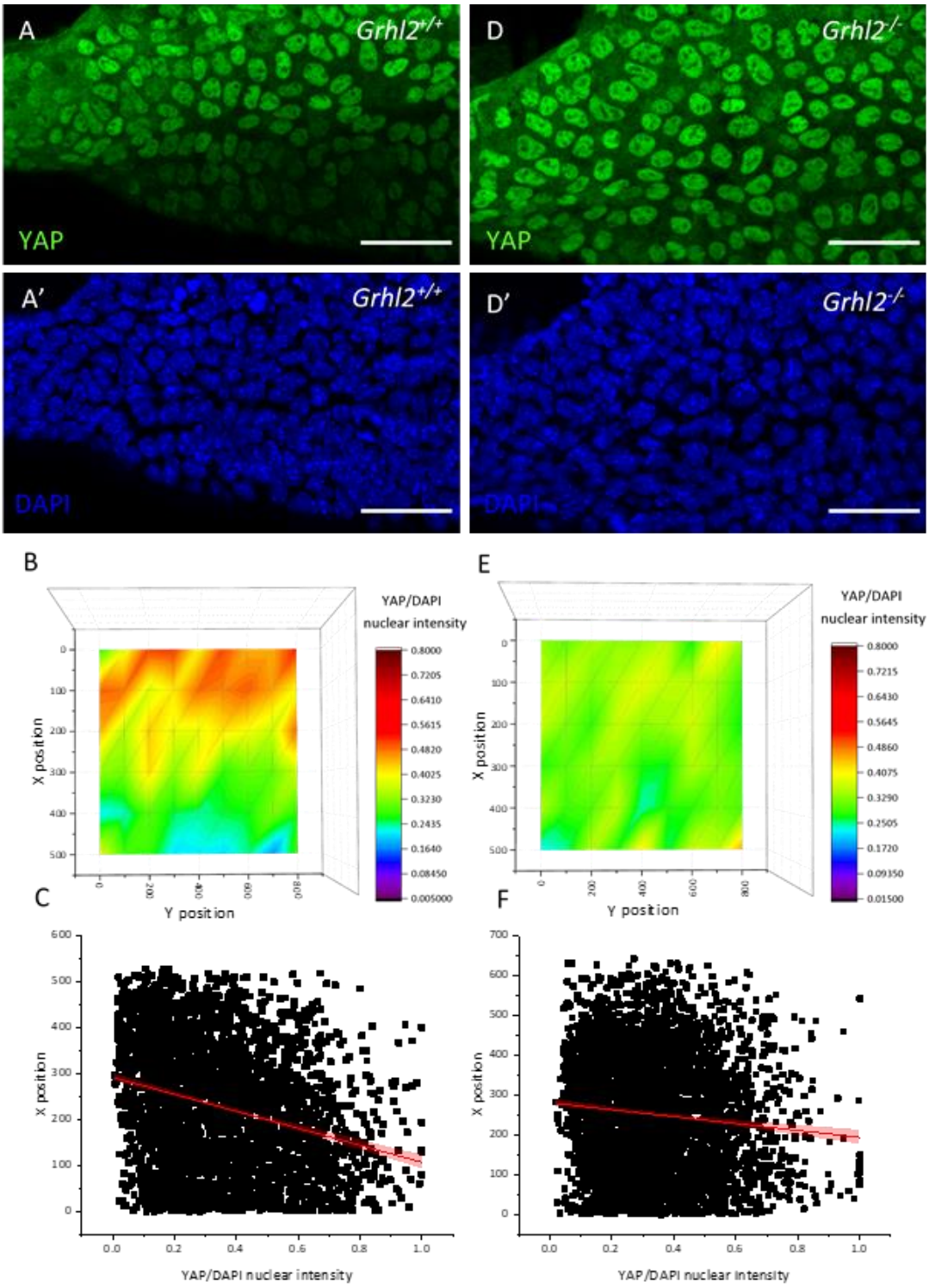

Figure 5.6 – Spatial analysis of YAP nuclear translocation in Grhl2$^{-/-}$ embryos.

The high-low ML gradient of YAP nuclear translocation is lost in Grhl2$^{-/-}$ mutants. A, D) Representative image of PNP stained with YAP (A, D) and DAPI (A', D') in E9.5 wild type (A) and Grhl2$^{-/-}$ (D) embryos. B, E) Heat map showing wild type (B) and mutant (E) YAP/DAPI nuclear intensity along the ML axis, with the midline X position = 0. C, F) Scatter plot showing the YAP/DAPI nuclear intensity for individual nuclei for wild type (C) and mutant (F), with the midline X position = 0. Both slopes are significantly different from 0 (C = ANOVA, $p < 2 \times 10^{-59}$; F = ANOVA, $p < 7 \times 10^{-11}$). The difference in slope is significant (f test, $p < 0.05$). Scale bars = 50 µm.

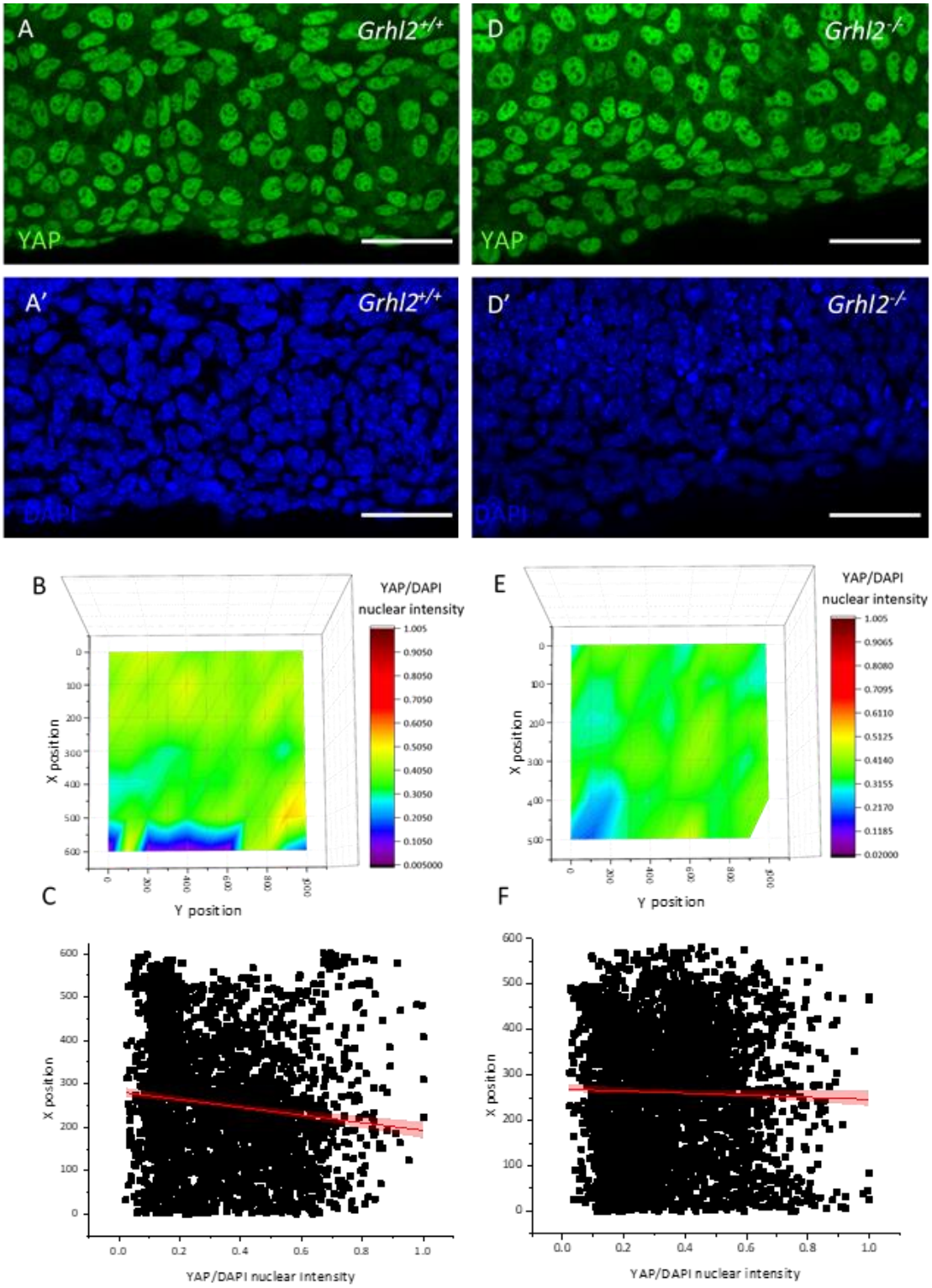

Figure 5.7 – Somite region spatial analysis of YAP nuclear translocation in Grhl2$^{-/-}$ embryos.

No ML gradient of YAP nuclear translocation is found in the SE over the SR in wild type or Grhl2$^{-/-}$ mutant embryos. A, D) Representative image of PNP stained with YAP (A, D) and DAPI (A', D') in E9.5 wild type (A) and Grhl2$^{-/-}$ (D) embryos. B, E) Heat map showing wild type (B) and mutant (E) YAP/DAPI nuclear intensity along the ML axis, with the midline X position = 0. C, F) Scatter plot showing the YAP/DAPI nuclear intensity for individual nuclei for wild type (C) and mutant (F), with the midline X position = 0. The slope in WT is significantly different from 0 (ANOVA, $p < 8 \times 10^{-10}$) while the mutant gradient is not different from 0 (ANOVA, $p > 0.05$). The difference in gradient is significant (f test, $p < 0.05$). Scale bars = 50 µm.

To investigate whether the disrupted gradient at the ZP was due to increased YAP nuclear translocation, YAP intensity was compared between the nuclei and the cytoplasm (see Chapter 2.8.3). This showed considerable variation in wild types but not in mutants, which could potentially be explained by the range of stages of embryos (as defined by number of somites) within the groups. Indeed, when nuclear/cytoplasmic intensity was compared in relation to number of somites, there was a gradual decrease in the difference between nuclear and cytoplasmic intensity with increasing somite number in wild types but no correlation in mutants (Figure 5.8). There was no significant difference between the gradients (f test, $p > 0.05$).

This change in nuclear/cytoplasmic intensity could be due to overall changes in expression or changes in the levels of phosphorylated YAP, which would prevent nuclear translocation of the protein. A western blot was carried out to analyse the levels of total and phosphorylated YAP in the caudal region of wild type and *Grhl2*$^{-/-}$ E9.5 embryos, over a range of somites (Figure 5.9A). There was a trend towards increased YAP and pYAP relative to GAPDH in mutant *Grhl2*$^{-/-}$ embryos compared to control *Grhl2*$^{+/+}$ (Figure 5.9B, C). There was also a trend towards increased pYAP relative to total YAP in knockouts, suggesting that YAP transcriptional activity is lower in mutants compared to controls (Figure 5.9D).

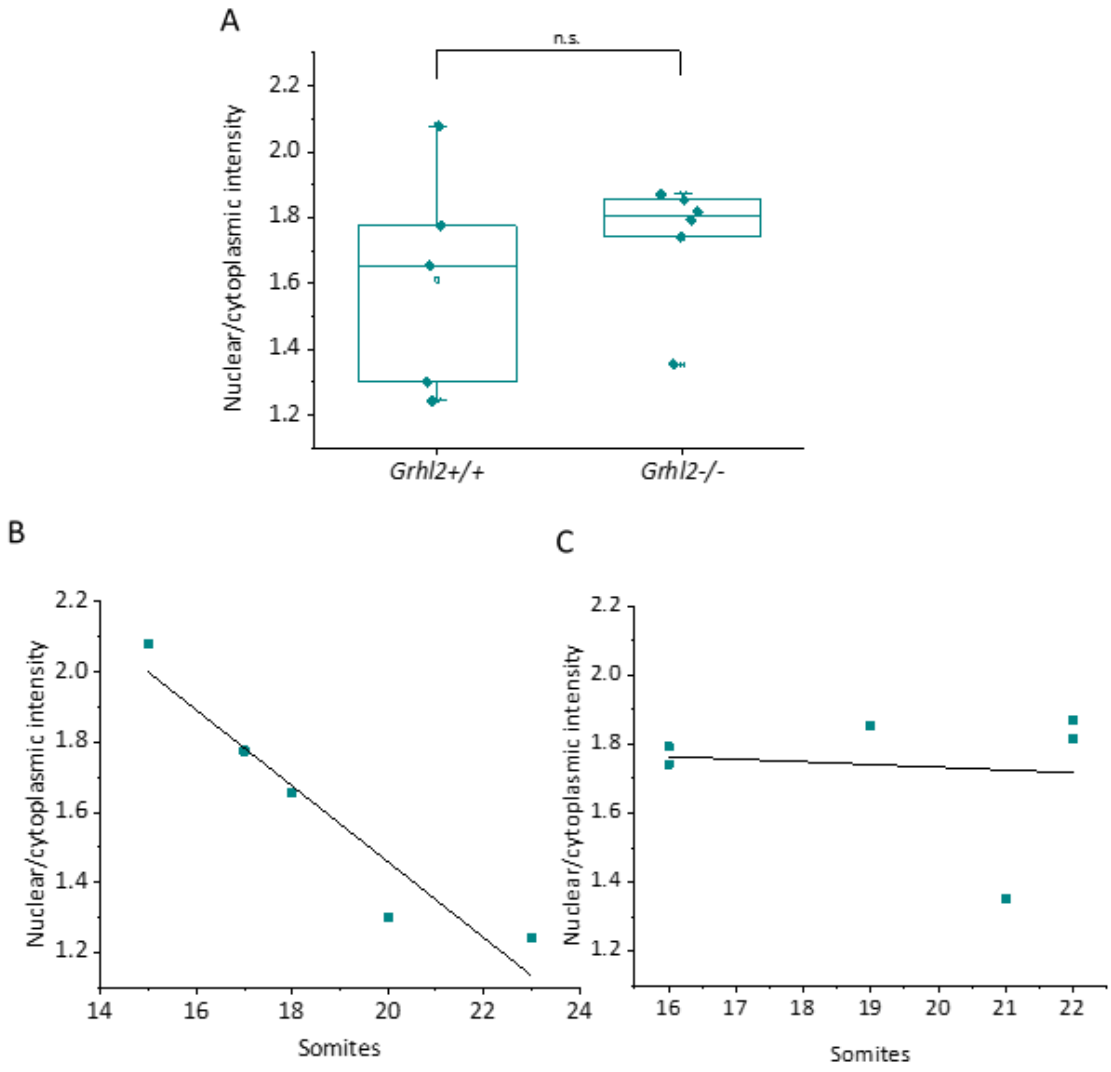

Figure 5.8 – Analysis of nuclear and cytoplasmic YAP levels by somite stage.

Nuclear/cytoplasmic YAP intensity decreases with increasing somite stage in wild types but stays high in Grhl2$^{-/-}$ mutants. A) Nuclear/cytoplasmic YAP is highly varied within the wild type group but not Grhl2$^{-/-}$ mutants. There is no significant difference between groups (two-sample t-test, $p > 0.05$). B) Nuclear/cytoplasmic YAP intensity decreases with increasing somite stage in wild type embryos. The negative slope is significantly different from 0 (ANOVA, $p < 0.02$) C) Nuclear/cytoplasmic YAP intensity does not change with somite stage in Grhl2$^{-/-}$ mutants (ANOVA, $p > 0.05$). The difference in slope is not significantly different (f test, $p > 0.05$).

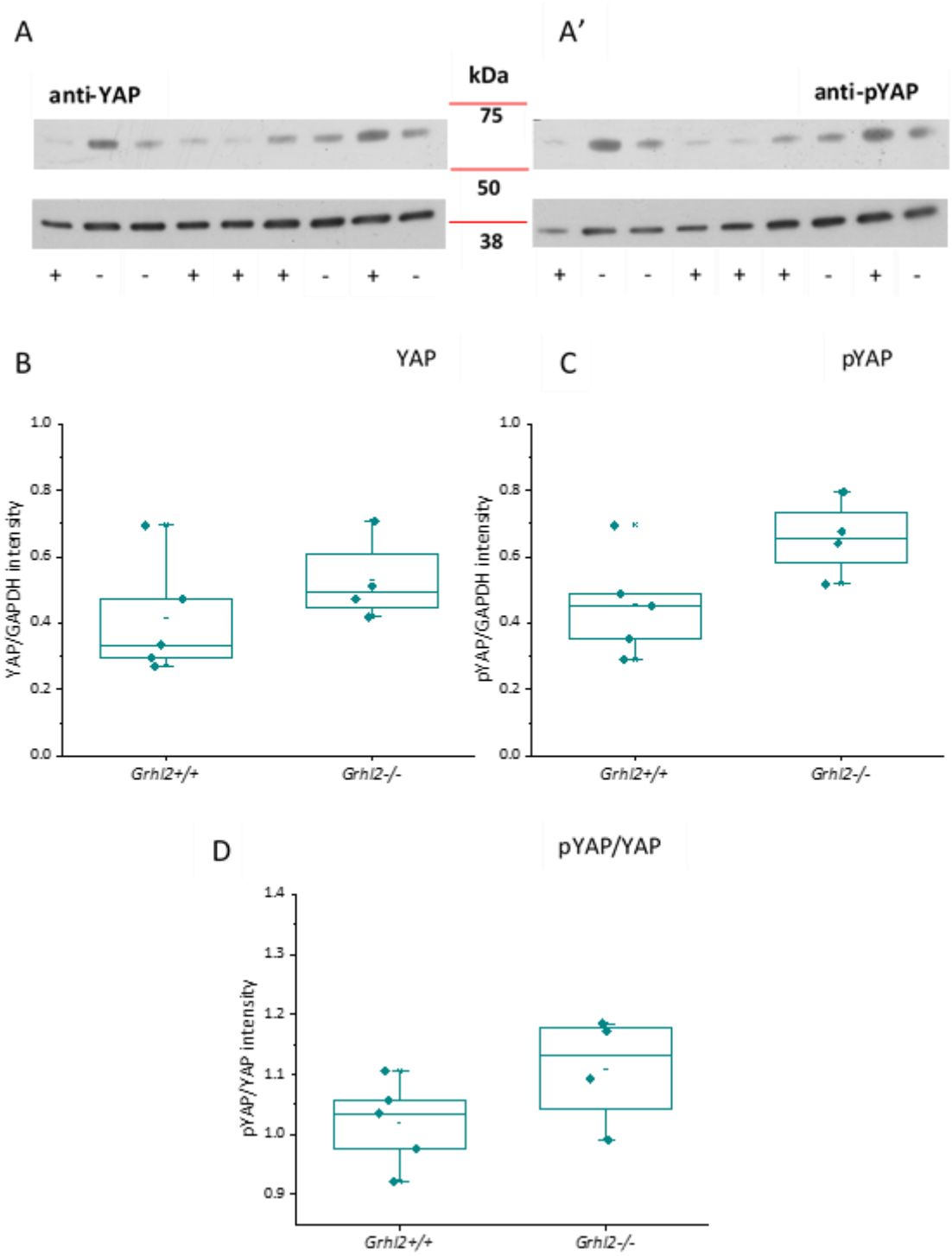

Figure 5.9 – Western blot analysis of total and phosphorylated-YAP levels.

There is a trend towards increased global and nuclear levels of YAP protein in the caudal E9.5 embryo. A) Representative western blots of YAP (A) and pYAP (A'), showing genotypes Grhl2$^{+/+}$ (+) and Grhl2$^{-/-}$ (-). B) There is a trend towards increased total YAP levels (normalised to GAPDH) in the mutant Grhl2$^{-/-}$ embryos compared to controls. C) There is a trend towards increased pYAP levels (normalised to GAPDH) in the mutant Grhl2$^{-/-}$ embryos compared to controls. D) There is a trend towards increased pYAP levels relative to total YAP in the mutant Grhl2$^{-/-}$ embryos compared to controls.

5.2.3 - Abnormal *Grhl3* expression does not disrupt SE biomechanics

The mechanisms behind failed NTC in *Grhl3* mutants are unknown. To analyse the potential biomechanical mechanisms, two different crosses were used. First, *ct/ct*$^{TgGrhl3/0}$ mice were crossed to generate *ct/ct* and *ct/ct*$^{TgGrhl3/TgGrhl3}$ embryos. *ct/ct*$^{TgGrhl3/0}$ hemizygous embryos, which are c*t/ct* mice harbouring a single copy of a *Grhl3* BAC, were analysed as the control group, as they do not show NTDs (Gustavsson et al., 2007). *ct/ct*$^{TgGrhl3/TgGrhl3}$ embryos have two copies of the *Grhl3* BAC and overexpress *Grhl3*, and ~68% of embryos develop spina bifida (De Castro et al., 2018a). Although the mechanism behind failed closure in *ct/ct* embryos is already known, they were included in all analyses as ablation experiments were performed before genotyping. The second cross was between *Grhl3*$^{f/-}$ embryos, to generate *Grhl3*$^{f/f}$ controls and *Grhl3*$^{-/-}$ knockout embryos.

Cell shape was analysed in both crosses in the SE rostral to the PNP using the same method as in Chapters 3 and 4. Cell shape revealed the midline elongation characteristic of C57BL/6 embryos in all genotypes (Figure 5.10) except *Grhl3*$^{-/-}$. The midline elongation was not observed in all *ct/ct* and *ct/ct*$^{TgGrhl3/TgGrhl3}$ samples, but appeared to be even more distinct in some *ct/ct*$^{TgGrhl3/TgGrhl3}$ samples, showing that the overexpression of *Grhl3* causes highly variable phenotypes (Figure 5.11.) *Grhl3*$^{-/-}$ embryos were very abnormal, with small, irregularly shaped cells along the midline, abnormal ZO-1 staining and less smooth cell borders (Figure 5.12A, B). The smaller midline cells could also explain a clear midline 'streak' of ZO-1, due to a higher density of cell borders (Figure 5.12A, B). It is worth noting that in older embryos (17 - 19 somites), this midline 'streak' was not observed, although the uneven ZO-1 staining and smaller midline cells persisted (Figure 5.12C). The expression of E-cadherin appeared normal in all genotypes (Figure 5.13) except *Grhl3*$^{-/-}$, which showed distinct clusters of intracellular E-cadherin expression (Figure 5.14).

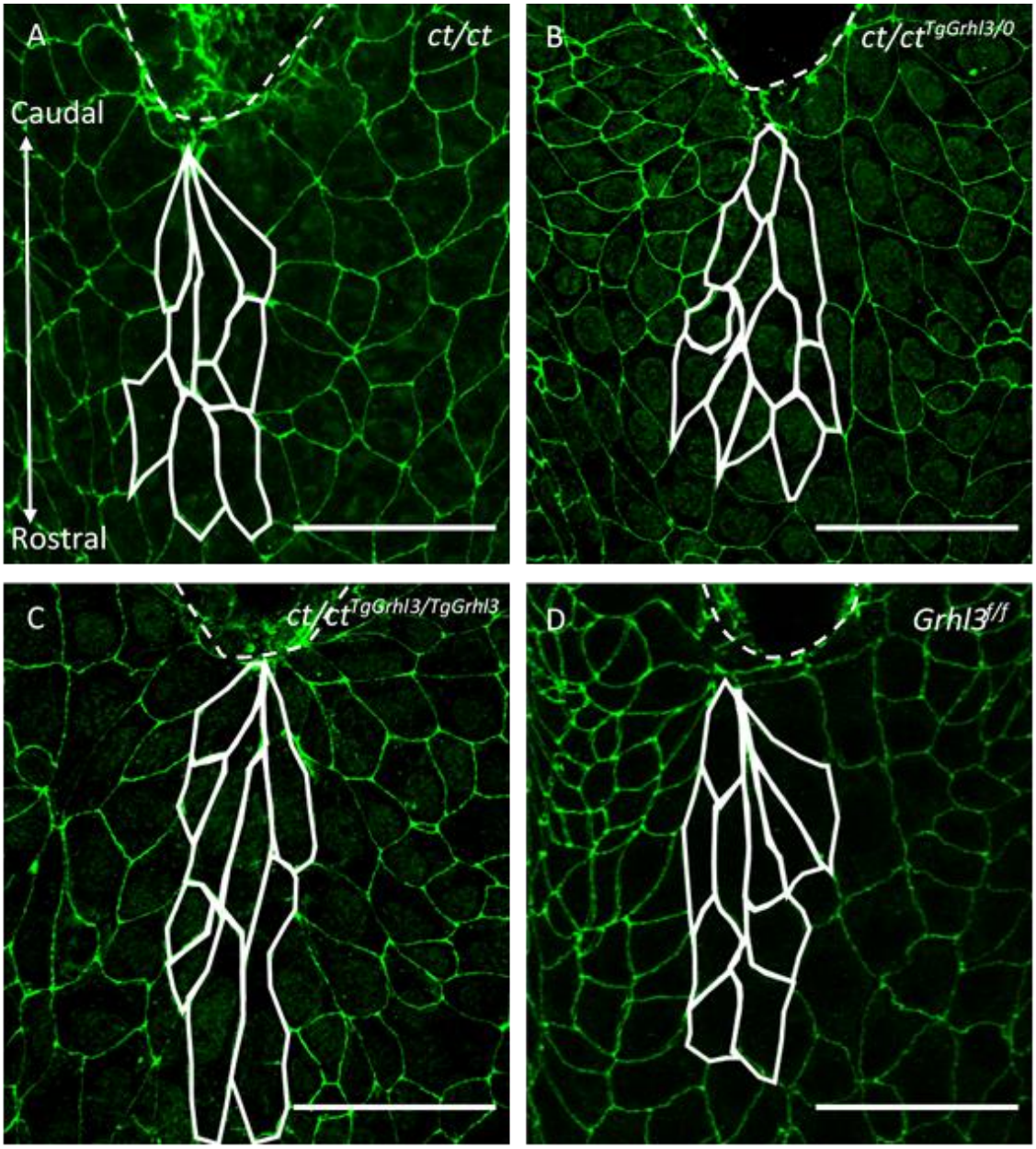

Figure 5.10 – Normal SE cell shape in Grhl3 mutants.

Representative whole mount ZO-1 immunofluorescence staining of the E9.5 spinal NT in the recently closed SE from the dorsal view, showing characteristic RC elongation of cells. Genotypes shown are A) ct/ct, B) ct/ct$^{TgGrhl3/0}$, C) ct/ct$^{TgGrhl3/TgGrhl3}$ and D) Grhl3$^{f/f}$. White dashed line = outline of PNP. Rostral-caudal indicated in (A). Scale bars = 50 µm.

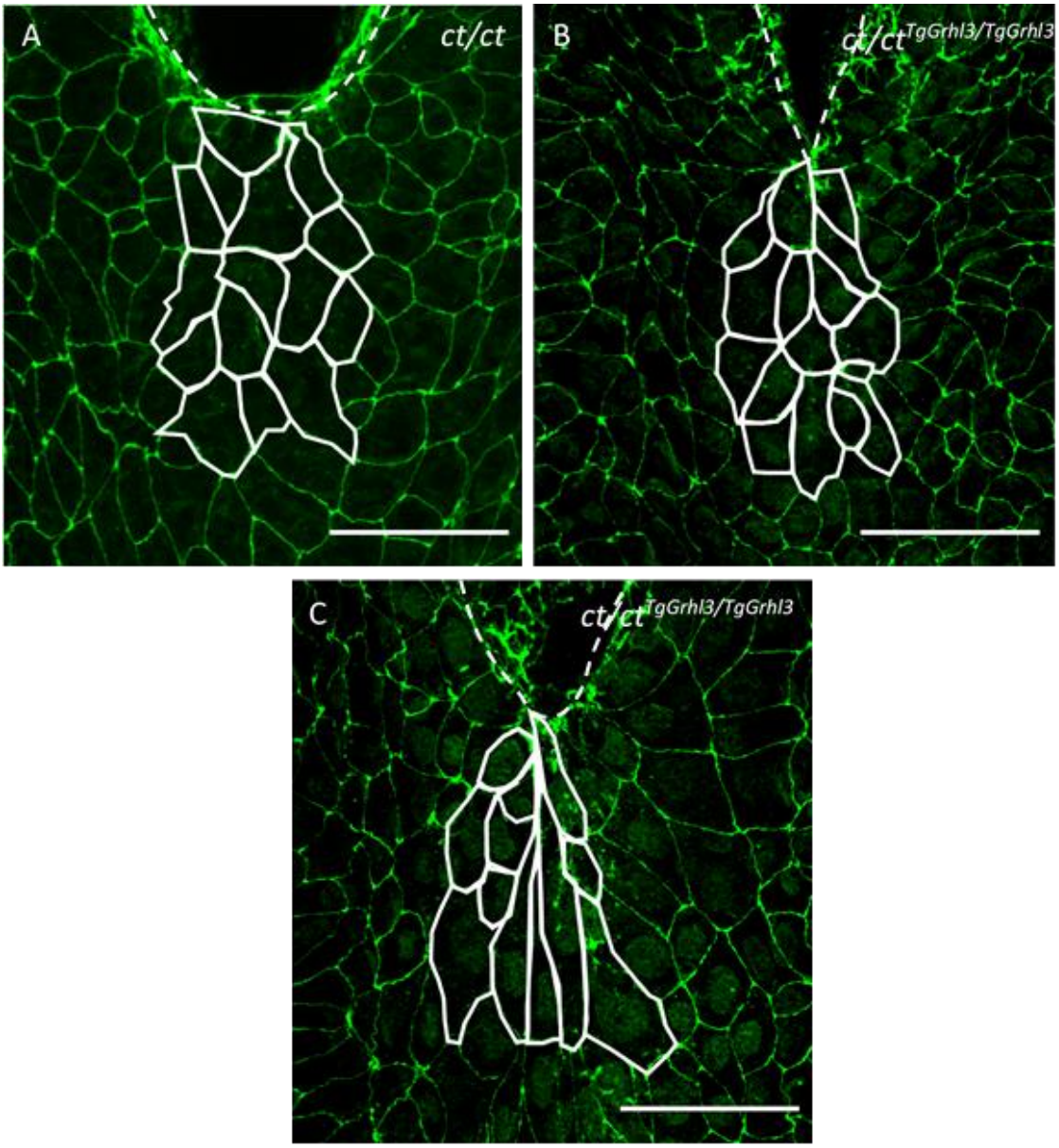

Figure 5.11 – Abnormal SE cell shape in Grhl3 mutants.

Representative ZO-1 immunofluorescence staining of E9.5 SE showing variation in cell shape within mutant genotypes. Some ct/ct (A) and ct/ct$^{TgGrhl3/TgGrhl3}$ (B) samples do not show RC elongation, while some ct/ct$^{TgGrhl3/TgGrhl3}$ show a more extreme elongation. White dashed line = outline of PNP. Scale bars = 50 µm.

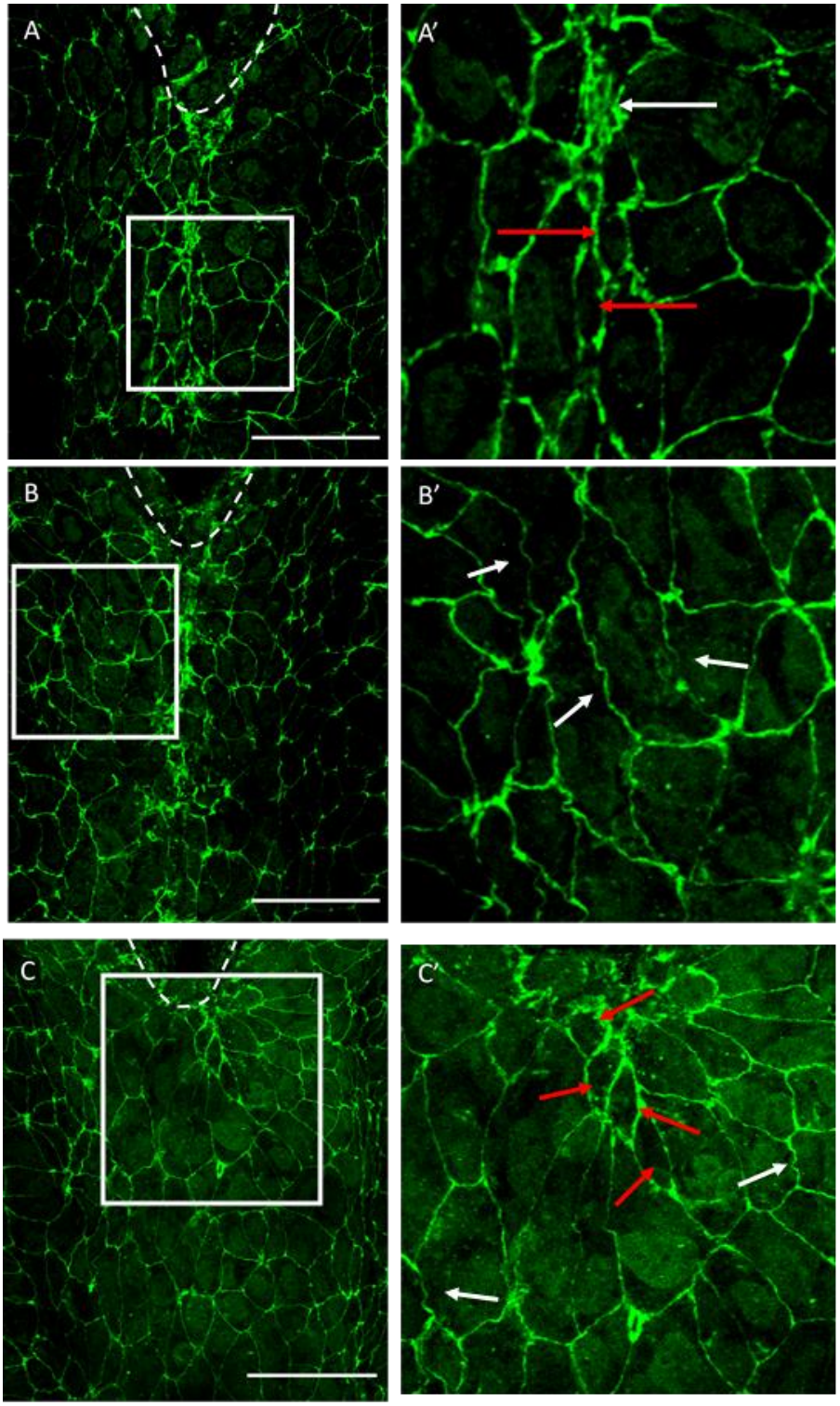

Figure 5.12 – Abnomal ZO-1 staining in Grhl3$^{-/-}$ mutants.

Representative ZO-1 immunofluorescence staining of E9.5 Grhl3$^{-/-}$ SE showing abnormal ZO-1 staining and cell shape. Grhl3$^{-/-}$ embryos between 14 - 16 somites (A, B) show an abnormal accumulation of ZO-1 along the midline (white arrow, A'), abnormally small cells (red arrows, A') and irregular cell borders (white arrows, B'). The midline accumulation is lost in samples >17 somites, however irregular cell borders (white arrows, C') and small cells (red arrows, C') are still observed. White dashed line = outline of PNP. Scale bars = 50 µm.

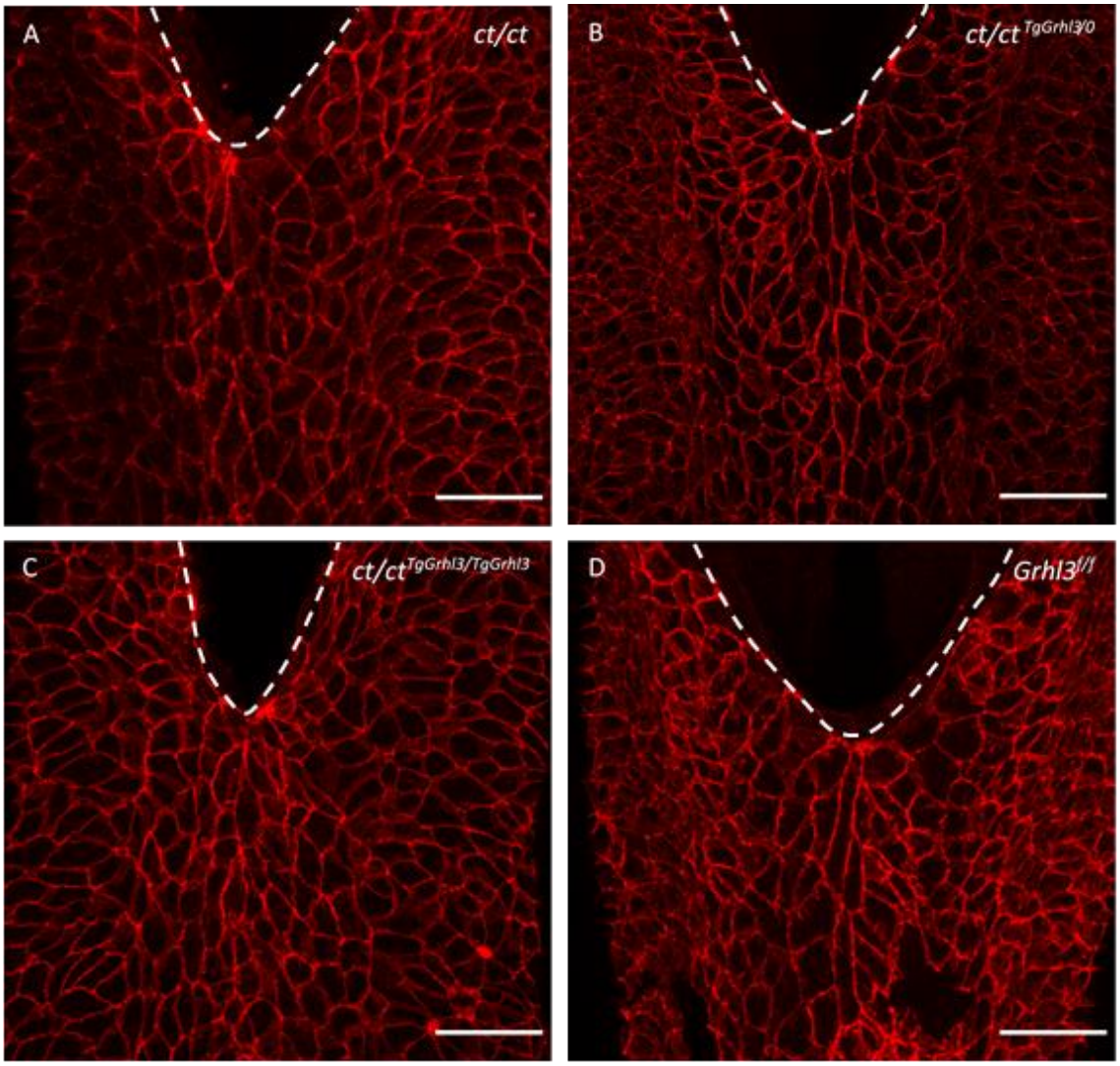

Figure 5.13 – Normal E-cadherin staining in Grhl3 mutants.

Representative E-cadherin immunofluorescence staining of E9.5 SE showing normal membrane staining. Genotypes shown are A) ct/ct, B) ct/ct$^{TgGrhl3/0}$, C) ct/ct$^{TgGrhl3/TgGrhl3}$ and D) Grhl3$^{f/f}$. White dashed line = outline of PNP. Scale bars = 50 µm.

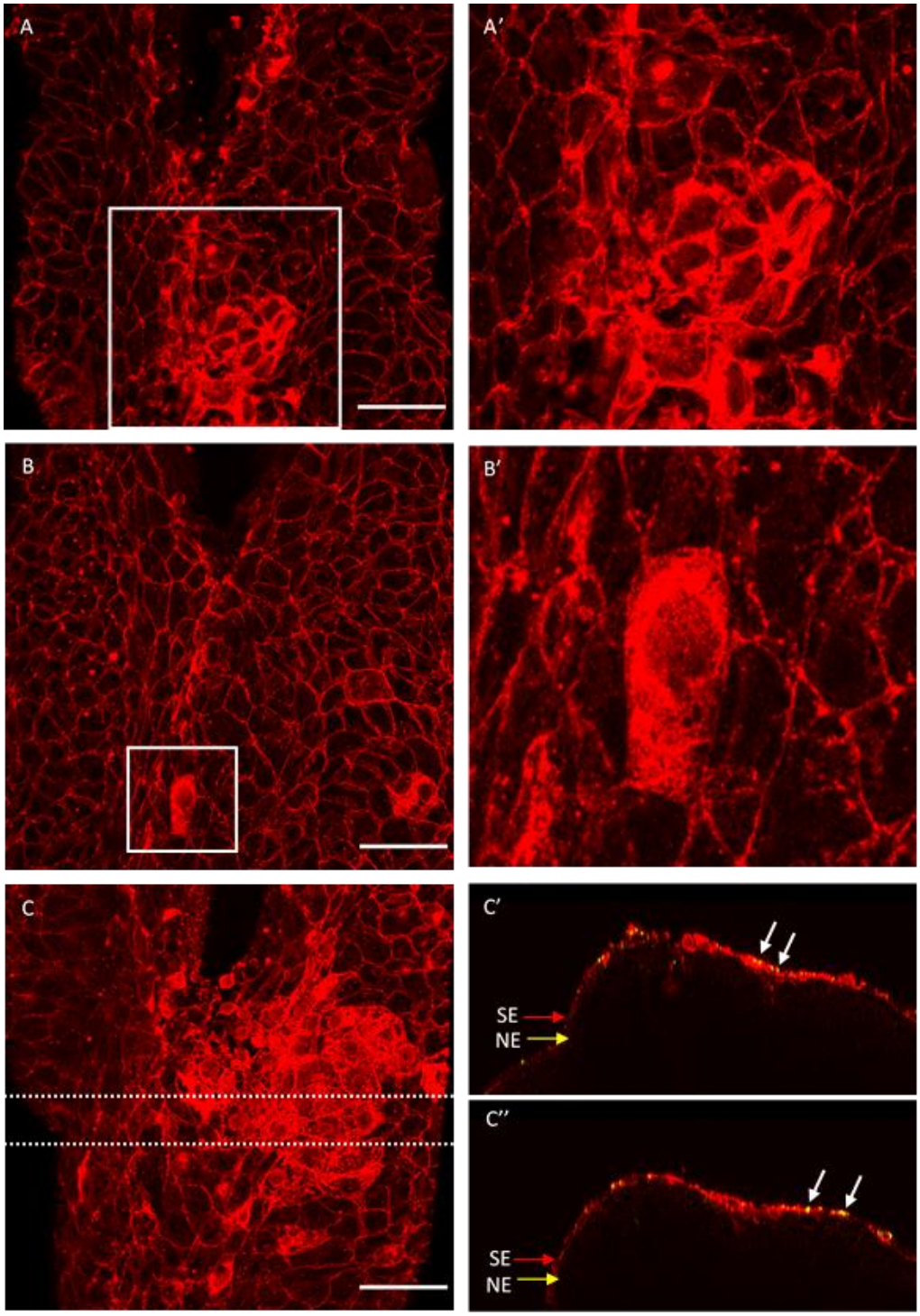

Figure 5.14 - Abnormal E-cadherin staining in Grhl3$^{-/-}$ mutants.

Representative E-cadherin immunofluorescence staining of E9.5 Grhl3$^{-/-}$ SE showing abnormal intracellular 'clusters'. Grhl3$^{-/-}$ embryos contain clusters of high E-cadherin, with membrane staining much brighter than in wild type (A, A') and with some cells showing intracellular staining (B,B'). Image reslice (C, C' = top cross-section , C'' = bottom cross-section) reveals that these clusters are within the SE and not extruding cells/amnion, as shown by colocalization with ZO-1 (C', C'', yellow dots indicated by white arrows). SE and NE indicated by red and yellow arrows respectively. Scale bars = 50 µm.

To further analyse cell elongation in *Grhl3* mutants, the aspect ratio of SE along the RC midline was analysed. Mutant midline SE cells did not have a significantly different aspect ratio compared to controls in either cross, however there was a trend towards a reduced aspect ratio in loss-of-function mutants (*ct/ct* and *Grhl3*$^{-/-}$) and an increased aspect ratio in *ct/ct*$^{TgGrhl3/TgGrhl3}$ embryos (Figure 5.15A, B), consistent with the exaggerated elongation phenotype seen in some overexpression mutants (Figure 5.11C). Interestingly, when the controls were compared to the aspect ratio in C57BL/6 embryos (Chapter 3), there was significant variation between the groups (Figure 5.15C, ANOVA, $p < 0.04$). Post-hoc mean comparisons (Tukey and Bonferroni tests) did not identify a significant pair-wise difference, which is likely due to low statistical power.

To further explore possible changes in midline cell shape in these mutants, a larger region of SE cells was analysed, consisting of lateral regions on both sides of the midline (see Chapter 2.8.2 for method). As expected, *Grhl3*$^{f/f}$ control embryos showed cells with a significantly higher aspect ratio along the midline compared to laterally (Figure 5.16D, t-test, $p < 0.003$), however *ct/ct*$^{TgGrhl3/0}$ midline and lateral cells were not significantly different (Figure 5.16B). Interestingly, *ct/ct*$^{TgGrhl3/TgGrhl3}$ embryos showed the characteristic midline elongation typical of wild types (Figure 5.16C, t-test, $p < 0.01$). Mutant *ct/ct* and *Grhl3*$^{-/-}$ embryos did not show a significantly different aspect ratio between midline and lateral cells (Figure 5.16A, E).

Analysis of additional cell shape parameters showed that there was no significant difference between wild types and mutants in midline cell orientation, area or circularity (Figure 5.17). There was a trend towards a lower area of midline *Grhl3*$^{-/-}$ cells compared to wild types, consistent with the presence of abnormally small cells (Figure 5.17D). When the larger region including the midline and lateral cells was analysed, there were also no significant differences in any of these parameters between genotypes (data not shown).

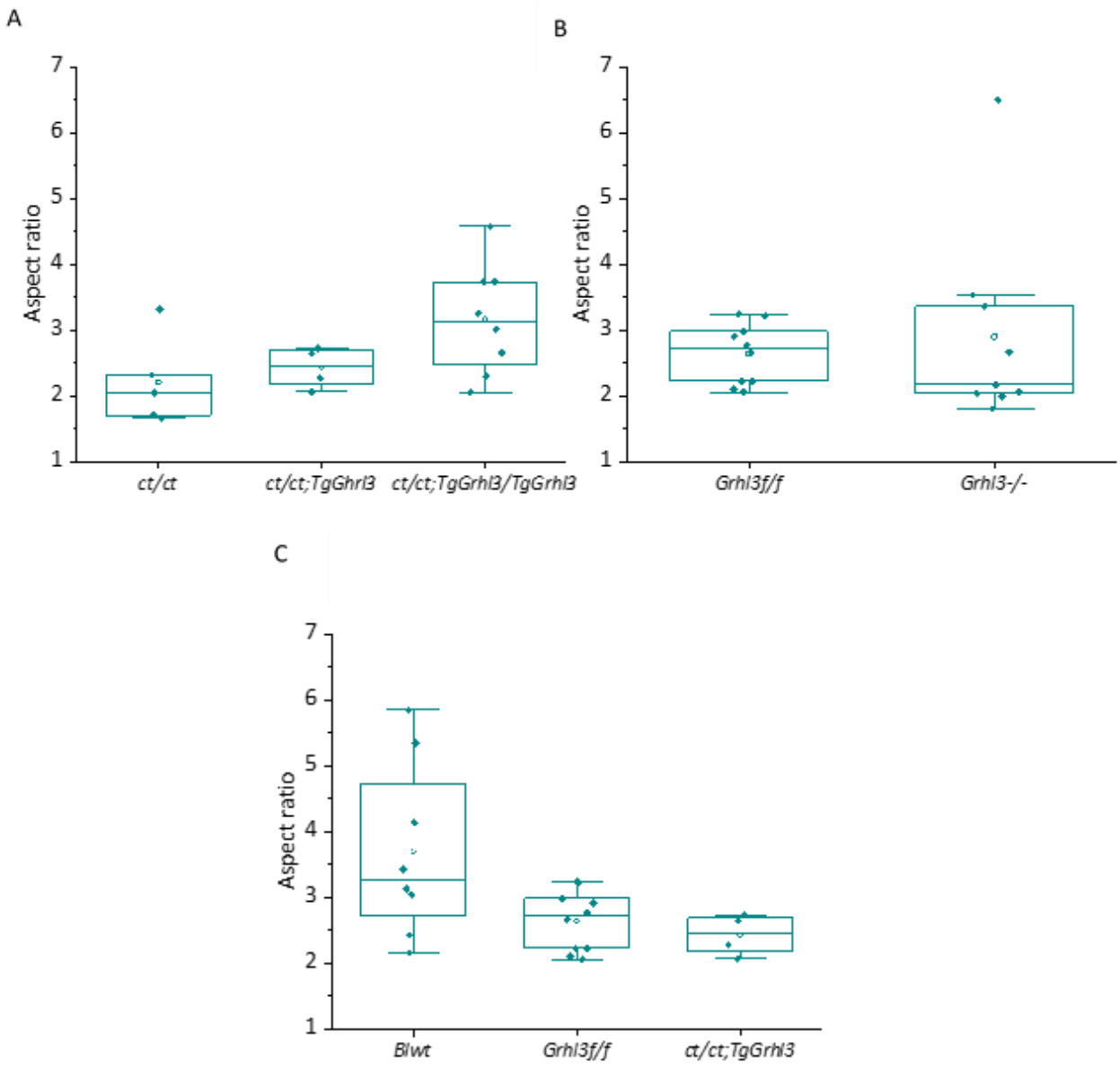

Figure 5.15 – SE cell shape analysis in Grhl3 mutants.

Midline aspect ratio of SE cells is not significantly affected by Grhl3 expression levels. A) There is no significant difference in midline SE aspect ratio between controls (ct/ct$^{TgGrhl3/0}$) and mutants, although there is a trend towards a lower aspect ratio in ct/ct and a higher aspect ratio in ct/ct$^{TgGrhl3/TgGrhl3}$. B) There is no significant difference in midline SE aspect ratio between Grhl3$^{f/f}$ controls and Grhl3$^{-/-}$ embryos. C) There is a significant difference between wild type strains (ANOVA, $p < 0.04$), however post hoc mean analysis did not identify the significantly different groups.

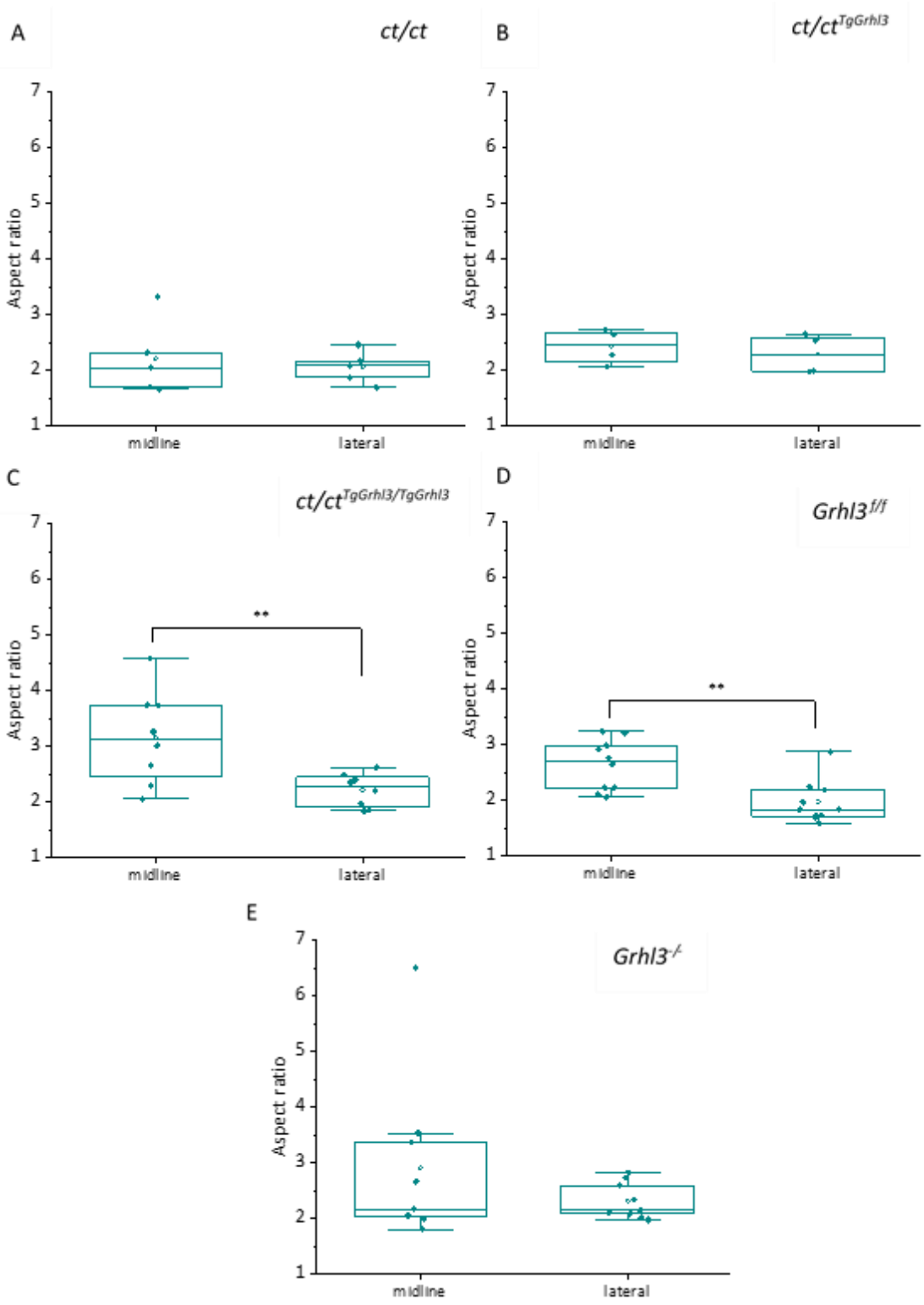

Figure 5.16 – Midline/lateral cell shape comparison in Grhl3 mutants.

The midline SE elongation compared to lateral cells is lost in some Grhl3 mutants. A,B,E) There is no significant difference between midline and lateral AR in ct/ct (A), ct/ct$^{TgGrhl3/0}$ (B) and Grhl3$^{-/-}$ embryos. C,D) Midline SE cells have a significantly higher AR compared to lateral in ct/ct$^{TgGrhl3/TgGrhl3}$ (C, t-test, $p < 0.01$) and Grhl3$^{f/f}$ (D, t-test, $p < 0.003$).

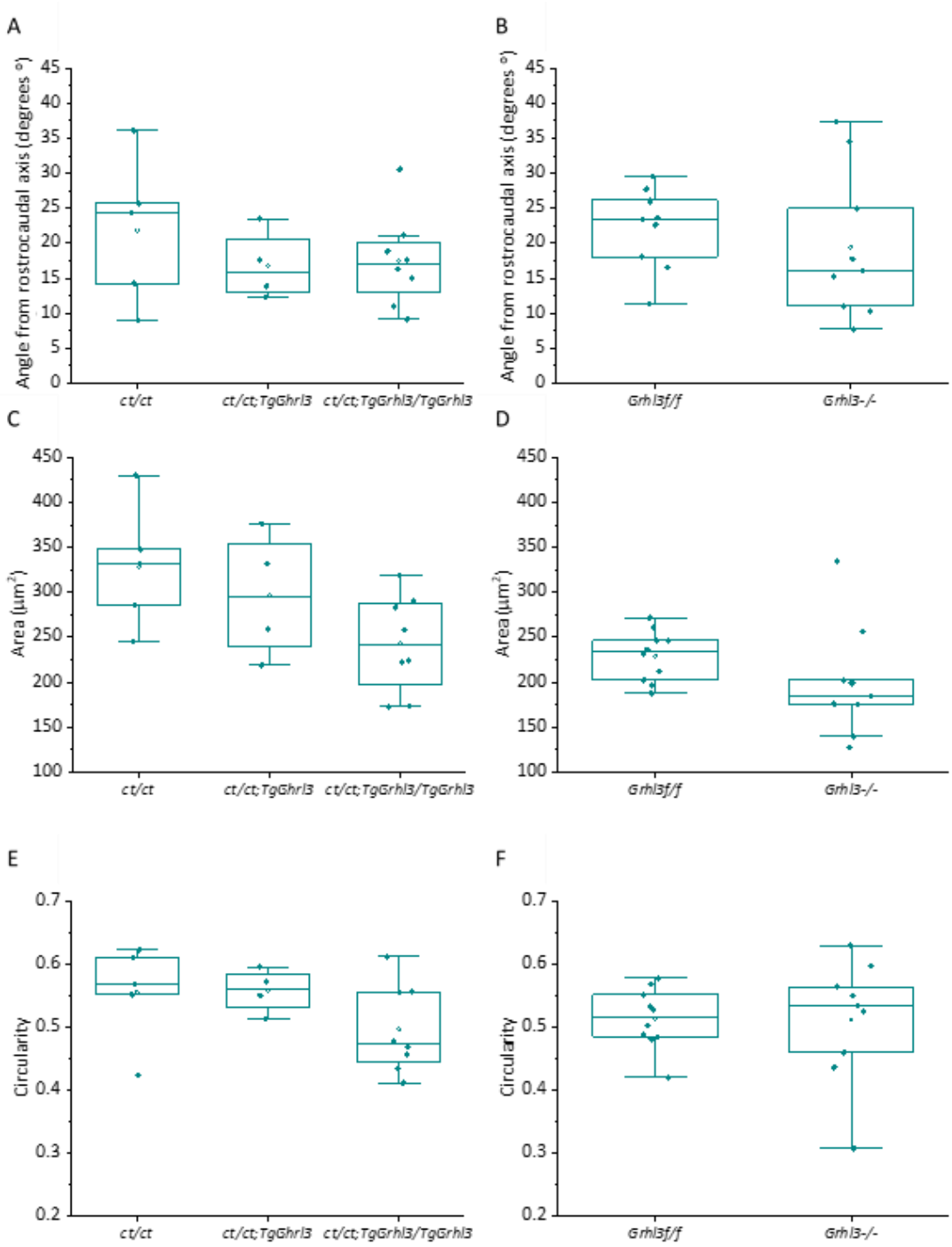

Figure 5.17 – Midline SE cell shape parameters analysis in Grhl3 mutants.

Midline SE orientation (A,B), area (C,D) and circularity (E,F) is comparable between genotypes.

Myosin heavy chain (MHC) and F-actin staining appeared normal in most *ct/ct* and *ct/ct*$^{TgGrhl3/TgGrhl3}$ embryos compared to controls (Figures 5.18, 5.19), showing clear accumulation along the neural folds where the actomyosin cable is found (white arrows). However, 1/5 *ct/ct* samples did not have a visible cable (Figure 5.19B), despite showing otherwise normal actin staining, and in 2/4 *ct/ct*$^{TgGrhl3/TgGrhl3}$ samples the actomyosin cable was particularly clear and appeared to reach further rostrally along the midline (red arrow, Figure 5.19F).

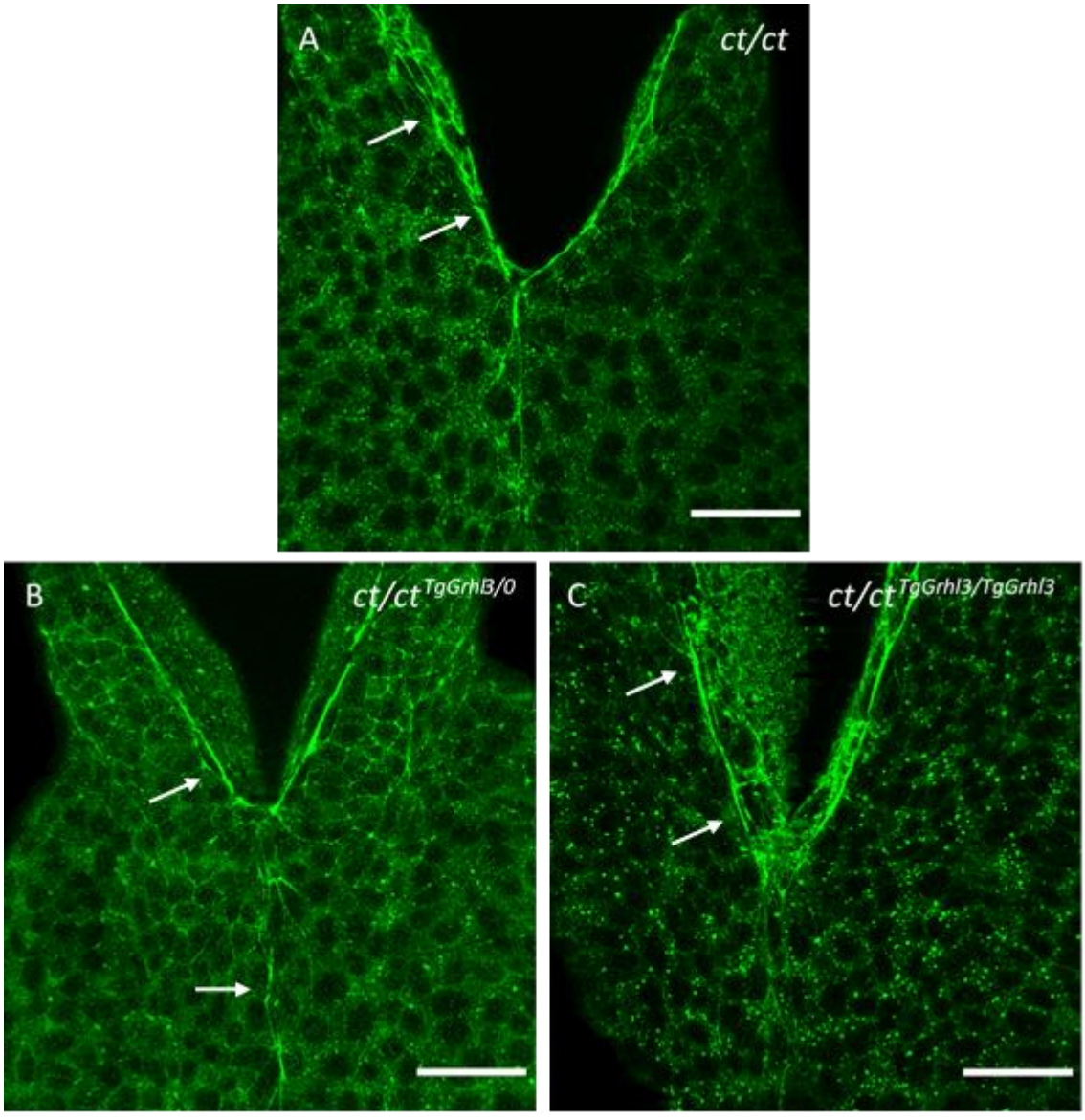

Figure 5.18 – Myosin heavy chain immunostaining in Grhl3 mutants.

MHC immunostaining appears normal in all genotypes. MHC is accumulated along the cable in ct/ct (A), ct/ct$^{TgGrhl3/0}$ *(B) and ct/ct*$^{TgGrhl3/TgGrhl3}$ *(C). Scale bars = 50 µm.*

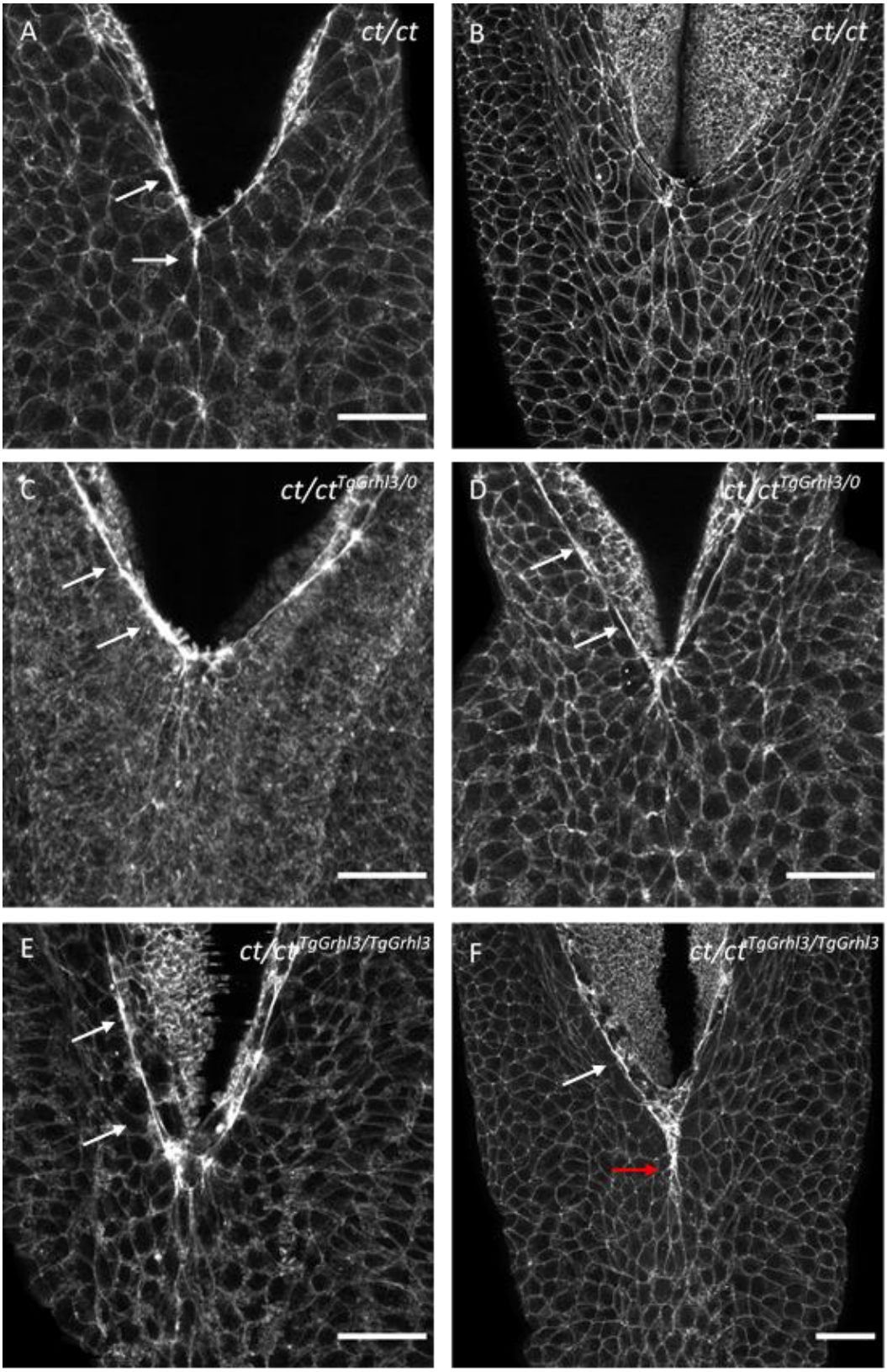

Figure 5.19 – F-actin immunostaining in Grhl3 mutants.

Phalloidin immunostaining appears normal in all genotypes. Actin accumulates along the cable in ct/ct (A), ct/ct$^{TgGrhl3/0}$ (C,D) and ct/ct$^{TgGrhl3/TgGrhl3}$ (E,F). 1/5 ct/ct samples did not have a visible cable (B), while the cable seemed brighter and to extend further rostrally in 2/4 ct/ct$^{TgGrhl3/TgGrhl3}$ sample (F). Scale bars = 50 µm.

In order to analyse potential differences in SE tension, at both the single cell and tissue level, laser ablation was used to compare the lateral recoil of the neural folds after ZP ablation and the initial recoil of individual cell borders in the region just rostral to the ZP. In addition, cable recoil was analysed after ablation. No significant differences were identified between genotypes at either the tissue (Figures 5.20, 5.21) or cell (Figures 5.22, 5.23) levels.

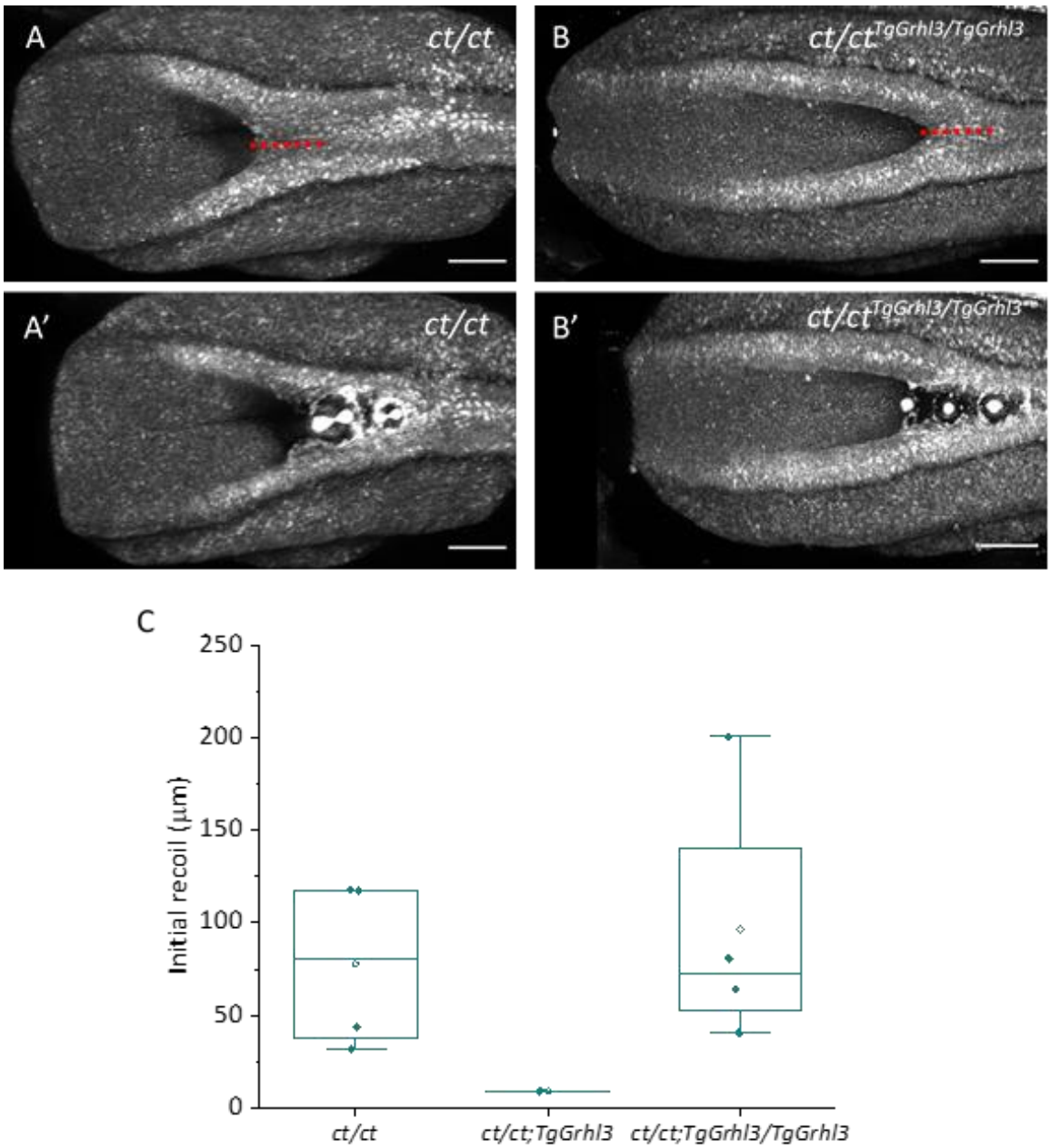

Figure 5.20 – Tissue laser ablation of the ZP in Grhl3 overexpression and ct embryos.

Recoil at the ZP after laser ablation is not significantly different between genotypes. A, B) Representative examples of ct/ct (A) and ct/ct$^{TgGrhl3/TgGrhl3}$ (B) E9.5 PNPs before (A, B) and after (A', B') ZP ablation. C) Quantification of initial lateral ZP recoil after laser ablation. Red dashed line = site of ablation. Scale bars = 100 µm.

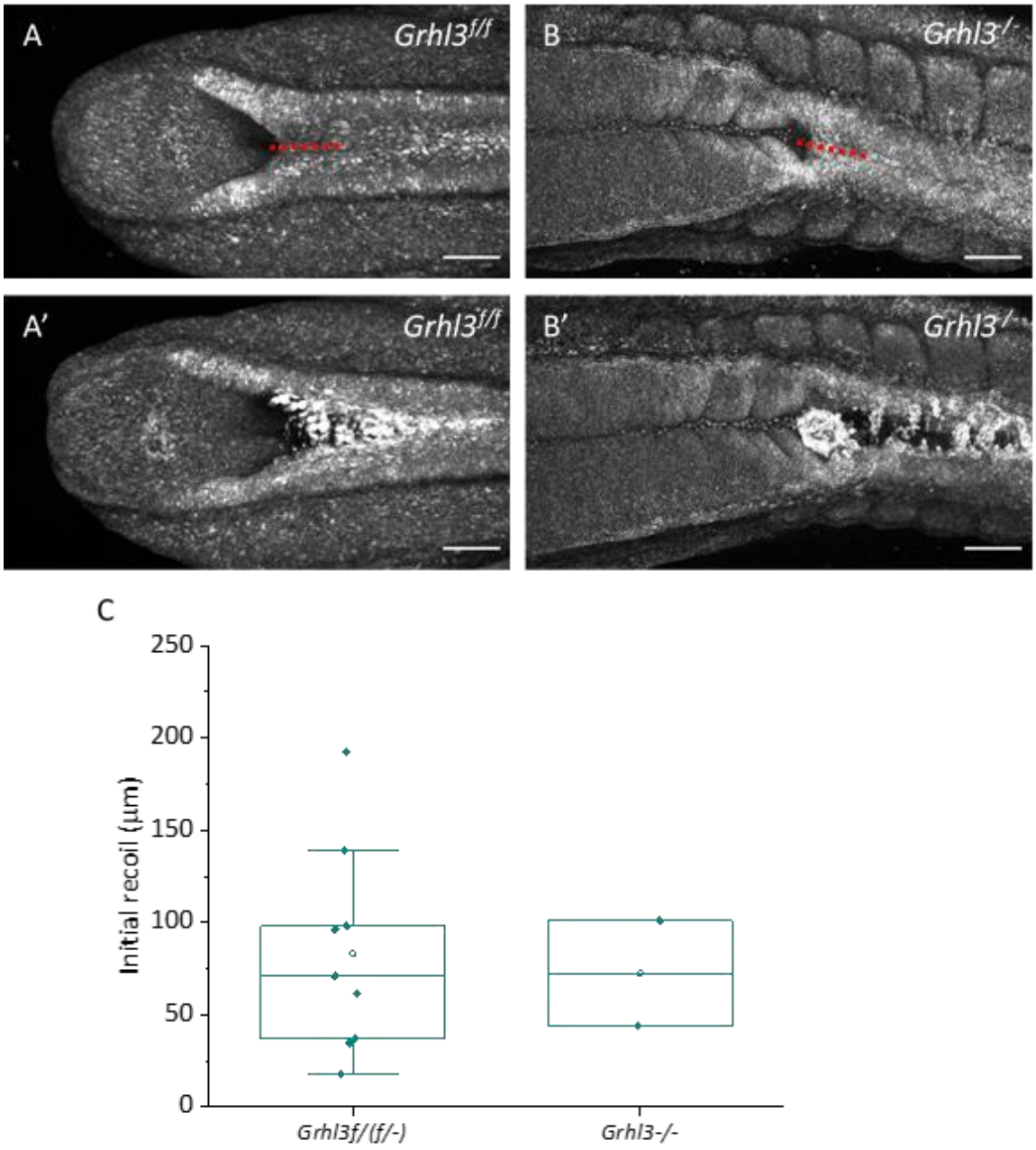

Figure 5.21 – Tissue laser ablation of the ZP in Grhl3 null embryos.

Recoil at the ZP after laser ablation is not significantly different between genotypes. A, B) Representative examples of Grhl3$^{f/f}$ (A) and Grhl3$^{-/-}$ (B) E9.5 PNPs before (A, B) and after (A', B') ZP ablation. C) Quantification of initial lateral ZP recoil after laser ablation. Red dashed line = site of ablation. Scale bars = 100 µm.

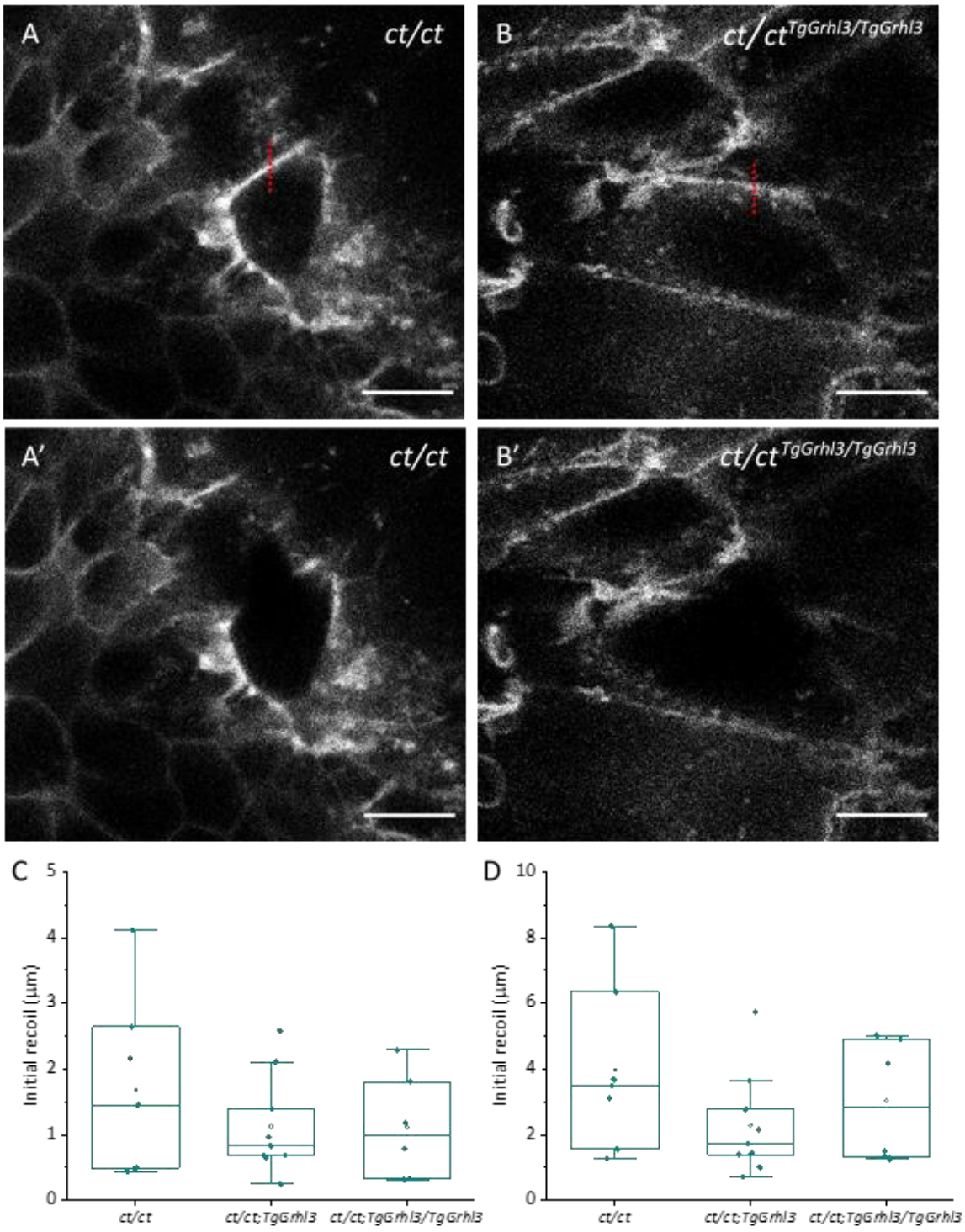

Figure 5.22 – Single cell and cable laser ablation in Grhl3 overexpression and ct embryos.

SE and cable recoil after laser ablation are not significantly different between genotypes. A,B) Representative single SE cells in ct/ct (A) and ct/ct$^{TgGrhl3/TgGrhl3}$ (B) E9.5 embryos before (A, B) and after (A', B') ablation. C) Quantification of initial recoil of single SE cell borders after ablation. D) Quantification of cable recoil after laser ablation. Red dashed line = site of ablation. Scale bars = 10 µm.

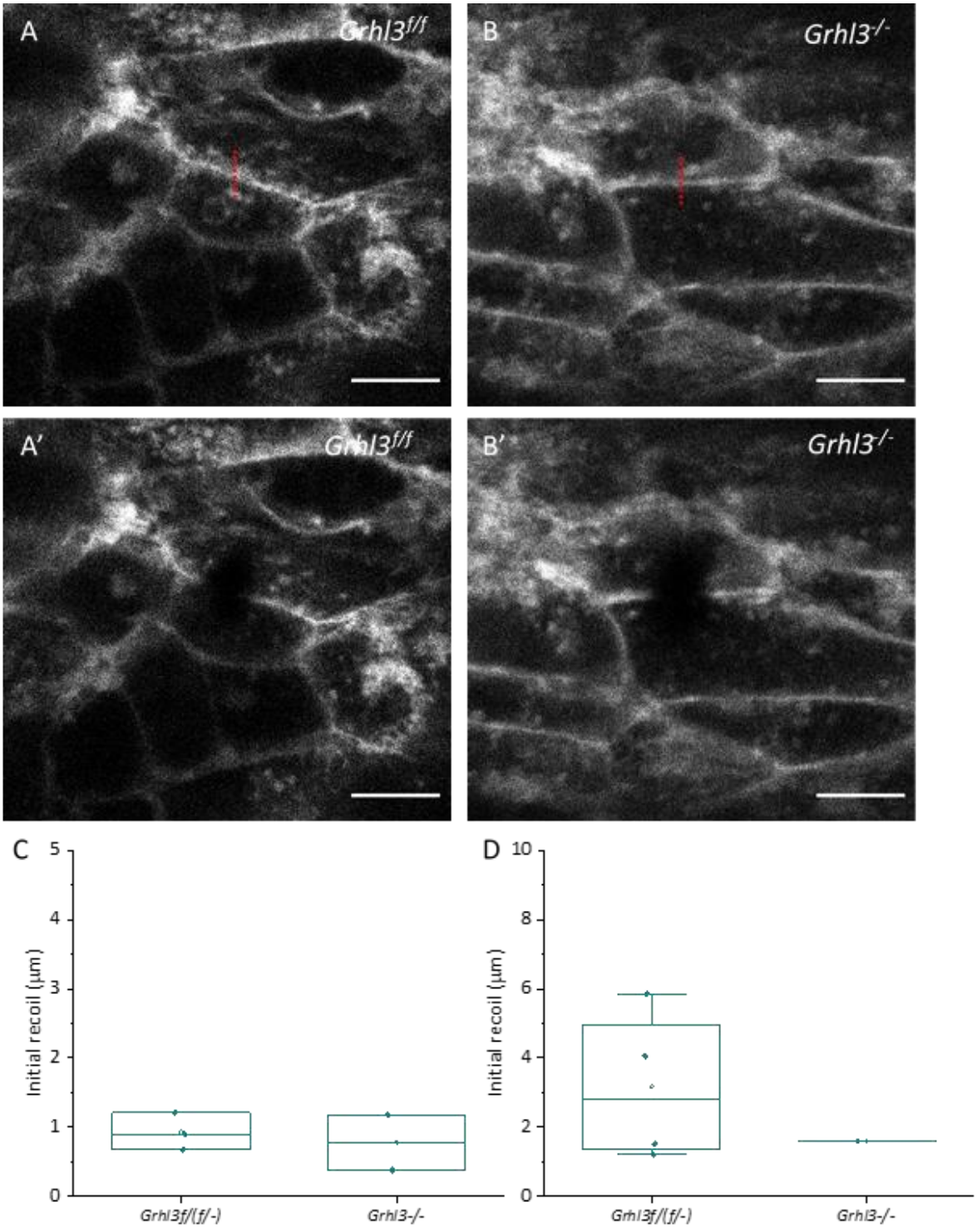

Figure 5.23 – Single cell and cable laser ablation in Grhl3 null embryos.

SE and cable recoil after laser ablation are not significantly different between genotypes. A,B) Representative single SE cells in Grhl3$^{f/f}$ (A) and Grhl3$^{-/-}$ (B) E9.5 embryos before (A, B) and after (A', B') ablation. C) Quantification of initial recoil of single SE cell borders after ablation. D) Quantification of cable recoil after laser ablation. Red dashed line = site of ablation. Scale bars = 10 µm.

5.2.4 - RNA-seq of *Grhl3* overexpression mutants suggests a different mechanism to *Grhl2*^{Axd}

The results presented thus far suggest that the SE of *Grhl3* mutants does not have as clear a biomechanical deficit as observed in *Grhl2* mutants. Therefore, RNA-seq technology was used to compare gene expression between the caudal region of E9.5 *ct/ct*$^{TgGrhl3/0}$ and *ct/ct*$^{TgGrhl3/TgGrhl3}$ embryos. This was to identify potentially novel mechanisms underlying failed NTC by comparing the effects of *Grhl2* overexpression, which alters SE mechanics, and *Grhl3* overexpression. These genotypes had previously been compared by RNA-seq in our group, however the number of differentially expressed genes was very low. The intact caudal region was used in the previous study and it is possible that the restricted expression of *Grhl3* in the SE, as a proportion of total tissue, and *Grhl3* expression in the hindgut masked any differential expression in this site.

For this experiment, the caudal region was microdissected along the ventrodorsal axis and only dorsal tissue was used for RNA-seq (methods Chapter 2.2.5). To confirm that the hindgut was successfully removed from dorsal tissue, expression of different ventrodorsal NT markers was compared between total and microdissected tissue RNA sequencing data, using TMM values to control for the differences in total reads (Robinson and Oshlack, 2010a). TMM (trimmed mean of M) values are normalised expression values obtained by comparing total gene expression over multiple samples, under the assumption that the majority of genes are not differentially expressed. This replaces the more commonly used method of normalising each sample to the total number of reads, which is more prone to errors due to differences between tissue types or amount of tissue (Robinson and Oshlack, 2010b). TMM values showed a significantly higher normalised expression of the hindgut marker *Sox17* (t-test, $p < 8 \times 10^{-6}$) and significantly lower normalised expression of *Pax3* (t-test, $p < 9 \times 10^{-5}$) in the whole caudal region compared to the dorsal tissue only, showing that microdissection successfully removed most of the ventral tissue (Figure 5.24).

Principal component analysis on microdissected samples revealed an unknown source of variation which separated out one sample from each genotype. Samples separated by sex clustered by principal component 2, however only 9 genes were DE between these groups (data not shown). One sample from each genotype was removed for all further analysis to remove this source of variability. 65 genes were differentially expressed between genotypes (FDR > 0.05), with 58 genes expressed at greater intensity in overexpression mutants (Figure 5.25). When all samples were compared without grouping by genotype, the majority of the 50 most variable genes varied between genotype groups (Figure 5.26). By comparing the sets of differentially

expressed genes between *Grhl2* (published in (Nikolopoulou et al., 2019)) and *Grhl3* overexpression data sets, only 3 genes were common (*Cdh1, Dsp, Erbb3*).

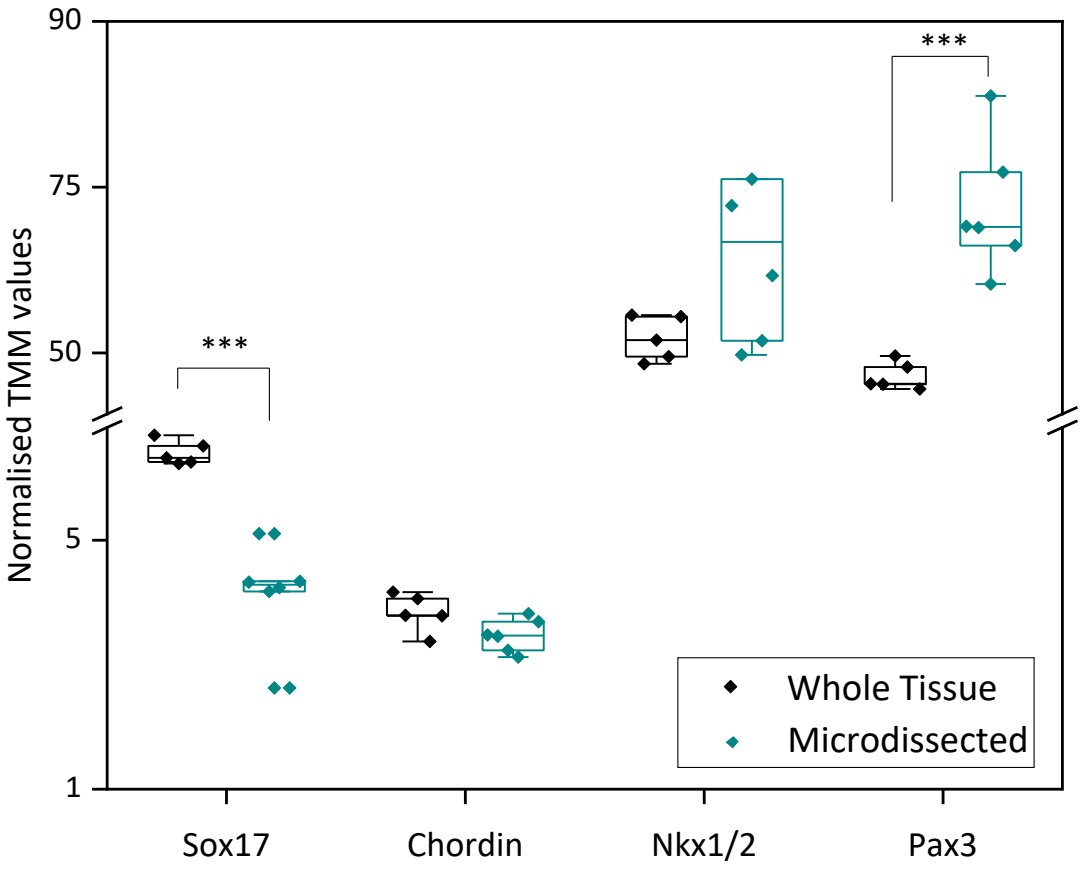

Figure 5.24 – Comparison of DV genes between whole and microdissected tissue.

Normalised TMM values of whole and microdissected tissue show significantly higher expression of ventrally expressed Sox17 ($p < 8 \times 10^{-6}$) and lower expression of dorsally expressed Pax3 ($p < 9 \times 10^{-5}$) in whole compared to microdissected tissue.

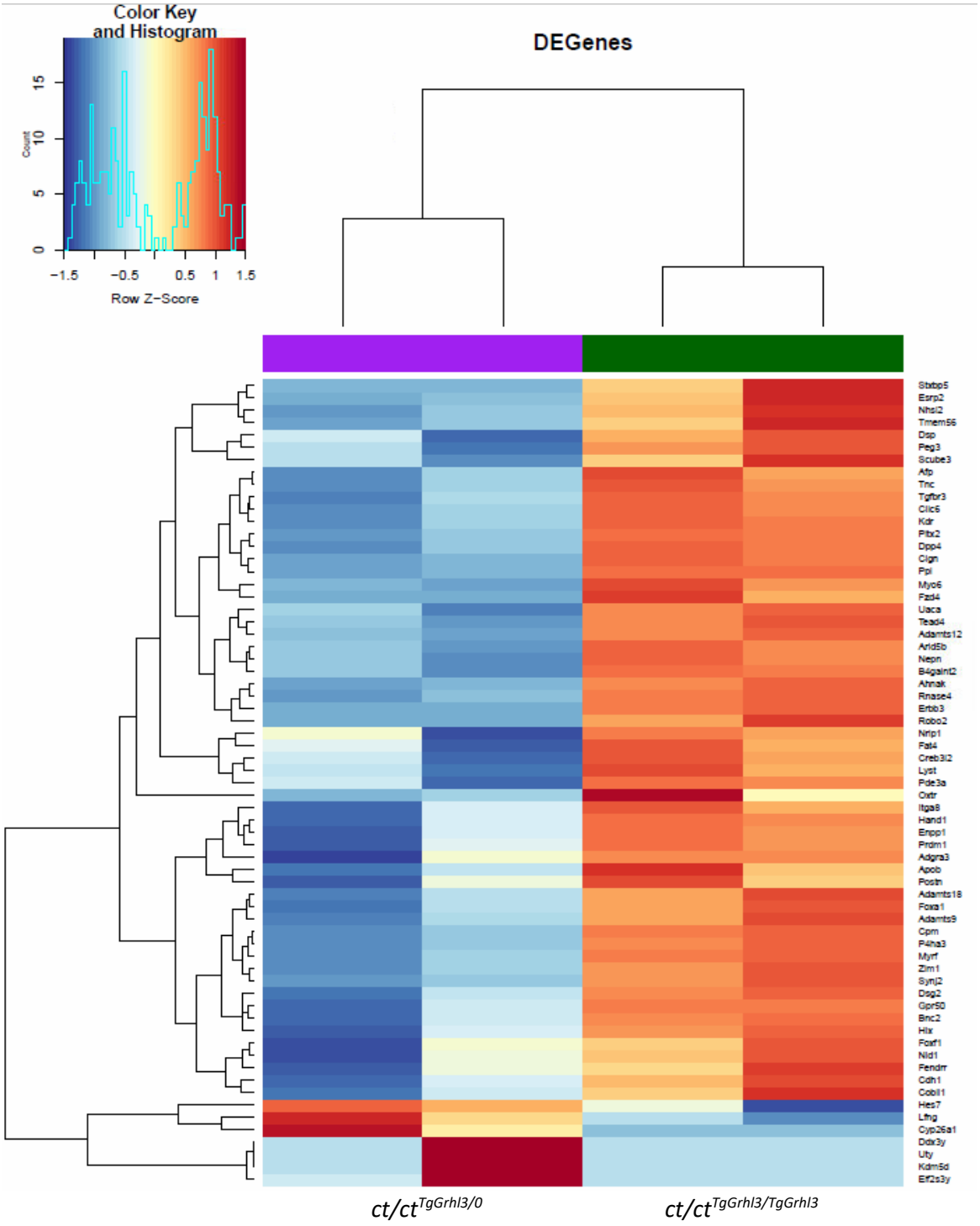

Figure 5.25 – Differentially expressed genes between control and overexpression Grhl3 embryos.

A heat map showing the 65 differentially expressed genes between ct/ct$^{TgGrhl3/0}$ and ct/ct$^{TgGrhl3/TgGrhl3}$ embryos (FDR > 0.05). 58/65 genes (89%) are upregulated in the overexpression mutants. Z-Score = scaling each row mean to equal 0 and centring and scaling expression using the S.D.

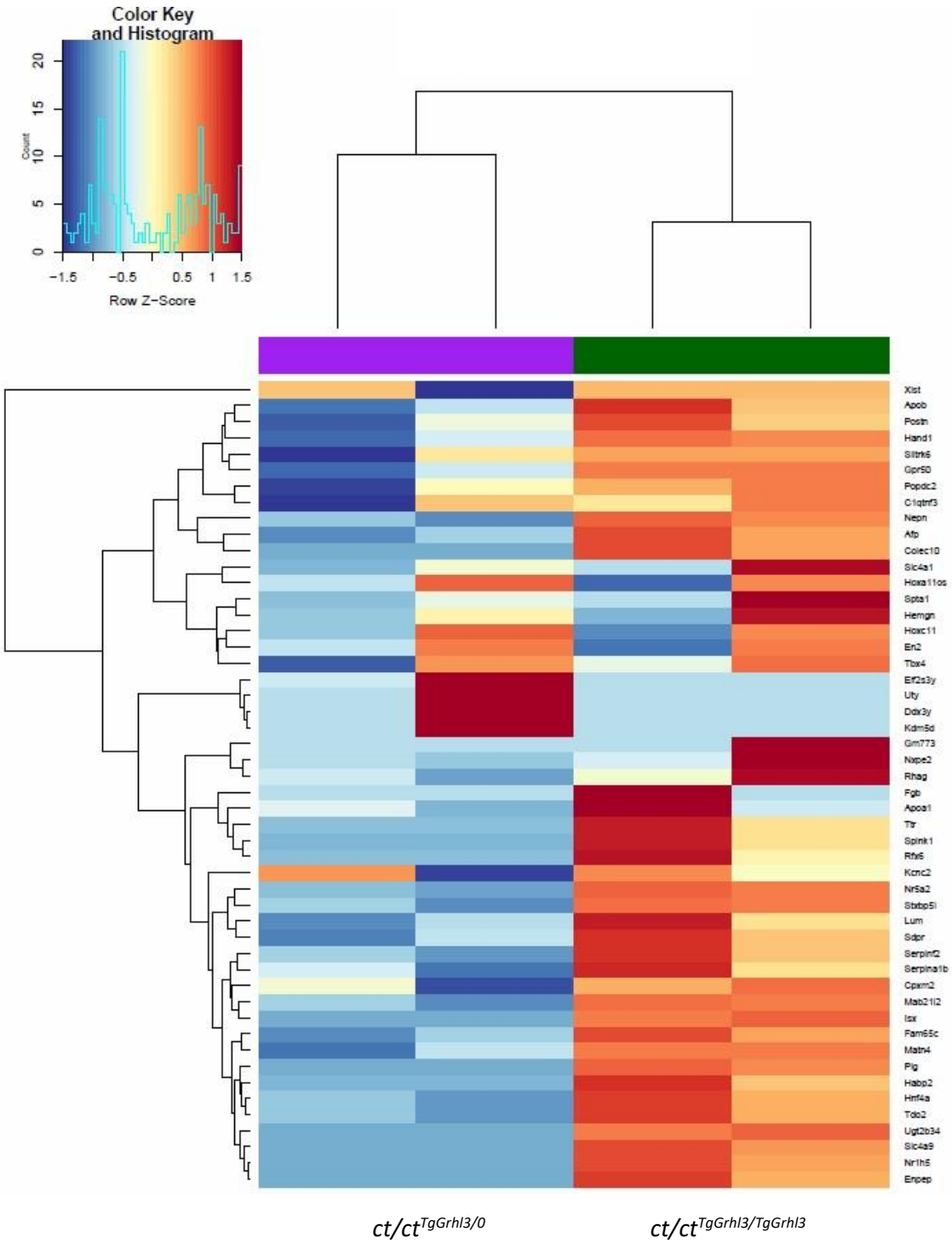

Figure 5.26 – 50 most significantly differentially expressed genes by genotype.

A heat map showing the 50 most variable genes across all samples when genotype was not taken into account. The majority of the variation clusters by genotype. Z-Score = scaling each row mean to equal 0 and centring and scaling expression using the S.D.

Gene set enrichment analysis (Mootha et al., 2003, Subramanian et al., 2005) revealed 936 gene sets which were significantly enriched (Figure 5.27, nominal pvalue < 5%). Of particular interest were the 4 GO terms relating to adhesion (cell-cell or cell-matrix). *Cdh1* was upregulated in both *Grhl2* and *Grhl3* overexpression, suggesting a common mechanism between mutants. The differential expression of several claudins that was identified in *Grhl2* mutants was not found in *Grhl3* mutants; rather, several genes associated with desmosomes were identified (*Ppl, Dsg2, Dsp, Ahnak*), suggesting a different mechanism behind abnormal cell-cell adhesion. Several extracellular matrix components, such as glycoproteins (*Tnc, Nid1*) and integrins (*Itgα8*), are also among the differentially expressed genes.

To further analyse how mutant *Grhl3* differs from *Grhl2*, GO terms were compared between both overexpression RNA-seq data sets. Interestingly, given the number of enriched GO terms in the *Grhl3* overexpression analysis, only two GO terms were common using an FDR of <1% (Figure 5.28A). Using less stringent conditions (FDR > 10%), a larger number of intersecting GO terms were identified (Figure 5.28B). Nevertheless, this analysis confirmed that differentially expressed genes are different between *Grhl2* and *Grhl3* mutants, further supporting the hypothesis that failed NTC in *Grhl3* overexpression mutants is by a different mechanism to that in *Grhl2* (*Axd*) mutants.

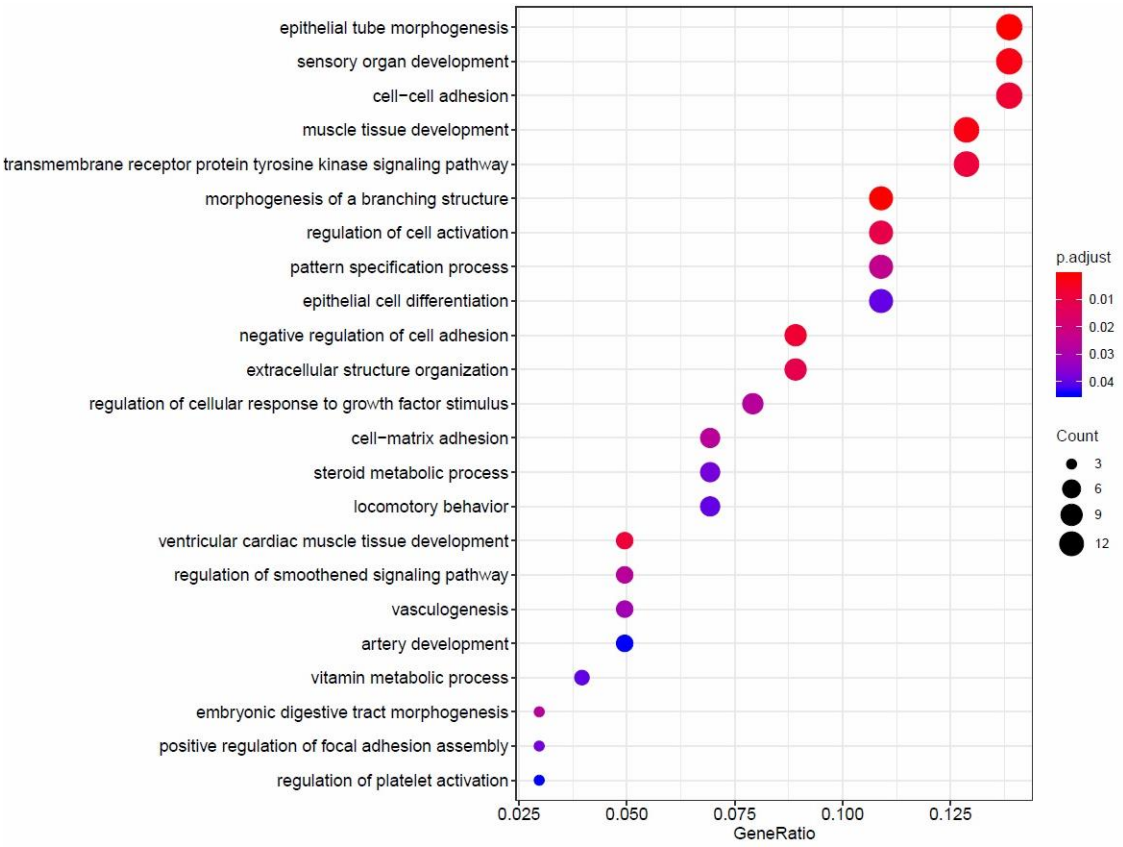

Figure 5.27 - Dot plot representing top 23 GO terms from gene set enrichment analysis.

Size of dot = number of genes enriched in the GO set. Colour of dot = significance of GO set. Gene ratio = ratio between p adjust:count.

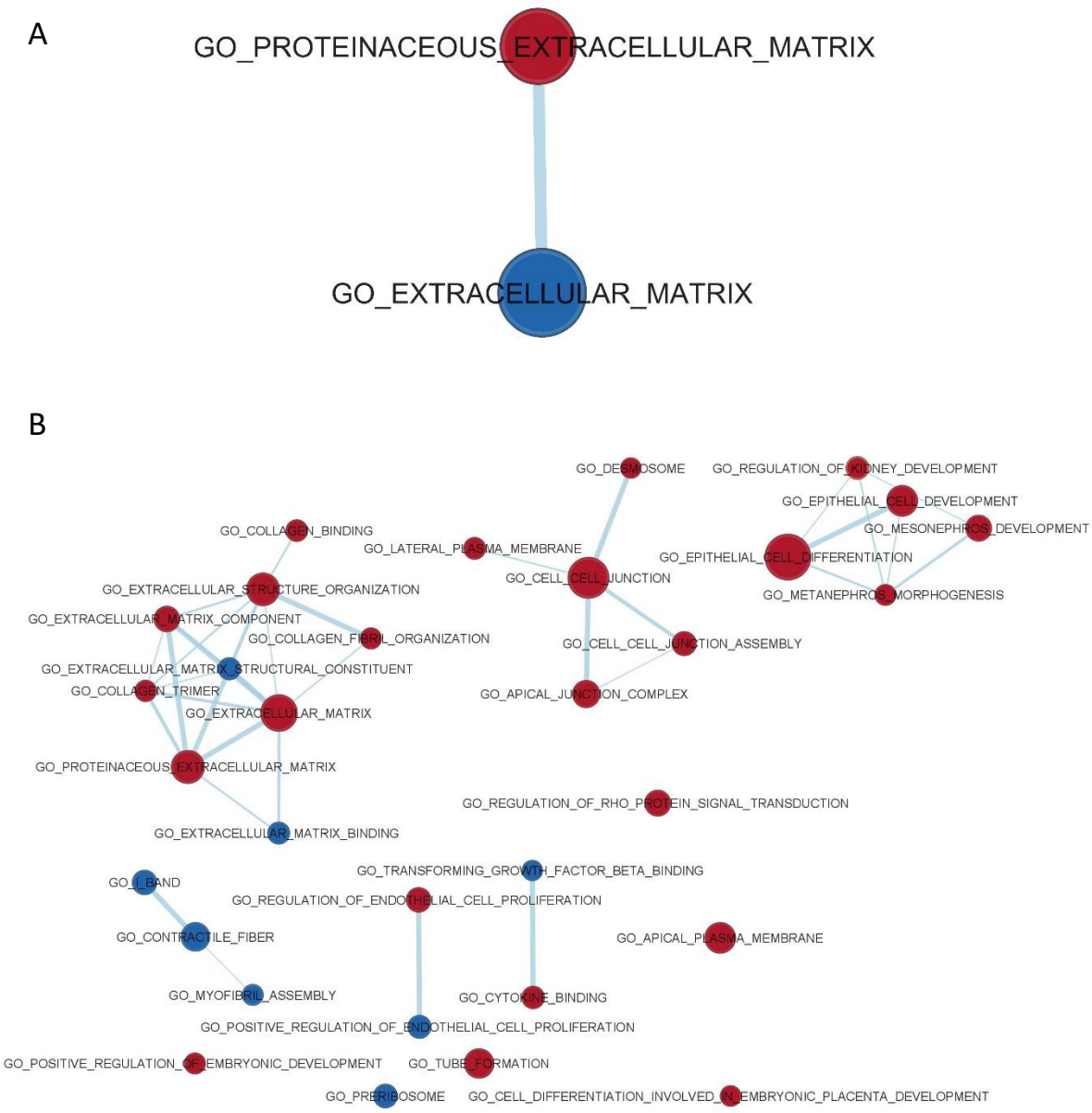

Figure 5.28 - Analysis of GO term intersection between Grhl2 and Grhl3 overexpression data sets.

Each GO term is significantly downregulated or enriched in both data sets. Red and blue dots represent up and down regulation of genes within the gene set. Size of dot represents significance of GO term. A) FDR > 0.01 for both data sets. B) FDR > 0.1 for both data sets.

5.3 - Discussion

5.3.1 - Loss- and gain-of-function of *Grhl2* causes NTDs by altering SE biomechanics

Recent work has shown that readouts of SE biomechanics are abnormal in *Grhl2* mutants (Nikolopoulou et al., 2019). Previously published differences in actomyosin expression, cell shape and tissue level tension have been further supported by data presented in this chapter: tissue and cell level laser ablations show significantly higher recoil in *Grhl2*$^{-/-}$ embryos, whereas *Axd/Axd* embryos are comparable to wild types. The increased tension in *Axd/Axd* but not *Grhl2*$^{-/-}$ embryos after needle incision in Nikolopoulou et al is not consistent with this data. However, this could be explained by the position of the incision – laser ablation experiments were directly at the ZP, whereas needle incisions were further rostral. Properties of the SE directly at the ZP are of greater relevance to closure, as the most recently closed region is likely to be similar to the SE on the open neural folds. As shown in Chapter 3, there are regional differences in SE recoil, and variations in recoil between genotypes may also vary between regions. Furthermore, culture of *Axd/Axd* embryos in blebbistatin partially rescues the enlarged PNP, supporting that these embryos do indeed show higher tension. Future work should include single border laser ablation in the region over the somites, as this would be a more valid comparison of ZP recoil data between regions than the use of needle incision.

High tension in the SE has previously been suggested to prevent closure in a computational model of axolotl NTC (Brodland et al., 2010). Pro- and anti-closure forces must be balanced for neurulation to successfully complete, and higher tension in *Grhl2*$^{-/-}$ embryos could prevent closure by increasing the contribution of anti-closure forces (Galea et al., 2017, Galea et al., 2018). However, this hypothesis depends on the assumption that higher recoil is a result of higher tension, and there are multiple reasons why this is unlikely to be the case in *Grhl2*$^{-/-}$ embryos. First, if these cells were under higher RC tension, an exaggerated midline elongation would be expected, but these cells in fact show the opposite (Nikolopoulou et al., 2019). Secondly, there are higher levels of phosphorylated YAP compared to total YAP in mutants compared to wild types, suggesting that these cells are under lower tension (Piccolo et al., 2014). Finally, there is a downregulation of epithelial genes and disruption of epithelial properties in these embryos – cells within epithelial tissues are generally tightly associated with each other and show high stiffness, resulting in high recoil of cells (Shook and Keller, 2003), and increased intracellular tension and extracellular forces are known to be important in driving MET (Kim et al., 2017).

How therefore can higher recoil in these embryos be explained? There are some known examples which challenge the classical view of the more epithelial the phenotype, the higher the tension. One study has shown that cells induced to undergo EMT initially show increased tension (Schneider et al., 2013). In another example, high tension at the edge of a migrating group of mesenchymal neural crest was observed, due to the presence of a highly contractile actomyosin cable (Shellard et al., 2018). In the *Grhl2*$^{-/-}$ SE, some cells lose their epithelial signature altogether and become more neural- the differences in mechanical properties between these cells and normal SE is unknown, and future work could focus on further understanding this.

An alternative explanation is that cellular tension has not changed between samples, but that the properties of the SE cause differences in recoil. One of the main functions of epithelial tissues is to withstand mechanical forces and maintain their shape – a downregulation of epithelial properties could prevent the SE from withstanding the anti-closure forces pulling laterally on the neural folds (Galea et al., 2017). This would also explain the wide morphology of the *Grhl2*$^{-/-}$ PNP. Future work analysing other mechanical properties such as tissue stiffness would be a valuable next step in supporting or disproving this hypothesis.

A particularly interesting phenotype in the *Grhl2*$^{-/-}$ embryos is the abnormal YAP expression. These mutants do not have higher YAP nuclear translocation along the midline, which is observed in control embryos, and pYAP/YAP is higher in mutants, suggesting lower transcriptional activity than in wild types. The meaning of this is not yet clear. YAP nuclear translocation is increased in cells under higher strain, which would suggest that mutant SE is under low tension compared to wild types. This conclusion contradicts the results from laser ablation, which would suggest higher tension. However, as already discussed, the current hypothesis is that greater recoil is a result of an inability of the SE to withstand anti-closure forces. It could be that the *Grhl2*$^{-/-}$ SE is under lower tension, but that the inability to withstand anti-closure forces is nonetheless substantial enough to show an increase in SE recoil. Alternatively, the defect could be in the ability of YAP to respond to mechanical cues. In one study, epithelial cells responded to strain through YAP1 and β-catenin nuclear activity, leading to rapid cell-cycle entry- importantly, this response depended on functional E-cadherin to detect and signal mechanical cues (Benham-Pyle et al., 2015). This suggests that a downregulation of *Cdh1* expression could inhibit the ability of SE to respond to mechanical cues.

Surprisingly, laser ablation of the actomyosin cable does not reveal a significant difference in recoil in *Grhl2*$^{-/-}$ embryos compared to wild types. High tension in the cable is believed to be

important in propagating closure by a mechanism similar to wound healing (Chapter 1.5.3.2), and a disrupted or absent cable may be unable to generate the tension required to promote closure. The fact that the cable was present in some *Grhl2*$^{-/-}$ samples, and that there was no significant difference in cable recoil between controls and mutants, suggests that this is unlikely to be the sole causative mechanism in these embryos. Nevertheless, the wide PNP in loss-of-function mutants does imply an absence of pro-closure forces generated by the actomyosin cable.

The mechanism behind failed closure in *Axd/Axd* embryos does not appear to be related to changes in cell or tissue tension- these are both comparable to wild types as measured by laser ablation. The very long and narrow PNP in these embryos suggests that globally, mechanical forces are successfully bringing the neural folds to the midline – an abnormally intense cable could provide higher than normal pro-closure forces in these mutants, despite a lack of differences in recoil after laser ablation. A local defect at the cellular level is therefore more likely. One hypothesis is that the 'super epithelial' phenotype may prevent junctional remodelling at the ZP. An upregulation of junctional proteins such as E-cadherin and claudins could result in stronger or more abundant adhesive complexes, preventing disassembly and reassembly of cell borders. SE aspect ratio is lower at the midline in *Axd/Axd* embryos compared to wild types - abnormal cell shape could reflect an inability of these cells to intrinsically change their shape. It would be valuable to visualise SE dynamics in *Axd/Axd* embryos to further probe this theory.

5.3.2 - *Grhl3* alters SE properties by a different mechanism to *Grhl2*

Grhl-2 and *-3* share consensus DNA binding sequences, suggesting they may have target genes in common and subsequently play similar roles in NTC (Ting et al., 2003b, Nikolopoulou et al., 2017). However, neither gene can fully compensate for the loss of the other, and unique target genes have been identified (Boglev et al., 2011). Analysis of the biomechanical properties which are disrupted in *Grhl2* mutant embryos shows that any biomechanical changes in *Grhl3* mutants are more subtle. It is important to consider the effect that phenotype penetrance may have on these results - both *ct/ct*$^{TgGrhl3/TgGrhl3}$ and *ct/ct* have incompletely penetrant NTDs, making quantification less reliable. It is possible that NTC would ultimately fail in those embryos with mechanical phenotypes outside of the normal range, such as a loss of or abnormally bright cable, or disrupted cell shape. It is also possible that any biomechanical differences that are more subtle than in *Grhl2* mutants were missed due to limitations of the techniques applied. Laser

ablation at the tissue level in particular is limited in mouse models because of the thickness of the tissue. A single ablation is not able to cut through the whole tissue, and a number of ablations at different positions in the dorsoventral axis have to be carried out (see methods Chapter 2.7.2). There is therefore a lag between the initial cut and the final image used to measure the recoil, meaning that any differences in the immediate recoil of the tissue could be missed. Similarly, it is possible that the significant increase in tissue-level recoil in *Grhl2*$^{-/-}$ mutants would not have been detected immediately after ablation. However, this issue does not apply in single cell ablations. The agreement between tissue and cell level recoil in both *Grhl-2* and *-3* mutants supports the validity of tissue level ablations.

Furthermore, analysis of cell shape in *Grhl3* mutants revealed no correlation between PNP length and SE aspect ratio along the midline of *ct/ct*$^{TgGrhl3/TgGrhl3}$ embryos (data not shown). Meanwhile, in *ct/ct* embryos, PNP length is comparable with wild types at E9.5, preventing this comparison from being made. Although the mechanism behind failed closure in *ct/ct* embryos is already attributed to a biomechanical deficit resulting from abnormal hindgut proliferation, this does not rule out a secondary SE biomechanical defect (Copp et al., 1988). The abnormal proliferation in embryos which go on to fail can only be identified at stages when the PNP is larger, i.e. after E10. Therefore, it would be interesting to know if samples with defective hindgut proliferation have SE cells shaped outside of the normal range.

A potential confounding factor in the analysis of *Grhl3* overexpression mutants is that the phenotype of 'control' *ct/ct*$^{TgGrhl3/0}$ embryos is not comparable to wild type (C57Bl/6) embryos. It could be that *Grhl3* expression is not at normal levels, despite being sufficient to rescue NTDs, and indeed quantitative RT-PCR of *Grhl3* shows higher expression in *ct/ct*$^{TgGrhl3/0}$ compared to *+*^{ct}*/+*^{ct} congenic controls (Gustavsson et al., 2007). This is further supported by the low penetrance of NTDs (15%) when the BAC is transferred onto a BALB-c background (De Castro et al., 2018a). The lack of midline SE elongation in these controls could have made comparisons with mutants less meaningful.

Although *ct/ct* and overexpression mutants have incomplete NTD penetrance, 100% of *Grhl3*$^{-/-}$ embryos develop SB; indeed, these embryos showed the most severe phenotype, with abnormal ZO-1 and E-cadherin expression. The abnormal clusters of E-cadherin are reminiscent of the phenotype seen in *Grhl2*$^{-/-}$ SE, with only patches of SE affected as opposed to the entire tissue. However, these clusters are positive for E-cadherin, whereas in *Grhl2*$^{-/-}$, E-cadherin expression is lost and N-cadherin and Sox2 are expressed in its place (Nikolopoulou et al., 2019). Abnormal E-cadherin staining suggests that there is disruption of cell-cell adhesion, either as a result of

abnormal *Cdh1* expression or as an indirect result of disrupted SE integrity, as hypothesised in *Grhl2*$^{-/-}$. It would be of interest to determine if other components of apical junctional complexes, which are also differentially expressed in *Grhl2* mutants, are abnormally distributed, and whether these clusters are functionally disrupting neurulation or are an artifact of failed closure.

In addition, how F-actin and myosin heavy chain are expressed in *Grhl3*$^{-/-}$ embryos has not yet been analysed, making it difficult to completely rule out a mechanism of failed NTC which involves impaired biomechanics of the SE. The F-actin cable is significantly disrupted around the closing eyelid in *Grhl3*$^{-/-}$*;LMO4*$^{-/-}$ mutant mice, manifesting in failed eyelid fusion and suggesting the cable is an important player in *Grhl3* function (Hislop et al., 2008). It is unknown if the cable is disrupted in *Grhl3*$^{-/-}$; this cannot be ruled out by a lack of altered cable recoil, as the disrupted cable in *Grhl2*$^{-/-}$ embryos is not reflected by laser ablation. Hislop et al. did not perform laser ablation on the eyelid cable in *Grhl3*$^{-/-}$ embryos, so it is unknown if recoil is disrupted in this model. Nevertheless, cell shape and single border recoil are comparable between *Grhl3* null and wild type SE, suggesting that even if there is a biomechanical defect, the mechanism behind failed NTC is not the same as in *Grhl2*$^{-/-}$.

GRHL proteins are transcription factors and therefore predicted to exert their effects on NTC via regulation of transcription of target genes. RNA-seq analysis is a common technique for identifying signalling pathways that are disturbed downstream of a gene of interest. In order to characterise the target genes of *Grhl3*, the mRNA from dorsal NT and SE tissue from overexpression mutants were compared to controls, and a series of potentially interesting genes were identified. However, this experiment was limited by the low number of *Grhl3* expressing cells in the sample. Although the samples were dissected along the dorsoventral axis, this would not be enough to eliminate all *Grhl3* negative cells and would therefore make any differentially expressed genes between wild types and mutants more difficult to detect. Taking this into account, it may be valuable to analyse genes which were almost significantly differentially expressed but which are predicted to be important, for example searching for more cell-cell adhesion molecules, ECM components or YAP targets. Alternatively, future experiments would benefit from using a cell-sorting approach to eliminate *Grhl3* negative cells. For example, breeding *Grhl3-Cre* and a fluorescent reporter onto the *Grhl3*$^{ct/ct;TgGrhl3}$ background would allow cells from *Grhl3* overexpression mutants to be sorted and used for RNA-seq analysis.

Despite this caveat, desmosome components were particularly enriched in this experiment, with *Ppl, Dsg2, Dsp,* and *Ahnak* all significantly upregulated in overexpression mutants compared to controls. Desmosome junctions are inter- and intra-cellular complexes that play a role in cellular

adhesion and cytoskeleton integrity, and in some instances can become hyper-adhesive, rendering them especially strong in comparison to adherens junctions (Garrod et al., 2005, Garrod and Chidgey, 2008). Desmosomes form inter- and intra-cellular links via a desmosome-intermediate filament complex, which consists of a central outer dense plaque (ODP) linking intercellular desmosomal cadherins and intracellular intermediate filaments (Garrod and Chidgey, 2008). Desmosomes are most widely studied in the context of human cardiac and skin diseases, for example Pemphigus is a group of autoimmune diseases which attack desmosomes and lead to severe blistering (Kasperkiewicz et al., 2017). Desmosomes are also involved in development, and are first expressed at the lateral borders of trophectoderm cells at E3.5 (Fleming et al., 1991). Knockout of various desmosome components leads to early embryonic lethality, with *Dsc3*$^{-/-}$, *Dsg2*$^{-/-}$ and *Dsp*$^{-/-}$ embryos dying at E2.5, E4.5 and E6.5 respectively (Garrod and Chidgey, 2008). Other desmosome component mutants, such as *Jup*$^{-/-}$ and *Pkp2*$^{-/-}$, die of heart defects around mid-gestation due to thin cardiac walls, resulting in ruptures and blood leakage (Bierkamp et al., 1996, Grossmann et al., 2004). Of note, these studies all analyse the effects of loss-of-function mutations, and the effects of desmosome component overexpression are unknown.

How dysregulation of desmosome components in *Grhl3* mutants could affect NTC is unclear - desmosomal complexes are known to be abnormal in *Grhl1*$^{-/-}$ mutant mouse embryos, leading to impaired hair growth and thickened skin (Wilanowski et al., 2008), yet no role for desmosome dysfunction in NTDs in *Grhl-2* and *-3* mutants has been suggested. Although desmosomes were not implicated in the 'super epithelial' phenotype of *Axd/Axd* embryos, it is possible that an analogous mechanism may arise in *Grhl3* overexpression mutants. For example, desmosomes play a role in cell adhesion, and some *Grhl3* over-expressing embryos do indeed show a long and narrow PNP. However, this is never as pronounced as in *Axd/Axd* embryos, and the biomechanical properties of both overexpression mutants are not comparable. It could be that the number of components in the desmosomal complex allows partial desmosomal function due to gene redundancy, explaining why only some *Grhl3* overexpression mutants develop NTDs.

Finally, several components of the ECM were upregulated in *Grhl3* overexpression mutants. The ECM is vital in providing a substrate for the SE as mechanical support, and mutations in a large range of ECM components have been linked to NTC (see Chapter 1.5.3.4). In a recent study from our lab, 56% of *Grhl3-Cre-Itgb1*$^{f/f}$ embryos developed SB, due to loss of a SE-secreted, integrin-rich focal point at the ZP (Mole et al., 2020). It is possible that *Grhl3*, as a TF expressed in the SE specifically around the ZP and the neural folds, regulates expression of ECM components of this focal point. The more severe phenotype seen in *Grhl3*$^{-/-}$ compared to *Grhl3-Cre-Itgb1*$^{f/f}$ embryos

may be due to *Grhl3* acting upstream of integrin expression – however this hypothesis depends on *Grhl3*$^{-/-}$ mutants showing reciprocal downregulation of ECM components, and the RNA sequencing data presented in this chapter focuses only on overexpression mutants. How an upregulation of ECM components might prevent closure is unclear, but it is possible that an abnormally strong focal point could prevent the remodelling of cell rosettes. Future work could analyse expression of ECM components and investigate the cell dynamics of rosettes around the ZP using live imaging, in order to investigate this hypothesis.

Chapter 6 - What is the role of hypomorphic *Grhl3* in *Vangl2$^{Lp/+}$;Grhl3$^{ct/ct}$* mutant mouse embryos?

6.1 - Introduction

Although *Lp* homozygous mutant (*Vangl2$^{Lp/Lp}$*) embryos develop 100% craniorachischisis, resulting from failure of closure 1, open NTDs are rare in heterozygotes, which instead show 100% TFDs (Strong and Hollander, 1949). However, multiple interacting pathways have been identified which worsen NTD phenotypes that originate at later developmental stages in heterozygotes. Heterozygous mutants are more useful for studying the role of PCP gene mutations in human SB and anencephaly, rather than the more severe and rarer craniorachischisis found in homozygotes – missense mutations with a large variety of phenotypes have been identified in humans (Murdoch et al., 2014). Mouse embryos with mutations in more than one gene can cause more severe NTDs as a result of genetic interactions. This can imply either direct exacerbation of known mutant phenotypes or an additive effect of distinct molecular mechanisms.

In addition to the *Vangl2^{Lp}* mouse line, mutations in multiple other PCP family members cause craniorachischisis when homozygous, including *Celsr1* and *Scrib*. *Vangl2* interacts with heterozygous mutations in these genes – while heterozygous *Vangl2, Celsr1* and *Scrib* mutations alone do not cause open NTDs, compound heterozygotes show craniorachischisis with varying penetrance (Curtin et al., 2003, Murdoch et al., 2003, Murdoch et al., 2014). The mechanisms behind these severe phenotypes in compound heterozygotes are likely to be exacerbation of the same CE mechanism, as the downstream effects of PCP members are comparable. A number of non-PCP genes have also been identified as interacting factors, for example, mutations in *Ptk7* and *Cobl* cause highly penetrant SB and EX respectively when in combination with *Vangl2^{Lp}* (Carroll et al., 2003, Paudyal et al., 2010). It could be that, similarly to PCP compound mutants, these non-PCP genes are interacting with *Vangl2* to worsen the PCP phenotype. However, given that these genes are not classical PCP members, an alternative mechanism might be at play – these mutants might therefore be useful in identifying novel, non-PCP roles of genes such as *Vangl2*.

Grhl3 is one of the non-PCP interacting genes found to worsen the *Vangl2* effect. 67% of *Vangl2$^{+/-}$;Grhl3$^{+/-}$* double mutant embryos develop lumbo-sacral or high sacral SB (Caddy et al., 2010). Meanwhile, when *Vangl2$^{Lp/+}$* mice are crossed to the *ct* strain, in which *Grhl3* is the major mutant gene, double mutant embryos show severe NTDs: *Vangl2$^{Lp/+}$;Grhl3$^{ct/ct}$* and

Vangl2$^{Lp/+}$;*Grhl3*$^{ct/+}$ embryos develop 74% and 41% SB respectively (Stiefel et al., 2003) (Pryor et al., unpublished). Embryos from this cross have a significantly larger PNP at E9.5 compared to *Grhl3*$^{ct/ct}$ embryos, resulting in a larger spinal lesion (Pryor et al., unpublished). *Grhl3* is a gene for which there is little evidence of a role in PCP signalling, and it is unknown how it might interact with *Vangl2* to cause NTDs. Whether these genes interact in a way which exacerbates their known mechanisms, or whether the effect is additive involving separate mechanisms at a molecular level, remains unclear.

Recent work began to study this question by first analysing known *ct* and *Lp* cellular phenotypes in the *Vangl2*$^{Lp/+}$ x *Grhl3*$^{ct/ct}$ cross. As *Grhl3* is the main mutant gene in the *ct* strain, this is a useful tool for analysing the *Vangl2/Grhl3* interaction, although effects of other mutant loci are always possible. Hindgut proliferation was not significantly altered in double mutants (*Vangl2*$^{Lp/+}$;*Grhl3*$^{ct/(ct/+)}$) compared to *Grhl3*$^{ct/(ct/+)}$ embryos alone. Similarly, axial length was not reduced in double mutants compared to *Vangl2*$^{Lp/+}$;*Grhl3*$^{+/+}$ mutants, suggesting that a *Vangl2* mechanism other than CE is involved in NTC at later stages of neurulation. CE was comparably defective in *Vangl2*$^{Lp/+}$;*Grhl3*$^{+/+}$ and *Vangl2*$^{Lp/+}$;*Grhl3*$^{ct/ct}$ embryos, as measured using DiI labelling during culture to visualise extension of the caudal region (Pryor et al., unpublished). Therefore, neither mutant allele exacerbates the known mutant phenotype of the other allele. Indeed, a trend towards reduced ventral curvature in double mutants compared to *Grhl3*$^{ct/ct}$ embryos further supports that the contributory effect of the *ct/ct* genotype is not via an effect on hindgut proliferation and axial curvature, as described in *ct/ct* embryos (Copp et al., 1988).

The possibility that a direct interaction between *Vangl2* and *Grhl3* occurs in the same tissue was analysed using *in situ* hybridisation. This revealed that *Grhl3* and *Vangl2* transcripts overlap in the NE and the hindgut during the stages studied (E9.0-9.5). However, qRT-PCR revealed no change in expression of either gene, arguing against a direct gene-gene transcriptional regulatory interaction. This could instead imply a protein-protein interaction, whereby loss of one protein alters the function of the other. Indeed, such an interaction has been reported in mouse neurulation, with loss of *Grhl3* preventing membrane localisation of *Vangl2* in the E8.5 SE (Kimura-Yoshida et al., 2018). However, the lack of suitable antibodies has prevented this from being further investigated in our lab.

It is possible that the worsened NTDs in double mutants is due to a novel mechanism, not previously found to contribute to NTDs. Indeed, it has been found that E9.5 embryos of both *Vangl2*$^{Lp/+}$;*Grhl3*$^{ct/ct}$ and *Vangl2*$^{+/+}$;*Grhl3*$^{ct/ct}$ genotypes show a reduction in proliferation in the *Grhl3* expressing region of the tailbud (Pryor et al., unpublished). This suggests that the

phenotype in *Vangl2*$^{Lp/+}$*;Grhl3*$^{ct/(ct/+)}$ double mutants may be caused by an additive mechanism, whereby a *ct* and *Lp* effect combine to lead to more severe NTDs. In this chapter, this mechanism is further explored, using overexpression of *Grhl3,* or treatments to stimulate proliferation in the tailbud, to attempt to rescue NTDs.

6.2 - Results

In order to generate *Vangl2*$^{Lp/+}$;*Grhl3*$^{ct/(ct/+)}$ double mutant embryos, a colony of double heterozygotes was generated through an initial cross of *Vangl2*$^{Lp/+}$ x *Grhl3*$^{ct/ct}$ mice. The resulting *Vangl2*$^{Lp/+}$;*Grhl3*$^{ct/+}$ double heterozygotes were then crossed to *Grhl3*$^{ct/ct}$ or *Grhl3*$^{ct/ct;TgGrhl3}$ mice for all the following experiments. This experimental design means that all resulting embryos will have a genetic background which is 75% *ct*. Although embryos are referred to as *Grhl3*$^{ct/(ct/+)}$ throughout this chapter, the potential effects of a background which is majority *ct* must be considered, given that there are multiple known modifying genes within the *ct* strain.

6.2.1 - Overexpression of *Grhl3* does not rescue NTDs in *Vangl2*$^{Lp/+}$;*Grhl3*$^{ct/ct}$ double mutants

In *ct/ct* mutant mice, *Grhl3* is a hypomorphic allele. NTDs can be rescued in this strain by introducing a BAC transgene encompassing the entire *Grhl3* gene and regulatory region (see Chapter 1.3 (Gustavsson et al., 2007)). This led to the hypothesis that breeding the *Grhl3* transgene into *Vangl2*$^{Lp/+}$;*Grhl3*$^{ct/ct}$ double mutants would improve NTD rates, by rescuing the *ct* contribution to the overall phenotype. To generate double mutants, *ct/ct* females were crossed to *Vangl2*$^{Lp/+}$ males, generating *Vangl2*$^{Lp/+}$;*Grhl3*$^{ct/+}$ mice with TFDs. *Grhl3*$^{ct/ct;TgGrhl3/0}$ mice were then crossed to these double heterozygotes, or alternatively to *Vangl2*$^{Lp/+}$ mice, and their offspring were collected at E11.5, genotyped for the *Vangl2* allele and presence of the *Grhl3*-transgene, and scored for NTDs (Table 6.1).

The introduction of the *Grhl3* transgene did not reduce penetrance of NTDs in any of the genotypes analysed. Interestingly although there was a partial rescue of SB in *Vangl2*$^{Lp/+}$;*Grhl3*$^{ct/ct;TgGrhl3/0}$ compared to *Vangl2*$^{Lp/+}$;*Grhl3*$^{ct/ct}$, incidence of SB was more severe in *Vangl2*$^{Lp/+}$;*Grhl3*$^{ct/+;TgGrhl3/0}$ compared to *Vangl2*$^{Lp/+}$;*Grhl3*$^{ct/+}$ in both crosses (Table 6.1). This finding suggests that there is an additional genetic interaction between *Vangl2*^{Lp} and *ct*^{TgGrhl3} leading to spinal NTDs (De Castro et al., 2018a). Indeed, overexpression of *Grhl3* is known to cause NTDs, supporting this hypothesis.

In order to exclude the possibility that the *Vangl2*^{Lp} mutation affects expression of the *Grhl3* transgene, qRT-PCR was carried out on samples derived from the caudal region of E10.5 embryos from a *Vangl2*$^{Lp/+}$;*Grhl3*$^{ct/+}$ *x Grhl3*$^{ct/ct;TgGrhl3/0}$ experimental cross. Presence of mutant *Vangl2* did not affect *Grhl3* expression (Figure 6.1).

Genotype	No. embryos	Spinal Phenotype % (n)		
		Straight tail	Tail flexion defects	Spina bifida & tail flexion defects
A. *Vangl2$^{Lp/+}$* x *Grhl3$^{ct/ct; TgGrhl3/0}$*				
Vangl2$^{+/+}$; Grhl3$^{ct/+}$	4	100 (4)	0 (0)	0 (0)
Vangl2$^{+/+}$; Grhl3$^{ct/+;TgGrhl3/0}$	11	55 (6)	45 (5)	0 (0)
Vangl2$^{Lp/+}$; Grhl3$^{ct/+}$	12	8 (1)	92 (11)	0 (0)
Vangl2$^{Lp/+}$; Grhl3$^{ct/+; TgGrhl3/0}$	13	0 (0)	23 (3)	77 (10)*
B. *Vangl2$^{Lp/+}$;Grhl3$^{ct/+}$* x *Grhl3$^{ct/ct; TgGrhl3/0}$*				
Vangl2$^{+/+}$; Grhl3$^{ct/+}$	14	86 (12)	14 (2)	0 (0)
Vangl2$^{+/+}$; Grhl3$^{ct/+;TgGrhl3/0}$	9	78 (7)	22 (2)	0 (0)
Vangl2$^{+/+}$; Grhl3$^{ct/ct}$	11	55 (6)	45 (5)	0 (0)
Vangl2$^{+/+}$; Grhl3$^{ct/ct;TgGrhl3/0}$	8	88 (7)	12 (1)	0 (0)
Vangl2$^{Lp/+}$; Grhl3$^{ct/+}$	6	0 (0)	100 (6)	0 (0)
Vangl2$^{Lp/+}$; Grhl3$^{ct/+; TgGrhl3/0}$	11	0 (0)	82 (9)	18 (2)
Vangl2$^{Lp/+}$; Grhl3$^{ct/ct}$	9	0 (0)	22 (2)	78 (7)
Vangl2$^{Lp/+}$; Grhl3$^{ct/ct; TgGrhl3/0}$	11	0 (0)	55 (6)	45 (5)

Table 6.1 - Phenotype of embryos from a Vangl2$^{Lp/+}$ (a) or Vangl2$^{Lp/+}$;Grhl3$^{ct/+}$ (b) x Grhl3$^{ct/ct;TgGrhl3/0}$ experimental cross.

A) Mice heterozygous for the mutant ct allele show significantly higher penetrance of SB with TFDs in the presence of both mutant Lp and the Grhl3 transgene (indicated by asterix) as opposed to either mutant allele alone ($p<0.05$, Chi Square). B) Mice with one or two copies of the mutant ct allele showed higher penetrance of TFDs and SB in the presence of a single Lp allele. This was not rescued by the presence of the Grhl3 transgene. Litters were analysed at E11.5. n = 6 and 9 litters in experimental crosses A) and B) respectively (De Castro et al., 2018a). Number of embryos in each group is indicated in brackets.

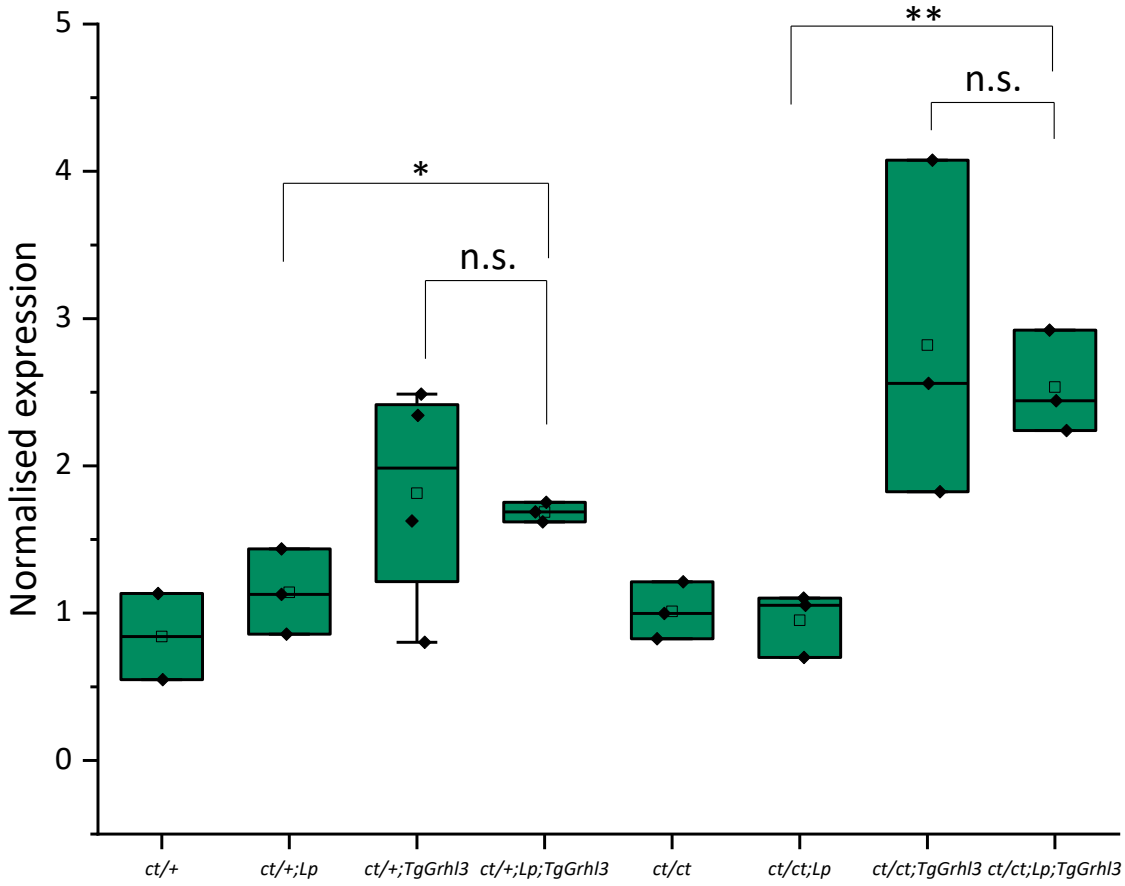

Figure 6.1 – qPCR to analyse Grhl3 expression in double mutants with and without the Grhl3 transgene.

*Increased expression of Grhl3 by the Grhl3 transgene is not affected by mutant Vangl2. Insertion of a Grhl3 transgene significantly increased expression of Grhl3 (t-test, * $p < 0.04$, ** $p < 0.003$). There was no significant difference between genotypes containing the transgene either with or without the mutant Lp allele (t-test, $p > 0.05$).*

6.2.2 - NTDs in *Vangl2*$^{Lp/+}$;*Grhl3*$^{ct/ct}$ double mutants are not rescued by increasing proliferation

Although overexpressing *Grhl3* did not rescue NTDs in double mutants, this does not disprove the hypothesis that disrupted *Grhl3* expression contributes to the phenotype via a distinct cellular mechanism. The lack of rescue could be due to an interaction between overexpression of *Grhl3* and *Vangl2,* or because the genetic interaction is via a non-*Grhl3* contribution of the *ct/ct* genotype. Previous work suggested that there may be reduced proliferation in the tail bud region of double mutant embryos as a result of the *ct/ct* genotype (Sophie Pryor, unpublished). It was reasoned that by increasing proliferation the severity of the phenotype may be reduced. Oral formate or inositol treatment, or intraperitoneal (IP) injection of adenine and thymidine,

have all been shown to partially rescue NTDs in *ct/ct* embryos (Greene and Copp, 1997, Cogram et al., 2004, Leung et al., 2013, Sudiwala et al., 2016) and to increase cell proliferation in the hindgut endoderm. The effect of all three treatments was therefore analysed in *Vangl2*$^{Lp/+}$*;Grhl3*$^{ct/(ct/+)}$ mutants.

The effect of formate or inositol were both tested by maternal treatment via drinking water (see methods Chapter 2.1.2). However, neither treatment significantly rescued the phenotype for any of the genotypes (Fisher's exact or Chi square, Tables 6.2 - 6.3, Figures 6.2 - 6.3). Of note, the protective effect of inositol or formate previously reported was not reproduced in this cross, possibly due to genetic background differences introduced by the *Vangl2*$^{Lp/+}$ strain. Interestingly, there was a trend towards a reduced proportion of SB affected *Vangl2*$^{Lp/+}$*;Grhl3*$^{ct/+}$ embryos after formate treatment and *Vangl2*$^{Lp/+}$*;Grhl3*$^{ct/ct}$ embryos after inositol treatment. Of particular note, one *Vangl2*$^{Lp/+}$*;Grhl3*$^{ct/ct}$ embryo displayed a straight tail after inositol treatment, which had not been observed previously in untreated embryos. Surprisingly, there was an increased proportion of SB affected *Vangl2*$^{Lp/+}$*;Grhl3*$^{ct/ct}$ embryos after formate treatment, suggesting that increased proliferation can also have a detrimental effect.

Adenine and thymidine were administered via IP injection at days E7.0, 8.0 and 9.0, before embryo collection at E9.5. Again, neither treatment significantly rescued NTDs (Fisher's exact or Chi square, Table 6.4, Figure 6.4). There was nevertheless a trend towards a reduced proportion of SB and EX affected *Vangl2*$^{Lp/+}$*;Grhl3*$^{ct/+}$ and *Vangl2*$^{Lp/+}$*;Grhl3*$^{ct/ct}$ embryos.

Genotype	No. embryos	Spinal Phenotype % (n)			
		Straight tail	Tail flexion defects	Spina bifida	Spina bifida & exencephaly
A. Control					
Vangl2$^{+/+}$; Grhl3$^{ct/+}$	8	88 (7)	12 (1)	0 (0)	0 (0)
Vangl2$^{Lp/+}$; Grhl3$^{ct/+}$	23	0 (0)	74 (17)	22 (5)	4 (1)
Vangl2$^{+/+}$; Grhl3$^{ct/ct}$	14	50 (7)	36 (5)	14 (2)	0 (0)
Vangl2$^{Lp/+}$; Grhl3$^{ct/ct}$	14	0 (0)	50 (7)	50 (7)	0 (0)
B. Formate treatment					
Vangl2$^{+/+}$; Grhl3$^{ct/+}$	10	100 (10)	0 (0)	0 (0)	0 (0)
Vangl2$^{Lp/+}$; Grhl3$^{ct/+}$	13	0 (0)	92 (12)	8 (1)	0 (0)
Vangl2$^{+/+}$; Grhl3$^{ct/ct}$	15	54 (8)	33 (5)	13 (2)	0 (0)
Vangl2$^{Lp/+}$; Grhl3$^{ct/ct}$	13	0 (0)	31 (4)	69 (9)	0 (0)

Table 6.2 - Phenotype of Vangl2$^{Lp/+}$;Grhl3$^{ct/+}$ x Grhl3$^{ct/ct}$ experimental cross after oral formate treatment.

There was no significant rescue of any genotype after treatment. Chi Square, $p > 0.05$ (for Vangl2$^{+/+}$;Grhl3$^{ct/ct}$ genotype). Fisher's exact, $p > 0.05$ (all other genotypes). For statistical comparisons, SB and SB+EX were pooled to give a total number of embryos with SB. Number of embryos in each group is indicated in brackets.

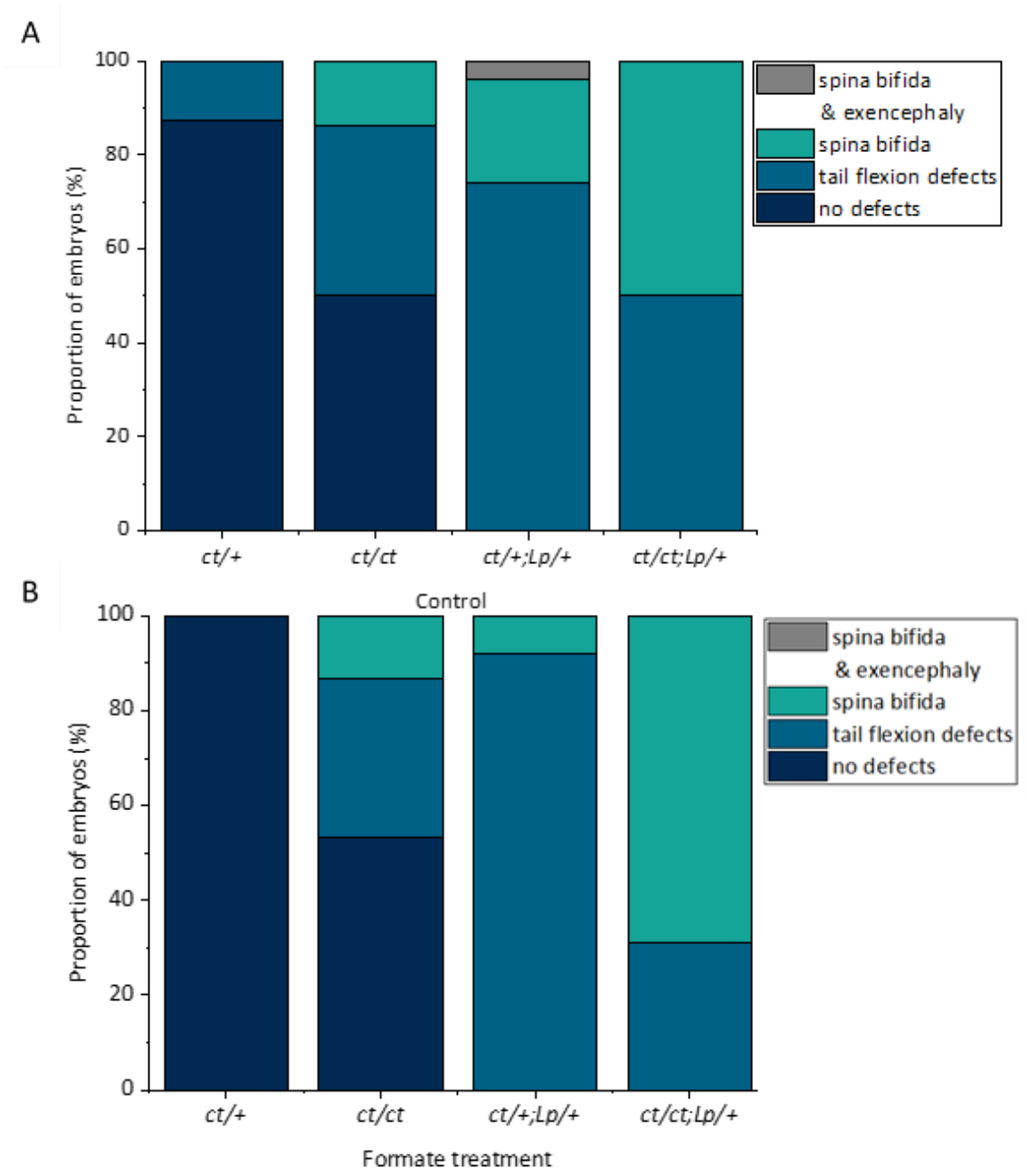

Figure 6.2 – Graphs showing phenotypes of control (A) and formate treated (B) embryos from Vangl2$^{Lp/+}$;Grhl3$^{ct/+}$ x Grhl3$^{ct/ct}$ experimental cross.

There was no significant rescue for any of the genotypes, although there was a trend towards a reduced proportion of SB affected Vangl2$^{Lp/+}$;Grhl3$^{ct/+}$ embryos and an increased proportion of SB affected Vangl2$^{Lp/+}$;Grhl3$^{ct/ct}$ embryos after formate treatment. For statistical comparisons, SB and SB+EX were pooled to give a total number of embryos with SB.

Genotype	No. embryos	Spinal Phenotype % (n)		
		Straight tail	Tail flexion defects	Spina bifida
A. Control				
Vangl2$^{+/+}$; Grhl3$^{ct/+}$	7	100 (7)	0 (0)	0 (0)
Vangl2$^{Lp/+}$; Grhl3$^{ct/+}$	6	0 (0)	100 (6)	0 (0)
Vangl2$^{+/+}$; Grhl3$^{ct/ct}$	6	50 (3)	50 (3)	0 (0)
Vangl2$^{Lp/+}$; Grhl3$^{ct/ct}$	8	0 (0)	50 (4)	50 (4)
B. Inositol treatment				
Vangl2$^{+/+}$; Grhl3$^{ct/+}$	12	92 (11)	8 (1)	0 (0)
Vangl2$^{Lp/+}$; Grhl3$^{ct/+}$	7	0 (0)	100 (7)	0 (0)
Vangl2$^{+/+}$; Grhl3$^{ct/ct}$	12	50 (6)	33 (4)	17 (2)
Vangl2$^{Lp/+}$; Grhl3$^{ct/ct}$	12	8 (1)	59 (7)	33 (4)

Table 6.3 - Phenotype of Vangl2$^{Lp/+}$;Grhl3$^{ct/+}$ x Grhl3$^{ct/ct}$ experimental cross after oral inositol treatment.

There was no significant rescue of any genotype after treatment. Chi Square, p > 0.05 (for Vangl2$^{+/+}$;Grhl3$^{ct/ct}$ and Vangl2$^{Lp/+}$;Grhl3$^{ct/ct}$ genotypes). Fisher's exact, p > 0.05 (for Vangl2$^{+/+}$;Grhl3$^{ct/+}$). Number of embryos in each group is indicated in brackets.

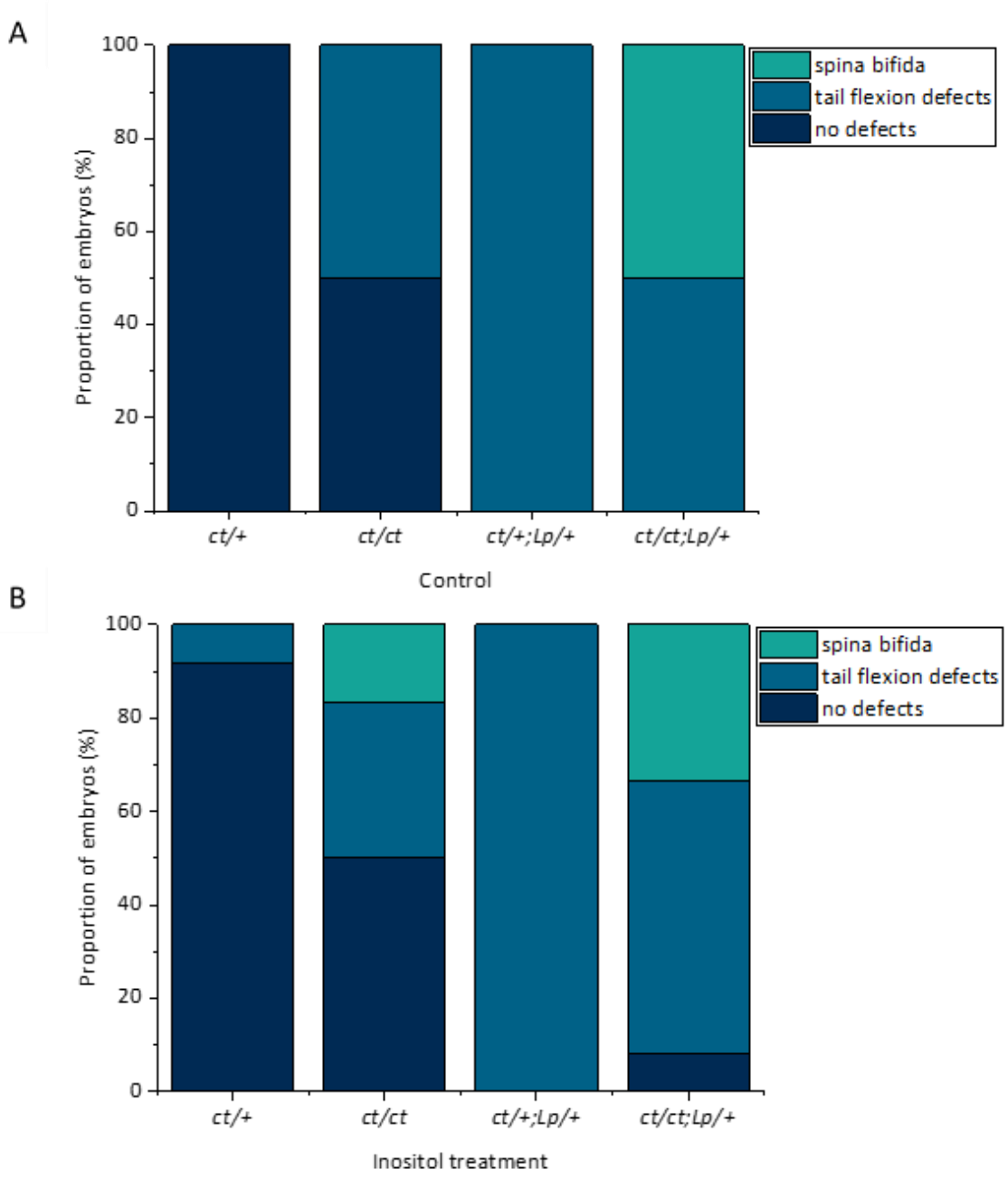

Figure 6.3 – Graphs showing phenotypes of control (A) and inositol treated (B) embryos from Vangl2$^{Lp/+}$;Grhl3$^{ct/+}$ x Grhl3$^{ct/ct}$ experimental cross.

There was no significant rescue for any of the genotypes, although there was a trend towards a reduced proportion of SB affected Vangl2$^{Lp/+}$;Grhl3$^{ct/ct}$ embryos after inositol treatment.

Genotype	No. embryos	Spinal Phenotype % (n)				
		Straight tail	Tail flexion defects	Spina bifida	Tail flexion defects & exencephaly	Spina bifida & exencephaly
A. Control						
Vangl2$^{+/+}$; Grhl3$^{ct/+}$	7	100 (7)	0 (0)	0 (0)	0 (0)	0 (0)
Vangl2$^{Lp/+}$; Grhl3$^{ct/+}$	12	0 (0)	75 (9)	17 (2)	8 (1)	0 (0)
Vangl2$^{+/+}$; Grhl3$^{ct/ct}$	13	54 (7)	38 (5)	0 (0)	0 (0)	8 (1)
Vangl2$^{Lp/+}$; Grhl3$^{ct/ct}$	10	0 (0)	20 (2)	60 (6)	10 (1)	10 (1)
B. Adenine/thymidine treatment						
Vangl2$^{+/+}$; Grhl3$^{ct/+}$	18	100 (18)	0 (0)	0 (0)	0 (0)	0 (0)
Vangl2$^{Lp/+}$; Grhl3$^{ct/+}$	10	0 (0)	90 (9)	0 (0)	10 (1)	0 (0)
Vangl2$^{+/+}$; Grhl3$^{ct/ct}$	10	60 (6)	30 (3)	10 (1)	0 (0)	0 (0)
Vangl2$^{Lp/+}$; Grhl3$^{ct/ct}$	15	0 (0)	40 (6)	60 (9)	0 (0)	0 (0)

Table 6.4 - Phenotype of Vangl2$^{Lp/+}$;Grhl3$^{ct/+}$ x Grhl3$^{ct/ct}$ experimental cross after IP injection of adenine/thymidine.

There was no significant rescue of any genotype after treatment. Chi Square, p > 0.05 (for Vangl2$^{+/+}$;Grhl3$^{ct/ct}$ genotype). Fisher's exact, p > 0.05 (for Vangl2$^{Lp/+}$;Grhl3$^{ct/+}$ and Vangl2$^{Lp/+}$;Grhl3$^{ct/ct}$). For statistical comparisons, SB and SB+EX, and TFDs and TFDs+EX, were pooled to give a total number of embryos with SB and TFDs respectively. Number of embryos in each group is indicated in brackets.

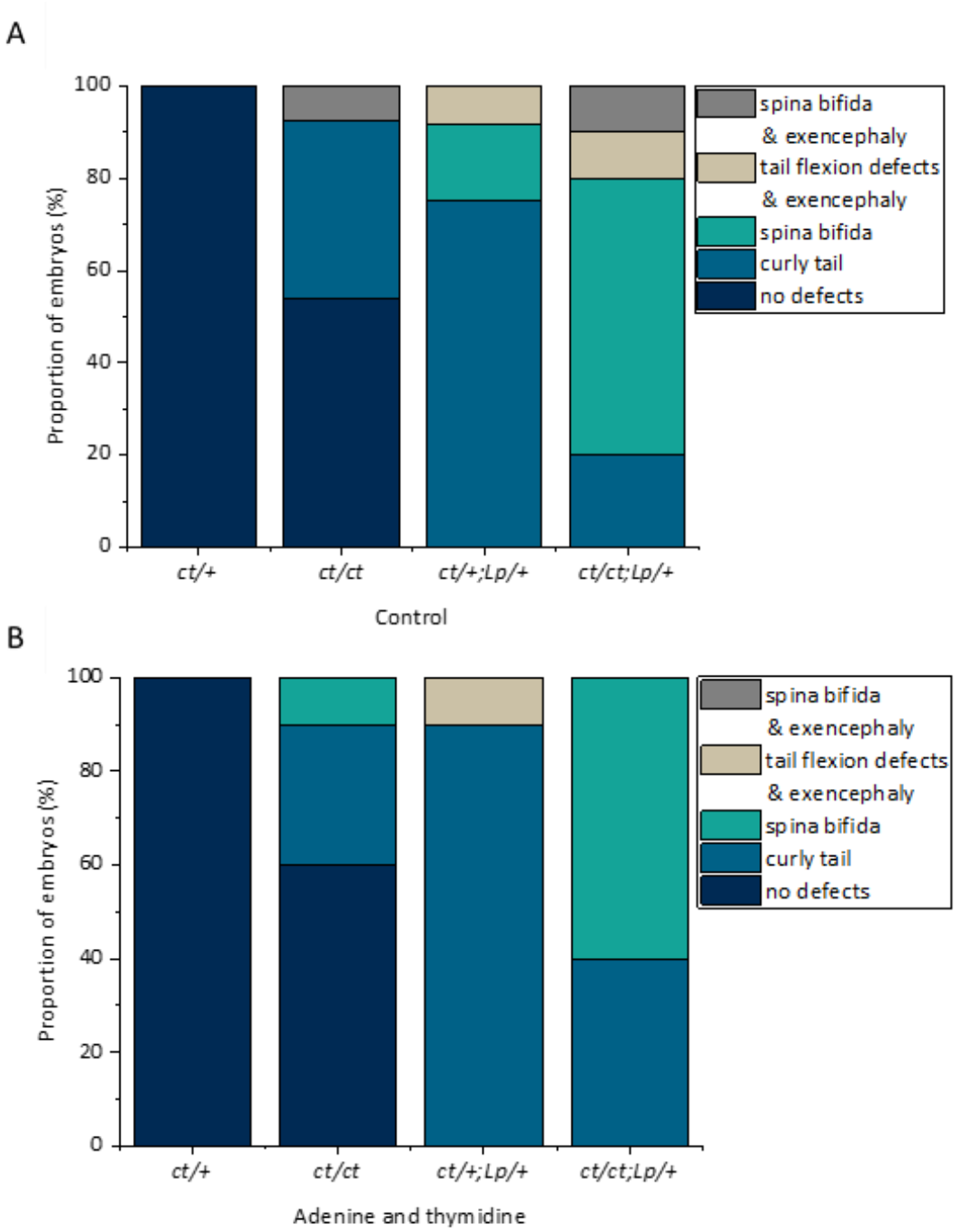

Figure 6.4 – Graphs showing phenotypes of control (A) and adenine/thymidine treated (B) embryos from Vangl2$^{Lp/+}$;Grhl3$^{ct/+}$ x Grhl3$^{ct/ct}$ experimental cross.

There was no significant rescue for any of the genotypes, although there was a trend towards a reduced proportion of SB and EX affected Vangl2$^{Lp/+}$;Grhl3$^{ct/+}$ and Vangl2$^{Lp/+}$;Grhl3$^{ct/ct}$ embryos after adenine/thymidine injection. For statistical comparisons, SB and SB+EX, and TFDs and TFDs+EX, were pooled to give a total number of embryos with SB and TFDs respectively.

6.2.3 - IP treatment increases proliferation in the tailbud region

The fact that treatments expected to increase proliferation did not rescue NTDs in any genotype could be explained by two possibilities: decreased proliferation in the tail bud is not the exacerbating mechanism in these double mutants, or these treatments were failing to increase proliferation in the tailbud. The second possibility was tested using an EdU proliferation assay in combination with pHH3 immunofluorescence (Figure 6.5, see methods Chapter 2.1.2). Due to a lack of embryos containing the mutant *Vangl2*$^{Lp/+}$ allele in this experiment, groups were compared by their *ct* genotype. Adenine/thymidine treatment led to an increased proportion of pHH3-positive cells (late G2 - M phase) in the tailbud, suggesting increased proliferation rate. However, EdU incorporation (labels cells during S phase) did not reveal a significant effect of treatment on labelling, suggesting a similar proportion of cells in S-phase during the labelling period (Figures 6.5 - 6.6). There are two possible explanations for the comparable EdU labelling between treated and untreated groups: first, if there is any pro-proliferative effect of nucleotide treatment it is not mediated during S-phase, or second, the EdU staining technique is not sensitive enough to detect differences in EdU incorporation between groups.

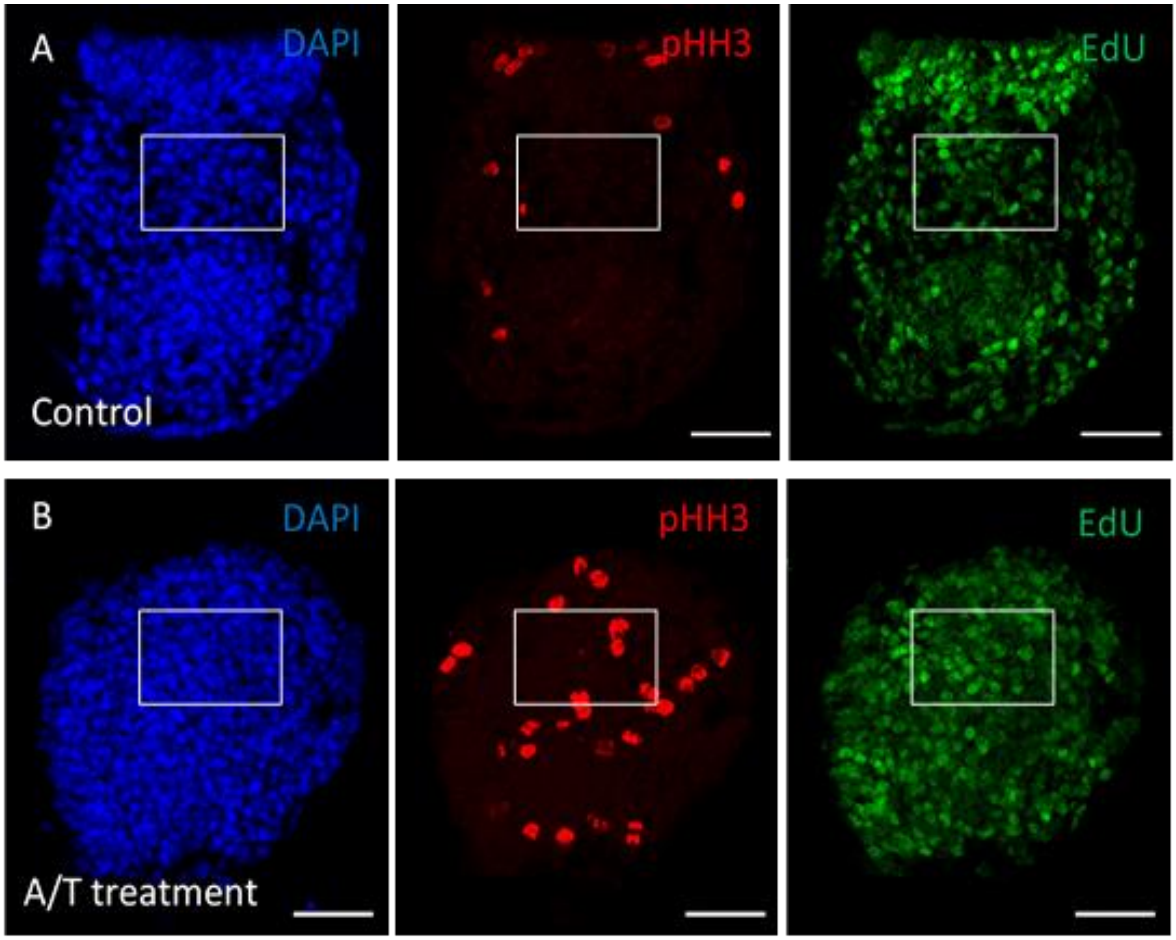

Figure 6.5 – Tailbud pHH3 and EdU staining from control and adenine/thymidine treated embryos.

pHH3 and EdU incorporation can be used to measure the number of cells in the tailbud in G2/M phase and S-phase respectively. A,B) Representative images of control (A) and adenine/thymidine treated (B) E9.5 tailbuds showing DAPI, pHH3 and EdU fluorescence. The white box represents the region analysed. Scale bars = 50 µm.

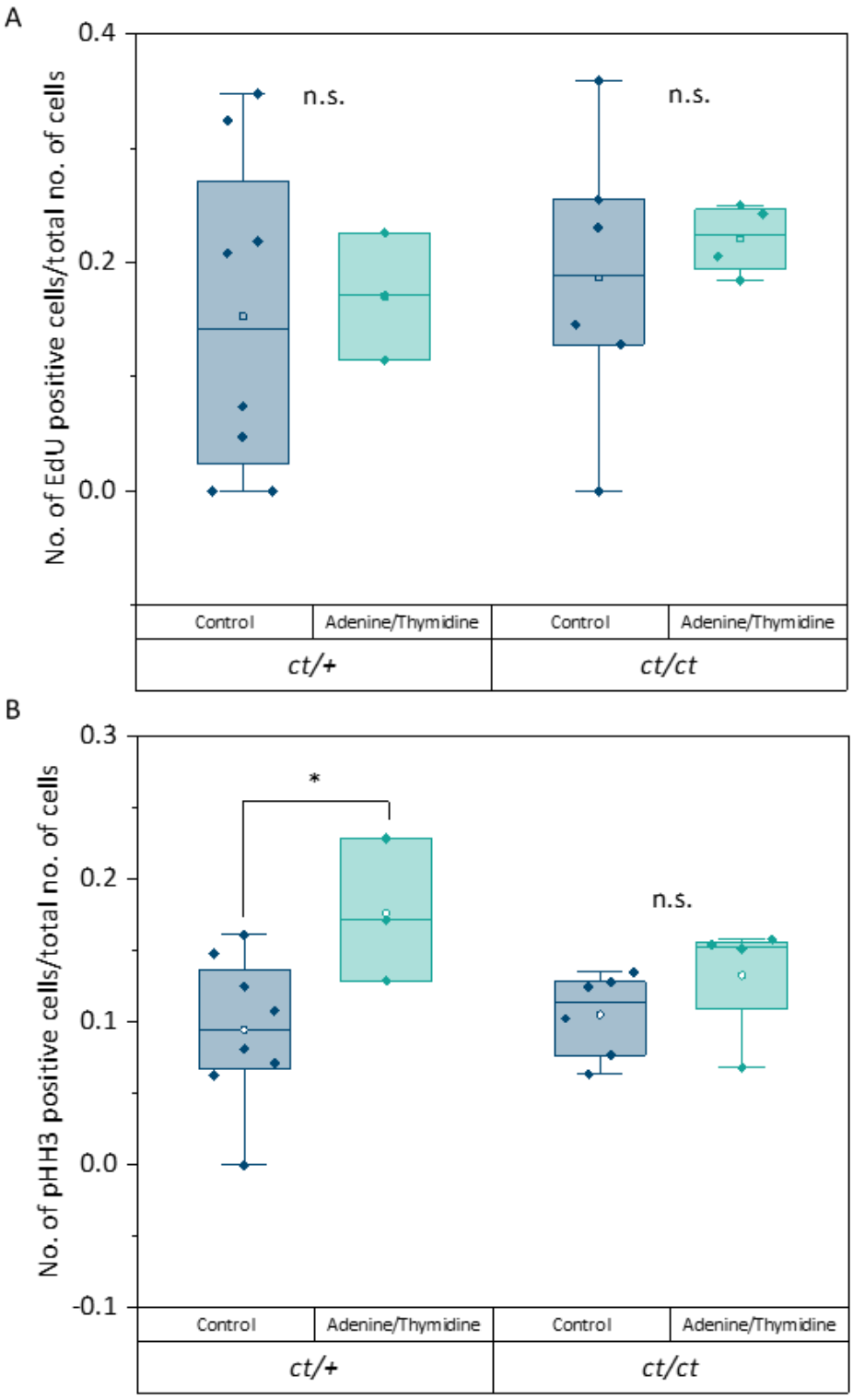

Figure 6.6 – Tailbud pHH3 and EdU quantification from control and adenine/thymidine treated embryos.

Adenine/thymidine treatment significantly increases the number of cells in G2/M phase in the tailbud as measured by pHH3 immunostaining, but not the number of cells which pass through S phase, as measured by an EdU assay. A, B) Quantification of the proportion of total cells (number of DAPI positive cells) which are positive for EdU (A) and pHH3 (B). There are significantly more pHH3 positive cells after adenine/thymidine treatment in ct/+ embryos (t-test, $p < 0.05$).

6.2.4 – EdU can be administered via *ex utero* embryo culture

EdU staining is a widely used assay to determine the proportion of cells which pass through S-phase during the labelling period as a measure of proliferation, however it is more commonly used in cells than *in vivo.* IP administration of EdU may not be as sensitive a technique, as there is a delay between embryo collection and fixation where cells may continue to progress through the cell cycle and incorporate EdU. Indeed, samples collected after this technique were difficult to analyse, due to the saturation of EdU positive staining (Figure 6.6), and a computational filter had to be applied to every image in order to reduce the signal and obtain a non-biased value. An alternative method was therefore tested where CD1 embryos were cultured for a short time in a considerably lower concentration of EdU (between 500 µM and 1 mM). Various concentrations and times were tested; at the lower concentration of 500 µM, short culture windows of 30 minutes were not sufficient for EdU incorporation, while longer culture windows of 1 - 2 hours produced clear staining (Figure 6.7). High quality staining was also obtained at a higher concentration of 1 mM, although the lower proportion of pHH3 positive cells in this group compared to samples in Figure 6.6B and 6.8A suggests this higher concentration may itself affect proliferation. Importantly, the staining in positive samples did not saturate the image, which allowed analysis without a computational filter. Nevertheless, for the purposes of this preliminary study to compare *in vivo* and *in vitro* methods of EdU administration, EdU positive cells were counted using the same filter; the range of positive cells was greater in the culture samples, demonstrating it as a more sensitive method for detecting differences in proliferation (Figure 6.8).

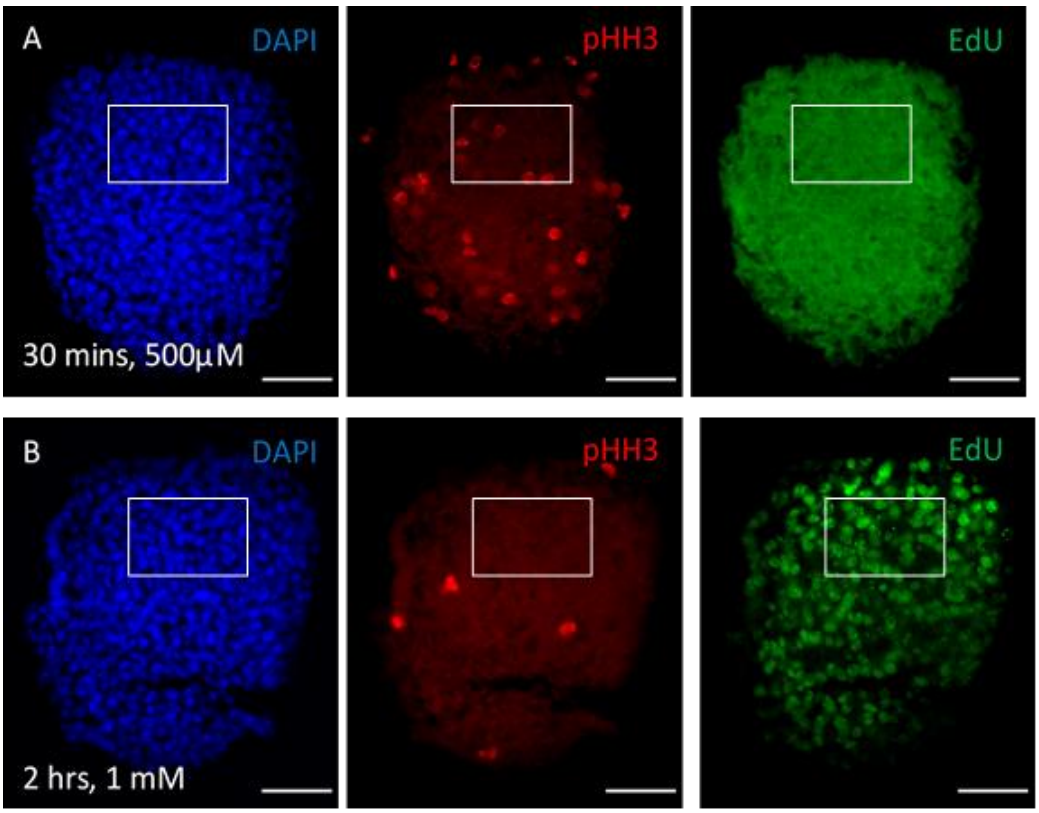

Figure 6.7 – Tailbud pHH3 and EdU staining after in vitro EdU administration.

Longer culture periods and a higher EdU concentration give high quality EdU staining in mouse embryos. A) E9.5 tailbuds do not show positive EdU staining after embryos are cultured in 500 µM EdU solution for 30 minutes. B) E9.5 tailbuds show high quality staining after embryos are cultured in 1 mM EdU solution for 2 hours. Scale bars = 50 µm.

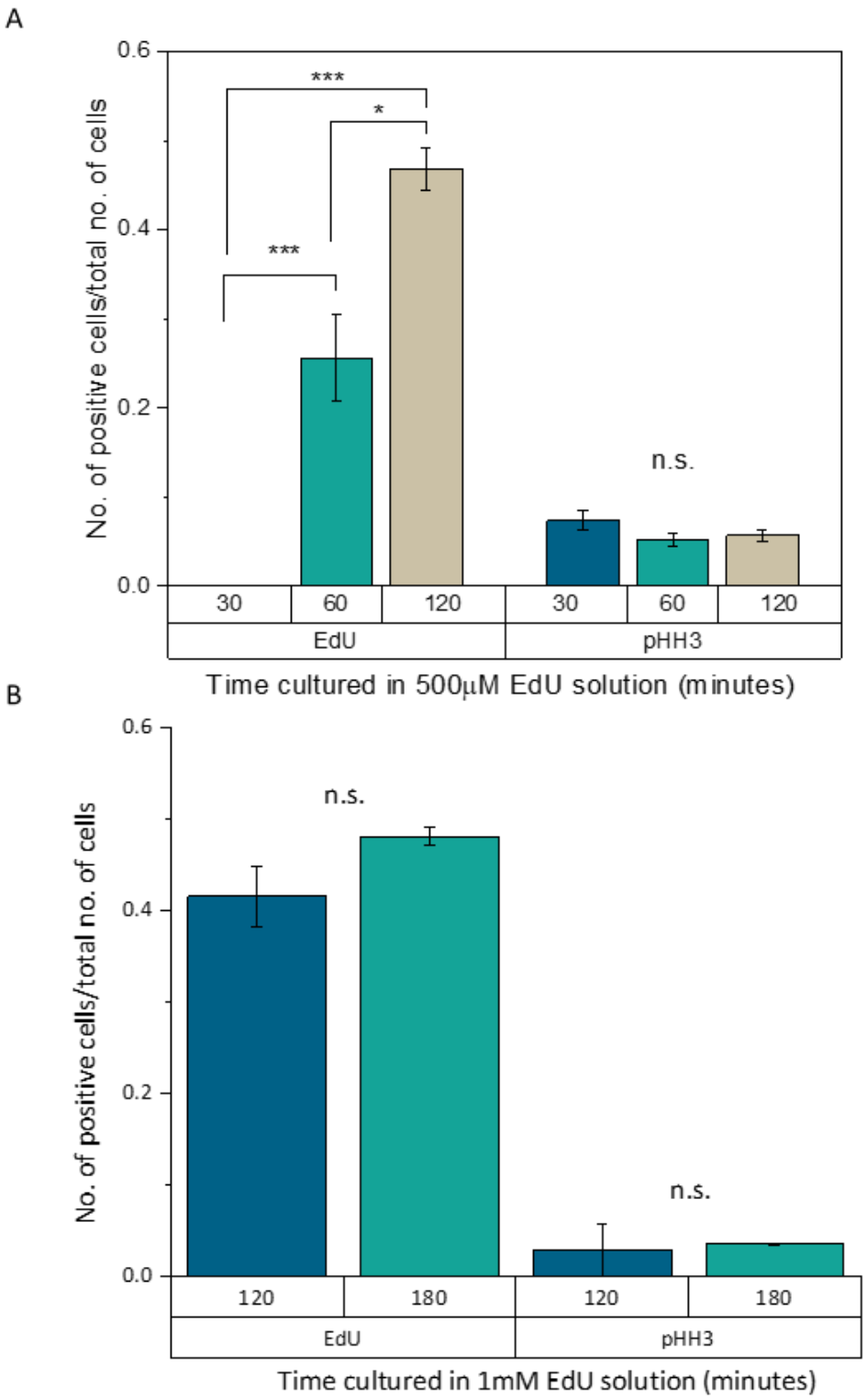

Figure 6.8 – Quantification of tailbud pHH3 and EdU staining after in vitro EdU administration.

Culture of E9.5 embryos in EdU solution gives high quality staining which can be easily analysed. A) 500 μM EdU solution stains an increasing proportion of cells with longer culture windows, with 120 minutes giving the optimum proportion. The number of positive cells at 60 minutes was significantly higher than 30 minutes (t-test, $p < 6 \times 10^{-4}$), and the number of positive cells at 120 minutes was significantly higher than 30 and 60 minutes (t -test, $p < 6 \times 10^{-5}$ and 0.03 respectively). pHH3 incorporation was not affected by the culture length. B) At 1 mM concentration, EdU staining is optimum at 120 minutes, and is not significantly changed for longer culture periods. pHH3 incorporation was not affected by the culture length.

6.2.5 – EdU incorporation in culture does not reveal decreased tailbud proliferation in *ct/ct*

Having established a successful EdU culture method, this was utilised to repeat the previous comparison of tailbud proliferation between genotypes, either with or without adenine/thymidine treatment. A concentration of 500 µM was chosen with a 1 hour incubation, due to the possible effects of the 1 mM concentration on proliferation. The purpose of this experiment was firstly to test whether adenine/thymidine treatment was successfully increasing proliferation in the tailbud, and secondly to replicate previous findings that show reduced tailbud proliferation in *ct/ct* embryos, regardless of their *Vangl2* genotype (Pryor et al., unpublished). As shown in the culture optimisation experiment in the previous section, EdU culture was much more sensitive to differences in the number of cells which pass through S phase than *in vivo* administration, and adenine/thymidine treatment increased the number of EdU positive cells in 2/3 groups analysed, although significance was not reached due to low sample numbers (Figure 6.9A). When samples were combined by either their *ct* or *Lp* genotype, all groups analysed showed a non-significant increase after treatment (Figure 6.10). Only 1/3 groups analysed showed a significant increase in pHH3 positive cells, however the very low number of positive cells makes this a less sensitive technique to analyse proliferation differences (Figure 6.9B). These results suggest that adenine/thymidine treatment is successfully increasing proliferation in the tailbud.

As a preliminary experiment with very low sample numbers, not all genotypes were represented, making it difficult to draw conclusions on the effects of genotype. Surprisingly, using EdU to measure the number of cells which pass through S-phase, control homozygous *Grhl3*$^{ct/ct}$ embryos showed a trend towards an increased number of cells passing through S phase compared to heterozygous *Grhl3*$^{ct/+}$, regardless of *Vangl2* genotype (Figure 6.9A, 6.10A). This difference was lost after adenine/thymidine treatment. The effect of *Vangl2* genotype was also analysed, despite previous findings that proliferation was not affected by the *Lp* allele. Again, these results were surprising, showing a trend towards an increased proportion of cells in S-phase in mutant *Vangl2*$^{Lp/+}$ embryos compared to controls (Figure 6.10B).

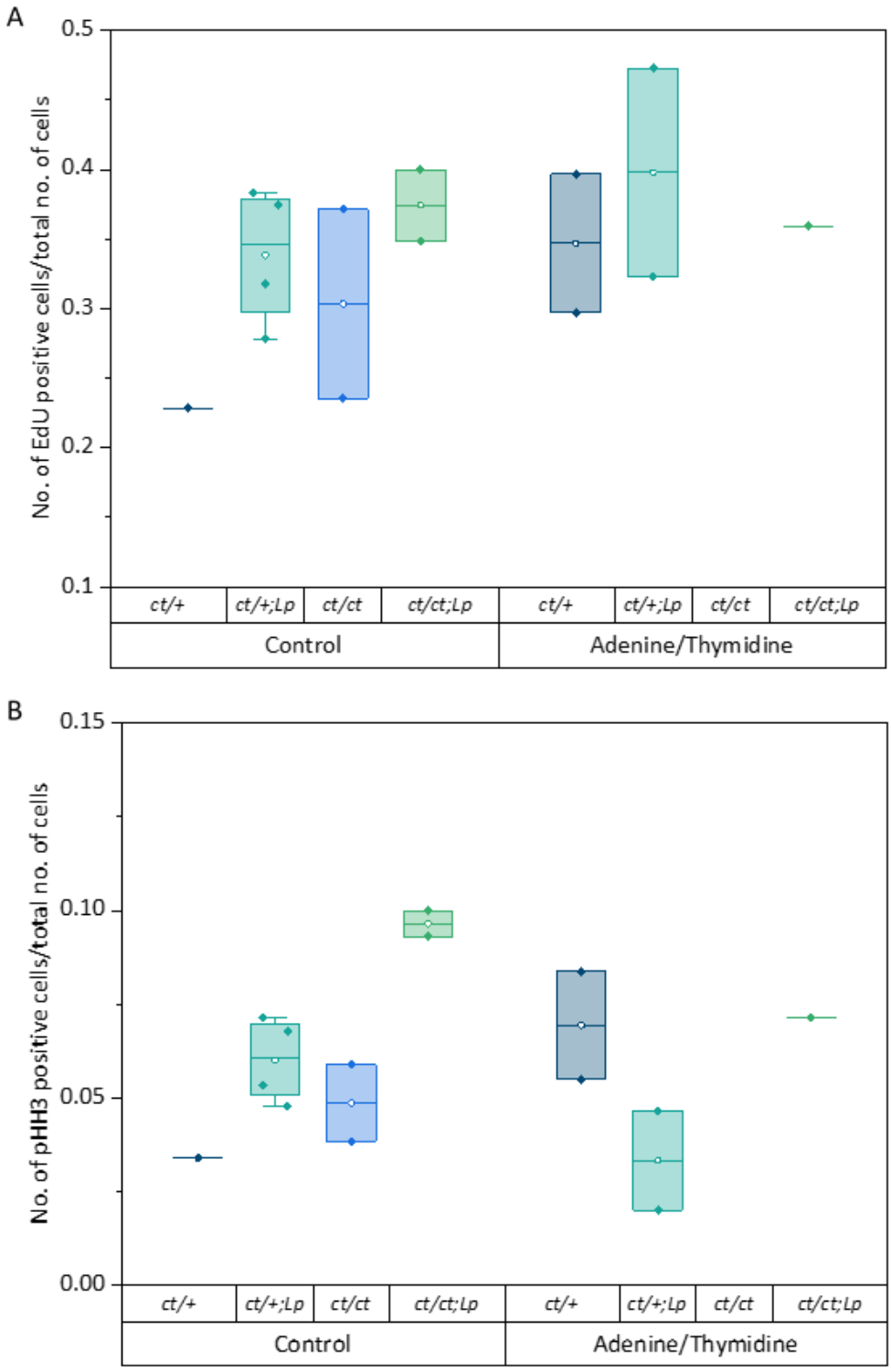

Figure 6.9 – Quantification of tailbud pHH3 and EdU from control and adenine/thymidine treated embryos after in vitro EdU administration.

Culture in EdU is more sensitive to changes in the number of cells which pass through S-phase after adenine/thymidine treatment than in vivo administration. A) The number of EdU positive cells increased after treatment in 2/3 genotypes, with the final comparison not possible due to low sample size. In the control group, both mutant ct and Lp cause a trend towards increased tailbud EdU incorporation, by comparing ct/+ and ct/ct either with or without mutant Lp, and vice versa. B) Only 1/3 groups showed an increased number of cells in G2 - M phase after adenine/thymidine treatment by analysing the number of pHH3 positive cells.

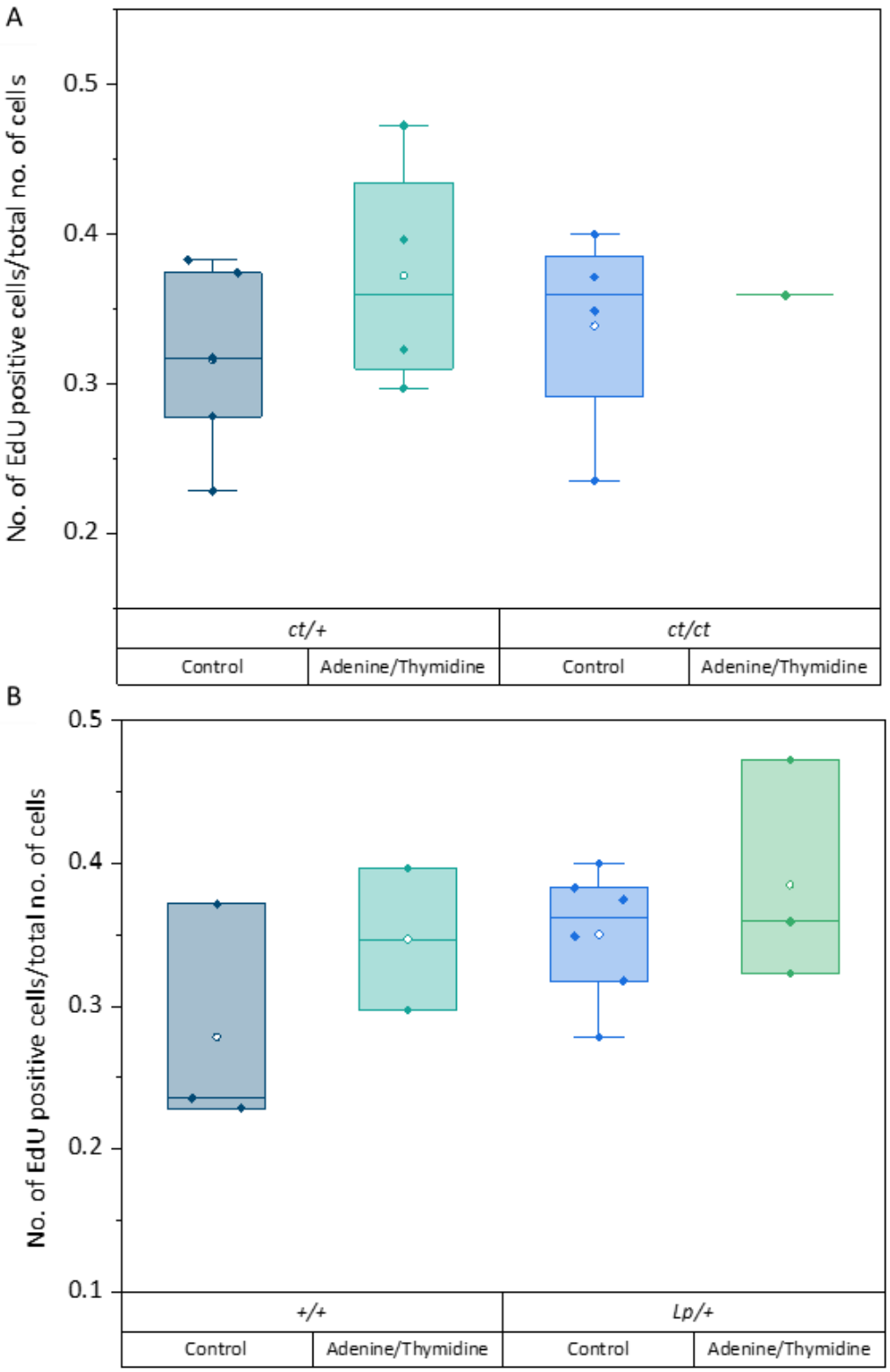

Figure 6.10 – Quantification of tailbud pHH3 and EdU by ct or Lp genotype from control and adenine/thymidine treated embryos after in vitro Edu administration.

Both mutant Lp and ct embryos show a trend towards an increased number of cells which pass through S phase in the tailbud compared to controls. A) Homozygous ct/ct embryos show a trend towards increased tailbud S-phase progression compared to heterozygotes when Lp genotype is not considered. B) Mutant Lp embryos show a trend towards increased tailbud EdU incorporation compared to wild types when ct genotype is not considered.

6.3 - Discussion

In this chapter, reduced tailbud proliferation as the potential mechanism underlying the contribution of the *ct* genotype to *Lp/ct* NTDs was explored using genetic and experimental approaches. Neither increasing expression of *Grhl3* or treatments expected to stimulate proliferation provided direct evidence that this is the exacerbating mechanism in *Lp/ct* double mutants. However, some evidence prevents this hypothesis from being ruled out.

First, as discussed in Chapter 5, overexpression of *Grhl3* also causes NTDs. In $Grhl3^{ct/ct;TgGrhl3/0}$ embryos, expression of *Grhl3* is slightly higher than that found in BALB/c wild type mice, and it is clear that neurulation is very sensitive to the levels of this gene (see Chapter 1.4.4 and Figure 1.4). The more severe phenotype in double mutants could be due to an additive genetic interaction between the mutant $Vangl2^{Lp}$ allele and *Grhl3* overexpression.

Second, although inositol, formate and IP injection of an adenine/thymidine solution are all treatments known to partially rescue hypo-proliferation in the hindgut in *ct/ct* embryos, none of these treatments have been proven to stimulate tailbud proliferation. Previous work has shown that inositol stimulates proliferation in the hindgut but not the NE or notochord, while the effect on the tailbud region (which consists of NE and mesoderm precursors) was not examined (Cogram et al., 2004). Intraperitoneal injection of nucleotides significantly rescues the phenotype in *ct* embryos and stimulates proliferation in the NE as well as the hindgut, suggesting that it may stimulate broader regions and could have an effect on the tailbud (Leung et al., 2013).

Nevertheless, the work presented in this chapter does not support reduced tailbud proliferation as a causative mechanism, both by failing to rescue NTDs and replicating tailbud differences between genotypes. Measuring the number of cells which pass through S phase during the labelling period by EdU incorporation during culture suggests that adenine/thymidine treatment does increase tailbud proliferation. However, a particularly surprising finding from this work is that administration of EdU via IP injection and embryo culture shows a trend towards increased incorporation in the tailbud (indicative of cell cycle progression/proliferation) in $Grhl3^{ct/ct}$ compared to $Grhl3^{ct/+}$ embryos, although this is very mild. It is possible that there is a defect in progression to G2/M phase caused by the *ct* genotype, which would explain reduced pHH3 staining in previous work (Pryor et al., unpublished). However, there was no difference in the number of pHH3-positive cells, thus failing to support this hypothesis.

It must also be taken into account that the genotypes compared in this study are not the same as the previous work which showed reduced proliferation – this was between $Grhl3^{ct/ct}$ and $Grhl3^{+/+}$, and was therefore comparing mice with different levels of the *ct* background (Pryor et

al., unpublished). It is possible that the background effects of the *ct* strain influence proliferation by directly affecting the potential *Grhl3*^{ct} proliferative defect. In addition, the proportion of NTDs in double mutants are lower in this experiment than previously reported. The *ct* strain has been known to show especially variable penetrance – early publications reported ~50% SB affected embryos, while this has dramatically reduced to ~10% (van Straaten and Copp, 2001). It could be that the degree of proliferation differences have also drifted over time, although this is unlikely, given that the rates of NTDs in our colony have been relatively stable for over 10 years.

Finally, it is possible that differences in proliferation in the adenine/thymidine treated groups could not be detected using EdU because EdU is a thymidine analogue (Chehrehasa et al., 2009). This suggests that these two molecules could be in competition when binding to DNA, thus reducing the number of EdU positive cells. Even if this is the case, adenine/thymidine treatment did not rescue NTDs, supporting the conclusion that tailbud proliferation is not a causative mechanism in these mutants.

Future work should focus on first, increasing sample sizes to rule out a proliferation defect in the tailbud as a mechanism contributing to NTDs, and second, identifying novel causative mechanisms. It is possible that the *Vangl2/ct* and *Vangl2/Grhl3* interactions involve partially different mechanisms. Indeed, two publications analysing the interaction of *Grhl3* and *Vangl2* implicate the SE or epidermis as an important tissue, perhaps unsurprising due to the expression patterns of *Grhl3*. In 2010, work from Stephen Jane's group showed that 67% of *Vangl2*$^{+/-}$*;Grhl3*$^{+/-}$ embryos develop SB, and although their work did not further analyse the mechanisms behind NTDs in these mutants, they showed that both early and late embryonic wound healing in the epidermis was abnormal (Caddy et al., 2010). This was via specific binding of *Grhl3* to a promoter region of *RhoGEF19*, which regulates the PCP pathway by activating RhoA signalling. Importantly, actin dynamics were disrupted in these embryos: first, the actin cable which normally forms around lesions during wound healing showed a disorganised structure; second, leading edge cells failed to polarise, which is essential for normal cell migration (Caddy et al., 2010). Nevertheless, our lab has been unable to reproduce the finding that *RhoGEF19* expression is affected by *Grhl3*, and there is little evidence that it is involved in regulating PCP family members.

More recently, a potential interaction between these genes was analysed in a *Grhl3* misexpressing mouse model, which showed clear upregulation of actin in mutant E4.5-5.5 embryos (Kimura-Yoshida et al., 2018). The misexpression of *Grhl3* in these embryos was ubiquitous, leading to failure of growth and development after implantation and making these

findings difficult to reconcile with neurulation. However, the authors also analysed the phenotype of mutant mice which retained GRHL3 protein in the nucleus (*Grhl3*$^{NLS/NLS}$), thus preventing potential cytoplasmic interactions with VANGL2 – 57% of these embryos developed mild SB. When crossed with *Vangl2*$^{Lp/+}$ mutant mice, 29% of *Vangl2*$^{Lp/+}$;*Grhl3*$^{NLS/+}$ embryos showed SB, further supporting an interaction in the cytoplasm as the causative mechanism. On the other hand, *Grhl3* is a known transcription factor, making any direct interactions more likely to be at the gene expression level than at the protein level. Finally, AFM of *Grhl3*$^{Cre/Cre}$ embryos showed that loss of *Grhl3* led to a reduced stiffness in the SE (Kimura-Yoshida et al., 2018).

Together, these studies suggest that it would be useful to analyse the biomechanical properties of the SE in double mutants. As discussed in Chapter 5, *Grhl3* mutants do not appear to have a biomechanical defect. Loss of *Vangl2* in *Grhl3* expressing domains disrupts polarisation of both SE and NE cells, leading to mild SB in 67% of embryos – however, the incomplete penetrance of the phenotype, combined with a varying proportion of recombined cells in the NE, implies that the causative biomechanical deficit is in the NE (Galea et al., 2018). Interactions between these genes may reveal a novel interaction between *Grhl3* and the PCP pathway in causing spinal NTDs. The publications discussed here suggest that this could be via one or a combination of the following defects: abnormal formation of the F-actin cable running along the PNP; disrupted polarisation and/or migration of SE cells during closure; defective biomechanical tissue properties such as stiffness.

Nevertheless, the possibility that tailbud proliferation is abnormal and causative must not be disregarded – increased sample sizes are necessary, and it is not yet clear if hypomorphic *Grhl3* causes tailbud proliferation to increase, decrease or neither. If previous work is confirmed and tailbud proliferation is decreased, the lack of rescue from any proliferation-stimulating treatments suggests that this mechanism is not causative. However, if tailbud proliferation is increased in double mutants, these treatments could in fact exacerbate NTDs. Cell cycle length analyses, for example by labelling samples with EdU over set intervals and collecting samples throughout the labelling period, could provide a more precise insight to cell dynamics in the tailbud (Nowakowski et al., 1989). Clearly, the pathology of these double mutants is highly complex, and remains an ongoing challenge in our understanding of multigenic NTDs.

Chapter 7 - General Discussion

7.1 – Summary of key findings

The main aim of the work presented in this thesis was to characterise the biomechanical properties and function of the SE during primary neurulation. Abnormal mechanics can cause NTDs, as in the *Zic2*$^{Kum/Kum}$ and *Grhl3*$^{Cre/+}$;*Vangl2*$^{Fl/Fl}$, both of which are believed to show a primary defect in the NE (Galea et al., 2017, Galea et al., 2018). Meanwhile, whether the SE plays an active biomechanical part in closure, or is passively shaped by the NE, was not known. The severe NTDs in *Grhl-2* and *-3* mutants, and the SE-derived protrusions which mediate the first contact between the neural folds, suggest the former (Rolo et al., 2016b, Nikolopoulou et al., 2019). This thesis begins to answer this question.

Previous observations that the midline SE are rostrocaudally elongated were confirmed in Chapter 3. These cells show a significantly higher aspect ratio compared to lateral SE, and their long axes are rostrocaudally oriented. Single border laser ablation was developed and optimised in the E9.5 mouse embryo SE, in order to investigate the hypothesis that the SE midline is passively stretched. Although midline cells do show higher levels of YAP nuclear translocation, indicative of higher strain, and midline cells at the ZP recoil significantly more than lateral cells, they in fact show lower recoil compared to SE overlying the pre-somitic mesoderm and somite region. As well as this, length or angle of the ablated cell border does not correlate with recoil. This suggests a model whereby first, cell shape does not predict recoil in the SE, and second, SE shape at the ZP may reflect active cell behaviours.

In Chapter 4, the effects of treatments predicted to alter SE biomechanics on NTC were investigated. Blebbistatin treatment showed a trend towards reduced recoil in treated SE cells compared to vehicle, suggesting that laser ablation in this system provides an indication of actomyosin mediated tension. E-cadherin blocking antibody revealed a complex role of this adherens junction protein during closure. Limitations of the technique, as discussed in Chapter 4, make it difficult to conclude that E-cadherin function is required for closure, however the biomechanical abnormalities observed in this experiment strongly suggest that normal SE cell adhesion is important for closure.

Indeed, study of *Grhl-2* and *-3* loss- and gain-of-function mutants supports this conclusion, showing that the SE must maintain its epithelial properties during primary neurulation. *Grhl2* mutants show a distinct loss of normal SE cell shape, abnormal actomyosin organisation in the SE and along the cable, and in the case of *Grhl2*$^{-/-}$ embryos, display increased tissue and cell level

recoil and an abnormal pattern of YAP nuclear translocation (Chapter 5 and (Nikolopoulou et al., 2019)). While recoil, cell shape and actomyosin are not significantly disrupted in *Grhl3* mutants, epithelial dynamics may still be altered through altered desmosomal function. Importantly, the data from Chapter 5 further supports the hypothesis that the SE actively facilitates closure.

Finally, Chapter 6 explored an alternative, non-biomechanical function of *Grhl3* in *Vangl2*$^{Lp/+}$;*Grhl3*$^{ct/ct}$ double mutant embryos. Reduced tailbud proliferation has been previously observed in these compound mutants using pHH3 staining as a measure of mitotic index, leading to the hypothesis that this is the contributing mechanism of mutant *Grhl3* in causing NTDs. However, EdU incorporation did not support this, either suggesting that proliferation is not reduced or that progression of cells from S phase to G2/M phase is decreased. If the former is the case, alternative mechanisms must be considered – as *Grhl3* is predominantly expressed in the SE, a cellular mechanism in which this tissue is abnormal is a possibility. Importantly, overexpression of *Grhl3* in *Vangl2*$^{Lp/+}$;*Grhl3*$^{ct/+;TgGrhl3}$ embryos can also cause severe NTDs that are not present in either of the individual heterozygotes, thus identifying an additional genetic interaction and providing a model for future analysis.

7.2 – Dissecting the molecular contribution of SE components in spinal closure

Much of the existing evidence for the causative role of the SE in NTDs comes from the study of genetic mutants. The disadvantage of genetic models is that, in the majority of cases, a number of molecules are disrupted by the main mutant gene; in more complex models such as *ct*, multiple mutant loci interact to produce the mutant phenotype. As a result, it is a challenge to dissect out the role and the relative importance of individual components in these models. Experimental manipulation of individual components can overcome this challenge. In Chapter 4, pharmacological blockade of E-cadherin in cultured mouse embryos began to unravel how cell-cell adhesion specifically in the SE is important for spinal closure. E8.5 embryos cultured for 24 hours in 1:200 blocking antibody showed a significantly higher PNP curvature than controls; some of these samples also showed a lack of or abnormal F-actin cable. The trend towards increased SE recoil after laser ablation in E9.5 embryos cultured for 2 hours provides a third phenotype, alongside the PNP curvature and abnormal cable, which is reminiscent of the *Grhl2*$^{-/-}$ phenotype.

An interesting observation from Chapter 4 is that loss of E-cadherin function does not alter SE cell shape along the midline. The fact that PNP curvature was altered, while PNP length was not,

suggests that the elongated shape found in wild types is a more reliable predictor of PNP length. Meanwhile, PNP curvature can be abnormal while cell elongation persists, suggesting that cell shape cannot be the only biomechanical readout to predict closure progression. Whether the ML YAP gradient of nuclear translocation is still present in embryos lacking E-cadherin function but with normal cell shape, will be an important question to dissect out the relevance of the YAP gradient to closure.

Overall, the PNP curvature, F-actin cable and SE recoil phenotype observed in embryos lacking normal E-cadherin function provides strong evidence that misexpression of *Cdh1* is a major driver of abnormal mechanics in the SE, causing failed closure in *Grhl2* mutants. Claudins are also required for closure in chick and mouse – in one study, culture of chick and mouse embryos in claudin blocking peptides prevented closure, concomitant with abnormal CE movements and apical constriction in the NE (Baumholtz et al., 2017). This suggests that cell-cell adhesion mediated by tight junctions is also an important player during neurulation, and although this paper focused on the role of claudins in the NE, it is likely that the SE was also affected. Whether desmosome components also play a similar role is unknown, and would provide an interesting question for future work.

7.3 – The role of E-cadherin and YAP along the rostrocaudal midline

In Figure 4.4, immunostaining for the E-cadherin blocking antibody did not detect signal along the midline or along the neural folds. This was reflected in the more intense staining of the non-blocking antibody in the same regions, in both treated and control embryos. These results strongly suggest that E-cadherin turnover is higher along the midline and along the neural folds, with the rapid internalisation of E-cadherin blocking antibody preventing its detection in these regions. Higher midline staining of Claudin-4 in wild type embryos has previously been observed, providing additional evidence for such a mechanism (Nikolopoulou et al., 2019). It is a requirement of cells along the neural folds to reorganise their borders and swap neighbours during fusion, potentially explaining this finding. Of note, brighter midline E-cadherin was not clear in *Grhl3* mutant embryos in Chapter 5 – this could be due to the different antibody used, or the differential staining after blocking antibody treatment in Chapter 4 could be a result of culture artifact. The latter is unlikely, given that the culture period was very short (1.5 hours) and that differential staining of adhesion molecules has previously been observed (Nikolopoulou et al., 2019).

A possible role of midline E-cadherin could be in the regulation of myosin activity. In *Ciona robusta* NTC, homotypic Cadherin-2 interactions along the midline and behind the zipper (i.e. rostral to the ZP) have been shown to inhibit myosin activity, and in turn direct myosin activity to the heterotypic NE-SE cell borders directly at the ZP and along the neural folds (Hashimoto and Munro, 2019). It is possible that E-cadherin plays a similar role rostral to the ZP, however this is not supported by the high levels of E-cadherin around the PNP, which according to this model would prevent the high actomyosin activity reflected by the cable. Similarly, redirection of actomyosin activity away from the ZP midline could provide an explanation for the low recoil of SE in this region, however the midline upregulation of E-cadherin extends much further rostrally into regions of high recoil, making such a mechanism unlikely.

Alternatively, actomyosin could regulate E-cadherin localisation. In mammary epithelial monolayers, E-cadherin activity is required for Myosin-2 accumulation at cell borders, and conversely, inhibition of Myosin-II prevents local concentration of E-cadherin at cell-cell contacts without changing its overall expression (Shewan et al., 2005). This finding was replicated in rat fibroblastic NRK cells the following year, with both ROCK inhibition and blebbistatin treatment disrupting localisation of P-cadherin to punctate AJs (Miyake et al., 2006). This suggests that the actomyosin cable could regulate E-cadherin, explaining the greater E-cadherin abundance detected around the PNP and along the RC midline.

The midline abundance of E-cadherin relative to lateral regions (Chapter 4) is notably similar to higher midline translocation of YAP. YAP nuclear translocation has not yet been analysed along the neural folds, due to higher tissue curvature making imaging of this region difficult. However, preliminary observations suggest that YAP is more abundant along the neural folds, correlating with E-cadherin (G. Galea, pers. comm.). As discussed in Chapter 3, differences in midline ECM composition and the cytoplasmic actin cytoskeleton are unlikely to explain midline YAP activity, suggesting that adhesion molecules may be the primary signalling centre controlling YAP nuclear translocation.

Multiple components of AJs have been implicated in regulation of Hippo signalling, and it is known to be an important negative regulator of cell crowding, however a direct relationship between E-cadherin and YAP activation has not yet been proven in this system (Fulford et al., 2018). Nevertheless, this correlation, and the fact that YAP activation is abnormal in *Grhl2*$^{-/-}$ mutants, supports a mechanism by which down-regulation of AJ components leads to impaired YAP activation. An important future objective is to identify the downstream targets of YAP activation, in order to explore the function of high midline (and potential high neural fold)

activity. YAP is most commonly implicated in growth control pathways (Davis and Tapon, 2019). The SE shows a scattered pattern of pHH3 staining (unpublished data), however whether proliferation rates are different along the midline compared to laterally has not been investigated.

A possible function of YAP activity in this context is regulation of SE migration. For example, YAP/TAZ activity has been shown to stimulate angiogenesis downstream of VEGF-VEGFR2 signalling, by regulating expression of pro-migratory genes (Wang et al., 2017). In this study, silencing YAP/TAZ activity in mouse brain endothelioma and human brain microvascular endothelial cells prevented VEGF-dependent wound healing after a scratch assay, concomitant with reduced Rac1 signalling and lamellipodia formation (Wang et al., 2017). Whether this role of YAP/TAZ is via direct Hippo signalling is unclear. In another example, Hippo signalling promotes cell migration, but not by inhibiting YAP activity. Instead, Hippo directly activates migration and inhibits pro-migratory YAP through a negative feedback loop (Lucas et al., 2013). This study used border cell migration in the early *Drosophila* egg chamber as a model to study the role of Hippo signalling on migration – in this system, actin polymerisation around the outside of the migrating border cell cluster is positively regulated by direct Hippo and Yki (*Drosophila* homologue of YAP), with loss of Hippo and ectopic Yki expression causing reduced and accelerated border cell migration respectively (Lucas et al., 2013). E-cadherin mediated adhesion is also required between border cells for clusters to migrate successfully, raising the question of how E-cadherin adhesion and YAP is linked in this system (Cai et al., 2014) Clearly, the role of YAP in different developmental events is varied and complex, and its function and importance in spinal NTC is an interesting question for future work. The pro-migratory role of YAP activity in the above examples could suggest that midline YAP activity is important for the rostral migration of SE cells as they leave the ZP.

A crucial step before studying these possible roles for YAP is to confirm the presence of the YAP gradient. A limitation with the immunostaining method used in this thesis is that it is not supported by independent methods, such as immunostaining for TAZ and YAP upstream regulators (e.g. LATS1). It will then be important to identify suitable target genes and study their expression – the previously published *Grhl2* RNA-seq data could be useful to identify genes known to be regulated by YAP activity. Finally, immunostaining for YAP and potential targets on sections could be an important independent method to support the gradient; however, this would be a more useful approach when analysing target expression, because it would not differentiate between nuclear and cytoplasmic levels of YAP.

7.4 – Regulation of SE cell adhesion as a key mechanism driving spinal neurulation in *Grhl-2* and *-3* mutants

Grhl2 mutants have provided a valuable model for studying the biomechanical mechanisms involved in spinal closure. In particular, previous RNA sequencing data implicated adhesion molecules characteristic of an epithelial phenotype in NTD pathology (Nikolopoulou et al., 2019). As discussed above, culture of embryos in blocking E-cadherin antibody provides evidence for misexpression of *Cdh1* as a major causative mechanism behind NTDs in *Grhl2* mutants. Nevertheless, the precise mechanisms by which abnormal adhesion prevents closure remain unclear.

As discussed in Chapter 5, the current hypothesis for failed closure in *Grhl2* null mutants is an inability of SE cells to withstand anti-closure forces. By definition, tissue stiffness is an important property of the epithelium to maintain its shape by balancing opposing forces. A loss of epithelial integrity would reduce the ability of the tissue to resist outwards forces, possibly caused by growth, cell migration and hydrostatic pressures. The origin of these anti-closure forces is not yet clear. However, it is unlikely that the SE is the origin of anti-closure forces, as if this were the case, a less intact SE in *Grhl2*$^{-/-}$ embryos would be expected to allow closure to progress. The NE is therefore a more likely candidate. In *Grhl2*$^{-/-}$ embryos, reduced SE integrity would cause the neural folds to separate, thus explaining increased tissue level recoil after laser ablation. It is also possible that increased single cell recoil could be explained by a loss of SE integrity, although rostrocaudally-oriented anti-closure forces have not been identified. It will be important to test the tissue stiffness of the *Grhl2*$^{-/-}$ SE, using techniques such as micropipette aspiration, to explore this theory.

Meanwhile, how the abnormal cell shape and YAP nuclear translocation in *Grhl2*$^{-/-}$ embryos is explained by loss of SE adhesion and/or other epithelial properties is not yet clear. As discussed above, YAP may be regulated by E-cadherin, explaining its reduced overall activity revealed by western blot. In turn, loss of YAP activity could prevent the pro-migratory role of YAP proposed above, thus explaining why *Grhl2*$^{-/-}$ SE cells are not elongated. The lack of understanding of YAP's function in NTC makes these suggestions purely speculative, thus highlighting YAP as an important target for future work. A particularly important question is whether the altered midline YAP activity directly contributes to failed closure or is a marker of altered SE biomechanics.

Overexpression of *Grhl2* is less well studied, with many of the parameters studied in this project not showing significant differences from wild types. If these embryos have a mechanism opposite to that proposed above for *Grhl2* loss of function, tissue stiffness and/or cell-cell adhesion would be increased. The shape of the PNP, which is very long and narrow, supports a theory where the neural folds successfully reach the midline by resisting anti-closure forces and through the action of the intact actomyosin cable. Furthermore, the close proximity of the neural folds suggests a local inability of cells to fuse at the midline, a process which requires junctional remodelling. Inhibition of E-cadherin in cancer cells promotes migration – it can be reasoned therefore that an upregulation of E-cadherin may prevent cellular migration, although in some contexts loss of E-cadherin has this effect (Cai et al., 2014, Bruner and Derksen, 2018). As suggested in Chapter 5, the abnormal cell shape of *Grhl2*$^{Axd/Axd}$ SE could be due to an inability of cells to reorganise their junctions. If these cells are unable to migrate rostrally away from the ZP, this could prevent the formation of new borders along the midline. Live imaging would be required to support this. Importantly, if this is indeed the case, the active migration of cells rostrally from the ZP could be defined as a requirement for closure, and thus act as a 'pro-closure' mechanism. Further, culture of *Grhl2*$^{Axd/Axd}$ in blocking E-cadherin antibody could implicate E-cadherin as the major AJ component facilitating this mechanism. Based on the above discussion, a current working model of the mechanisms behind the observed biomechanical phenotypes in both normal and *Grhl2* mutant embryos is summarised in Figures 7.1 and 7.2.

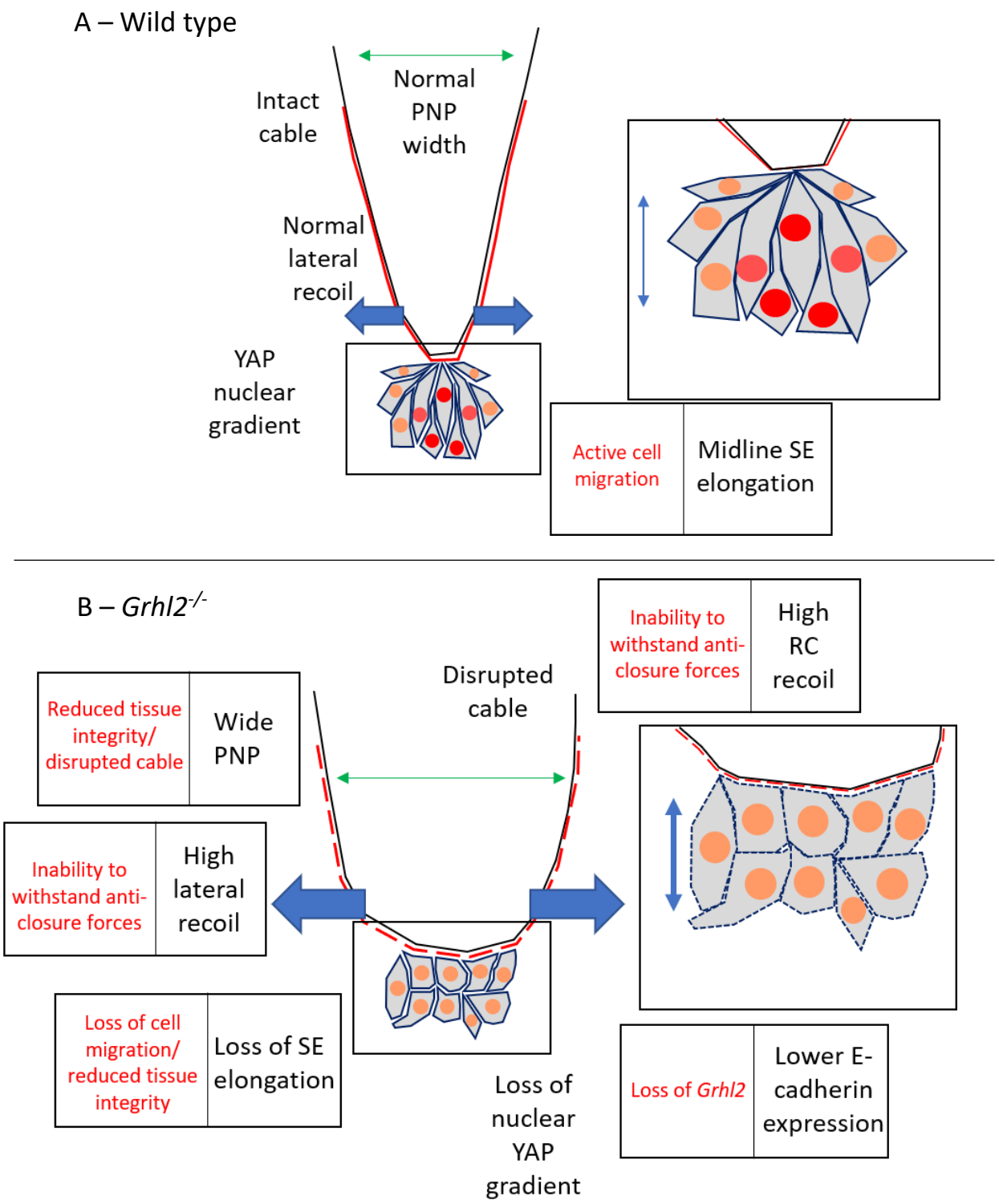

Figure 7.1 – Schematic summarising the current working model of the biomechanical phenotypes in wild type and Grhl2$^{-/-}$ spinal closure.

Black text describes the observed phenotype and red text gives possible explanations for the observed phenotype. Green arrow = PNP width. Red line = F-actin cable. Blue arrows = recoil after laser ablation.

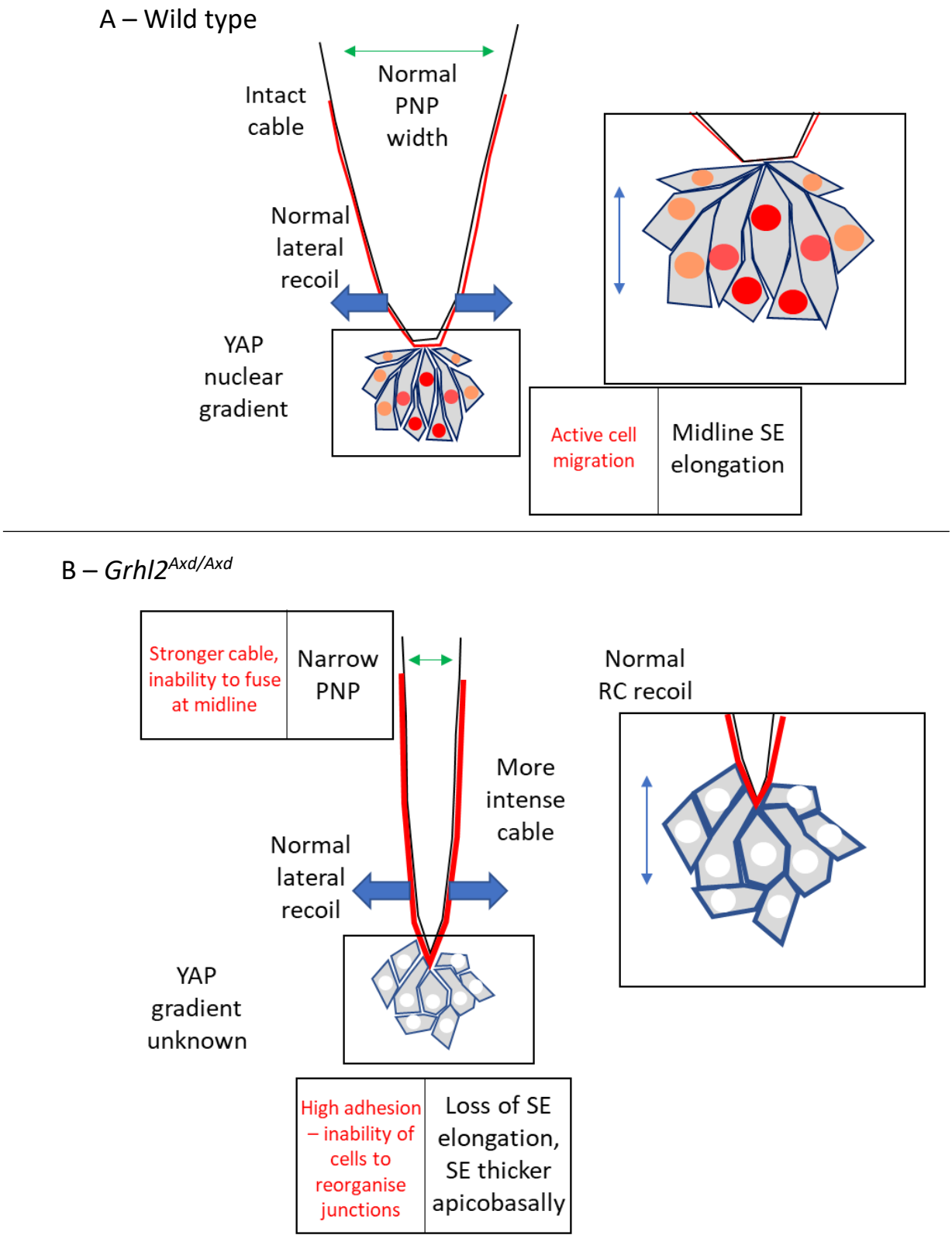

Figure 7.2 – Schematic summarising the current working model of the biomechanical phenotypes in wild type and Grhl2$^{Axd/Axd}$ spinal closure.

Black text describes the observed phenotype and red text gives possible explanations for the observed phenotype. Green arrow = PNP width. Red line = F-actin cable. Blue arrows = recoil after laser ablation.

Whether abnormal adhesion is a causative mechanism in *Grhl3* mutants is not yet clear. The role of desmosomes at the midline and around the neural folds could be comparable to that observed in wound healing. In wounded epidermis, desmosomes around the leading edge are switched from a hyper-adhesive state to the default Ca^{2+}-dependent state, and desmosome internalisation is triggered by pro-migration signals (Garrod et al., 2005). Upregulation of desmosomal components may prevent this from occurring, thus inhibiting active SE migration around the neural folds.

Desmosomes are more commonly studied in the context of tissue integrity (Todorović et al., 2013). The difference between *Grhl-2* and *-3* overexpression mutants could be due to the amount the gene is overexpressed and/or how widely the gene is expressed within the tissue. *Grhl3* is not expressed in the entire SE, suggesting that changes in tissue integrity as a whole may be less pronounced than for *Grhl2* – a comparison between *Grhl-2* and *-3* tissue stiffness would be a useful future direction. It is nevertheless important to remember that the mechanisms underlying *Grhl-2* and *-3* related NTDs, and even between loss- and gain-of-function mutants of the same gene, may not be comparable or reciprocal, and alternative non-biomechanical mechanisms could be involved. Additional mutants, such as $Vangl2^{Lp/+};Grhl3^{ct/ct}$, could provide clues to other such mechanisms.

7.5 – Closing remarks

Overall, this thesis begins to implicate the SE as a vital tissue in facilitating NTC. As one of the most common birth defects, NTDs remain a serious medical challenge, with an immensely complex genetic and environmental aetiology. The requirements of biological processes to meet a given threshold can be appreciated by studies such as those presented here. This can be at either the genetic or physical level. At the biomechanical level, physical limits have to be met. For example, cellular adhesion, tissue tension and epithelial integrity must be within a threshold for a developmental process to succeed. Biomechanics is a field which begins to consider the big picture – if a general mechanical property, e.g. tissue tension, depends on multiple cellular mechanisms, this provides a wider scope for potential therapies.

At the genetic level, expression of some genes, in this case *Grhl-2* and *-3,* must be within a very narrow threshold, highlighting how precise genetic regulation must be. When investigating genetic risk for NTDs, it is commonplace to search for mutations in the coding region. Mouse models such as *ct* and *Axd* show that screening for regulatory mutations should also be a focus in the future, perhaps helping to identify more women at risk of having affected pregnancies. In addition, double mutant mouse models such as the *Lp/ct* strain demonstrate how multiple mutations can interact and predispose to NTDs. Mouse models such as those investigated in this thesis can be used to investigate the mechanisms behind increased risk, providing direction for the development of novel preventative therapies.

Chapter 8 - Bibliography

ADZICK, N. S., THOM, E. A., SPONG, C. Y., BROCK, J. W., BURROWS, P. K., JOHNSON, M. P., HOWELL, L. J., FARRELL, J. A., DABROWIAK, M. E., SUTTON, L. N., GUPTA, N., TULIPAN, N. B., D'ALTON, M. E. & FARMER, D. L. 2011. A Randomized Trial of Prenatal versus Postnatal Repair of Myelomeningocele. *N Engl J Med,* 364**,** 993-1004.

AIGOUY, B., UMETSU, D. & EATON, S. 2016. Segmentation and Quantitative Analysis of Epithelial Tissues. *Methods Mol Biol,* 1478**,** 227-239.

AMANO, M., NAKAYAMA, M. & KAIBUCHI, K. 2010. Rho-kinase/ROCK: A key regulator of the cytoskeleton and cell polarity. *Cytoskeleton (Hoboken),* 67**,** 545-54.

ANDONIADOU, C. L. & MARTINEZ-BARBERA, J. P. 2013. Developmental mechanisms directing early anterior forebrain specification in vertebrates. *Cell Mol Life Sci,* 70**,** 3739-52.

ATTARDI, L. D. & TJIAN, R. 1993. Drosophila tissue-specific transcription factor NTF-1 contains a novel isoleucine-rich activation motif. *Gene Dev,* 7**,** 1341-1353.

ATTARDI, L. D., VON SEGGERN, D. & TJIAN, R. 1993. Ectopic expression of wild-type or a dominant-negative mutant of transcription factor NTF-1 disrupts normal Drosophila development. *Proc Natl Acad Sci U S A,* 90**,** 10563-10567.

AUDEN, A., CADDY, J., WILANOWSKI, T., TING, S. B., CUNNINGHAM, J. M. & JANE, S. M. 2006. Spatial and temporal expression of the Grainyhead-like transcription factor family during murine development. *Gene Expr Patterns,* 6**,** 964-70.

BALMER, S., NOWOTSCHIN, S. & HADJANTONAKIS, A. K. 2016. Notochord morphogenesis in mice: Current understanding & open questions. *Dev Dyn,* 245**,** 547-57.

BAMBARDEKAR, K., CLEMENT, R., BLANC, O., CHARDES, C. & LENNE, P. F. 2015. Direct laser manipulation reveals the mechanics of cell contacts in vivo. *Proc Natl Acad Sci U S A,* 112**,** 1416-21.

BARCZYK, M., CARRACEDO, S. & GULLBERG, D. 2010. Integrins. *Cell Tissue Res,* 339**,** 269-80.

BASOLI, F., GIANNITELLI, S. M., GORI, M., MOZETIC, P., BONFANTI, A., TROMBETTA, M. & RAINER, A. 2018. Biomechanical Characterization at the Cell Scale: Present and Prospects. *Front Physiol,* 9**,** 1449.

BAUMHOLTZ, A. I., SIMARD, A., NIKOLOPOULOU, E., OOSENBRUG, M., COLLINS, M. M., PIONTEK, A., KRAUSE, G., PIONTEK, J., GREENE, N. D. E. & RYAN, A. K. 2017. Claudins are essential for cell shape changes and convergent extension movements during neural tube closure. *Dev Biol,* 428**,** 25-38.

BEGNAUD, S., CHEN, T., DELACOUR, D., MEGE, R. M. & LADOUX, B. 2016. Mechanics of epithelial tissues during gap closure. *Curr Opin Cell Biol,* 42**,** 52-62.

BEIER, D. R., DUSHKIN, H. & TELLE, T. 1995. Haplotype analysis of intra-specific backcross curly-tail mice confirms the localization of ct to Chromosome 4. *Mamm Genome,* 6**,** 269-272.

BELL, J. E., GORDON, A. & MOLONEY, A. F. J. 1980. The association of hydrocephalus and Arnold-Chiari malformation with spina bifida in the fetus. *Neuropath and Appl Neurobio,* 6**,** 29-39.

BENDIX, P. M., KOENDERINK, G. H., CUVELIER, D., DOGIC, Z., KOELEMAN, B. N., BRIEHER, W. M., FIELD, C. M., MAHADEVAN, L. & WEITZ, D. A. 2008. A quantitative analysis of contractility in active cytoskeletal protein networks. *Biophys J,* 94**,** 3126-36.

BENHAM-PYLE, B. W., PRUITT, B. L. & NELSON, W. J. 2015. Cell adhesion. Mechanical strain induces E-cadherin-dependent Yap1 and beta-catenin activation to drive cell cycle entry. *Science,* 348**,** 1024-7.

BERTET, C., SULAK, L. & LECUIT, T. 2004. Myosin-dependent junction remodelling controls planar cell intercalation and axis elongation. *Nature,* 429**,** 667-671.

BIERKAMP, C., MCLAUGHLIN, K. J., SCHWARZ, H., HUBER, O. & KEMLER, R. 1996. Embryonic Heart and Skin Defects in Mice Lacking Plakoglobin. *Dev Biol,* 180**,** 780-785.

BINNIG, G., QUATE, C. F. & GERBER, C. 1986. Atomic force microscope. *Phys Rev Lett,* 56**,** 930-933.
BLAIR, S. & MCNEILL, H. 2018. Big roles for Fat cadherins. *Curr Opin Cell Biol,* 51**,** 73-80.
BOGLEV, Y., WILANOWSKI, T., CADDY, J., PAREKH, V., AUDEN, A., DARIDO, C., HISLOP, N. R., CANGKRAMA, M., TING, S. B. & JANE, S. M. 2011. The unique and cooperative roles of the Grainy head-like transcription factors in epidermal development reflect unexpected target gene specificity. *Dev Biol,* 349**,** 512-22.
BOLTE, S. & CORDELIERES, F. P. 2006. A guided tour into subcellular colocalization analysis in light microscopy. *J Microscopy,* 224**,** 213-232.
BOOPATHY, G. T. K. & HONG, W. 2019. Role of Hippo Pathway-YAP/TAZ Signaling in Angiogenesis. *Front Cell Dev Biol,* 7**,** 49.
BORG, M. 2017. The detection of spina bifida at 11-13+6 weeks' gestation. *Sonography,* 4**,** 31-35.
BORGHI, N., SOROKINA, M., SHCHERBAKOVA, O. G., WEIS, W. I., PRUITT, B. L., NELSON, W. J. & DUNN, A. R. 2012. E-cadherin is under constitutive actomyosin-generated tension that is increased at cell-cell contacts upon externally applied stretch. *Proc Natl Acad Sci U S A,* 109**,** 12568-73.
BOUVARD, D., BRAKEBUSCH, C., GUSTAFSSON, E., ASZODI, A., BENGTSSON, T., BERNA, A. & FASSLER, R. 2001. Functional Consequences of Integrin Gene Mutations in Mice. *Circ Res,* 89**,** 211-223.
BOYD, P. A., DEVIGAN, C., KHOSHNOOD, B., LOANE, M., GARNE, E., DOLK, H. & GROUP, E. W. 2008. Survey of prenatal screening policies in Europe for structural malformations and chromosome anomalies, and their impact on detection and termination rates for neural tube defects and Down's syndrome. *BJOG,* 115**,** 689-96.
BRAY, S. J., JOHNSON, W. A., HIRSH, J., HEBERLEIN, U. & TIJAN, R. 1988. A cis-acting element and associated binding factor required for CNS expression of the Drosophila melanogaster dopa decarboxylase gene. *EMBO,* 7**,** 177-188.
BRAY, S. J. & KAFATOS, F. C. 1991. Developmental function of Elf-1: an essential transcription factor during embryogenesis in *Drosophila*. *Gene Dev,* 5**,** 1672-1683.
BRODLAND, G. W., CHEN, X., LEE, P. & MARSDEN, M. 2010. From genes to neural tube defects (NTDs): insights from multiscale computational modeling. *HFSP J,* 4**,** 142-52.
BROOK, F. A., SHUM, A. S. W., VAN STRAATEN, H. W. M. & COPP, A. J. 1991. Curvature of the caudal region is responsible for failure of neural tube closure in the curly tail {ct) mouse embryo. *Development,* 113**,** 671-678.
BROUNS, M. R., DE CASTRO, S. C., TERWINDT-ROUWENHORST, E. A., MASSA, V., HEKKING, J. W., HIRST, C. S., SAVERY, D., MUNTS, C., PARTRIDGE, D., LAMERS, W., KOHLER, E., VAN STRAATEN, H. W., COPP, A. J. & GREENE, N. D. 2011. Over-expression of Grhl2 causes spina bifida in the Axial defects mutant mouse. *Hum Mol Genet,* 20**,** 1536-46.
BRUNER, H. C. & DERKSEN, P. W. B. 2018. Loss of E-Cadherin-Dependent Cell-Cell Adhesion and the Development and Progression of Cancer. *Cold Spring Harb Perspect Biol,* 10.
BUCK, R. C. 1980. Reorientation response of cells to repeated stretch and recoil of the substratum. *Exp Cell Res,* 127**,** 470-474.
BURDSAL, C. A., DAMSKY, C. H. & PEDERSON, R. A. 1993. The role of E-cadherin and integrins in mesoderm differentiation and migration at the mammalian primitive streak. *Development,* 118**,** 829-844.
CADDY, J., WILANOWSKI, T., DARIDO, C., DWORKIN, S., TING, S. B., ZHAO, Q., RANK, G., AUDEN, A., SRIVASTAVA, S., PAPENFUSS, T. A., MURDOCH, J. N., HUMBERT, P. O., PAREKH, V., BOULOS, N., WEBER, T., ZUO, J., CUNNINGHAM, J. M. & JANE, S. M. 2010. Epidermal wound repair is regulated by the planar cell polarity signaling pathway. *Dev Cell,* 19**,** 138-47.

CAI, D., CHEN, S. C., PRASAD, M., HE, L., WANG, X., CHOESMEL-CADAMURO, V., SAWYER, J. K., DANUSER, G. & MONTELL, D. J. 2014. Mechanical feedback through E-cadherin promotes direction sensing during collective cell migration. *Cell,* 157**,** 1146-59.

CAMERER, E., BARKER, A., DUONG, D. N., GANESAN, R., KATAOKA, H., CORNELISSEN, I., DARRAGH, M. R., HUSSAIN, A., ZHENG, Y. W., SRINIVASAN, Y., BROWN, C., XU, S. M., REGARD, J. B., LIN, C. Y., CRAIK, C. S., KIRCHHOFER, D. & COUGHLIN, S. R. 2010. Local protease signaling contributes to neural tube closure in the mouse embryo. *Dev Cell,* 18**,** 25-38.

CAMPBELL, I. D. & HUMPHRIES, M. J. 2011. Integrin structure, activation, and interactions. *Cold Spring Harb Perspect Biol,* 3.

CAMPBELL, K. & CASANOVA, J. 2016. A common framework for EMT and collective cell migration. *Development,* 143**,** 4291-4300.

CAPALDO, C. T., FARKAS, A. E. & NUSRAT, A. 2014. Epithelial adhesive junctions. *F1000Prime Rep,* 6**,** 1.

CARPINELLI, M. R., DE VRIES, M. E., AUDEN, A., BUTT, T., DENG, Z., PARTRIDGE, D. D., MILES, L. B., GEORGY, S. R., HAIGH, J. J., DARIDO, C., BRABLETZ, S., BRABLETZ, T., STEMMLER, M. P., DWORKIN, S. & JANE, S. M. 2020. Inactivation of Zeb1 in GRHL2-deficient mouse embryos rescues mid-gestation viability and secondary palate closure. *Dis Model Mech*.

CARROLL, E. A., GERRELLI, D., GASCA, S., BERG, E., BEIER, D. R., COPP, A. J. & KLINGENSMITH, J. 2003. Cordon-bleu is a conserved gene involved in neural tube formation. *Developmental Biology,* 262**,** 16-31.

CHAN, A., MCCAUL, K. A., CUNDY, P. J., HAAN, E. A. & BYON-SCOTT, R. 1997. Perinatal risk factors for developmental dysplasia of the hip. *Arch Dis Child,* 76**,** F94-100.

CHAN, C. J., COSTANZO, M., RUIZ-HERRERO, T., MONKE, G., PETRIE, R. J., BERGERT, M., DIZ-MUNOZ, A., MAHADEVAN, L. & HIIRAGI, T. 2019. Hydraulic control of mammalian embryo size and cell fate. *Nature,* 571**,** 112-116.

CHEHREHASA, F., MEEDENIYA, A. C., DWYER, P., ABRAHAMSEN, G. & MACKAY-SIM, A. 2009. EdU, a new thymidine analogue for labelling proliferating cells in the nervous system. *J Neurosci Methods,* 177**,** 122-30.

CHEN, B. & HALES, B. F. 1995. Antisense Oligonucleotide Down-Regulation of E-Cadherin in the Yolk Sac and Cranial Neural Tube Malformations. *Biol Reprod,* 53**,** 1229-1238.

CHEN, D. Y., CREST, J., STREICHAN, S. J. & BILDER, D. 2019. Extracellular matrix stiffness cues junctional remodeling for 3D tissue elongation. *Nat Commun,* 10**,** 3339.

CHEN, W., YI, J. K., SHIMANE, T., MEHRAZARIN, S., LIN, Y. L., SHIN, K. H., KIM, R. H., PARK, N. H. & KANG, M. K. 2016. Grainyhead-like 2 regulates epithelial plasticity and stemness in oral cancer cells. *Carcinogenesis,* 37**,** 500-10.

CHIANG, C., LITINGTUNG, Y., LEE, E., YOUNG, K. E., CORDEN, J. L., WESTPHAL, H. & BEACHY, P. A. 1996. Cyclopia and defective axial patterning in mice lacking Sonic hedgehog gene function. *Nature,* 383**,** 407-413.

CHUNG, V. Y., TAN, T. Z., TAN, M., WONG, M. K., KUAY, K. T., YANG, Z., YE, J., MULLER, J., KOH, C. M., GUCCIONE, E., THIERY, J. P. & HUANG, R. Y. 2016. GRHL2-miR-200-ZEB1 maintains the epithelial status of ovarian cancer through transcriptional regulation and histone modification. *Sci Rep,* 6**,** 19943.

CIEPLY, B., FARRIS, J., DENVIR, J., FORD, H. L. & FRISCH, S. M. 2013. Epithelial-mesenchymal transition and tumor suppression are controlled by a reciprocal feedback loop between ZEB1 and Grainyhead-like-2. *Cancer Res,* 73**,** 6299-309.

CIEPLY, B., RILEY, P. T., PIFER, P. M., WIDMEYER, J., ADDISON, J. B., IVANOV, A. V., DENVIR, J. & FRISCH, S. M. 2012. Suppression of the epithelial-mesenchymal transition by Grainyhead-like-2. *Cancer Res,* 72**,** 2440-53.

CLEAVER, O. & KRIEG, P. A. 2001. Notochord patterning of the endoderm. *Dev Biol,* 234**,** 1-12.

COCKBURN, K. & ROSSANT, J. 2010. Making the blastocyst: lessons from the mouse. *J Clin Invest,* 120**,** 995-1003.
COCKROFT, D. L., BROOK, F. A. & COPP, A. J. 1992. lnositol Deficiency Increases the Susceptibility to Neural Tube Defects of Genetically Predisposed (Curly Tail) Mouse Embryos In Vitro. *Teratology,* 45**,** 223-232.
COGRAM, P., HYNES, A., DUNLEVY, L. P., GREENE, N. D. & COPP, A. J. 2004. Specific isoforms of protein kinase C are essential for prevention of folate-resistant neural tube defects by inositol. *Hum Mol Genet,* 13**,** 7-14.
COPP, A. J. 1985. Relationship between timing of posterior neuropore closure and development of spinal neural tube defects in mutant (curly tail) and normal mouse embryos in culture. *J. Embryol. exp. Morph.,* 88**,** 39-54.
COPP, A. J., ADZICK, N. S., CHITTY, L. S., FLETCHER, J. M., HOLMBECK, G. N. & SHAW, G. M. 2015. Spina bifida. *Nat Rev Dis Primers,* 1**,** 15007.
COPP, A. J., BROOK, F. A. & ROBERTS, H. J. 1988. A cell-type-specific abnormality of cell proliferation in mutant (curly tail) mouse embryos developing spinal neural tube defects. *Development,* 104**,** 285-295.
COPP, A. J., CHECIU, I. & HENSON, J. N. 1994. Developmental Basis of Severe Neural Tube Defects in the *loop-tail (Lp)* Mutant Mouse: Use of Microsatellite DNA Markers to Identify Embryonic Genotype. *Dev Biol,* 165**,** 20-29.
COPP, A. J. & GREENE, N. D. 2010. Genetics and development of neural tube defects. *J Pathol,* 220**,** 217-30.
COPP, A. J. & GREENE, N. D. 2013. Neural tube defects--disorders of neurulation and related embryonic processes. *Wiley Interdiscip Rev Dev Biol,* 2**,** 213-27.
COPP, A. J., GREENE, N. D. & MURDOCH, J. N. 2003. Dishevelled: linking convergent extension with neural tube closure. *Trends in Neurosci,* 26**,** 453-455.
COPP, A. J. & GREENE, N. D. E. 2016. Neural Tube Defects. *eLS***,** 1-12.
COPP, A. J., SELLER, M. J. & POLANI, P. E. 1982. Neural tube development in mutant (*curly tail*) and normal mouse embryos: the timing of posterior neuropore closure *in vivo* and *in vitro*. *J Embryol,* 69**,** 151-167.
COTTON, J. L., LI, Q., MA, L., PARK, J. S., WANG, J., OU, J., ZHU, L. J., IP, Y. T., JOHNSON, R. L. & MAO, J. 2017. YAP/TAZ and Hedgehog Coordinate Growth and Patterning in Gastrointestinal Mesenchyme. *Dev Cell,* 43**,** 35-47 e4.
CURTIN, J. A., QUINT, E., TSIPOURI, V., ARKELL, R. M., CATTANACH, B., COPP, A. J., HENDERSON, D. J., SPURR, N., STANIER, P., FISHER, E. M., NOLAN, P. M., STEEL, K. P., BROWN, S. D. M., GRAY, I. C. & MURDOCH, J. N. 2003. Mutation of Celsr1 Disrupts Planar Polarity of Inner Ear Hair Cells and Causes Severe Neural Tube Defects in the Mouse. *Current Biology,* 13**,** 1129-1133.
DARIDO, C., GEORGY, S. R., WILANOWSKI, T., DWORKIN, S., AUDEN, A., ZHAO, Q., RANK, G., SRIVASTAVA, S., FINLAY, M. J., PAPENFUSS, A. T., PANDOLFI, P. P., PEARSON, R. B. & JANE, S. M. 2011. Targeting of the tumor suppressor GRHL3 by a miR-21-dependent proto-oncogenic network results in PTEN loss and tumorigenesis. *Cancer Cell,* 20**,** 635-48.
DARTSCH, P. C. & BETZ, E. 1989. Response of cultured endothelial cells to mechanical stimulation. *Basic Res Cardiol,* 84**,** 268-281.
DAVEY, C. F. & MOENS, C. B. 2017. Planar cell polarity in moving cells: think globally, act locally. *Development,* 144**,** 187-200.
DAVIDSON, B. P., KINDER, S. J., STEINER, K., SCHOENWOLF, G. C. & TAM, P. P. L. 1999. Impact of Node Ablation on the Morphogenesis of the Body Axis and the Lateral Asymmetry of the Mouse Embryo during Early Organogenesis. *Dev Biol,* 211**,** 11-26.
DAVIS, J. R. & TAPON, N. 2019. Hippo signalling during development. *Development,* 146.

DE CASTRO, S. C., MALHAS, A., LEUNG, K. Y., GUSTAVSSON, P., VAUX, D. J., COPP, A. J. & GREENE, N. D. 2012. Lamin b1 polymorphism influences morphology of the nuclear envelope, cell cycle progression, and risk of neural tube defects in mice. *PLoS Genet,* 8**,** e1003059.

DE CASTRO, S. C. P., GUSTAVSSON, P., MARSHALL, A. R., GORDON, W. M., GALEA, G., NIKOLOPOULOU, E., SAVERY, D., ROLO, A., STANIER, P., ANDERSEN, B., COPP, A. J. & GREENE, N. D. E. 2018a. Over-expression of Grainyhead-like 3 causes spina bifida and interacts genetically with mutant alleles of Grhl2 and Vangl2 in mice. *Hum Mol Genet*.

DE CASTRO, S. C. P., HIRST, C. S., SAVERY, D., ROLO, A., LICKERT, H., ANDERSEN, B., COPP, A. J. & GREENE, N. D. E. 2018b. Neural tube closure depends on expression of Grainyhead-like 3 in multiple tissues. *Dev Biol,* 435**,** 130-137.

DE ROBERTIS, E. M. 2006. Spemann's organizer and self-regulation in amphibian embryos. *Nat Rev Mol Cell Biol,* 7**,** 296-302.

DEL BIGIO, M. R. 2010. Neuropathology and structural changes in hydrocephalus. *Dev Disabil Res Rev,* 16**,** 16-22.

DESSAUD, E., MCMAHON, A. P. & BRISCOE, J. 2008. Pattern formation in the vertebrate neural tube: a sonic hedgehog morphogen-regulated transcriptional network. *Development,* 135**,** 2489-503.

DUCUING, A. & VINCENT, S. 2016. The actin cable is dispensable in directing dorsal closure dynamics but neutralizes mechanical stress to prevent scarring in the Drosophila embryo. *Nat Cell Biol,* 18**,** 1149-1160.

DUNN, N. R., VINCENT, S. D., OXBURGH, L., ROBERTSON, E. J. & BIKOFF, E. K. 2004. Combinatorial activities of Smad2 and Smad3 regulate mesoderm formation and patterning in the mouse embryo. *Development,* 131**,** 1717-28.

DUPONT, S., MORSUT, L., ARAGONA, M., ENZO, E., GIULITTI, S., CORDENONSI, M., ZANCONATO, F., LE DIGABEL, J., FORCATO, M., BICCIATO, S., ELVASSORE, N. & PICCOLO, S. 2011. Role of YAP/TAZ in mechanotransduction. *Nature,* 474**,** 179-83.

DZAMBA, B. J., JAKAB, K. R., MARSDEN, M., SCHWARTZ, M. A. & DESIMONE, D. W. 2009. Cadherin adhesion, tissue tension, and noncanonical Wnt signaling regulate fibronectin matrix organization. *Dev Cell,* 16**,** 421-32.

EICHHOLZER, M., TÖNZ, O. & ZIMMERMANN, R. 2006. Folic acid: a public-health challenge. *Lancet,* 367**,** 1352-1361.

ELBEDIWY, A. & THOMPSON, B. J. 2018. Evolution of mechanotransduction via YAP/TAZ in animal epithelia. *Curr Opin Cell Biol,* 51**,** 117-123.

ELBEDIWY, A., VANYAI, H., DIAZ-DE-LA-LOZA, M. D., FRITH, D., SNIJDERS, A. P. & THOMPSON, B. J. 2018. Enigma proteins regulate YAP mechanotransduction. *J Cell Sci,* 131.

ESCUIN, S., VERNAY, B., SAVERY, D., GURNIAK, C. B., WITKE, W., GREENE, N. D. & COPP, A. J. 2015. Rho-kinase-dependent actin turnover and actomyosin disassembly are necessary for mouse spinal neural tube closure. *J Cell Sci,* 128**,** 2468-81.

ESSIEN, F. B., HAVILAND, M. B. & NAIDOFF, A. E. 1990. Expression of a New Mutation (*Axd*) Causing Axial Defects in Mice Correlates With Maternal Phenotype and Age. *Teratology,* 42**,** 183-194.

EVANS, M. J., CARLTON, M. B. L. & RUSS, A. P. 1997. Gene trapping and functional genomics. *Trends Genet,* 13**,** 370-374.

FARHADIFAR, R., ROPER, J. C., AIGOUY, B., EATON, S. & JULICHER, F. 2007. The influence of cell mechanics, cell-cell interactions, and proliferation on epithelial packing. *Curr Biol,* 17**,** 2095-104.

FASSLER, R. & MEYER, M. 1995. Consequences of lack of B1 integrin gene expression in mice. *Genes Dev,* 9**,** 1896-1908.

FEIL, R., BROCARD, J., MASCREZ, B., LEMEUR, M., METZGER, D. & CHAMBON, P. 1996. Ligand-activated site-specific recombination in mice. *Proc Natl Acad Sci U S A,* 93**,** 10887-10890.

FIETZ, S. A., NAMBA, T., KIRSTEN, H., HUTTNER, W. B. & LACHMANN, R. 2020. Signs of Reduced Basal Progenitor Levels and Cortical Neurogenesis in Human Fetuses with Open Spina Bifida at 11-15 Weeks of Gestation. *J Neurosci,* 40**,** 1766-1777.

FLEMING, T. P., GARROD, D. R. & ELSMORE, A. J. 1991. Desmosome biogenesis in the mouse preimplantation embryo. *Development,* 112**,** 527-539.

FLEMING, T. P., SHETH, B. & FESENKO, I. 2001. Cell adhesion in the preimplantation mammalian embryo and its role in trophectoderm differentiation and blastocyst morphogenesis. *Front Biosci,* 6**,** 1000-1007.

FONS, J. M., MOZAFFARI, M., MALIK, D., MARSHALL, A. R., CONNOR, S., GREENE, N. D. E. & TUCKER, A. S. 2020. Epithelial dynamics shed light on the mechanisms underlying ear canal defects. *Development,* 147.

FORRAI, A. & ROBB, L. 2005. The gene trap resource: a treasure trove for hemopoiesis research. *Exp Hematol,* 33**,** 845-56.

FRANTZ, C., STEWART, K. M. & WEAVER, V. M. 2010. The extracellular matrix at a glance. *J Cell Sci,* 123**,** 4195-200.

FULFORD, A., TAPON, N. & RIBEIRO, P. S. 2018. Upstairs, downstairs: spatial regulation of Hippo signalling. *Curr Opin Cell Biol,* 51**,** 22-32.

GALEA, G. L., CHO, Y. J., GALEA, G., MOLE, M. A., ROLO, A., SAVERY, D., MOULDING, D., CULSHAW, L. H., NIKOLOPOULOU, E., GREENE, N. D. E. & COPP, A. J. 2017. Biomechanical coupling facilitates spinal neural tube closure in mouse embryos. *Proc Natl Acad Sci U S A,* 114**,** E5177-E5186.

GALEA, G. L., NYCHYK, O., MOLE, M. A., MOULDING, D., SAVERY, D., NIKOLOPOULOU, E., HENDERSON, D. J., GREENE, N. D. E. & COPP, A. J. 2018. Vangl2 disruption alters the biomechanics of late spinal neurulation leading to spina bifida in mouse embryos. *Dis Model Mech,* 11.

GARROD, D. & CHIDGEY, M. 2008. Desmosome structure, composition and function. *Biochim Biophys Acta,* 1778**,** 572-87.

GARROD, D. R., BERIKA, M. Y., BARDSLEY, W. F., HOLMES, D. & TABERNERO, L. 2005. Hyper-adhesion in desmosomes: its regulation in wound healing and possible relationship to cadherin crystal structure. *J Cell Sci,* 118**,** 5743-54.

GEELEN, J. A. G. & LANGMAN, J. 1979. Ultrastructural Observations on Closure of the Neural Tube in the Mouse. *Anat Embryol,* 156**,** 73-88.

GEORGE, E. L., GEORGES-LABOUESSE, E. N., PATEL-KING, R. S., RAYBURN, H. & HYNES, R. O. 1993. Defects in mesoderm, neural tube and vascular development in mouse embryos lacking fibronectin. *Development,* 119**,** 1079-1091.

GIRALDO, P. & MONTOLIU, L. 2001. Size matters: use ofYACs, BACs and PACs in transgenic animals. *Transgenic Res,* 10**,** 83-103.

GOLDEN, J. A. & CHERNOFF, G. F. 1993. Intermittent Pattern of Neural Tube Closure in Two Strains of Mice. *Teratology,* 47**,** 73-80.

GORDON, W. M., ZELLER, M. D., KLEIN, R. H., SWINDELL, W. R., HO, H., ESPETIA, F., GUDJONSSON, J. E., BALDI, P. F. & ANDERSEN, B. 2014. A GRHL3-regulated repair pathway suppresses immune-mediated epidermal hyperplasia. *J Clin Invest,* 124**,** 5205-18.

GOVIND, S., KOZMA, R., MONFRIES, C., LIM, L. & AHMED, S. 2001. Cdc42Hs Facilitates Cytoskeletal Reorganization and Neurite Outgrowth by Localizing the 58-kD Insulin Receptor Substrate to Filamentous Actin. *J Cell Biol,* 152**,** 579-594.

GREENE, N. D. & COPP, A. J. 1997. Inositol prevents folate-resistant neural tube defects in the mouse. *Nat Med,* 3**,** 60-66.

GREENE, N. D. & COPP, A. J. 2014. Neural tube defects. *Annu Rev Neurosci,* 37**,** 221-42.
GREENE, N. D., GERRELLI, D., VAN STRAATEN, H. W. M. & COPP, A. J. 1998. Abnormalities of floor plate, notochord and somite differentiation in the loop-tail (Lp) mouse: a model of severe neural tube defects. *Mech Dev,* 73**,** 59-72.
GREENE, N. D., LEUNG, K. Y. & COPP, A. J. 2017. Inositol, Neural Tube Closure and the Prevention of Neural Tube Defects. *Birth Defects Res,* 109**,** 68-80.
GREENE, N. D., LEUNG, K. Y., GAY, V., BURREN, K., MILLS, K., CHITTY, L. S. & COPP, A. J. 2016. Inositol for the prevention of neural tube defects: a pilot randomised controlled trial. *Br J Nutr,* 115**,** 974-83.
GREENE, N. D., STANIER, P. & COPP, A. J. 2009. Genetics of human neural tube defects. *Hum Mol Genet,* 18**,** R113-29.
GRITSMAN, K., TALBOT, W. S. & SCHIER, A. F. 2000. Nodal signaling patterns the organizer. *Development,* 127**,** 921-932.
GROSSMANN, K. S., GRUND, C., HUELSKEN, J., BEHREND, M., ERDMANN, B., FRANKE, W. W. & BIRCHMEIER, W. 2004. Requirement of plakophilin 2 for heart morphogenesis and cardiac junction formation. *J Cell Biol,* 167**,** 149-60.
GROUP, M. V. S. R. 1991. Prevention of neural tube defects: Results of the Medical Research Council Vitamin Study. *Lancet,* 338**,** 131-137.
GRUNEBERG, H. 1954. Genetical Studies on the Skeleton of the Mouse: VIII. Curly-Tail. *J Gen,* 52**,** 52-67.
GUHA, T. K., WAI, A. & HAUSNER, G. 2017. Programmable Genome Editing Tools and their Regulation for Efficient Genome Engineering. *Comput Struct Biotechnol J,* 15**,** 146-160.
GURNIAK, C. B., PERLAS, E. & WITKE, W. 2005. The actin depolymerizing factor n-cofilin is essential for neural tube morphogenesis and neural crest cell migration. *Dev Biol,* 278**,** 231-41.
GURUMURTHY, C. B. & LLOYD, K. C. K. 2019. Generating mouse models for biomedical research: technological advances. *Dis Model Mech,* 12.
GUSTAVSSON, P., COPP, A. J. & GREENE, N. D. 2008. Grainyhead genes and mammalian neural tube closure. *Birth Defects Res A Clin Mol Teratol,* 82**,** 728-35.
GUSTAVSSON, P., GREENE, N. D., LAD, D., PAUWS, E., DE CASTRO, S. C., STANIER, P. & COPP, A. J. 2007. Increased expression of Grainyhead-like-3 rescues spina bifida in a folate-resistant mouse model. *Hum Mol Genet,* 16**,** 2640-6.
HAIGO, S. L., HILDEBRAND, J. D., HARLAND, R. M. & WALLINGFORD, J. B. 2003. Shroom induces apical constriction and is required for hingepoint formation during neural tube closure. *Curr Biol,* 13**,** 2125-37.
HALDER, G. & JOHNSON, R. L. 2011. Hippo signaling: growth control and beyond. *Development,* 138**,** 9-22.
HARTSOCK, A. & NELSON, W. J. 2008. Adherens and tight junctions: structure, function and connections to the actin cytoskeleton. *Biochim Biophys Acta,* 1778**,** 660-9.
HASAN, K. M., ELUVATHINGAL, T. J., KRAMER, L. A., EWING-COBBS, L., DENNIS, M. & FLETCHER, J. M. 2008. White matter microstructural abnormalities in children with spina bifida myelomeningocele and hydrocephalus: a diffusion tensor tractography study of the association pathways. *J Magn Reson Imaging,* 27**,** 700-9.
HASHIMOTO, H. & MUNRO, E. 2019. Differential Expression of a Classic Cadherin Directs Tissue-Level Contractile Asymmetry during Neural Tube Closure. *Dev Cell,* 51**,** 158-172 e4.
HASHIMOTO, H., ROBIN, F. B., SHERRARD, K. M. & MUNRO, E. M. 2015. Sequential contraction and exchange of apical junctions drives zippering and neural tube closure in a simple chordate. *Dev Cell,* 32**,** 241-55.

HEISSLER, S. M., CHINTHALAPUDI, K. & SELLERS, J. R. 2015. Kinetic characterization of the sole nonmuscle myosin-2 from the model organism Drosophila melanogaster. *FASEB J,* 29**,** 1456-66.

HELLER, E., KUMAR, K. V., GRILL, S. W. & FUCHS, E. 2014. Forces generated by cell intercalation tow epidermal sheets in mammalian tissue morphogenesis. *Dev Cell,* 28**,** 617-32.

HENRIQUE, D., ABRANCHES, E., VERRIER, L. & STOREY, K. G. 2015. Neuromesodermal progenitors and the making of the spinal cord. *Development,* 142**,** 2864-75.

HERTZLER, D. A., 2ND, DEPOWELL, J. J., STEVENSON, C. B. & MANGANO, F. T. 2010. Tethered cord syndrome: a review of the literature from embryology to adult presentation. *Neurosurg Focus,* 29**,** E1.

HISLOP, N. R., CADDY, J., TING, S. B., AUDEN, A., VASUDEVAN, S., KING, S. L., LINDEMAN, G. J., VISVADER, J. E., CUNNINGHAM, J. M. & JANE, S. M. 2008. Grhl3 and Lmo4 play coordinate roles in epidermal migration. *Dev Biol,* 321**,** 263-72.

HSU, P. D., LANDER, E. S. & ZHANG, F. 2014. Development and applications of CRISPR-Cas9 for genome engineering. *Cell,* 157**,** 1262-1278.

HUGHES, A., GREENE, N. D. E., COPP, A. J. & GALEA, G. L. 2018. Valproic acid disrupts the biomechanics of late spinal neural tube closure in mouse embryos. *Mech Dev,* 149**,** 20-26.

HUTSON, M. S., TOKUTAKE, Y., CHANG, M., BLOOR, J. W., VENAKIDES, S., KIEHART, D. P. & EDWARDS, G. S. 2003. Forces for Morphogenesis Investigated with Laser Microsurgery and Quantitative Modeling. *Science,* 300**,** 145-149.

HYAFIL, F., BABINET, C. & JACOB, F. 1981. Cell-Cell Interactions in Early Embryogenesis: A Molecular Approach to the Role of Calcium. *Cell,* 26**,** 447-454.

ITASAKI, N. 2015. Vertebrate Embryo: Neural Patterning. *eLS***,** 1-8.

JACOBS, J., ATKINS, M., DAVIE, K., IMRICHOVA, H., ROMANELLI, L., CHRISTIAENS, V., HULSELMANS, G., POTIER, D., WOUTERS, J., TASKIRAN, II, PACIELLO, G., GONZALEZ-BLAS, C. B., KOLDERE, D., AIBAR, S., HALDER, G. & AERTS, S. 2018. The transcription factor Grainy head primes epithelial enhancers for spatiotemporal activation by displacing nucleosomes. *Nat Genet,* 50**,** 1011-1020.

JARRETT, O., STOW, J. L., YAP, A. S. & KEY, B. 2002. Dynamin-dependent endocytosis is necessary for convergent extension movements in *Xenopus* animal cap explants. *Int J Dev Biol,* 46**,** 467-473.

JENSEN, P. J., TELEGAN, B., LAVKER, R. M. & WHEELOCK, M. J. 1997. E-cadherin and P-cadherin have partially redundant roles in human epidermal stratification. *Cell Tissue Res,* 288**,** 307-316.

JURANEK, J., FLETCHER, J. M., HASAN, K. M., BREIER, J. I., CIRINO, P. T., PAZO-ALVAREZ, P., DIAZ, J. D., EWING-COBBS, L., DENNIS, M. & PAPANICOLAOU, A. C. 2008. Neocortical reorganization in spina bifida. *Neuroimage,* 40**,** 1516-22.

JUSTICE, M. J., SIRACUSA, L. D. & STEWART, A. F. 2011. Technical approaches for mouse models of human disease. *Dis Model Mech,* 4**,** 305-10.

KALE, G. R., YANG, X., PHILIPPE, J.-M., MANI, M., LENNE, P.-F. & LECUIT, T. 2018. Distinct contributions of tensile and shear stress on E-cadherin levels during morphogenesis. *bioRxiv*.

KAMRAN, Z., ZELLNER, K., KYRIAZES, H., KRAUS, C. M., REYNIER, J. B. & MALAMY, J. E. 2017. In vivo imaging of epithelial wound healing in the cnidarian Clytia hemisphaerica demonstrates early evolution of purse string and cell crawling closure mechanisms. *BMC Dev Biol,* 17**,** 17.

KASHGARI, G., MEINECKE, L., GORDON, W., RUIZ, B., YANG, J., MA, A. L., XIE, Y., HO, H., PLIKUS, M. V., NIE, Q., JESTER, J. V. & ANDERSEN, B. 2020. Epithelial Migration and Non-adhesive Periderm Are Required for Digit Separation during Mammalian Development. *Dev Cell,* 52**,** 764-778 e4.

KASPERKIEWICZ, M., ELLEBRECHT, C. T., TAKAHASHI, H., YAMAGAMI, J., ZILLIKENS, D., PAYNE, A. S. & AMAGAI, M. 2017. Pemphigus. *Nat Rev Dis Primers,* 3**,** 17026.

KELLER, R., DAVIDSON, L., EDLUND, A., ELUL, T., EZIN, M., SHOOK, D. & SKOGLUND, P. 2000. Mechanisms of convergence and extension by cell intercalation. *Philos Trans R Soc Lond B Biol Sci,* 355**,** 897-922.

KERSBERGEN, A., BEST, S. A., DWORKIN, S., AH-CANN, C., DE VRIES, M. E., ASSELIN-LABAT, M. L., RITCHIE, M. E., JANE, S. M. & SUTHERLAND, K. D. 2018. Lung morphogenesis is orchestrated through Grainyhead-like 2 (Grhl2) transcriptional programs. *Dev Biol,* 443**,** 1-9.

KIBAR, Z., VOGAN, K. J., GROULX, N., JUSTICE, M. J., UNDERHILL, D. A. & GROS, P. 2001. Ltap, a mammalian homolog of *Drosophila Strabismus/Van Gogh*, is altered in the mouse neural tube mutant Loop-tail. *Nat Genet,* 28**,** 251-255.

KIECKER, C., BATES, T. & BELL, E. 2016. Molecular specification of germ layers in vertebrate embryos. *Cell Mol Life Sci,* 73**,** 923-47.

KILE, B. T. & HILTON, D. J. 2005. The art and design of genetic screens: mouse. *Nat Rev Genet,* 6**,** 557-67.

KIM, H. Y., JACKSON, T. R. & DAVIDSON, L. A. 2017. On the role of mechanics in driving mesenchymal-to-epithelial transitions. *Semin Cell Dev Biol,* 67**,** 113-122.

KIMURA-YOSHIDA, C., MOCHIDA, K., NAKAYA, M. A., MIZUTANI, T. & MATSUO, I. 2018. Cytoplasmic localization of GRHL3 upon epidermal differentiation triggers cell shape change for epithelial morphogenesis. *Nat Commun,* 9**,** 4059.

KIRKE, P. N., MOLLOY, A. M., DALY, L. E., BURKE, H., WEIR, D. G. & SCOTT, J. M. 1993. Maternal plasma folate and vitamin B_{12} are independent risk factors for neural tube defects. *Q J Med,* 86**,** 703-708.

KLAPHOLZ, B. & BROWN, N. H. 2017. Talin - the master of integrin adhesions. *J Cell Sci,* 130**,** 2435-2446.

KORENROMP, M. J., VAN GOOL, J. D., BRUINESE, H. W. & KRIEK, R. 1986. Early fetal leg movements in myelomeningocele. *The Lancet,* 327**,** 869-928.

KOVACS, E. M., GOODWIN, M., ALI, R. G., PATERSON, A. D. & YAP, A. S. 2002. Cadherin-Directed Actin Assembly: E-Cadherin Physically Associates with the Arp2/3 Complex to Direct Actin Assembly in Nascent Adhesive Contacts. *Curr Biol,* 12**,** 379-382.

KUDOH, T., CONCHA, M. L., HOUART, C., DAWID, I. B. & WILSON, S. W. 2004. Combinatorial Fgf and Bmp signalling patterns the gastrula ectoderm into prospective neural and epidermal domains. *Development,* 131**,** 3581-92.

KUDRYAVTSEVA, E. I., SUGIHARA, T. M., WANG, N., LASSO, R. J., GUDNASON, J. F., LIPKIN, S. M. & ANDERSEN, B. 2003. Identification and characterization of Grainyhead-like epithelial transactivator (GET-1), a novel mammalian Grainyhead-like factor. *Dev Dyn,* 226**,** 604-17.

KURODA, H., WESSELY, O. & DE ROBERTIS, E. M. 2004. Neural induction in Xenopus: requirement for ectodermal and endomesodermal signals via Chordin, Noggin, beta-Catenin, and Cerberus. *PLoS Biol,* 2**,** E92.

LAI, Z. C., WEI, X., SHIMIZU, T., RAMOS, E., ROHRBAUGH, M., NIKOLAIDIS, N., HO, L. L. & LI, Y. 2005. Control of cell proliferation and apoptosis by mob as tumor suppressor, mats. *Cell,* 120**,** 675-85.

LAM, M. S. Y., LISICA, A., RAMKUMAR, N., HUNTER, G., MAO, Y., CHARRAS, G. & BAUM, B. 2020. Isotropic myosin-generated tissue tension is required for the dynamic orientation of the mitotic spindle. *Mol Biol Cell,* 31**,** 1370-1379.

LANGE, A. W., SRIDHARAN, A., XU, Y., STRIPP, B. R., PERL, A. K. & WHITSETT, J. A. 2015. Hippo/Yap signaling controls epithelial progenitor cell proliferation and differentiation in the embryonic and adult lung. *J Mol Cell Biol,* 7**,** 35-47.

LANGILLE, B. L. & ADAMSON, S. L. 1980. Relationship between Blood Flow Direction and Endothelial Cell Orientation at Arterial Branch Sites in Rabbits and Mice. *Circ Res,* 48**,** 481-488.
LAPLANTE, C. & NILSON, L. A. 2011. Asymmetric distribution of Echinoid defines the epidermal leading edge during Drosophila dorsal closure. *J Cell Biol,* 192**,** 335-48.
LARUE, L., OHSUGI, M., HIRCHENHAIN, J. & KEMLER, R. 1994. E-cadherin null mutant embryos fail to form a trophectoderm epithelium. *Proc Natl Acad Sci U S A,* 91**,** 8263-8267.
LECUIT, T., LENNE, P. F. & MUNRO, E. 2011. Force generation, transmission, and integration during cell and tissue morphogenesis. *Annu Rev Cell Dev Biol,* 27**,** 157-84.
LEE, T., SHAH, C. & XU, E. Y. 2007. Gene trap mutagenesis: a functional genomics approach towards reproductive research. *Mol Hum Reprod,* 13**,** 771-9.
LEGLAND, D., ARGANDA-CARRERAS, I. & ANDREY, P. 2016. MorphoLibJ: integrated library and plugins for mathematical morphology with ImageJ. *Bioinformatics,* 32**,** 3532-3534.
LEMIRE, R. J. 1968. Variations in Development of the Caudal Neural Tube in Human Embryos (Horizons XIV-XXI). *Teratology,* 2**,** 361-370.
LETTS, V. A., SCHORK, N. J., COPP, A. J., BERNFIELD, M. & FRANKEL, W. N. 1995. A Curly-Tail Modifier Locus, *mct1*, on Mouse Chromosome 17. *Genomics,* 29.
LEUNG, K. Y., DE CASTRO, S. C., SAVERY, D., COPP, A. J. & GREENE, N. D. 2013. Nucleotide precursors prevent folic acid-resistant neural tube defects in the mouse. *Brain,* 136**,** 2836-41.
LEW, S. M. & KOTHBAUER, K. F. 2007. Tethered cord syndrome: an updated review. *Pediatr Neurosurg,* 43**,** 236-48.
LIANG, X., MICHAEL, M. & GOMEZ, G. A. 2016. Measurement of Mechanical Tension at Cell-cell Junctions Using Two-photon Laser Ablation. *Bio Protoc,* 6.
LINDQVIST, M., HORN, Z., BRYJA, V., SCHULTE, G., PAPACHRISTOU, P., AJIMA, R., DYBERG, C., ARENAS, E., YAMAGUCHI, T. P., LAGERCRANTZ, H. & RINGSTEDT, T. 2010. Vang-like protein 2 and Rac1 interact to regulate adherens junctions. *J Cell Sci,* 123**,** 472-83.
LIU, Z., VAN GRUNSVEN, L. A., VAN ROSSEN, E., SCHROYEN, B., TIMMERMANS, J. P., GEERTS, A. & REYNAERT, H. 2010. Blebbistatin inhibits contraction and accelerates migration in mouse hepatic stellate cells. *Br J Pharmacol,* 159**,** 304-15.
LOYER, N., KOLOTUEV, I., PINOT, M. & LE BORGNE, R. 2015. Drosophila E-cadherin is required for the maintenance of ring canals anchoring to mechanically withstand tissue growth. *Proc Natl Acad Sci U S A,* 112**,** 12717-22.
LUCAS, E. P., KHANAL, I., GASPAR, P., FLETCHER, G. C., POLESELLO, C., TAPON, N. & THOMPSON, B. J. 2013. The Hippo pathway polarizes the actin cytoskeleton during collective migration of Drosophila border cells. *J Cell Biol,* 201**,** 875-85.
MAHAFFEY, J. P., GREGO-BESSA, J., LIEM, K. F., JR. & ANDERSON, K. V. 2013. Cofilin and Vangl2 cooperate in the initiation of planar cell polarity in the mouse embryo. *Development,* 140**,** 1262-71.
MAK, L. L. 1978. Ultrastructural Studies of Amphibian Neural Fold Fusion. *Dev Biol,* 65**,** 435-446.
MANIOU, E., STADDON, M. F., MARSHALL, A. R., GREENE, N. D. E., COPP, A. J., BANERJEE, S. & GALEA, G. L. 2021. Hindbrain neuropore tissue geometry determines asymmetric cell-mediated closure dynamics in mouse embryos. *Proc Natl Acad Sci U S A,* 118.
MARCHAL, L., LUXARDI, G., THOME, V. & KODJABACHIAN, L. 2009. BMP inhibition initiates neural induction via FGF signaling and Zic genes. *Proc Natl Acad Sci U S A,* 106**,** 17437–17442.
MARINARI, E., MEHONIC, A., CURRAN, S., GALE, J., DUKE, T. & BAUM, B. 2012. Live-cell delamination counterbalances epithelial growth to limit tissue overcrowding. *Nature,* 484**,** 542-5.

MARTINEZ ARIAS, A. & STEVENTON, B. 2018. On the nature and function of organizers. *Development,* 145.

MASSA, V., GREENE, N. D. & COPP, A. J. 2009a. Do cells become homeless during neural tube closure? *Cell Cycle,* 8.

MASSA, V., SAVERY, D., YBOT-GONZALEZ, P., FERRARO, E., RONGVAUX, A., CECCONI, F., FLAVELL, R., GREENE, N. D. & COPP, A. J. 2009b. Apoptosis is not required for mammalian neural tube closure. *Proc Natl Acad Sci U S A,* 106**,** 8233-8238.

MATIS, M. & AXELROD, J. D. 2013. Regulation of PCP by the Fat signaling pathway. *Genes Dev,* 27**,** 2207-20.

MCCLEERY, W. T., VELDHUIS, J., BENNETT, M. E., LYNCH, H. E., MA, X., BRODLAND, G. W. & HUTSON, M. S. 2019. Elongated Cells Drive Morphogenesis in a Surface-Wrapped Finite-Element Model of Germband Retraction. *Biophys J,* 117**,** 157-169.

MCLAUGHLIN, M. E., KRUGER, G. M., SLOCUM, K. L., CROWLEY, D., MICHAUD, N. A., HUANG, J., MAGENDANTZ, M. & JACKS, T. 2007. The Nf2 tumor suppressor regulates cell– cell adhesion during tissue fusion. *Proc Natl Acad Sci U S A,* 104**,** 3261–3266.

MCSHANE, S. G., MOLE, M. A., SAVERY, D., GREENE, N. D., TAM, P. P. & COPP, A. J. 2015. Cellular basis of neuroepithelial bending during mouse spinal neural tube closure. *Dev Biol,* 404**,** 113-24.

MIKAWA, T., POH, A. M., KELLY, K. A., ISHII, Y. & REESE, D. E. 2004. Induction and patterning of the primitive streak, an organizing center of gastrulation in the amniote. *Dev Dyn,* 229**,** 422-32.

MIYAKE, Y., INOUE, N., NISHIMURA, K., KINOSHITA, N., HOSOYA, H. & YONEMURA, S. 2006. Actomyosin tension is required for correct recruitment of adherens junction components and zonula occludens formation. *Exp Cell Res,* 312**,** 1637-50.

MOLE, M. A., GALEA, G. L., ROLO, A., WEBERLING, A., NYCHYK, O., DE CASTRO, S. C., SAVERY, D., FASSLER, R., YBOT-GONZALEZ, P., GREENE, N. D. E. & COPP, A. J. 2020. Integrin-Mediated Focal Anchorage Drives Epithelial Zippering during Mouse Neural Tube Closure. *Dev Cell,* 52**,** 321-334 e6.

MONTELL, D. J., KESHISHIAN, H. & SPRADLING, A. C. 1991. Laser Ablation Studies of the Role of the Drosophila Oocyte Nucleus in Pattern Formation. *Science,* 254**,** 290-293.

MOOTHA, V. K., LINDGREN, C. M., ERIKSSON, K., SUBRAMANIAN, A., SIHAG, S., LEHAR, J., PUIGSERVER, P., CARLSSON, E., RIDDERSTRALE, M., LAURILA, E., HOUSTIS, N., DALY, M. J., PATTERSON, N., MESIROV, J. P., GOLUB, T. R., TAMAYO, P., SPIEGELMAN, B., LANDER, E. S., HIRSCHHORN, J. N., ALTSHULER, D. & GROOP, L. C. 2003. PGC-1α-responsive genes involved in oxidative phosphorylation are coordinately downregulated in human diabetes. *Nat Genet,* 34**,** 267-273.

MORELLI, L. G., URIU, K., ARES, S. & OATES, A. C. 2012. Computational Approaches to Developmental Patterning. *Science,* 336**,** 187-191.

MUNJAL, A. & LECUIT, T. 2014. Actomyosin networks and tissue morphogenesis. *Development,* 141**,** 1789-93.

MURDOCH, J. N., DAMRAU, C., PAUDYAL, A., BOGANI, D., WELLS, S., GREENE, N. D., STANIER, P. & COPP, A. J. 2014. Genetic interactions between planar cell polarity genes cause diverse neural tube defects in mice. *Dis Model Mech,* 7**,** 1153-63.

MURDOCH, J. N., DOUDNEY, K., PATERNOTTE, C., COPP, A. J. & STANIER, P. 2001. Severe neural tube defects in the loop-tail mouse result from mutation of Lpp1, a novel gene involved in floor plate specification. *Hum Mol Genet,* 10**,** 2593-2601.

MURDOCH, J. N., HENDERSON, D. J., DOUDNEY, K., GASTON-MASSUET, C., PHILLIPS, H. M., PATERNOTTE, C., ARKELL, R., STANIER, P. & COPP, A. J. 2003. Disruption of scribble (Scrb1) causes severe neural tube defects in the circletail mouse. *Hum Mol Genet,* 12**,** 87-98.

MURRELL, M., OAKES, P. W., LENZ, M. & GARDEL, M. L. 2015. Forcing cells into shape: the mechanics of actomyosin contractility. *Nat Rev Mol Cell Biol,* 16**,** 486-98.

NANES, B. A. & KOWALCZYK, A. P. 2012. Adherens junction turnover: regulating adhesion through cadherin endocytosis, degradation, and recycling. *Subcell Biochem,* 60**,** 197-222.

NEUMANN, P. E., FRANKEL, W. N., LETTS, V. A., COFFIN, J. M., COPP, A. J. & BERNFIELD, M. 1994. Multifactorial inheritance of neural tube defects: localization of the major gene and recognition of modifiers in *ct* mutant mice. *Nat Genet,* 6**,** 357-362.

NEW, D. A. T. 1966. Development of rat embryos cultured in blood sera. *J Reprod Fert,* 12**,** 509-524.

NEW, D. A. T. 1978. Whole-embryo culture and the study of mammalian embryos during organogenesis. *Biol Rev,* 53**,** 81-122.

NIETO, M. A. 2013. Epithelial plasticity: a common theme in embryonic and cancer cells. *Science,* 342**,** 1234850.

NIEUWKOOP, P. D. 1967. The "organization centre". II. Field phenomena, their origin and significance. *Acta Biothera,* 17**,** 151-177.

NIKOLOPOULOU, E., GALEA, G. L., ROLO, A., GREENE, N. D. & COPP, A. J. 2017. Neural tube closure: cellular, molecular and biomechanical mechanisms. *Development,* 144**,** 552-566.

NIKOLOPOULOU, E., HIRST, C. S., GALEA, G., VENTURINI, C., MOULDING, D., MARSHALL, A. R., ROLO, A., DE CASTRO, S. C. P., COPP, A. J. & GREENE, N. D. E. 2019. Spinal neural tube closure depends on regulation of surface ectoderm identity and biomechanics by Grhl2. *Nat Commun,* 10**,** 2487.

NOMURA, T. 1988. X-Ray and chemically induced germ-line mutation causing phenotypical anomalies in mice. *Mutation Research,* 198**,** 309-320.

NOWAKOWSKI, R. S., LEWIN, S. B. & MILLER, M. W. 1989. Bromodeoxyuridine immunohistochemical determination of the lengths of the cell cycle and the DNA-synthetic phase for an anatomically defined population. *J Neurocytol,* 18**,** 311-318.

NTIMBANI, J., KELLY, A. & LEKGWARA, P. 2020. Myelomeningocele - A literature review. *Interdisciplinary Neurosurgery,* 19.

NUSSLEIN-VOLHARD, C., WIESCHAUS, E. & KLUDING, H. 1984. Mutations affecting the pattern of the larval cuticle in *Drosophila melanogaster*. *Roux's Arch Dev Biol,* 193**,** 267-282.

OH, H. & IRVINE, K. D. 2009. In vivo analysis of Yorkie phosphorylation sites. *Oncogene,* 28**,** 1916-27.

OLIVERA-MARTINEZ, I., HARADA, H., HALLEY, P. A. & STOREY, K. G. 2012. Loss of FGF-dependent mesoderm identity and rise of endogenous retinoid signalling determine cessation of body axis elongation. *PLoS Biol,* 10**,** e1001415.

PAI, Y. J., LEUNG, K. Y., SAVERY, D., HUTCHIN, T., PRUNTY, H., HEALES, S., BROSNAN, M. E., BROSNAN, J. T., COPP, A. J. & GREENE, N. D. 2015. Glycine decarboxylase deficiency causes neural tube defects and features of non-ketotic hyperglycinemia in mice. *Nat Commun,* 6**,** 6388.

PALOMAKI, G. E., BUPP, C., GREGG, A. R., NORTON, M. E., OGLESBEE, D., BEST, R. G. & COMMITTEE, A. B. G. S. O. T. L. Q. A. 2020. Laboratory screening and diagnosis of open neural tube defects, 2019 revision: a technical standard of the American College of Medical Genetics and Genomics (ACMG). *Genet Med,* 22**,** 462-474.

PALTOGLOU, S., DAS, R., TOWNLEY, S. L., HICKEY, T. E., TARULLI, G. A., COUTINHO, I., FERNANDES, R., HANSON, A. R., DENIS, I., CARROLL, J. S., DEHM, S. M., RAJ, G. V., PLYMATE, S. R., TILLEY, W. D. & SELTH, L. A. 2017. Novel Androgen Receptor Coregulator GRHL2 Exerts Both Oncogenic and Antimetastatic Functions in Prostate Cancer. *Cancer Res,* 77**,** 3417-3430.

PAN, X., ZHANG, R., XIE, C., GAN, M., YAO, S., YAO, Y., JIN, J., HAN, T., HUANG, Y., GONG, Y., WANG, J. & YU, B. 2017. GRHL2 suppresses tumor metastasis via regulation of transcriptional activity of RhoG in non-small cell lung cancer. *Am J Transl Res,* 9**,** 4217-4226.

PANCIERA, T., AZZOLIN, L., CORDENONSI, M. & PICCOLO, S. 2017. Mechanobiology of YAP and TAZ in physiology and disease. *Nat Rev Mol Cell Biol,* 18**,** 758-770.

PARSONS, J. T., HORWITZ, A. R. & SCHWARTZ, M. A. 2010. Cell adhesion: integrating cytoskeletal dynamics and cellular tension. *Nat Rev Mol Cell Biol,* 11**,** 633-43.

PASAKARNIS, L., FREI, E., CAUSSINUS, E., AFFOLTER, M. & BRUNNER, D. 2016. Amnioserosa cell constriction but not epidermal actin cable tension autonomously drives dorsal closure. *Nat Cell Biol,* 18**,** 1161-1172.

PATTHEY, C., EDLUND, T. & GUNHAGA, L. 2009. Wnt-regulated temporal control of BMP exposure directs the choice between neural plate border and epidermal fate. *Development,* 136**,** 73-83.

PAUDYAL, A., DAMRAU, C., PATTERSON, V. L., ERMAKOV, A., FORMSTONE, C., LALANNE, Z., WELLS, S., LU, X., NORRIS, D. P., DEAN, C. H., HENDERSON, D. J. & MURDOCH, J. N. 2010. The novel mouse mutant, chuzhoi, has disruption of Ptk7 protein and exhibits defects in neural tube, heart and lung development and abnormal planar cell polarity in the ear. *BMC Dev Biol,* 10**,** 87.

PEDREIRA, D. A., REECE, E. A., CHMAIT, R. H., KONTOPOULOS, E. V. & QUINTERO, R. A. 2016. Fetoscopic repair of spina bifida: safer and better? *Ultrasound Obstet Gynecol,* 48**,** 141-7.

PEETERS, M. C., GEELEN, J. L. M. C., HEKKING, J. W., CHAVANNES, N., GERAEDTS, J. P. & VAN STRAATEN, H. W. 1998. Reduced Glucose Consumption in the Curly Tail Mouse Does Not Initiate the Pathogenesis Leading to Spinal Neural Tube Defects. *J. Nutr.,* 128**,** 1819-1828.

PEETERS, M. C., HEKKING, J. W., VAINAS, T., DRUKKER, J. & VAN STRAATEN, H. W. 1997. Spatio-temporal curvature pattern of the caudal body axis for non-mutant and *curly tail* mouse embryos during the period of caudal neural tube closure. *Anat Embryol,* 195**,** 259-266.

PEETERS, M. C., SHUM, A. S. W., HEKKING, J. W., COPP, A. J. & VAN STRAATEN, H. W. 1996. Relationship between altered axial curvature and neural tube closure in normal and mutant (curly tail) mouse embryos. *Anat Embryol,* 193**,** 123-130.

PENG, Y. & AXELROD, J. D. 2012. Asymmetric protein localization in planar cell polarity: mechanisms, puzzles, and challenges. *Curr Top Dev Biol,* 101**,** 33-53.

PERA, E. M., IKEDA, A., EIVERS, E. & DE ROBERTIS, E. M. 2003. Integration of IGF, FGF, and anti-BMP signals via Smad1 phosphorylation in neural induction. *Genes Dev,* 17**,** 3023-8.

PICCOLO, S., DUPONT, S. & CORDENONSI, M. 2014. The biology of YAP/TAZ: hippo signaling and beyond. *Physiol Rev,* 94**,** 1287-312.

QUAN, Y., XU, M., CUI, P., YE, M., ZHUANG, B. & MIN, Z. 2015. Grainyhead-like 2 Promotes Tumor Growth and is Associated with Poor Prognosis in Colorectal Cancer. *J Cancer,* 6**,** 342-50.

RAMSBOTTOM, S. A., SHARMA, V., RHEE, H. J., ELEY, L., PHILLIPS, H. M., RIGBY, H. F., DEAN, C., CHAUDHRY, B. & HENDERSON, D. J. 2014. Vangl2-regulated polarisation of second heart field-derived cells is required for outflow tract lengthening during cardiac development. *PLoS Genet,* 10**,** e1004871.

RAY, H. J. & NISWANDER, L. A. 2016. Grainyhead-like 2 downstream targets act to suppress epithelial-to-mesenchymal transition during neural tube closure. *Development,* 143**,** 1192-204.

REESE, R. M., HARRISON, M. M. & ALARID, E. T. 2019. Grainyhead-like Protein 2: The Emerging Role in Hormone-Dependent Cancers and Epigenetics. *Endocrinology,* 160**,** 1275-1288.

RIDLEY, A. J. 2011. Life at the leading edge. *Cell,* 145**,** 1012-22.
RIFAT, Y., PAREKH, V., WILANOWSKI, T., HISLOP, N. R., AUDEN, A., TING, S. B., CUNNINGHAM, J. M. & JANE, S. M. 2010. Regional neural tube closure defined by the Grainy head-like transcription factors. *Dev Biol,* 345**,** 237-45.
ROBINSON, M. D. & OSHLACK, A. 2010a. A scaling normalization method for differential expression analysis of RNA-seq data. *Genome Biology,* 11.
ROBINSON, M. D. & OSHLACK, A. 2010b. A scaling normalization method for differential expression analysis of RNA-seq data. *Genome Biol,* 11.
ROGERS, C. D., MOODY, S. A. & CASEY, E. S. 2009. Neural induction and factors that stabilize a neural fate. *Birth Defects Res C Embryo Today,* 87**,** 249-62.
ROLO, A., ESCUIN, S., GREENE, N. D. E. & COPP, A. J. 2016a. Rho GTPases in mammalian spinal neural tube closure. *Small GTPases,* 9**,** 283-289.
ROLO, A., SAVERY, D., ESCUIN, S., DE CASTRO, S. C., ARMER, H. E., MUNRO, P. M., MOLE, M. A., GREENE, N. D. & COPP, A. J. 2016b. Regulation of cell protrusions by small GTPases during fusion of the neural folds. *Elife,* 5**,** e13273.
ROTHS, J. B., FOXWORTH, W. B., MCARTHUR, M. J., MONTGOMERY, C. A. & KIER, A. B. 1999. Spontaneous and engineered mutant mice as models for experimental and comparative pathology: History, comparison, and developmental technology. *Lab Animal Sci,* 49**,** 12-34.
ROZARIO, T. & DESIMONE, D. W. 2010. The extracellular matrix in development and morphogenesis: a dynamic view. *Dev Biol,* 341**,** 126-40.
SAADAI, P. & FARMER, D. L. 2012. Fetal surgery for myelomeningocele. *Clin Perinatol,* 39**,** 279-88.
SADLER, T. W. 1979. Culture of early somite mouse embryos during organogenesi. *J Embryol Exp Morph,* 49**,** 17-25.
SAGNER, A. & BRISCOE, J. 2019. Establishing neuronal diversity in the spinal cord: a time and a place. *Development,* 146.
SAMARAGE, C. R., WHITE, M. D., ALVAREZ, Y. D., FIERRO-GONZALEZ, J. C., HENON, Y., JESUDASON, E. C., BISSIERE, S., FOURAS, A. & PLACHTA, N. 2015. Cortical Tension Allocates the First Inner Cells of the Mammalian Embryo. *Dev Cell,* 34**,** 435-47.
SAWYER, J. M., HARRELL, J. R., SHEMER, G., SULLIVAN-BROWN, J., ROH-JOHNSON, M. & GOLDSTEIN, B. 2010. Apical constriction: a cell shape change that can drive morphogenesis. *Dev Biol,* 341**,** 5-19.
SCHINDELIN, J., ARGANDA-CARRERAS, I., FRISE, E., KAYNIG, V., LONGAIR, M., PIETZSCH, T., PREIBISCH, S., RUEDEN, C., SAALFELD, S., SCHMID, B., TINEVEZ, J. Y., WHITE, D. J., HARTENSTEIN, V., ELICEIRI, K., TOMANCAK, P. & CARDONA, A. 2012. Fiji: an open-source platform for biological-image analysis. *Nat Methods,* 9**,** 676-82.
SCHNEIDER, D., BARONSKY, T., PIETUCH, A., ROTHER, J., OELKERS, M., FICHTNER, D., WEDLICH, D. & JANSHOFF, A. 2013. Tension monitoring during epithelial-to-mesenchymal transition links the switch of phenotype to expression of moesin and cadherins in NMuMG cells. *PLoS One,* 8**,** e80068.
SCHNEIDER, M. R. & KOLLIGS, F. T. 2015. E-cadherin's role in development, tissue homeostasis and disease: Insights from mouse models: Tissue-specific inactivation of the adhesion protein E-cadherin in mice reveals its functions in health and disease. *Bioessays,* 37**,** 294-304.
SCHOENWOLF, G. C. 1984. Histological and Ultrastructural Studies of Secondary Neurulation in Mouse Embryos. *American J of Anat,* 169**,** 361-376.
SCHOENWOLF, G. C. & DELONGO, J. 1980. Ultrastructure of Secondary Neurulation in the Chick Embryo. *American J of Anat,* 158**,** 43-63.
SCHOENWOLF, G. C. & FRANKS, M. V. 1984. Quantitative Analyses of Changes in Cell Shapes during Bending of the Avian Neural Plate. *Dev Biol,* 105**,** 257-272.

SHELLARD, A., SZABO, A., TREPAT, X. & MAYOR, R. 2018. Supracellular contraction at the rear of neural crest cell groups drives collective chemotaxis. *Science,* 362**,** 339-343.
SHEN, M. M. 2007. Nodal signaling: developmental roles and regulation. *Development,* 134**,** 1023-34.
SHEWAN, A. M., MADDUGODA, M., KRAEMER, A., STEHBENS, S. J., VERMA, S., KOVACS, E. M. & YAP, A. S. 2005. Myosin 2 is a key Rho kinase target necessary for the local concentration of E-cadherin at cell-cell contacts. *Mol Biol Cell,* 16**,** 4531-42.
SHIMAMURA, K. & TAKEICHI, M. 1992. Local and transient expression of E-cadherin involved in mouse embryonic brain morphogenesis. *Development,* 116**,** 1011-1019.
SHINDO, A. 2018. Models of convergent extension during morphogenesis. *Wiley Interdiscip Rev Dev Biol,* 7.
SHOJA, M. M., JOHAL, J., OAKES, W. J. & TUBBS, R. S. 2018. Embryology and pathophysiology of the Chiari I and II malformations: A comprehensive review. *Clin Anat,* 31**,** 202-215.
SHOOK, D. & KELLER, R. 2003. Mechanisms, mechanics and function of epithelial-mesenchymal transitions in early development. *Mech Dev,* 120**,** 1351-83.
SHUM, A. S., TANG, L. S., COPP, A. J. & ROELINK, H. 2010. Lack of motor neuron differentiation is an intrinsic property of the mouse secondary neural tube. *Dev Dyn,* 239**,** 3192-203.
SHUM, A. S. W. & COPP, A. J. 1996. Regional differences in morphogenesis of the neuroepithelium suggest multiple mechanisms of spinal neurulation in the mouse. *Anat Embryol,* 194**,** 65-73.
SMITH, L. J. & STEIN, K. F. 1962. Axial Elongation in the Mouse and its Retardation in Homozygous Looptail Mice. *J Embryol Exp Morph,* 10**,** 73-87.
SMUTNY, M., BEHRNDT, M., CAMPINHO, P., RUPRECHT, V. & HEISENBERG, C. P. 2015. UV laser ablation to measure cell and tissue-generated forces in the zebrafish embryo in vivo and ex vivo. *Methods Mol Biol,* 1189**,** 219-35.
SPEMANN, H. & MANGOLD, H. 1924. Induction of Embryonic Primordia by Implantation of Organizers from a Different Species. *Arch Mikr Anat Entw Mech,* 100**,** 599-638.
STANFORD, W. L., COHN, J. B. & CORDES, S. P. 2001. Gene-trap mutagenesis: Past, present and beyond. *Nat Rev Genet,* 2**,** 756-768.
STEIN, K. F. & RUDIN, I. A. 1953. Development of mice homozygous for the gene for looptail. *J Hered,* 44**,** 59-69.
STEMPLE, D. L. 2005. Structure and function of the notochord: an essential organ for chordate development. *Development,* 132**,** 2503-12.
STERN, C. D. 2005. Neural induction: old problem, new findings, yet more questions. *Development,* 132**,** 2007-21.
STIEFEL, D., SHIBATA, T., MEULI, M., DUFFY, P. G. & COPP, A. J. 2003. Tethering of the spinal cord in mouse fetuses and neonates with spina bifida. *J Neurosurg,* 99**,** 206-213.
STOREY, K. G., GORIELY, A., SARGENT, C. M., BROWN, J. M., BURNS, H. D., ABUD, H. M. & HEATH, J. K. 1998. Early posterior neural tissue is induced by FGF in the chick embryo. *Development,* 125**,** 473-484.
STRONG, L. C. & HOLLANDER, W. F. 1949. Hereditary Loop-Tail in the House Mouse: Accompanied by Imperforate Vagina and with Lethal Craniorachischisis When Homozygous. *J Hered,* 40**,** 329-334.
SUBRAMANIAN, A., TAMAYO, P., MOOTHA, V. K., MUKHERJEE, S., EBERT, B. L., GILLETTE, M. A., PAULOVICH, A., POMEROY, S. L., GOLUB, T. R., LANDER, E. S. & MESIROV, J. P. 2005. Gene set enrichment analysis: A knowledge-based approach for interpreting genome-wide expression profiles. *Proc Natl Acad Sci U S A,* 102**,** 15545-15550.
SUDIWALA, S., DE CASTRO, S. C., LEUNG, K. Y., BROSNAN, J. T., BROSNAN, M. E., MILLS, K., COPP, A. J. & GREENE, N. D. 2016. Formate supplementation enhances folate-dependent nucleotide biosynthesis and prevents spina bifida in a mouse model of folic acid-resistant neural tube defects. *Biochimie,* 126**,** 63-70.

SUNDARARAJAN, V., PANG, Q. Y., CHOOLANI, M. & HUANG, R. Y.-J. 2020. Spotlight on the Granules (Grainyhead-Like Proteins) – From an Evolutionary Conserved Controller of Epithelial Trait to Pioneering the Chromatin Landscape. *Frontiers in Molecular Biosciences,* 7.

SUZUKI, M., MORITA, H. & UENO, N. 2012. Molecular mechanisms of cell shape changes that contribute to vertebrate neural tube closure. *Dev Growth Differ,* 54**,** 266-76.

TAKAOKA, K. & HAMADA, H. 2012. Cell fate decisions and axis determination in the early mouse embryo. *Development,* 139**,** 3-14.

TAPON, N., HARVEY, K. F., BELL, D. W., WAHRER, D. C. R., SCHIRIPO, T. A., HABER, D. A. & HARIHARAN, I. K. 2002. *salvador* Promotes Both Cell Cycle Exit and Apoptosis in *Drosophila* and Is Mutated in Human Cancer Cell Lines. *Cell,* 110**,** 467-478.

THOMAS, W. A., BOSCHER, C., CHU, Y. S., CUVELIER, D., MARTINEZ-RICO, C., SEDDIKI, R., HEYSCH, J., LADOUX, B., THIERY, J. P., MEGE, R. M. & DUFOUR, S. 2013. alpha-Catenin and vinculin cooperate to promote high E-cadherin-based adhesion strength. *J Biol Chem,* 288**,** 4957-69.

TIAN, T., LEI, Y., CHEN, Y., KARKI, M., JIN, L., FINNELL, R. H., WANG, L. & REN, A. 2020. Somatic mutations in planar cell polarity genes in neural tissue from human fetuses with neural tube defects. *Hum Genet*.

TING, S. B., CADDY, J., WILANOWSKI, T., AUDEN, A., CUNNINGHAM, J. M., ELIAS, P. M., HOLLERAN, W. M. & JANE, S. M. 2005. The Epidermis of Grhl3-Null Mice Displays Altered Lipid Processing and Cellular Hyperproliferation. *Organogenesis,* 2**,** 33-35.

TING, S. B., WILANOWSKI, T., AUDEN, A., HALL, M., VOSS, A. K., THOMAS, T., PAREKH, V., CUNNINGHAM, J. M. & JANE, S. M. 2003a. Inositol- and folate-resistant neural tube defects in mice lacking the epithelial-specific factor Grhl-3. *Nat Med,* 9**,** 1513-9.

TING, S. B., WILANOWSKI, T., CERRUTI, L., ZHAO, L. L., CUNNINGHAM, J. M. & JANE, S. M. 2003b. The identification and characterization of human Sister-of-Mammalian Grainyhead (SOM) expands the *grainyhead*-like family of developmental transcription factors. *Biochem J,* 370**,** 953-962.

TODOROVIĆ, V., KLIGYS, K. R., DUSEK, R. L., JONES, J. C. R. & GREEN, K. J. 2013. Desmosomes and Hemidesmosomes. *Encyclopedia of Biological Chemistry.*

TORBAN, E., WANG, H. J., GROULX, N. & GROS, P. 2004. Independent mutations in mouse Vangl2 that cause neural tube defects in looptail mice impair interaction with members of the Dishevelled family. *J Biol Chem,* 279**,** 52703-13.

TORBAN, E., WANG, H. J., PATENAUDE, A. M., RICCOMAGNO, M., DANIELS, E., EPSTEIN, D. & GROS, P. 2007. Tissue, cellular and sub-cellular localization of the Vangl2 protein during embryonic development: effect of the Lp mutation. *Gene Expr Patterns,* 7**,** 346-54.

TORRES-REYES, L. A., ALVARADO-RUIZ, L., PIÑA-SÁNCHEZ, P., MARTÍNEZ-SILVA, M. G., RAMOS-SOLANO, M., OLIMÓN-ANDALÓN, V., ORTIZ-LAZARENO, P. C., HERNÁNDEZ-FLORES, G., BRAVO-CUELLAR, A., AGUILAR-LEMARROY, A. & JAVE-SUAREZ, L. F. 2014. Expression of transcription factor grainyhead-like 2 is diminished in cervical cancer. *Int J Clin Exp Pathol,* 7**,** 7409-7418.

TSAI, P. S., BLINDER, P., MIGLIORI, B. J., NEEV, J., JIN, Y., SQUIER, J. A. & KLEINFELD, D. 2009. Plasma-mediated ablation: an optical tool for submicrometer surgery on neuronal and vascular systems. *Curr Opin Biotechnol,* 20**,** 90-9.

TSENG, Q., DUCHEMIN-PELLETIER, E., DESHIERE, A., BALLAND, M., GUILLOU, H., FILHOL, O. & THERY, M. 2012. Spatial organization of the extracellular matrix regulates cell-cell junction positioning. *Proc Natl Acad Sci U S A,* 109**,** 1506-11.

TUNGGAL, J. A., HELFRICH, I., SCHMITZ, A., SCHWARZ, H., GUNZEL, D., FROMM, M., KEMLER, R., KRIEG, T. & NIESSEN, C. M. 2005. E-cadherin is essential for in vivo epidermal barrier function by regulating tight junctions. *EMBO J,* 24**,** 1146-56.

TZOUANACOU, E., WEGENER, A., WYMEERSCH, F. J., WILSON, V. & NICOLAS, J. F. 2009. Redefining the progression of lineage segregations during mammalian embryogenesis by clonal analysis. *Dev Cell,* 17**,** 365-76.

UEDA, Y., KIMURA-YOSHIDA, C., MOCHIDA, K., TSUME, M., KAMEO, Y., ADACHI, T., LEFEBVRE, O., HIRAMATSU, R. & MATSUO, I. 2020. Intrauterine Pressures Adjusted by Reichert's Membrane Are Crucial for Early Mouse Morphogenesis. *Cell Rep,* 31**,** 107637.

UV, A. E., THOMPSON, C. R. L. & BRAY, S. J. 1994. The Drosophila Tissue-Specific Factor Grainyhead Contains Novel DNA-Binding and Dimerization Domains Which Are Conserved in the Human Protein CP2. *Mol Cell Biol,* 14**,** 4020-4031.

VAN ALLEN, M. I., KALOUSEK, D. K., CHERNOFF, G. F., JURILOFF, D., HARRIS, M., MCGILLIVRAY, B. C., YONG, S., LANGLOIS, S., MACLEOD, P. M., CHITAYAT, D., FRIEDMAN, J. M., WILSON, R. D., MCFADDEN, D., PANTZAR, J., RITCHIE, S. & HALL, J. G. 1993. Evidence for Multi-Site Closure of the Neural Tube in Humans. *American J of Med Genet,* 47**,** 723-743.

VAN STRAATEN, H. W. M. & COPP, A. J. 2001. *Curly tail*: a 50 year history of the mouse spina bifida model. *Anat Embryol,* 203**,** 225-237.

VAN STRAATEN, H. W. M. & HEKKING, J. W. M. 1991. Development of floor plate, neurons and axonal outgrowth pattern in the early spinal cord of the notochord-deficient chick embryo. *Anat Embryol,* 184**,** 55-63.

VAN STRAATEN, H. W. M., HEKKING, J. W. M., WIERTZ-HOESSELS, E. J. L. M., THORS, F. & DRUKKER, J. 1988. Effect of the notochord on the differentiation of a floor plate area in the neural tube of the chick embryo. *Anat Embryol,* 177**,** 317-324.

VERBRUGGEN, S. W., KAINZ, B., SHELMERDINE, S. C., HAJNAL, J. V., RUTHERFORD, M. A., ARTHURS, O. J., PHILLIPS, A. T. M. & NOWLAN, N. C. 2018. Stresses and strains on the human fetal skeleton during development. *J R Soc Interface,* 15.

VICENTE-MANZANARES, M., WEBB, D. J. & HORWITZ, A. R. 2005. Cell migration at a glance. *J Cell Sci,* 118**,** 4917-9.

WALLINGFORD, J. B. 2002. Neural tube closure requires Dishevelled-dependent convergent extension of the midline. *Development,* 129**,** 5815-5825.

WANG, J., MARK, S., ZHANG, X., QIAN, D., YOO, S. J., RADDE-GALLWITZ, K., ZHANG, Y., LIN, X., COLLAZO, A., WYNSHAW-BORIS, A. & CHEN, P. 2005. Regulation of polarized extension and planar cell polarity in the cochlea by the vertebrate PCP pathway. *Nat Genet,* 37**,** 980-5.

WANG, X., FREIRE VALLS, A., SCHERMANN, G., SHEN, Y., MOYA, I. M., CASTRO, L., URBAN, S., SOLECKI, G. M., WINKLER, F., RIEDEMANN, L., JAIN, R. K., MAZZONE, M., SCHMIDT, T., FISCHER, T., HALDER, G. & RUIZ DE ALMODOVAR, C. 2017. YAP/TAZ Orchestrate VEGF Signaling during Developmental Angiogenesis. *Dev Cell,* 42**,** 462-478 e7.

WATERMAN, R. E. 1976. Topographical Changes Along the Neural Fold Associated with Neurulation in the Hamster and Mouse. *Am J Anat,* 146**,** 151-172.

WATT, F. M. & HODIVALA, K. J. 1994. Fibronectin and integrin knockouts come unstuck. *Curr Biol,* 4**,** 270-272.

WERNER, S., FREY, S., RIETHDORF, S., SCHULZE, C., ALAWI, M., KLING, L., VAFAIZADEH, V., SAUTER, G., TERRACCIANO, L., SCHUMACHER, U., PANTEL, K. & ASSMANN, V. 2013. Dual roles of the transcription factor grainyhead-like 2 (GRHL2) in breast cancer. *J Biol Chem,* 288**,** 22993-3008.

WERTH, M., WALENTIN, K., AUE, A., SCHONHEIT, J., WUEBKEN, A., PODE-SHAKKED, N., VILIANOVITCH, L., ERDMANN, B., DEKEL, B., BADER, M., BARASCH, J., ROSENBAUER, F., LUFT, F. C. & SCHMIDT-OTT, K. M. 2010. The transcription factor grainyhead-like 2 regulates the molecular composition of the epithelial apical junctional complex. *Development,* 137**,** 3835-45.

WHITE, M. D., BISSIERE, S., ALVAREZ, Y. D. & PLACHTA, N. 2016. Mouse Embryo Compaction. *Curr Top Dev Biol,* 120**,** 235-58.

WILANOWSKI, T., CADDY, J., TING, S. B., HISLOP, N. R., CERRUTI, L., AUDEN, A., ZHAO, L. L., ASQUITH, S., ELLIS, S., SINCLAIR, R., CUNNINGHAM, J. M. & JANE, S. M. 2008. Perturbed desmosomal cadherin expression in grainy head-like 1-null mice. *EMBO J,* 27**,** 886-97.

WILANOWSKI, T., TUCKFIELD, A., CERRUTI, L., O'CONNELL, S., SAINT, R., PAREKH, V., TAO, J., CUNNINGHAM, J. M. & JANE, S. M. 2002. A highly conserved novel family of mammalian developmental transcription factors related to *Drosophila grainyhead*. *Mech Dev,* 114**,** 37-50.

WILLIAMS, B. B., CANTRELL, V. A., MUNDELL, N. A., BENNETT, A. C., QUICK, R. E. & JESSEN, J. R. 2012. VANGL2 regulates membrane trafficking of MMP14 to control cell polarity and migration. *J Cell Sci,* 125**,** 2141-7.

WILLIAMS, M., YEN, W., LU, X. & SUTHERLAND, A. 2014. Distinct apical and basolateral mechanisms drive planar cell polarity-dependent convergent extension of the mouse neural plate. *Dev Cell,* 29**,** 34-46.

WU, S., LIU, Y., ZHENG, Y., DONG, J. & PAN, D. 2008. The TEAD/TEF family protein Scalloped mediates transcriptional output of the Hippo growth-regulatory pathway. *Dev Cell,* 14**,** 388-98.

WU, Y. I., FREY, D., LUNGU, O. I., JAEHRIG, A., SCHLICHTING, I., KUHLMAN, B. & HAHN, K. M. 2009. A genetically encoded photoactivatable Rac controls the motility of living cells. *Nature,* 461**,** 104-8.

XIONG, F., MA, W., BENAZERAF, B., MAHADEVAN, L. & POURQUIE, O. 2020. Mechanical Coupling Coordinates the Co-elongation of Axial and Paraxial Tissues in Avian Embryos. *Dev Cell*.

YAMAGUCHI, Y. & MIURA, M. 2013. How to form and close the brain: insight into the mechanism of cranial neural tube closure in mammals. *Cell Mol Life Sci,* 70**,** 3171-86.

YANAGISHITA, M. 1993. Function of proteoglycans in the extracellular matrix. *Acta Pathologica Japonica,* 43**,** 283-293.

YANG, X., VASUDEVAN, P., PAREKH, V., PENEV, A. & CUNNINGHAM, J. M. 2013. Bridging cancer biology with the clinic: relative expression of a GRHL2-mediated gene-set pair predicts breast cancer metastasis. *PLoS One,* 8**,** e56195.

YBOT-GONZALEZ, P., COGRAM, P., GERRELLI, D. & COPP, A. J. 2002. Sonic hedgehog and the molecular regulation of mouse neural tube closure. *Development,* 129**,** 2507-2517.

YBOT-GONZALEZ, P. & COPP, A. J. 1999. Bending of the Neural Plate During Mouse Spinal Neurulation Is Independent ofActin Microfilaments. *Dev Dyn,* 215**,** 273-283.

YBOT-GONZALEZ, P., GASTON-MASSUET, C., GIRDLER, G., KLINGENSMITH, J., ARKELL, R., GREENE, N. D. & COPP, A. J. 2007a. Neural plate morphogenesis during mouse neurulation is regulated by antagonism of Bmp signalling. *Development,* 134**,** 3203-11.

YBOT-GONZALEZ, P., SAVERY, D., GERRELLI, D., SIGNORE, M., MITCHELL, C. E., FAUX, C. H., GREENE, N. D. & COPP, A. J. 2007b. Convergent extension, planar-cell-polarity signalling and initiation of mouse neural tube closure. *Development,* 134**,** 789-99.

YIN, H., COPLEY, C. O., GOODRICH, L. V. & DEANS, M. R. 2012. Comparison of phenotypes between different vangl2 mutants demonstrates dominant effects of the Looptail mutation during hair cell development. *PLoS One,* 7**,** e31988.

YONEMURA, S., WADA, Y., WATANABE, T., NAGAFUCHI, A. & SHIBATA, M. 2010. alpha-Catenin as a tension transducer that induces adherens junction development. *Nat Cell Biol,* 12**,** 533-42.

YU, Z., LIN, K. K., BHANDARI, A., SPENCER, J. A., XU, X., WANG, N., LU, Z., GILL, G. N., ROOP, D. R., WERTZ, P. & ANDERSEN, B. 2006. The Grainyhead-like epithelial transactivator Get-

1/Grhl3 regulates epidermal terminal differentiation and interacts functionally with LMO4. *Dev Biol,* 299**,** 122-36.

YUAN, M., WANG, J. & FANG, F. 2020. Grainyhead-Like Genes Family May Act as Novel Biomarkers in Colon Cancer. *Onco Targets Ther,* 13**,** 3237-3245.

ZHANG, H., LIU, C. Y., ZHA, Z. Y., ZHAO, B., YAO, J., ZHAO, S., XIONG, Y., LEI, Q. Y. & GUAN, K. L. 2009. TEAD transcription factors mediate the function of TAZ in cell growth and epithelial-mesenchymal transition. *J Biol Chem,* 284**,** 13355-62.